Nanomechanics of two-dimensional materials: From tuning phonons to probing excitons

Dissertation
zur Erlangung des Grades eines
Doktors der Naturwissenschaften *(Dr. rer. nat.)*

am Fachbereich Physik
der Freien Universität Berlin

vorgelegt von
Jan Niklas Kirchhof

Berlin, 2023

Erstgutachter: Prof. Dr. Kirill I. Bolotin
Zweitgutachterin: Prof. Dr. Stephanie Reich
Drittgutachter: Prof. Dr. Tobias Korn

Tag der Disputation: 3. Mai 2024

Für meine Familie.

Abstract

Nanoelectromechanical systems (NEMS) based on two-dimensional (2D) materials represent the ultimate – atomic-scale – size limit for the miniaturization of mechanical devices. When employed as resonators, these devices bring a range of remarkable features. Due to their small effective mass, they oscillate at very high frequencies (up to gigahertz). Furthermore, it is easy to drive them in their non-linear regime. Additionally, they come with the exceptional ability to broadly tune their resonance frequencies. In this thesis, I realize two unique systems capitalizing on these properties.

First, I conceptualize a tunable phononic crystal made from graphene. By periodically patterning a suspended graphene membrane, I transform it into the world's thinnest possible phononic crystal. This device features a phononic band gap in the megahertz range, which we can broadly tune using an electrostatic gating approach. Under electrostatic pressure up to 30 kPa, we observe a frequency upshift of the entire phononic system by 350 %. In the next step, we demonstrate full control of the band gap size. By carefully tension engineering our suspended phononic crystal, we are able to dynamically reduce the size of the phononic band gap – down to completely closing it. This change in hierarchy/topology in the phononic band structure can be seen as the mechanical simulation of a metal-insulator transition (mMIT). Upon placing an artificial irregularity in our phononic lattice, we can spatially localize a mechanical 'defect mode'. This mode is mechanically isolated from its environment, which makes it a highly coherent mechanical oscillator and a potential reservoir for storing quantum information. By taking advantage of our tunable system, we can now control the frequency and the degree of localization of the defect mode, which allows us to dynamically couple it to external excitations. Finally, we make use of the mMIT by constructing and studying a phononic transistor analog, which is controlled by simply applying a gate voltage and has an on/off ratio of 10^5 (100 dB).

Second, I develop a platform for nanomechanical spectroscopy (NMS) of 2D materials. Specifically, I show that a purely mechanical measurement can be used as an ultrasensitive spectroscopic probe for transition metal dichalcogenides (TMDs) and plasmonic nanostructures. We extract the optical absorption of a 2D material from frequency shifts of a hybrid NEMS resonator vs. the wavelength of incoming light. In combination with optical reflectivity data, we derive — without any further assumptions — the full dielectric function of the material under study. Our measurement is fast (τ_{rise} = 135 ns), sensitive (noise-equivalent power: NEP = 890 fW/$\sqrt{\text{Hz}}$) and we can characterize 2D materials in a broad spectral range of 1.2 – 3.1 eV. This method is a direct measurement of absorption, which has practical advantages compared to common optical spectroscopy approaches. Furthermore, while being comparable in performance, it overcomes limitations inherent to conventional optical methods, such as the complications associated with measurements at high magnetic fields and low temperatures.

Summarizing, I developed a concept to add tunability to the field of phononics and an approach to spectroscopically characterize 2D materials based on mechanical measurements. These are powerful tools to realize tunable condensed matter physics analogs in phononic systems and to observe hitherto undetected phenomena in 2D materials.

Kurzfassung

Nanoelektromechanische Systeme (NEMS) auf der Basis zweidimensionaler (2D)-Materialien stellen die ultimative – atomare – Größenbegrenzung für die Miniaturisierung mechanischer Systeme dar. Wenn diese als Resonatoren eingesetzt werden, bringen sie eine Reihe bemerkenswerter Eigenschaften mit sich. Aufgrund ihrer geringen effektiven Masse oszillieren sie mit sehr hohen Frequenzen (bis in den Gigahertz-Bereich). Darüber hinaus lassen sie sich leicht in ihren nichtlinearen Bereich betreiben. Zusätzlich verfügen sie über die außergewöhnliche Funktionalität, dass man ihre Resonanzfrequenzen breit abzustimmen kann. In dieser Dissertation realisiere ich zwei einzigartige nanomechanische Systeme, die auf diesen Eigenschaften beruhen.

Erstens konzipiere ich einen abstimmbaren phononisches Kristall aus Graphen. Durch die Implementation eines periodischen Musters in eine freistehenden Graphenmembran verwandle ich diese in den dünnsten phononische Kristall der Welt. Dieser weist eine phononische Bandlücke im Megahertz-Bereich auf, die wir mittels eines elektrostatischen Gating-Ansatzes breit abstimmen können. Unter einem elektrostatischem Druck von bis zu 30 kPa beobachten wir eine Frequenzverschiebung des gesamten phononischen Systems von 350 %. Im nächsten Schritt demonstrieren wir die vollständige Kontrolle über die Größe der phononischen Bandlücke. Durch eine sorgfältfige Manipulation der mechanischen Spannung in unserem freistehendem phononischen Kristalls sind wir in der Lage die Größe der phononischen Bandlücke dynamisch zu reduzieren – bis sie sich vollständig schließt. Diese Änderung in der Hierarchie/Topologie der phononischen Bandstruktur kann als mechanische Simulation eines Metall-Isolator-Übergangs (mMIT) betrachtet werden. Durch das Platzieren einer künstlichen Unregelmäßigkeit in unserem phononischen Gitter können wir eine mechanische "Defektmode" räumlich lokalisieren. Diese Mode ist mechanisch von der Umgebung isoliert, was sie zu einem hochkohärenten mechanischen Oszillator und zu einem potenziellen Reservoir zur Speicherung von Quanteninformationen macht. Durch die Nutzung unseres abstimmbaren Systems können wir nun sowohl die mechanische Frequenz als auch den Grad der Lokalisierung der Defektmode kontrollieren. Das ermöglicht uns, sie dynamisch an externe Anregungen zu koppeln. Schließlich nutzen wir den mMIT, indem wir einen Transistor für Phononen konstruieren und untersuchen. Dieser Transistor kann durch das Anlegen einer Gate-Spannung gesteuert werden und weißt ein On/Off-Verhältnis von 10^5 (100 dB) auf.

Zweitens entwickle ich eine Plattform für die nanomechanische Spektroskopie (NMS) von 2D-Materialien. Insbesondere zeige ich, dass eine rein mechanische Messung zur ultrasensitiven spektroskopischen Charakterisierung von Übergangsmetall-Dichalkogeniden (TMDs) und plasmonische Nanostrukturen verwendet werden kann. Dafür extrahieren wir die optische Absorption eines 2D-Materials aus Frequenzverschiebungen eines hybriden NEMS-Resonators in Abhängigkeit von der Wellenlänge des einfallenden Lichts. In Kombination mit Messungen der optischen Reflektivität leiten wir – ohne weitere Annahmen – die komplette dielektrische Funktion des untersuchten Materials her. Dabei ist unsere Messung schnell (τ_{rise} = 135 ns), empfindlich (Äquivalente Rauschleistung: NEP = 890 fW/$\sqrt{\text{Hz}}$) und wir können 2D-Materialien in einem breiten Spektralbereich von 1.2 – 3.1 eV charakterisieren. Unsere Methode ist eine direkte Messung der Absorption, die praktische Vorteile gegenüber klassischen optischen Spektroskopiemethoden bietet. Darüber hinaus überwindet sie, bei vergleichbarer Spezifizierung, Einschränkungen klassischer optischer Methoden, wie die Komplikationen bei Messungen in hohen magnetischen Feldern und niedrigen Temperaturen.

List of publications

1. *Towards tunable graphene phononic crystals.*
   Y. Yu*, **J. N. Kirchhof***, A. Tsarapkin, V. Deinhart, O. Yucel, B. Höfer, K. Höflich, and K. I. Bolotin.
   Under review, Preprint: arXiv:2305.09577 (2023).

2. *Nanomechanical absorption spectroscopy of 2D materials with femtowatt sensitivity.*
   J. N. Kirchhof, Y. Yu, D. Yagodkin, N. Stetzuhn, D. B. de Araújo, K. Kanellopulos, S. Manas-Valero, E. Coronado, H. van der Zant, S. Reich, S. Schmid, and K. I. Bolotin.
   2D Materials **10**(3), 035012 (2023).

3. *Mechanically-tunable bandgap closing in 2D graphene phononic crystals.*
   J. N. Kirchhof and K. I. Bolotin.
   npj 2D Materials and Applications **7**, 10 (2023).

4. *Strain control of hybridization between dark and localized excitons in a 2D semiconductor.*
   P. Hernández López*, S. Heeg*, C. Schattauer, S. Kovalchuk, A. Kumar, D. J. Bock, **J. N. Kirchhof**, B. Höfer, K. Greben, D. Yagodkin, L. Linhart, F. Libisch, and K. I. Bolotin.
   Nature Communications **13**(1), 7691 (2022).

5. *Generating intense electric fields in 2D materials by dual ionic gating.*
   B. I. Weintrub, Y. Hsieh, S. Kovalchuk, **J. N. Kirchhof**, K. Greben, and K. I. Bolotin.
   Nature Communications **13**(1), 6601 (2022).

6. *Nanomechanical spectroscopy of 2D materials.*
   J. N. Kirchhof, Y. Yu, G. Antheaume, G. Gordeev, D. Yagodkin, P. Elliott, D. B. de Araújo, S. Sharma, S. Reich, and K. I. Bolotin.
   Nano Letters **22**(20), 8037–8044 (2022).

7. *Non-uniform strain engineering of 2D materials.*
   S. Kovalchuk*, **J. N. Kirchhof***, K. I Bolotin, and M. G. Harats.
   Israel Journal of Chemistry **62**(3-4), e202100115 (2022).

8. *Impact of gigahertz and terahertz transport regimes on spin propagation and conversion in the antiferromagnet IrMn.*

* Authors contributed equally to this work

O. Gueckstock, R. L. Seeger, T. S. Seifert, S. Auffret, S. Gambarelli, **J. N. Kirchhof**, K. I. Bolotin, V. Baltz, T. Kampfrath, and L. Nádvorník.
Applied Physics Letters **120**(6), 062408 (2022).

9. *The patterning toolbox FIB-o-mat: Exploiting the full potential of focused helium ions for nanofabrication.*
V. Deinhart, L. Kern, **J. N. Kirchhof**, S. Juergensen, J. Sturm, E. Krauss, T. Feichtner, S. Kovalchuk, M. Schneider, D. Engel, B. Pfau, B. Hecht, K. I. Bolotin, S. Reich, and K. Höflich.
Beilstein Journal of Nanotechnology **12**(1), 304-318 (2021).

10. *Tunable graphene phononic crystal.*
J. N. Kirchhof, K. Weinel, S. Heeg, V. Deinhart, S. Kovalchuk, K. Hoeflich, and K. I. Bolotin.
Nano Letters **21**(5), 2174–2182 (2020).

11. *In situ functionalization of graphene.*
K. Greben, S. Kovalchuk, A. M. Valencia, **J. N. Kirchhof**, S. Heeg, P. Rietsch, S. Reich, C. Cocchi, S. Eigler, and K. I. Bolotin.
2D Materials **8**(1), 015022 (2020).

12. *Neutral and charged excitons interplay in non-uniformly strain-engineered WS_2.*
S. Kovalchuk, M. G. Harats, G. López-Polín, **J. N. Kirchhof**, K. Höflich, and K. I. Bolotin.
2D Materials **7**(3), 035024 (2020).

13. *Dynamics and efficient conversion of excitons to trions in non-uniformly strained monolayer WS_2.*
M. G. Harats, **J. N. Kirchhof**, M. Qiao, K. Greben, and K. I. Bolotin.
Nature Photonics **14**(5), 324-329 (2020).

14. *Controlled assembly of artificial 2D materials based on the transfer of oxo-functionalized graphene.*
M. Hußmann, B. Weintrub, P. Feicht, G. Germer, **J. N. Kirchhof**, K. I. Bolotin, and S. Eigler.
Nanoscale Advances **2**(1), 176-181 (2020).

15. *Selective functionalization of graphene at defect-activated sites by arylazocarboxylic tert-butyl esters.*
C. E. Halbig, R. Lasch, J. Krüll, A. S. Pirzer, Z. Wang, **J. N. Kirchhof**, K. I. Bolotin, M. R. Heinrich, and S. Eigler.
Angewandte Chemie International Edition **58**(11), 3599-3603 (2019).

16. *Influence of SiO_2 or h-BN substrate on the room-temperature electronic transport in chemically derived single layer graphene.*
    Z. Wang, Q. Yao, Y. Hu, C. Li, M. Hußmann, B. Weintrub, **J. N. Kirchhof**, K. Bolotin, T. Taniguchi, K. Watanabe, and S. Eigler.
    RSC Advances **9** (65), 38011-38016 (2019).

17. *Microstructure and elastic constants of transition metal dichalcogenide monolayers from friction and shear force microscopy.*
    X. Xu, T. Schultz, Z. Qin, N. Severin, B. Haas, S. Shen, **J. N. Kirchhof**, A. Opitz, C. T. Koch, K. I. Bolotin, J. P Rabe, G. Eda, and N. Koch.
    Advanced Materials **30** (39), 1803748 (2018).

18. *Detecting ultrasound vibrations with graphene resonators.*
    G. J. Verbiest, **J. N. Kirchhof**, J. Sonntag, M. Goldsche, T. Khodkov, and C. Stampfer.
    Nano Letters **18** (8), 5132-5137 (2018).

Contents

1. Introduction

Throughout history, mankind has always strived to find stronger and at the same time lighter materials to build tools. Another key aspect became important in the last 100 years: The ability to minimize the spatial dimensions (miniaturization) of those 'tools' for fast and efficient electronic devices. Graphene combines these apparently opposite qualities in one material. It is the strongest material known (roughly 100 times stronger than steel) while being very lightweight [1, 2]. Furthermore, it maintains its structural integrity down to the atomic scale due to its layered structure and is therefore ideal for miniaturization [3]. Finally, graphene is an excellent electrical conductor [4, 5]. This combination of properties is unique in nature and invites us to create and study small and light, yet remarkably strong and flexible mechanical structures made from graphene. Because of that, over the last two decades, graphene has been implemented into nanoelectromechanical systems (NEMS), which enabled key experiments on non-linear dynamics [6–10], magnetic phase transitions [11, 12], or photothermal backaction effects [13–15] and makes an extremely sensitive probe for atomic-scale masses [16–19] and minuscule forces [19–21].

In this thesis (Fig. 1.1), I aim to contribute to that list by describing how graphene and other 2D materials can be used to (i) realize tunable phononic crystals, which allow studying phononic analogs of condensed matter phenomena and may become useful for mechanical storage of quantum information and (ii) develop new device concepts to perform nanomechanical spectroscopy, which may be more sensitive, more broadly applicable, and less prone to measurement artifacts than conventional optical approaches. Both goals rely on the control of tension (σ) in suspended 2D materials. In the first case, we apply electrostatic pressure to a graphene phononic crystal to change its tension and thereby manipulate its phononic band structure. In the second case, the absorption of light changes the tension in a 2D material, which is detected as a shift of the mechanical resonance frequency. The tunability of the presented phononic crystal is based on increasing tension in graphene. In contrast, in our nanomechanical spectroscopy approach, we detect absorbed light via the controllable release of tension in 2D materials.

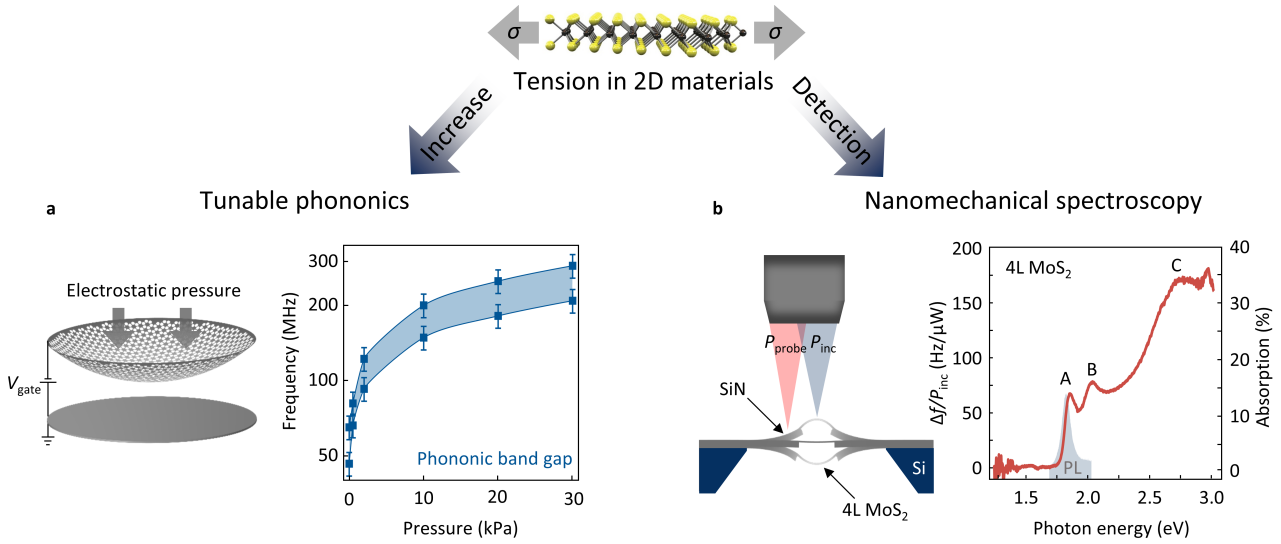

Figure 1.1: Thesis overview: Controlling tension in 2D materials. a, By periodic pattering we transform a suspended 2D material membrane into a phononic crystal. This highly flexible device can be mechanically manipulated by electrostatic gating. This allows us to increase the tension and tune the size and position of the phononic band gap. The phononic band gap vs. applied pressure is plotted in blue. **b**, When a 2D material-based resonator absorbs incoming light (P_{inc}), it heats up and tension is released. This induces a downshift in resonance frequency, which allows us to detect absorbed light and perform nanomechanical spectroscopy – as shown for a 4L MoS_2 sample, which features clear signatures of excitons (A, B, and C). Figure adapted from Ref. [22] and [23]. The illustration of the 2D material is taken from Ref. [24].

1.1. Tunable phononic crystals

A phononic crystal (PnC) is an artificially manufactured structure with a periodic variation of material properties, e.g. stiffness, mass, or stress [25, 26]. This periodic perturbation creates a meta-crystallographic order in the system leading to a vibrational band structure hosting acoustic Bloch waves, in analogy to the electronic band structure in solids (details in Sec. 2.5). A phononic crystal can thus control the propagation of phonons similarly to how a photonic crystal controls the propagation of photons [25–28]. In contrast to conventional solids, the lattice parameters of phononic crystals can be broadly varied and hence allow realizing analogs of fundamental solid-state physics phenomena over a vast range of sizes (10 nm – 1 m) and frequencies (Hz – THz) [29]. The patterning also allows to open phononic band gaps. In the frequency range of the band gap, no mechanical modes are allowed, and any incoming excitation is exponentially damped. A phononic band gap is a powerful tool for guiding [30–32], focusing [33–35], or suppressing phonons [25–28, 30]. Within these phononic band gaps, it is possible to engineer mechanical modes, which are localized on artificial irregularities (defect modes) [36–40]. These vibrational defect modes can be compared to localized mid-gap defect states in semiconductors. Defect modes in phononic lattices

are mechanically isolated from the environment, which reduces bending and radiation losses [36–38]. This leads to record-breaking high mechanical quality factors (Qs) of 10^6 to 10^8 [36–38]. These ultra-coherent resonances form an attractive platform for quantum information technology at room temperature, as their decoherence time exceeds the period of the oscillation [36, 38, 41].

Typically PnCs are made from silicon (Si) or silicon nitride (SiN) and feature lattice parameters in the order of 100 µm. These materials have excellent mechanical properties [42–46], and established complementary metal-oxide-semiconductor (CMOS) fabrication methods allow producing large (mm-size) and robust phononic crystals made from these materials. At the same time, Si or SiN membranes require a minimum thickness on the order of tens of nm. This makes them rigid, thus allowing operation only at fixed frequencies and limiting tunable coupling between mechanical entities. Furthermore, the lack of flexibility in common PnCs prevents accessing different mechanical states (e.g. insulating and conductive) or dynamic control of phonons. We want to overcome these limitations by combining the fields of phononics and 2D materials.

In our endeavor towards this goal, we design, fabricate, and simulate the thinnest possible phononic crystal made from suspended monolayer graphene [22]. Our approach for a tunable phononic crystal is based on a suspended graphene membrane, which we pattern into a PnC by cutting a periodic array of holes (Fig. 1.1a). We choose suspended graphene for its outstanding flexibility and mechanical tunability. The available size of suspended graphene, however, is limited compared to Si or SiN, and we must minimize the features of our phononic crystal beyond the resolution of classical lithography and find a way to pattern sensitive suspended graphene membranes. We overcome this by developing a suitable protocol using He-ion lithography, which makes it possible to reproducibly pattern suspended graphene with a resolution of 10 nm [22, 47]. In our device design, the suspended graphene PnC is electrically contacted and forms a capacitor with a closely-spaced gate electrode. Applying a voltage (V_{gate}) to the gate electrode induces an electrostatic pressure, which causes the entire PnC to deflect and allows us to manipulate the in-plane tension (Fig. 1.1a). This concept for mechanical tuning of a phononic crystal made from a suspended membrane allows us to realize the following key results:

First, we show that our system can be mechanically tuned over a broad range of frequencies. An increase in tension upshifts the entire phononic spectrum as the velocities (and thus the frequencies) of all phonons in a material depend on its tension (σ). In Fig. 1.1a, we plot the simulated tuning of the phononic band gap (blue) vs. applied pressure for a circular sample. The phononic band gap is highly sensitive to applied pressure and broadly tunable. For a realistic applied pressure of 30 kPa, we obtain more than 350 % tuning of the band gap position and thereby access a new regime of tunable phononics. This adds a new experimental knob to phononic systems, which provides dynamic control comparable to gating in electronic structures/systems.

Second, having shown that we can broadly tune the position of the phononic band gap in our graphene PnCs, we also demonstrate control of the band gap size. More precisely, we can controllably close the phononic band gap and thereby induce a transition from a mechanically insulating state to a mechanically conductive state. Such a change in hierarchy/topology in the phononic band structure can be seen as a mechanical analog to a metal-insulator transition (mMIT). Inducing this transition is based on engineering the tension distribution within the suspended phononic crystal (quantified by the degree of uniaxility σ_{xx}/σ_{yy}). Once this ratio reaches a critical value of 1.7, the phononic band gap closes and the device is no longer mechanically insulating. We design a device geometry where σ_{xx}/σ_{yy} is tuned by applying a gate voltage to a rectangular PnC, and that allows us to induce and probe the mMIT in realistic finite-size samples.

Third, we use our tunable phononic crystal to localize a mechanical mode on an artificial 'defect' in the center of the device. This defect mode is expected to show a strongly enhanced Q since it is decoupled from its environment and hence may be used to store quantum information. As we can fully control the phononic band gap in terms of position and size, we can now also control the frequency and degree of localization of the defect mode. For a circular sample, the defect mode stays within the band gap when pressure is applied and thus retains its localization. This will allow tunable resonant coupling to external systems. For a rectangular device, the band gap closes as we apply pressure. This is an effective way of controlling the coupling of the mode to its environment (controllable dephasing) and may potentially be useful for dispersive read-out. Furthermore, by reducing the size of the band gap, we are able to control bending and radiation losses and thereby will gain new insights into the mechanical dissipation channels in resonators based on 2D materials.

Fourth, we propose a transistor for MHz-frequency acoustic phonons based on the above-described mMIT. Our device shows an on/off ratio of 10^5 (100 dB suppression) and can be operated by simply applying a gate voltage of reasonable size (8 V). This is a valuable extension for phonon logic applications and invites the realization of a variety of logic gates in the future.

In summary, we have realized gate-tunable phononic crystals made from suspended graphene and thereby added a new experimental knob to phononics, which allows us to dynamically manipulate the phononic band gap over a large range of frequencies [22]. With this additional degree of freedom, it is possible to explore tunable phononic analogs to phenomena in condensed matter physics (e.g. phase transitions), which we demonstrate by presenting the mechanical equivalent of a metal-insulator transition [48].

1.2. Nanomechancial spectroscopy of 2D materials

Spectroscopic methods have been used to uncover a vast range of new physical phenomena in two-dimensional (2D) materials over the last decades. In particular, materials from the group of transition metal dichalcogenides (TMDs) feature a remarkable zoo of correlated phases including excitonic insulators [49, 50], Wigner crystals [51, 52], Bose-Einstein condensates [53, 54], and superconductors [55]. All these phenomena can be studied by analyzing the dielectric function, which fully describes the light-matter interaction in solids. Real and imaginary components of the dielectric function (ϵ_1 and ϵ_2) contain information regarding light absorption, propagation velocity, excitonic and plasmonic resonances, band gaps, and many-body effects. The dielectric function is usually experimentally determined via ellipsometry [56–59], by combining reflection and transmission measurements [60], or from spectrally resolved reflection contrast ($\Delta R/R$) using the Kramers-Kronig relations [61–63]. Despite the broad applicability of these techniques, they are hard or impossible to apply in many situations. For example, optical measurements under oblique angles, as required by ellipsometry measurements, are challenging at low temperatures, ultra-high vacuum environments, and/or high magnetic fields. Measurements of transmission require large and thin samples on transparent substrates and may be affected by scattering. The Kramers-Kronig analysis requires broadband measurements of reflection and depends on empirical models of the optical constants.

For 2D materials, these problems become more severe due to their limited sample size and sensitivity to their surrounding. To observe the above-mentioned correlated states, one requires uniform high-quality samples. Such samples are typically encapsulated in hexagonal boron nitride or suspended and are limited to sample sizes in the single-digit micron range. Transmission or ellipsometry measurements of such nanostructures at ultralow temperatures or high magnetic fields are challenging. Especially when studying plasmons or polaritons in patterned 2D materials in the form of photonic [64, 65] or phononic crystals [22], new optical characterization methods are needed. In addition, excitons in 2D materials are strongly screened by the dielectric environment. This screening perturbs the dielectric function which, influences the Kramers-Kronig analysis.

On the positive side, 2D materials have remarkable mechanical properties, and their atomic thickness allows for the fabrication of small and light NEMS resonators. These 2D material-based resonators have a reduced effective mass, increased resonance frequencies, easily accessible nonlinear regime, and the ability to tune resonance frequencies [66, 67]. This is a major technological boost, which allows using such resonators as probes for magnetic fields [68, 69], sound [19, 70–72], gases [19, 73], or even to study live bacteria [74]. The question I want to answer is, how can we use NEMS resonators to perform spectroscopy of 2D materials and thereby overcome the above-mentioned limitations of classical optical spectroscopy methods?

To realize such a nanomechanical spectroscopy (NMS) approach we need to design a nanomechanical resonator that controllably responds to the absorption of light in a 2D material of interest. Our sample design for this consists of a 2D material on top of a SiN membrane (Fig. 1.1b). The two components form a hybrid resonator, where they oscillate together in phase. When the resonator absorbs incoming light (P_{inc}), its average temperature increases, which results in a reduced resonance frequency as the in-plane tension is released due to thermal expansion. By varying the photon energy of the incoming light and monitoring the corresponding frequency shifts, we can extract the absorption coefficient of the 2D material (Fig. 1.1b). In combination with optical reflectivity data, we derive – without any further assumptions – the full dielectric function of the 2D material under study.

Although NMS has many fundamental advantages, our first approach lacks the sensitivity provided by state-of-the-art optical approaches, so in the following step, we improve the measurement sensitivity. The key points for achieving this are stress reduction in the SiN membranes and thermal decoupling of the 2D material, which leads to an enhanced response to absorbed light. This reduces the noise equivalent power (NEP) of NMS by two orders of magnitude, down to NEP = 890 fW/$\sqrt{\mathrm{Hz}}$. At the same time, we simplify the method by using base actuation, which allows us to study electrically insulating materials, makes sample loading straightforward, and provides a simple, yet robust calibration. Overall, our approach of using NEMS resonators to perform spectroscopy of 2D materials led to the following key results/advantages:

First, by restoring the full dielectric function, without any assumptions of other underlying optical constants, we are able to capture the complete picture of light-matter interaction effects in the studied 2D material. At the same time, our measurements are fast (τ_{rise} = 135 ns) and sensitive (NEP = 890 fW/$\sqrt{\mathrm{Hz}}$), and we can determine the dielectric function for TMD materials in the range 1.2 – 3.1 eV.

Second, in our approach, the 2D material is suspended and therefore unaffected by substrate-related screening- or doping effects. Additionally, we are able to prevent unwanted interaction with the probe laser, as we can measure the mechanical resonance via the SiN substrate (red beam in Fig. 1.1b).

Third, we do not require complicated transmission measurements or measurements at oblique angles, and therefore NMS should function at low temperatures and high magnetic fields. Also, our approach works well for small sample sizes ($\sim$ 1 µm).

Fourth, by using the 2D material itself to detect absorbed light, we can potentially access a broad spectral range from THz to UV, allowing us to study a large variety of 2D materials. Furthermore, the underlying detection mechanism of NMS is insensitive to the scattering of light and should in principle allow discriminating between scattered and absorbed light.

In summary, we have developed a nanomechanical platform to spectroscopically characterize 2D materials. Our approach is fast, broadband, and sensitive, and it provides fundamental advantages. We use NMS to study a range of (exotic) 2D structures with high resolution. This includes classic TMDs such as MoS_2, WS_2, and WSe_2, a layered magnetic semiconductor $CrPS_4$, from the class of ternary TMDs, and a plasmonic meta-structure consisting of gold nanoparticles. NMS paves the way to study the optical properties of 2D materials, where classical methods are limited, and will help to discover new physics in 2D materials.

1.3. Thesis outline

In a nutshell, the goals of this thesis are to conceptualize tunable phononic systems and to develop a sensitive nanomechanical probe to perform spectroscopy of 2D materials. As both goals employ 2D materials, I will first introduce 2D materials and motivate their use for our nanomechanical devices (Sec. 2.1). Next, I will describe their equations of motion in order to establish a common language regarding nanoelectromechanical resonators (Sec. 2.2). Then, I will present how 2D material-based resonators can be experimentally characterized (Sec. 2.3) and mechanically tuned (Sec. 2.4). Following this, I will discuss how 2D membranes can be transformed into phononic crystals by periodic patterning (Sec. 2.5). I will further explain the detection of light using nanomechanical resonators (Sec. 2.6). In chapter 3, I state my contribution to the publications forming this thesis, followed by chapter 4, which explains the connection between the papers. Finally, I summarize the results and give an outlook towards future experiments (Ch. 5).

2. Nanomechanics of two-dimensional materials

2.1. Graphene and transition metal dichalcogenides

I start by introducing 2D materials and discussing the reasons that prompted us to choose them to realize our nanoelectromechanical systems. Graphene is a single layer of carbon atoms arranged in a hexagonal lattice with a thickness given by the interlayer distance of graphite ($t = 3.35$ Å). It was first isolated by mechanical exfoliation in 2004 [3] and since then has been the subject of intense research due to its unique combination of mechanical [1, 2], electrical [4, 5], and thermal properties [75]. Graphene is an excellent conductor of electricity and heat, and it is also incredibly strong and flexible. These properties make it a promising material for a wide range of technological applications [76], including electronics, energy storage, biomedical devices, and nanoelectromechanical systems (NEMS) [66, 67]. At the same time, graphene is an ideal playground to explore fundamental physics questions, e.g. tunable superconductivity [77], relativistic fermions [4], fractional quantum hall effect [78], and ballistic charge transport at room temperature [4] (to name a few).

Every carbon atom in graphene forms a covalent sp^2 bond with its three nearest neighbors (as shown in Fig. 2.1a). The covalent bond is the strongest type of atomic bond and is responsible for graphene's record high Young's modulus $E = 1$ TPa [1]. This high in-plane stiffness combined with an intrinsically low defect density yields graphene's incredible breaking strength of 130 GPa [1]. To put this value into relation, one would need an elephant balanced on a pencil in order to break through a sheet of graphene with the thickness of plastic wrap (12.7 µm) as sketched in Fig. 2.1b [79].

The orbital of the fourth valence electron is oriented perpendicular to the graphene plane, where it forms delocalized bands of electrons. These π-bands dominate graphene's electronic and optical properties. The unit cell contains two atoms and is defined by the lattice vectors $\mathbf{a}_1$ and $\mathbf{a}_2$, as shown in Fig. 2.1c. The carbon atoms are separated by $d_{\text{C-C}} = 1.422$ Å and the lattice vectors have a length of $\sqrt{3}d_{\text{C-C}}$. The corresponding first Brillouin zone of graphene is a hexagon with the Γ point at its center and the high symmetry points M, K, and K' along its perimeter (Fig. 2.1d). The electronic band structure of graphene shows a linear dispersion around the K and K' points. Therefore graphene is a highly conductive semi-metal and can show electron mobilities up to $\mu = 200\,000\,\text{cm}^2\text{V}^{-1}\text{s}^{-1}$ [80]. The linear band structure also defines the optical absorption within graphene, which is mostly constant ($\sim 2.3\,\%$) over a large range of photon energies [81].

Shortly after the discovery of graphene, other 2D materials were also isolated by mechanical exfoliation [83]. This started with the class of binary transition metal dichalcogenides (TMDs) in the form MX_2, where M stands for a transition metal atom (Mo, W, etc.) and X represents a

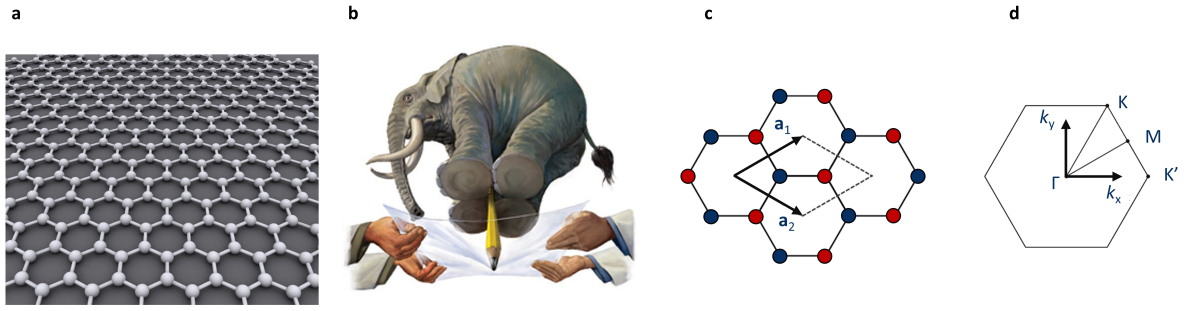

Figure 2.1: Lattice structure of graphene. a, Sketch of graphene on the atomic scale. The lattice is made up of carbon atoms (spheres) bound by covalent bonds and arranged in a hexagonal lattice. **b**, Visualization of graphene's mechanical strength: One would need an elephant balanced on a pencil in order to pierce through a sheet of graphene with the thickness of plastic wrap (12.7 µm) [79]. **c**, Unit cell of graphene's hexagonal crystal structure with the lattice vectors $\mathbf{a}_1$ and $\mathbf{a}_2$. **d**, The corresponding first Brillouin zone with the high-symmetry points Γ, K, and M – connected by the high symmetry lines. Figure panels (a) and (b) are taken from Ref. [82] and Ref. [79] respectively.

chalcogen atom (S, Se or Te). TMDs form a layered two-dimensional crystal with the metal atoms sandwiched between chalcogen atoms (Fig. 2.2a). In this lattice structure, each metal atom is bonded to six chalcogen atoms, forming trigonal prismatic coordination. The chalcogen atoms, on the other hand, are bonded to three metal atoms. The resulting lattice is composed of alternating molybdenum and sulfur atoms, which form a hexagonal pattern (Fig. 2.2b). TMDs in their 2H phase are semiconductors, and when they are thinned down to monolayer thickness they feature a direct band gap in the visible range [84], as shown in Fig. 2.2c. TMDs can host a variety of excitons, which are bound states of an electron and a hole that are attracted to each other by the electrostatic Coulomb force [83–85]. Due to their confinement to two dimensions and reduced dielectric screening, excitons in TMDs have large binding energies (~ 500 meV) and dominate the optical properties even at room temperature. TMDs are less conductive than graphene and have much lower charge carrier mobilities, however, they can be turned into an electrically insulating 'off' state and thus can be used as a channel material for transistors [24, 86, 87]. They also have a lower breaking strength and Young's modulus, but much more exciting optical properties and significantly stronger light-matter interaction than graphene.

2.2. 2D materials in motion

This section aims to describe the dynamics of suspended 2D materials to provide a background for understanding the mechanical systems studied in this thesis. To this end, I derive the equations of motion for a suspended membrane and briefly compare them to experimental results. A commonly

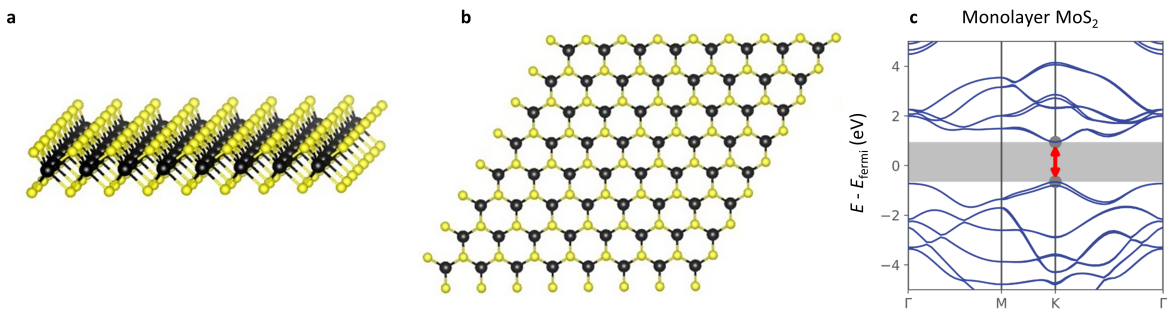

Figure 2.2: Lattice structure of TMDs. a, Atomic structure of a TMD monolayer. The metal atoms are shown in black and the chalcogen atoms are shown in yellow. **b**, Top view of a hexagonal TMD monolayer. **c**, Electronic band structure of a MoS_2 monolayer. The material features a direct band gap at the K point. The images in (a) and (b) are taken from Ref. [88]. Figure panel (c) is adapted from Ref. [89].

used sample concept for a 2D material-based NEMS resonator is shown in Fig. 2.3a. The device consists of a back gate (Si) separated by a layer of SiO_2 from the suspended 2D material, which is electrically contacted through a film of gold (Au). In the center of the device, the 2D material is suspended and can move freely. Before we look at a specific device, I start by describing the generalized motion of any mechanical resonator in the linear regime (following Ref. [90]). The complete, three-dimensional motion is given by the vector displacement function $\mathbf{R}(\mathbf{x}, t)$, which can be divided into an infinite number of independent modes. Assigning a label n to each mode, we can express the displacement function as:

$$\mathbf{R}(\mathbf{x}, t) = \sum_n a_\mathrm{n}(t)\mathbf{r}_\mathrm{n}(\mathbf{x}). \tag{2.1}$$

Here $\mathbf{r}_\mathrm{n}(\mathbf{x})$ describes the spatial mode shape of the n^{th} resonance mode, while the time dependence of the resonator's motion is given by the function $a_\mathrm{n}(t)$. Next, we normalize $\mathbf{r}_\mathrm{n}(\mathbf{x})$ such that the maximum value of $|\mathbf{r}_n(\mathbf{x})|$ equals unity. This normalization ensures that $a_\mathrm{n}(t)$ has units of distance and is in direct correspondence with the resonator's displacement at the point of measurement. For simple geometries (e.g. circular or square membrane), the mode shape ($\mathbf{r}_\mathrm{n}(\mathbf{x})$) can be calculated analytically, while for more complex geometries finite element method (FEM) simulations are needed.

In most cases, the motion of a mechanical resonator can be reduced to a one-dimensional displacement function (e.g. in the out-of-plane direction for a 2D membrane, as illustrated in

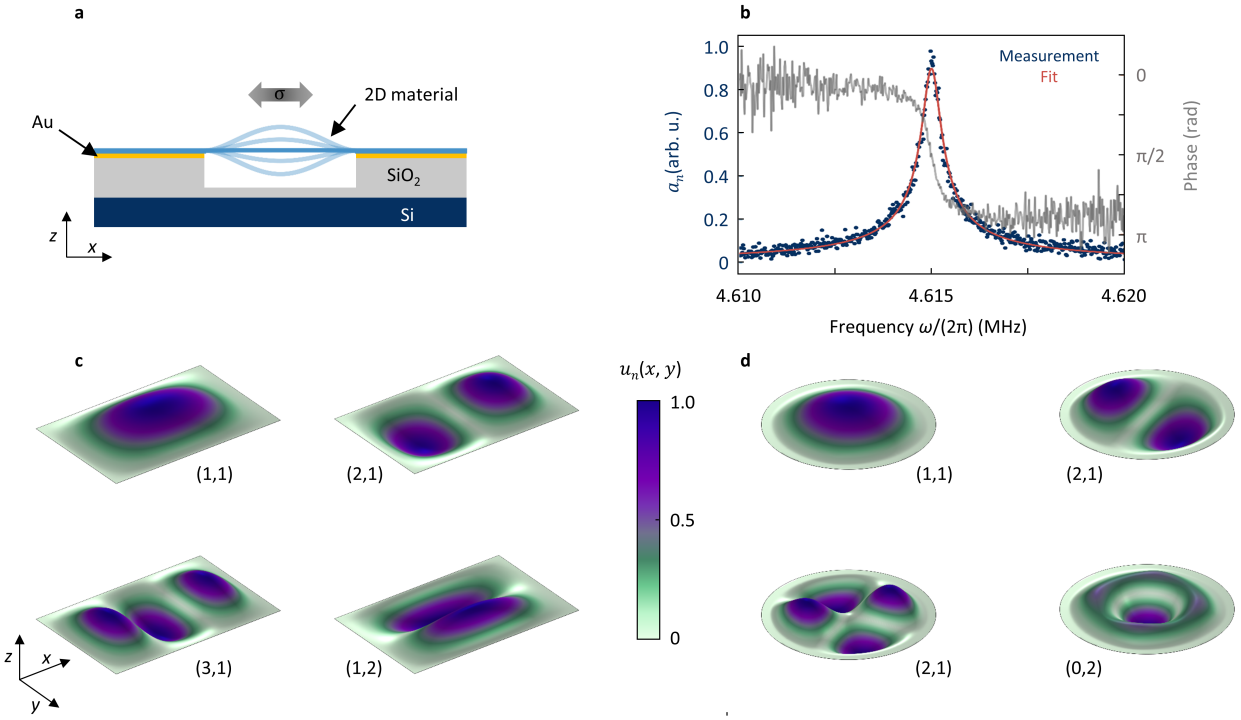

Figure 2.3: Two-dimensional membrane resonators. a, Sketch of a commonly used device geometry for 2D material-based resonators. The suspended region of the 2D material can move freely, while the clamped edges serve as boundary conditions and define the mode shape of the resonances. **b**, Measured amplitude and phase vs. frequency for an exemplary membrane resonator. By fitting a driven harmonic oscillator (red line), we can extract the resonance frequency and quality factor. **c**, Simulated mode shape of a rectangular clamped membrane resonator for the first four lowest modes. **d**, Simulated mode shape of a circular clamped membrane resonator for the first four lowest modes.

Fig. 2.3a). For small amplitudes in the out-of-plane direction, the in-plane motion is negligible so that the displacement can be reduced to the following displacement function:

$$z(x, y, t) = \sum_n z_n(x, y, t) = \sum_n a_n(t) u_n(x, y), \tag{2.2}$$

where $u_n(x, y)$ is the two-dimensional mode shape for the n^{th} mode of the resonator as a function of position x and y, and $a_n(t)$ is unchanged from Eq. 2.1. As before, we normalize $u_n(x, y)$ such that the maximum value of $|u_n(x, y)|$ is unity. Next, we can determine $a_n(t)$ by mapping each of the resonator's modes to a damped harmonic oscillator of the form:

$$\ddot{a}_n + \frac{\omega_n}{Q_n}\dot{a}_n + \omega_n^2 a_n = \frac{F(t)}{m_{\text{eff},n}}. \tag{2.3}$$

In this equation, $\omega_n = 2\pi f_n$, Q_n and $m_{eff,n}$ stand respectively for (angular) frequency, quality factor, and effective mass for the n^{th} mode of the resonator. $F(t)$ is a time-dependent driving force. We can also define an effective spring constant for the n^{th} mode as $k_{eff,n} = m_{eff,n}\omega_n^2$ [91]. Equations 2.1 – 2.3 fully describe the motion of mechanical resonators in the linear regime. The resonance frequency, quality factor, and mode shape (and thus $m_{eff,n}$) are ultimately determined by the device geometry and employed materials. When the system is exposed to an external periodic driving force ($F_{ext}\sin(\omega t)$), the amplitude of the steady-state oscillation is given by:

$$a_n(\omega) = \frac{F_{ext}Q_n/k_{eff,n}}{\sqrt{\left(1-\frac{\omega^2}{\omega_n^2}\right)^2 + \left(\frac{\omega}{\omega_n Q_n}\right)}}. \tag{2.4}$$

In Fig. 2.3b, we can compare this equation (red line) to experimental data (blue dots) and find good agreement. One finds a peak in amplitude when the membrane is driven at its resonance frequency ω_n. In the small damping limit (underdamped), the peak width of $a_n^2(\omega)$ defines the full-width-half-maximum (FWHM) of $\Delta\omega_{FWHM} = \omega_i/Q_i$. The linewidth is defined as $\Gamma = \Delta\omega_{FWHM}/(2\pi)$. From the experimental data, we can extract a Q of 8000 and a line width of 575 Hz. The phase angle, by which the mechanical motion lags behind the actuation force, is given by:

$$\phi_n = \arctan\left(\frac{\omega_n^2 - \omega^2}{\omega\omega_n/Q_n}\right). \tag{2.5}$$

The phase angle abruptly changes from π to zero and equals $\pi/2$ when the system is driven exactly at its resonance frequency. In Fig. 2.3b, we plot the measured phase angle for our example resonator and find exactly this behavior.

In order to derive an expression for the effective parameters (e.g. resonance frequency, effective mass and mode shape) of a 2D material-based resonator, let us look at the free vibration of a thin plate (of any shape) with uniform thickness h [92]:

$$\begin{aligned}\frac{D_x}{h}\frac{\partial^4 z(x,y,t)}{\partial x^4} + \frac{D_y}{h}\frac{\partial^4 z(x,y,t)}{\partial y^4} + 2\frac{D_{xy}}{h}\frac{\partial^4 z(x,y,t)}{\partial x^2\partial y^2} - \frac{\sigma_{xx}}{h}\frac{\partial^2 z(x,y,t)}{\partial x^2} \\ -\frac{\sigma_{yy}}{h}\frac{\partial^2 z(x,y,t)}{\partial y^2} - 2\frac{\sigma_{xy}}{h}\frac{\partial^2 z(x,y,t)}{\partial x\partial y} + \rho\frac{\partial^2 z(x,y,t)}{\partial t^2} = 0,\end{aligned} \tag{2.6}$$

where σ_{ij} are the in-plane tension components, D_i are the components of the bending rigidity, and ρ stands for the materials density. Suspended 2D materials typically show considerable built-in tension, whereas their flexural rigidity is usually tiny due to their atomic thickness. This means that elastic energy (and ultimately the resonance frequency) is dominated by the in-plane tension σ (in contrast to plates, where the bending terms are dominant). Therefore, we can neglect the first

three terms in equation 2.6. Finally, assuming an isotropic tension, with no shear component in the tension (i.e. $\sigma_{xx} = \sigma_{yy} = \sigma$ and $\sigma_{xy} = 0$), we arrive at:

$$\frac{\partial^2 z(x,y,t)}{\partial x^2} + \frac{\partial^2 z(x,y,t)}{\partial y^2} - \frac{h\rho}{\sigma}\frac{\partial^2 z(x,y,t)}{\partial x \partial y} = 0. \tag{2.7}$$

To solve this equation, we use the approach shown in Eq. 2.2 and separate the spatial and time dependence of the solution. We find that the time dependence is described by [90]:

$$a_{mn}(t) = c_{mn}\cos(\omega_{mn}t) + d_{mn}\sin(\omega_{mn}t), \tag{2.8}$$

where m and n are the indices for the modes in the x and y direction respectively and c_{mn} and d_{mn} allow us to adjust the solution to the initial state of motion of the resonator. By implementing the boundary conditions of a specific geometry, we can find the complete solution to Eq. 2.7. For a rectangular membrane clamped along its perimeter, the boundary conditions are given by:

$$u_{mn}(0,y) = u_{mn}(x,0) = u_{mn}(L_x,y) = u_{mn}(x,L_y) = 0, \tag{2.9}$$

where L_x and L_y are the spatial dimensions of the rectangle. The mode shape fulfilling this equation is given by (derivation in Ref. [90]):

$$u_{mn}(x,y) = \sin\left(\frac{\pi m x}{L_x}\right)\sin\left(\frac{\pi n y}{L_y}\right). \tag{2.10}$$

The mode shapes for the first four modes of a rectangular membrane are plotted in Fig. 2.3c. Based on this, we can find the resonance frequency of each of the (m,n) modes:

$$f_{mn} = \frac{\omega_{mn}}{2\pi} = \frac{1}{2}\sqrt{\frac{\sigma}{\rho}\left[\left(\frac{m}{L_x}\right)^2 + \left(\frac{n}{L_y}\right)^2\right]}. \tag{2.11}$$

For a circular membrane, the derivation can be repeated by transforming Eq. 2.7 to cylindrical coordinates. The solution to the spatial mode shape is then given by Bessel functions and results in a resonance frequency of:

$$f_{mn} = \frac{\omega_{mn}}{2\pi} = \frac{1}{2\pi}\sqrt{\frac{\sigma}{\rho}}\frac{\alpha_{mn}}{a}, \tag{2.12}$$

where a is the radius and α_{mn} is a numerical prefactor (which equals 2.4049 for the fundamental mode). The mode shapes for the lowest modes of a circular membrane are shown in Fig. 2.3d.

To fully describe the motion of a mechanical resonator, we need to have an expression for the effective mass $m_{eff,n}$, which maps an oscillation with an arbitrary mode shape to an ideal harmonic

motion (point-like mass on a spring). For a resonator of uniform density, oscillating in the out-of-plane direction (z), the effective mass of the nth mode can be derived from the potential energy and is given by [90]:

$$m_{\mathrm{eff,n}} = \rho \int dV \left| \frac{z(x,y,z,t)}{z_{\mathrm{max}}} \right|^2, \tag{2.13}$$

where z_{max} is the maximum displacement. The effective mass is a metric for the relative displacement of a resonance mode. Roughly speaking, a mode with a large effective mass moves more. For a square resonator, one obtains a mode-independent effective mass:

$$m_{\mathrm{eff,n}} = \frac{\rho h L_{\mathrm{x}} L_{\mathrm{y}}}{4} = \frac{m_{\mathrm{phys}}}{4}. \tag{2.14}$$

For a circular clamped membrane, one needs to integrate over the Bessel functions. The fundamental mode has an effective mass of $m_{\mathrm{eff,n}} \approx 0.27 m_{\mathrm{phys}}$, however, higher-order modes show large variations in effective mass. For complex geometries, the effective mass is typically numerically determined using finite element method (FEM) simulations.

2.3. Driving and detecting 2D material-based resonators

To experimentally characterize nanomechanical resonators, it is essential to understand suitable actuation and readout methods. Therefore, in this section, I briefly discuss commonly used interferometric motion detection schemes and driving mechanisms.

Let us start by looking at ways to generate out-of-plane motion in 2D material-based resonators via a periodic external force (compare Eq. 2.3 and 2.4). This can be achieved in various ways. The methods used in this thesis are (i) electrostatic actuation, (ii) base actuation, and, in some cases, (iii) optothermal actuation. For the electrostatic actuation, a periodically-varying voltage (V_{AC}) mixed with a DC voltage (V_{gate}) is applied to a gate electrode close to the suspended membrane (Fig. 2.4a,b). This results in a periodically modulated electrostatic force, which sets the membrane in motion and effectively drives the resonators. For the base actuation, the sample is placed on top of a piezoelectric element (Fig. 2.4a), which vibrates and thereby transfers the motion to the resonator via the substrate. For optothermal actuation, a modulated laser beam focused on the sample is used to periodically heat the resonator. This leads to thermal expansion and induces motion. For a comprehensive overview of actuation methods used in the area of research see Ref. [66, 67].

Next, we need to understand how the induced motion can be detected. This is commonly done using an interferometric, a capacitive, or a transductive readout approach. In this work, we employ interferometric readout based on (i) a Michelson and (ii) a Fabry–Pérot cavity. For details on other readout methods, refer to Ref. [66, 67].

In our Michelson interferometer [93–95], a beam of light emitted from a HeNe laser (wavelength λ) is directed towards a beamsplitter, which divides the beam into two parts with equal intensity (I_1 and I_2), as shown in Fig. 2.4a. One beam is reflected off a reference mirror and directed back towards the beamsplitter, while the second beam passes through an objective and is reflected off the sample. The two reflected beams recombine at the beamsplitter and interfere with each other. The resulting intensity is given by the following term:

$$I_{\text{total}} = I_1 + I_2 + 2\sqrt{I_1 I_2} \cdot cos\left(\frac{2\pi\Delta x}{\lambda}\right), \tag{2.15}$$

where Δx is the difference in length between the two optical paths. This signal is highly sensitive to small changes in path length and when the sample oscillates at a given frequency, the intensity of the light is modulated at this frequency. We use a photodetector to convert the light intensity into an electrical signal and record it using a lock-in amplifier. The lock-in amplifier is also used to generate the driving signal and can simultaneously provide a small gate voltage (for $V_{\text{gate}} > 10\,\text{V}$, we use an external voltage source in combination with a bias-T). More experimental details on this setup including a step-by-step manual are provided in the appendix (Sc. A.1). In our measurement configuration, we routinely achieve a displacement sensitivity of $\sim 100\,\text{fm}/\sqrt{\text{Hz}}$ (strain sensitivity: $3.3 \times 10^{-15}\ 1/\sqrt{\text{Hz}}$). Given the arm length of ~ 30 cm and small laser powers (<1 μW), this is a decent sensitivity value and more than sufficient for our experiments. Here I would like to note that with larger arm lengths, higher laser powers, and much more sophisticated stabilization mechanisms, it is possible to achieve a strain sensitivity of $1 \times 10^{-23}\ 1/\sqrt{\text{Hz}}$ [96] (as it is currently done at the Laser Interferometer Gravitational-Wave Observatory).

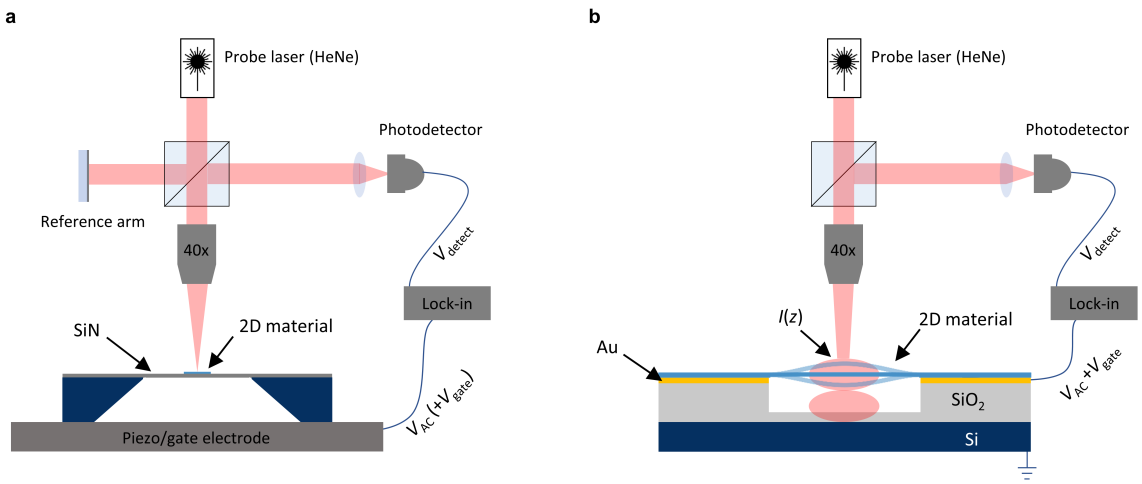

Figure 2.4: Interferometric readout of 2D material-based resonators. a, Michelson interferometer. A central beamsplitter divides the incoming laser beam into two paths. One arm of the interferometer is formed by the sample, and the total reflected light is highly sensitive to relative displacement, which allows us to detect mechanical motion with high resolution. **b**, Fabry–Pérot cavity interferometer. The sample itself forms an interferometer, resulting in a standing wave-like light intensity $I(z)$. When the suspend 2D material oscillates, the reflected light is modulated, which we use to probe the mechanical resonances.

In our Fabry–Pérot cavity interferometer [97, 98], the semi-transparent, suspended 2D material forms an optical cavity with the reflecting back gate (Fig. 2.4b). The incoming laser beam is reflected and interferes with itself, forming a standing wave light intensity field in the z-direction ($I(z)$), as shown in red-shaded in Fig. 2.4b. When the membrane oscillates, it is exposed to a varying light intensity and thus absorbs a varying amount of light. Additionally, the light reflected off the membrane and off the substrate interfere and also modulate the light intensity at the oscillation frequency. For graphene, this effect is relatively small because graphene has a low reflectivity. For TMDs, this contribution is larger. Both effects result in a modulation of the intensity of the total reflected light, which is detected using a photodetector. In this approach, the measured amplitude depends on the membrane position relative to $I(z)$ and is proportional to $\frac{\mathrm{d}I(z)}{\mathrm{d}z}$. The standing wave pattern of the light intensity in the cavity can give rise to backaction effects on the mechanical resonator [13–15]. These effects are interesting by themselves and, for example, allow to effectively cool resonance modes. However, they are not desirable for our nanomechanical spectroscopy (NMS) approach, as they also induce frequency shifts. These shifts will be indistinguishable from the purely heating-related shifts, which we use to determine the absorption of the 2D materials (details in Sec. 2.6). To avoid this, we use our Michelson interferometer for NMS.

Both measurement approaches provide us with the frequency-dependent displacement and the phase of the resonator (compare Fig. 2.3b), which we use to extract the resonance frequency (ω_n), quality factor (Q_n) and maximum amplitude (a_n). By spatially varying the position of the probe

beam, it is possible to restore the mode shape $u_n(x, y)$ [99] and derive the effective mass $m_{\text{eff,n}}$. 2D material-based resonators are typically measured in vacuum because they are easily damped by surrounding gases due to their low mass. The remaining dissipation mechanisms in resonators made from 2D materials depend on a large range of parameters and are, as of today, not entirely understood [66, 67].

2.4. Mechanical tuning of 2D materials

This section is devoted to discussing the mechanical tuning of suspended 2D materials, which we will need for the realization of tunable phononic systems. Probably the most remarkable mechanical feature of 2D materials is their flexibility. Due to its strong covalent in-plane bonds and low defect density, graphene can be stretched by 20 % before it ruptures [1]. This allows us to add tunability to nanomechanical resonators and provides a powerful experimental knob. By adjusting this knob, one can manipulate mechanical resonances, which enabled key experiments such as tunable back-action effects [13–15], non-linear dynamics [6–10], or studies of the chemical potential in graphene [100]. According to Eq. 2.11, the resonance frequency of a suspended membrane depends on its tension σ. When a suspended membrane is statically displaced, its tension increases, and thus the resonance frequencies of the system upshift. There are multiple approaches to controllably displace a suspended 2D membrane. The simplest method is to apply a voltage (V_{gate}) to a gate electrode in the vicinity of the suspended 2D material. In our case, the 2D material is conductive and electrically connected via a thin layer of gold (see Fig. 2.5a). Together with the silicon gate electrode (Si), the 2D material forms a capacitor. By applying V_{gate}, electrostatic pressure is generated, which displaces the membrane and induces tension. The resulting electrostatic pressure is defined as:

$$p_{\text{el}} = \frac{\epsilon_0}{2}\left(\frac{V_{\text{gate}}}{d}\right)^2, \tag{2.16}$$

where ϵ_0 is the vacuum permittivity and d is the initial separation between the gate and 2D membrane. The effect of applying a gate voltage on the resonance frequency is shown in Fig. 2.5b. Upon increasing the gate voltage, the fundamental resonance frequency shifts from $\sim$ 3 MHz to almost 8 MHz.

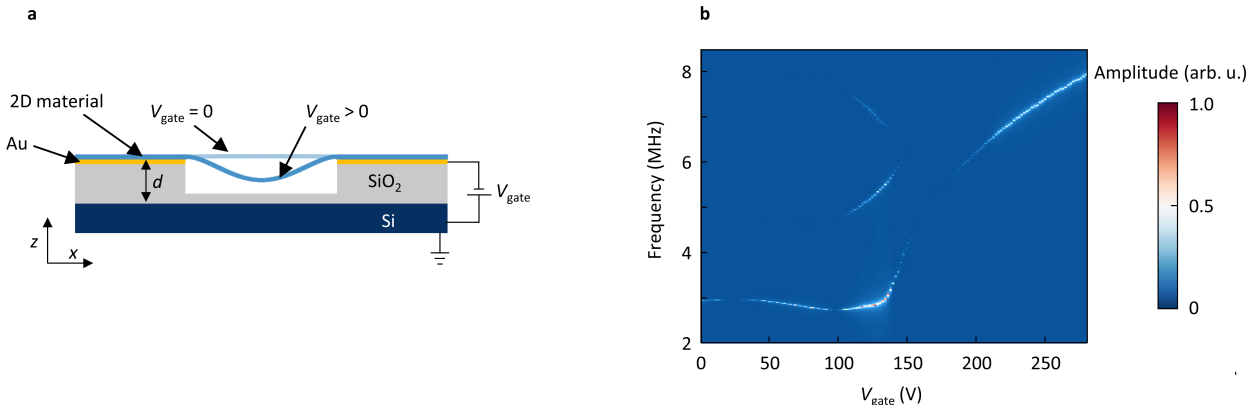

Figure 2.5: Mechanically tuning 2D materials. **a**, Tension induced via electrostatic gating. When a voltage (V_{gate}) is applied between the suspended 2D materials and the gate electrode below it, electrostatic pressure displaces the membrane and induces tension. **b**, Resonance frequency vs. applied gate voltage for a graphene resonator. With increasing gate voltage, the fundamental resonance frequency can be tuned from 3 MHz to almost 8 MHz. The measured amplitude of the resonance varies as the membrane is displaced. This is due to a variation in detection efficiency, which is proportional to the derivative of the light intensity in the cavity ($\frac{dI(z)}{dz}$).

For small gate voltages (<120 V), we observe an initial small downshift in frequency, which is attributed to an effect called capacitive softening [18, 67, 70, 101, 102]. This may seem surprising because the application of a voltage should increase tension and therefore result in a frequency upshift. To give an intuitive understanding of this effect, we look at the potential energy U_{pot}, which defines the effective spring constant of the resonator: $k_{\text{eff}} = \frac{d^2U_{\text{pot}}}{dz^2}$. When a voltage is applied to the membrane, the total potential energy also contains a term accounting for the electrical energy stored in the form of a plate capacitor: $U_{\text{pot}} = U_{\text{elastic}} + U_{\text{electric}}$. As the membrane is pulled closer to the gate electrode, the U_{electric}-term has a negative sign, which leads to a lowering of k_{eff} and thus an initial downshift in frequency before U_{elastic} starts to dominate at larger gate voltages (>120 V).

The mechanical tunability in 2D material-based NEMS resonators is remarkable, and the relative change in resonance frequency routinely reaches more than 100 % [18, 66, 67, 102], which makes resonators made from 2D materials highly tunable mechanical systems. The geometry of the suspended material determines the distribution of the induced tension [103, 104]. For a circular device, the induced tension is biaxial and mostly uniform. By using a rectangular device, one can control the degree of uniaxially (σ_{xx}/σ_{yy}) in the tension distribution. There are also other approaches to induce tension, e.g. a sharp AFM tip can be used to indent a suspended membrane and thereby create a highly localized tension hot spot [105]. In summary, NEMS resonators made from 2D materials form broadband tunable mechanical systems that can be easily manipulated, e.g. by applying a gate voltage.

2.5. From membranes to phononic crystals

Having understood the dynamics of 2D materials and knowing how they can be mechanically tuned, we still need to answer another question towards our goal of realizing tunable phononics: How can we transform a 2D membrane into a phononic crystal?

Before I discuss that question, I would like to introduce the concept of a phononic crystal (PnC). PnCs are engineered structures with a periodic variation of material properties, e.g. stiffness, mass, or stress [25, 26]. This periodic perturbation creates a meta-crystallographic order in the system and leads to a vibrational band structure hosting acoustic Bloch waves [25, 26]. A phononic band structure can be seen as an analog to the electronic band structure in solids. This brings the ability to control and manipulate mechanical excitations in the same way that traditional electronic crystals control the flow of electrons. PnCs come in 1D, 2D, or 3D versions (Fig. 2.6a), and their lattice parameter a can range from tens of nanometers to meters [29]. The resulting phonon frequencies cover a range from audible to humans ($\sim 100\,\mathrm{Hz}$) to heat waves ($\sim 10\,\mathrm{THz}$). Similar to phonons on the atomic scale, phonons in PnCs can have various polarization and different velocities for the propagation along different crystallographic axes. However, phonons on the atomic scale have a much smaller lattice parameter ($a \approx$ Å) and thus oscillate at much higher frequencies ($\omega > 10\,\mathrm{THz}$). When the lattice parameters of a PnC are chosen properly, a phononic band gap can be opened (gray in Fig. 2.6b). These band gaps, induced by destructive wave interference effects at the high symmetry points, occur for phonon wavelengths, which are comparable to the lattice parameter a. Mechanical waves with frequencies within the range of phononic band gaps cannot propagate, as they are strongly damped. This allows for controlling phonons towards many useful applications such as sonic filters [29], isolators [29, 106], waveguides [30–32], or phonon lenses [33–35]. Furthermore, phononic band gaps allow the creation of highly localized modes on artificial lattice irregularities. These mechanical 'defect' modes are shielded from their environment and show record-breaking quality factors as radiation and bending losses are strongly reduced [36–40].

As discussed in the previous sections, suspended 2D materials can be described as membranes and their mechanical behavior is dominated by their in-plane tension components σ_{ij}. This raises the question: How can we transform a 2D membrane into a phononic crystal? The simplified answer to this question is: By cutting a periodic pattern of holes into the membrane. In the next paragraphs, I will explain what (computational) tools we use to design and study our phononic crystals and provide some intuitive explanations for the origin of phononic band gaps.

Before we pattern our device with a phononic lattice, we must gain some understanding of what lattice parameters to employ for our system. To determine suitable lattice parameters, we perform phononic band structure calculations for an infinite lattice, without having to worry about fixed boundary conditions or finite-size effects for now. The unit cell of a phononic crystal can contain

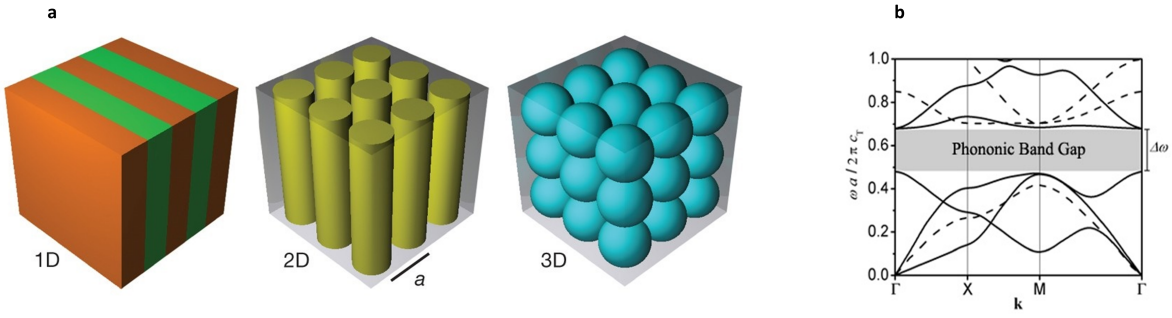

Figure 2.6: Phononic crystals. a, Sketch of phononic crystals with different dimensionality (1D, 2D and 3D). They are made of different elastic materials arranged in a periodic manner. Different colors indicate materials with different elastic properties. **b**, An example of a phononic band structure for a 2D phononic crystal. The non-dimensional frequencies $\omega a/2\pi c_T$ (with c_T being the transverse velocity) are plotted versus the phonon wave vector **k** along the high symmetry lines Γ–X–M–Γ of the corresponding first Brillouin zone. The range of forbidden frequencies, or phononic band gap, is shown in gray. Figure adapted from Ref. [29].

a very large number of atoms (4×10^7 carbon atoms in our case), which brings first-principles approaches for band structure calculations to their limits. Therefore, our method of choice is finite element method (FEM) modeling in Comsol Multiphysics. Fig. 2.7a depicts a unit cell for a honeycomb lattice of holes ($a = 1\,\mu\text{m}$, $d/a = 0.5$) with the corresponding first Brillouin zone shown below. By applying periodic (Floquet) boundary conditions to the unit cell, we can calculate the phononic band structure for an infinitely expanded lattice (Fig. 2.7b). For this, we parameterize the wave vector **k** to cover the desired path along the first Brillouin zone and then extract the resonance frequencies (eigenfrequencies) by numerically solving the generalized eigenvalue problem, which is defined by the stiffness and mass matrices. By plotting the eigenfrequencies vs. **k**, we obtain the phononic band structure. In this 'infinite model', we find a sizable band gap for out-of-plane modes around 50 MHz (more details in Ref. [22]). In this work, we focus entirely on out-of-plane modes. In the context of phononic crystals made from 2D materials, these modes are especially relevant as they are easy to excite and detect.

Making suspended samples from graphene comes along with limitations for a maximum device size, which is on the order of 20 to 30 µm. To verify that we can apply the results obtained from band structure calculations to a realistic sample of finite size, we need to identify the band gap in such a device. To do so, we switch to our 'finite model', which is computationally much more resource-hungry, but accounts for finite-size effects. Fig. 2.8a shows a sketch of a circular 2D membrane (diameter $D = 30\,\mu\text{m}$) with a honeycomb lattice of holes patterned into it. The lattice parameters are identical to the ones used in the infinite model, and we implement an artificial irregularity in the center to host a defect mode. To understand the phononic properties of the 'finite' device, we simulate the first 1500 mechanical eigenmodes of the device. The results of this are

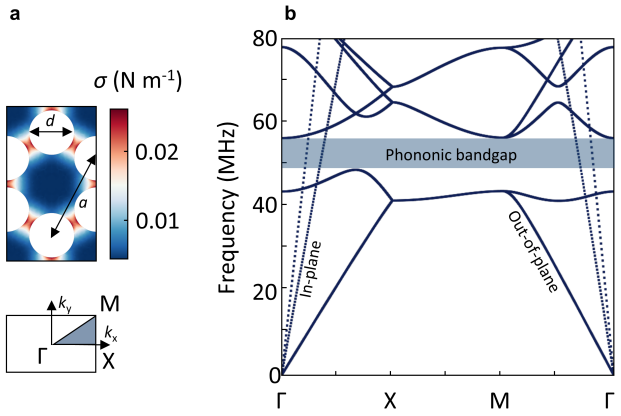

Figure 2.7: Band structure calculations for an infinite graphene phononic crystal. **a**, Unit cell of a honeycomb lattice of holes with redistributed tension (top) and the corresponding first Brillouin zone (bottom). **b**, Phononic band structure for the unit cell shown in (a). In-plane modes are plotted as dashed lines and out-of-plane modes as solid lines. We find a large phononic band gap for out-of-plane modes around 50 MHz (blue-shaded area). Figure adapted from Ref. [48].

shown in Fig. 2.8b, where eigenfrequency vs. mode number is plotted. The density of states is much lower in the region, which corresponds to the phononic band gap obtained from our band structure calculations (blue-shaded). This confirms that the band gap is sustained for smaller finite-size samples (discussed in more detail in Ref. [22]).

Having confirmed the presence of the band gap, we can look at some individual modes to intuitively understand the transition from a membrane to a PnC. In Fig. 2.8c, the displacement along a central line cut of some exemplary modes is plotted. The fundamental mode (I) shows one large antinode in its center and we can assign it a wavelength of roughly half of the device's diameter $D/2$. When we look at higher-order modes (II and III), we begin to see more and more antinodes and can assign subsequently smaller wavelengths (higher wave vectors $\mathbf{k}$) to the modes. For a sufficiently high mode number, at which the wavelength becomes comparable to a, a phononic band gap opens due to destructive interference. In this frequency range, we no longer observe standing waving but localized (evanescent) defect modes (IV). Above the band gap region, the modes are again extended over the entire range of the sample (V). So, by pattering a suspended membrane we can transform it into a phononic crystal. The holes cause mechanical excitations in the membrane to scatter and interfere with each other. While the mode shape of low-frequency modes still resembles that of a regularly suspended membrane, we find that towards higher frequencies the phononic pattern determines the mode shapes. In Fig. 2.8d, the entire mode shape of the central defect mode is plotted. The mode is highly localized around the central defect. Due to their suppressed displacement in large areas of the resonator, localized gap modes typically have largely reduced effective masses. The effective mass of our central defect mode is $m_{\mathrm{eff}} = 0.002 m_{\mathrm{phys}} = 0.72\,\mathrm{ag}$.

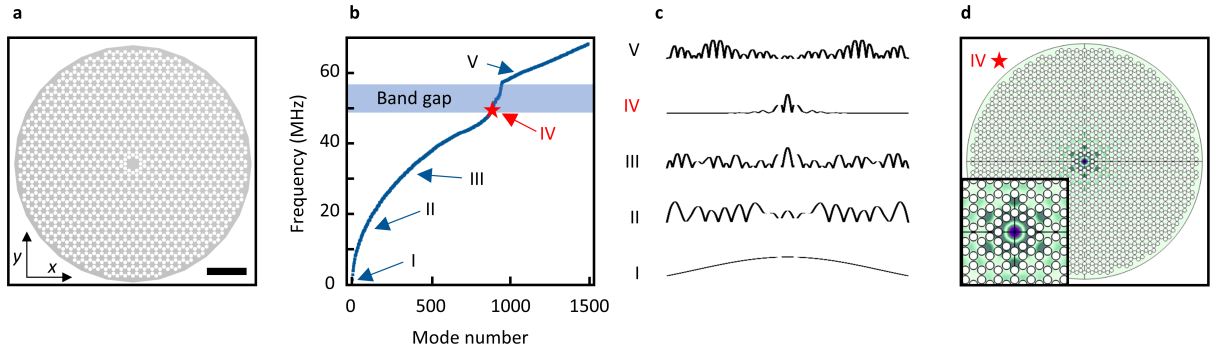

Figure 2.8: Finite-size phononic crystals. a, Device geometry for the finite system simulations (scale bar is 5 µm). The central 'defect' region is designed to host a localized vibrational mode, which is shielded from the environment by the phononic lattice. **b**, The first 1500 simulated eigenfrequencies vs. mode number for the PnC device shown in (a). The band gap region is shown in blue. **c**, Displacement along a line cut through the device for some highlighted modes: (I) Fundamental mode, (II and III) below the band gap, (IV) localized defect mode, and (V) above the band gap. **d**, Spatial mode shape of the defect mode localized at the central defect. The inset shows a zoom-in on the central region. Figure adapted from Ref. [22].

2.6. Nanomechanical resonators as spectroscopic probes

In this section, I discuss the mechanics of a resonator under illumination with the goal of understanding the underlying mechanism of our nanomechanical spectroscopy approach. Let us start by looking at the fundamental resonance of a membrane under uniform biaxial tension σ_0. In order to have a specific example, I choose a square membrane. Other geometries show the same basic behavior. The simulated mode shape of this square membrane resonator is shown in Fig. 2.9a and the resonance frequency is given by:

$$f_0 = \frac{1}{L}\sqrt{\frac{\sigma_0}{2\rho}}, \tag{2.17}$$

where L is the length and ρ the density. When we add a radiative light source with power P_{inc}, some portion of the incoming light is absorbed (P_{abs}), which heats up the membrane material and reduces the tension by:

$$\Delta\sigma = \alpha \Delta T \frac{E_{2D}}{1-\nu}, \tag{2.18}$$

where α is the thermal expansion coefficient, ΔT is the average temperature increase, E_{2D} is the 2D Young's modulus, and ν is the Poisson's ratio. One can calculate the 2D Young's modulus by simply multiplying the bulk modulus by the interlayer spacing of the 2D material. We can now express the heating-induced change in resonance frequency as:

$$\Delta f = \frac{1}{L}\sqrt{\frac{\sigma_0 - \Delta\sigma}{2\rho}} - f_0 = f_0\left(\sqrt{1+\frac{\Delta\sigma}{\sigma_0}} - 1\right) \approx f_0\left(\frac{\Delta\sigma}{2\sigma_0}\right). \tag{2.19}$$

The increase in temperature ΔT is directly proportional to the amount of light absorbed by the membrane:

$$\Delta T = \frac{\beta}{h\kappa} P_{\text{abs}}, \tag{2.20}$$

where β is a prefactor determined by the temperature profile in the membrane, κ is the thermal conductivity, and h is the thickness of the membrane. A simulated temperature profile with a laser spot focused on the center of the membrane is shown in Fig. 2.9b. The amount of incoming light is linked to the amount of absorbed light by the material's absorption coefficients (*Abs*). Thus, we can derive:

$$\Delta f = f_0 \frac{\alpha E_{2\text{D}}}{2\sigma_0(1-\nu)} \frac{\beta}{h\kappa} P_{\text{inc}} Abs. \tag{2.21}$$

Eq. 2.21 shows that the shift in frequency is linear in laser power. We can check this experimentally by looking at some measurement results. Fig. 2.9c shows the response (frequency shift) of a square SiN membrane resonator to laser illumination. The behavior is linear and thus makes an appropriate probe for the detection of absorbed light. In order to use this probe for performing absorption spectroscopy, we vary the photon energy ($E_\gamma = \hbar\omega$) of the incoming light, record the corresponding frequency shifts, and extract the absorption coefficient (*Abs*).

While the mechanics for a single material resonator of square or circular geometry can be derived analytically, more complex devices (e.g. hybrid devices with 2D materials incorporated) require numerical evaluation to quantitatively capture their behavior. In order to calibrate our measurements, we use simulations (e.g. for determining β) or the known absorption of a reference material (e.g. SiN). This allows us to extract the absorption coefficient in absolute units (% absorption) from the measured frequency shifts. All in all, we now understand the response of a membrane resonator to incoming light and have a platform to perform spectroscopy.

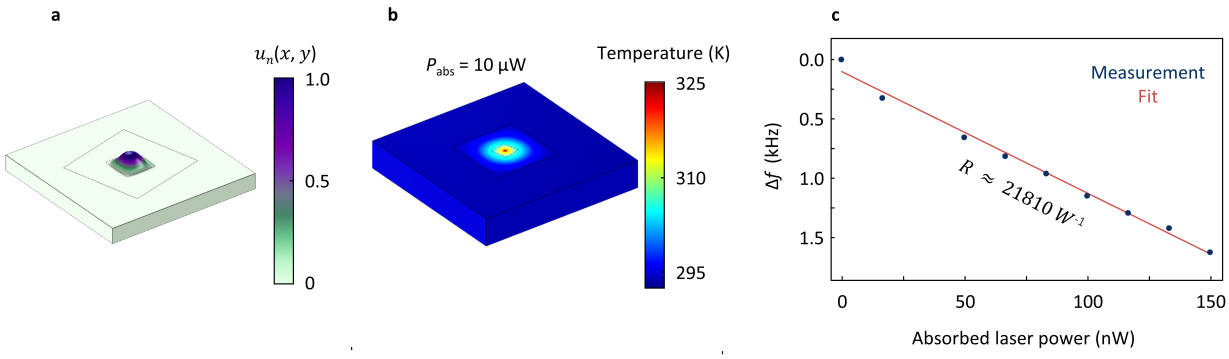

Figure 2.9: Nanomechanical detection of light. **a**, Simulated displacement of a nanomechanical resonator with a 2D material implemented. **b**, Simulated temperature profile upon laser heating in the center of the device. From this simulation, we can extract β. **c**, Measured frequency response of a TMD-SiN hybrid resonator with the excitation laser (E_γ = 1.9 eV) focused on the SiN area. The absorption of SiN at this photon energy is known and the measurement serves as a calibration. Figure adapted from Ref. [23] and [107].

3. Papers forming this thesis

1. *Tunable graphene phononic crystal.*
   J. N. Kirchhof, K. Weinel, S. Heeg, V. Deinhart, S. Kovalchuk, K. Hoeflich, and K. I. Bolotin.
   Nano Letters **21**(5), 2174–2182 (2020).

   I conceived the idea, performed the FEM simulations, and designed the phononic devices. Suspended graphene samples were fabricated by K. Weinel, S. Kovalchuk, and me. The Helium-FIB pattering procedures were developed and carried out by K. Höflich and V. Deinhart at HZB Berlin. S. Heeg acquired and analyzed the Raman spectroscopy data. K. I. Bolotin and I co-wrote the paper with input from all authors. K. I. Bolotin supervised the project. All authors discussed the results.

2. *Mechanically-tunable bandgap closing in 2D graphene phononic crystals.*
   J. N. Kirchhof and K. I. Bolotin.
   npj 2D Materials and Applications **7**, 10 (2023).

   K. I. Bolotin and I conceived the idea and co-wrote the manuscript. I designed the devices and performed the FEM simulations.

3. *Nanomechanical spectroscopy of 2D materials.*
   J. N. Kirchhof, Y. Yu, G. Antheaume, G. Gordeev, D. Yagodkin, P. Elliott, D. B. de Araújo, S. Sharma, S. Reich, and K. I. Bolotin.
   Nano Letters **22**(20), 8037–8044 (2022).

   K. I. Bolotin and I conceived the idea. I performed the interferometric measurements with the help of Y. Yu and G. Antheaume. Y. Yu, G. Antheaume, and D. Yagodkin fabricated suspended TMD samples. G. Gordeev helped to analyze the data. P. Elliott and S. Sharma performed the DFT calculations. D. B. de Araújo performed reference measurements. K. I. Bolotin and I co-wrote the paper with input from all authors. K. I. Bolotin supervised the project. All authors discussed the results.

4. *Nanomechanical absorption spectroscopy of 2D materials with femtowatt sensitivity.*
   J. N. Kirchhof, Y. Yu, D. Yagodkin, N. Stetzuhn, D. B. de Araújo, K. Kanellopulos, S. Manas-Valero, E. Coronado, H. van der Zant, S. Reich, S. Schmid, and K. I. Bolotin.
   2D Materials **10**(3), 035012 (2023).

   K. I. Bolotin and I conceived the idea. I performed the interferometric measurements with the help of Y. Yu. D. Yagodkin, Y. Yu, N. Stetzuhn, and D. B. de Araújo fabricated 2D material on silicon nitride samples. K. Kanellopulos and S. Schmid provided the silicon nitride substrates, helped to analyze the data, and to optimize the measurement sensitivity. S. Manas-Valero grew and provided the $CrPS_4$. K. I. Bolotin and I co-wrote the paper with input from all authors. K. I. Bolotin supervised the project. All authors discussed the results.

4. Connection of the papers

This thesis consists of two main storylines: (i) Creating a tunable phononic crystal and (ii) developing a nanomechanical approach for the spectroscopy of 2D materials. What brings both stories together is the control of tension within suspended 2D materials. The tunability of the presented phononic crystal relies on increasing tension in a suspended membrane, whereas the detection mechanism in our nanomechanical spectroscopy approach is based on the release of tension in 2D materials as they absorb light.

4.1. Tunable phononic crystals

The first main goal of this thesis is to conceptualize, fabricate, and understand a highly tunable phononic crystal. As described in the introduction and in Sec. 2.5, phononic crystals are periodically patterned metamaterials, which give rise to a band structure for mechanical excitations (phonons) and thus control the flow of sound, heat, and information [25, 26]. PnC-based devices have enabled breakthrough experiments on quantum information technology [108–112] and made acoustic waveguides [30–32], phonon lenses [33–35], and vibration shielding possible [36, 38]. At the same time, all modern PnCs are limited to operating at fixed frequencies.

Why do we want a tunable phononic crystal? Adding a new experimental 'knob' to tune phononic systems will open the door for a range of exciting applications and fundamental experiments. We expect that tunable (and ultracoherent) mechanical defect modes will allow precise control of the resonant coupling to external systems, thereby forming an exceptional sensor or a reservoir for storing quantum information technology. Thus, our advances may bridge the gap between phononics and quantum optics. It will also be possible to control the localization of mechanical defect modes, which will give insight into the dissipation mechanisms of nanomechanical resonators and result in increased mechanical quality factors. Furthermore, in phononic systems with an additional degree of freedom (frequency tunability), we will be able to dynamically manipulate the propagation of phonons and thus the flow of heat, sound, and information through matter. This can be used for a phononic transistor, which is a valuable extension for phonon logic applications. Finally, tunable phononic systems will make it possible to simulate condensed matter physics phenomena in mechanical systems. Specifically, we will be able to induce phase transitions (e.g. a metal-insulator transition) in phononic crystals.

How do we obtain a tunable phononic system? To realize a tunable phononic crystal, we use suspended graphene for its outstanding flexibility and mechanical tunability. Our design consists

of a circular suspended graphene membrane that is electrically contacted and forms a capacitor with a closely spaced gate electrode (Fig. 4.1a). By setting a voltage to the gate electrode, we can apply an electrostatic pressure (p_{el}) to the membrane, which causes the membrane to deflect, and induces biaxial and mostly uniform tension (details in Sec. 2.4). This increase in tension will directly manipulate the phononic system. Specifically, it upshifts the entire phononic spectrum as the velocities and thus the frequencies of all phonons in a material depend on its tension σ.

To check the overall feasibility of a suspended graphene phononic crystal, we need to fabricate a realistic prototype device that contains at least ~10 unit cells. If we compare the typical unit cell sizes of phononic crystals made from Si or SiN ($a \approx 100\,\mu\mathrm{m}$) to the size limitation for fabricating a suspended graphene membrane (20 - 30 µm), we realize that we need an alternative fabrication approach, compared to e.g. optical lithography and reactive ion etching (RIE). We overcome this obstacle by using He-ion beam lithography, which allows us to directly pattern holes into graphene with a resolution of less than 10 nm while introducing very few defects into the material [22, 47]. A prototype device with a honeycomb lattice of holes and a lattice constant of $a = 375\,\mathrm{nm}$ is shown in Fig. 4.1b. The circular area is suspended and forms the phononic crystal, which can move in the out-of-plane direction. The center part creates an artificial defect, that will host a localized defect mode (sketched in white). The frequency of the defect mode is designed to fall into the phononic band gap and thus is mechanically isolated from the rest of the substrate. This reduces bending and radiation losses of the oscillation and increases the quality factor and the coherence time of the mechanical resonance.

When we apply a gate voltage between the gate and the phononic crystal, the tension in the phononic crystal increases and the entire phononic spectrum upshifts in frequency. In Fig. 4.1c, we show the simulated tuning of the band gap (blue) and the defect mode (black) vs. applied pressure. For a realistic pressure of 30 kPa, we obtain more than 350 % tuning. The defect mode shows the same tuning behavior as the band gap and stays within the gap. Therefore the mode also maintains its localization, and its effective mass remains constant. The results introducing the concept of a tunable phononic crystal made from graphene, including fabrication, characterization via Raman spectroscopy, and extensive modeling were published in the first of the papers forming this thesis: Kirchhof *et al.*, Nano Letters **21**(5), 2174–2182 (2020). While this publication focuses on the fabrication and the theoretical exploration of tunable phononic crystals, ongoing experimental work with my colleague, Yuefeng Yu, shows the first signatures of a broadly tunable band gap in a graphene phononic crystal. I will provide these preliminary results in the outlook (Ch. 5).

After showing that we can use biaxial tension to tune the position of the phononic band gap in 2D phononic crystals made from graphene, we aim to also control the size of the band gap and thereby obtain full control of our phononic system. This will make it possible to induce a transition from a

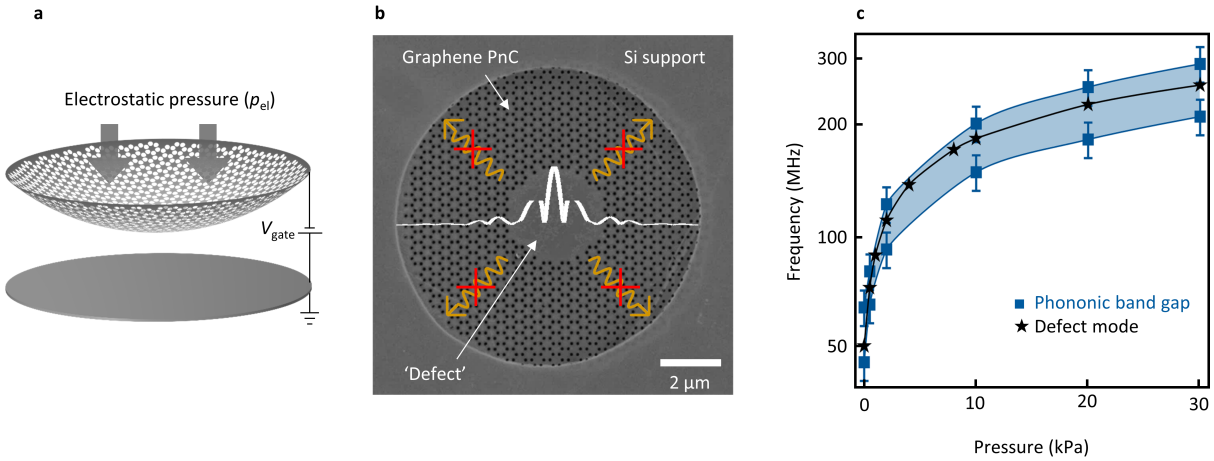

Figure 4.1: Tunable graphene phononic crystal. a, Sketch of the electrostatic tuning of a graphene PnC. When a voltage is applied to the gate below the suspended PnC, the electrostatic force causes the membrane to deflect and increases its tension. **b**, Prototype device of a graphene phononic crystal with a sketch of the defect mode localized in the center (white). The surrounding phononic pattern reduces radiation and bending losses (sketched in orange). **c**, Pressure dependence of the phononic band gap (blue) and the resonance frequency of the central defect mode (stars). The defect mode remains within the band gap even at high pressures. Figure adapted from Ref. [22].

gapped to a non-gapped phononic system. Such a change of hierarchy/topology in the phononic band structure can be seen as the mechanical equivalent of a metal-insulator transition (mMIT) and will allow controlling the localization of mechanical defect modes. Furthermore, it can be used as a phononic transistor and a reservoir for tunable quantum acoustics.

To realize a closing of the phononic band gap, we switch from the circular geometry to a rectangular stripe while using the same honeycomb phononic lattice as before. In such a geometry, out-of-plane phonons can be excited at one side (A, blue in Fig. 4.2a), e.g. optothermally by a modulated heating laser (details in Sec. 2.3), and travel through the device until they are detected interferometrically on the opposite side (B, red in Fig. 4.2a). By simulating the transmission from A to B, we have a direct probe for the phononic band gap. The results of such a mechanical transmission study are shown in Fig. 4.2b (blue). In our simulations, we find a clear band gap region, where the transmission is strongly suppressed (blue-shaded).

When electrostatic pressure is applied to the device, it induces a larger average tension along the x-direction (σ_{xx}) than in the y-direction (σ_{yy}). An increasing degree of uniaxililty ($\sigma_{xx}/\sigma_{yy} > 1$) in the tension distribution affects the phononic bands, such that the band gap size gradually decreases. At an applied pressure of 5 kPa ($\sigma_{xx}/\sigma_{yy} = 1.7$), the band gap is closed entirely and the region of suppressed transmission, associated with the band gap, vanishes (Fig. 4.2b, red). The phononic system undergoes a transition from mechanically insulating to mechanically conductive and allows us to effectively control the flow of phonons. This can be seen as the mechanical simulation of a

metal-insulator transition (mMIT). We thereby realized the equivalent of a condensed matter phase transition in a phononic system and on a much larger scale. Controlling the size of the band gap

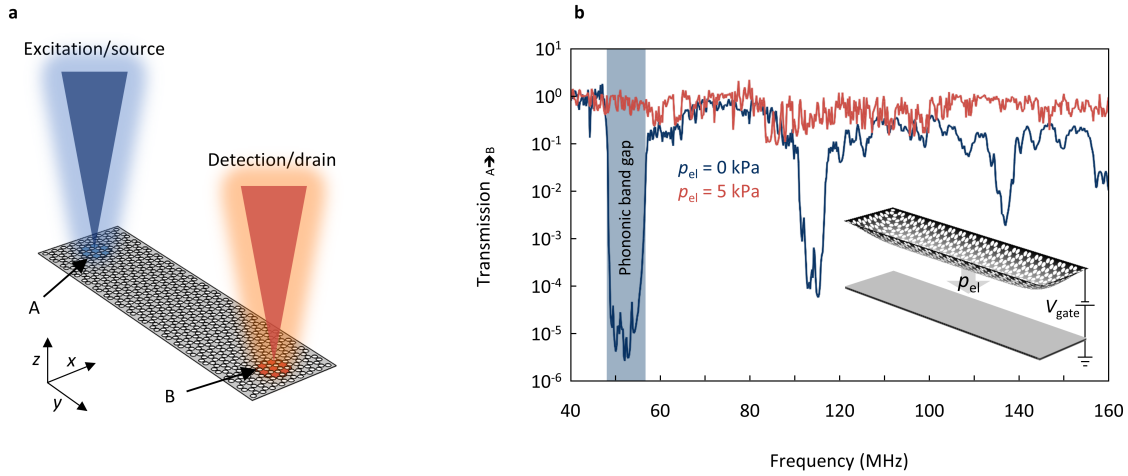

Figure 4.2: Band gap closing (mMIT) in a graphene phononic crystal. a, Transmission geometry for a rectangular phononic device. At point A, mechanical motion is excited by a frequency-modulated laser (blue). After traveling through the device, the vibrational wave is detected at point B by a second laser spot (red). **b**, Simulated transmission from A to B vs. excitation frequency for the device shown in (a) without (blue) and with (red) applied electrostatic pressure. For $p_{el} = 0$ kPa a clear band gap region is visible (blue-shaded), where transmission of mechanical motion through the device is suppressed by 10^5 (100 dB). When electrostatic pressure is applied (see inset), the device deforms, and a highly uniaxial tension distribution is generated ($\sigma_{xx}/\sigma_{yy} = 1.7$). This causes the phononic band gap to close, which we can confirm in the transmission spectrum, where the region of suppressed transmission vanishes. Fig. adapted from Ref. [48].

also provides control of the localization of the vibrational defect modes. These defect modes can be compared to the localization of mid-gap defect states in semiconductors. Upon reducing the size of the phononic band gap using our tension engineering approach, we can increase the spatial spread of the defect mode and observe a behavior similar to the localization-delocalization transition in crystalline solids. To show this, we place an artificial defect within the phononic lattice.

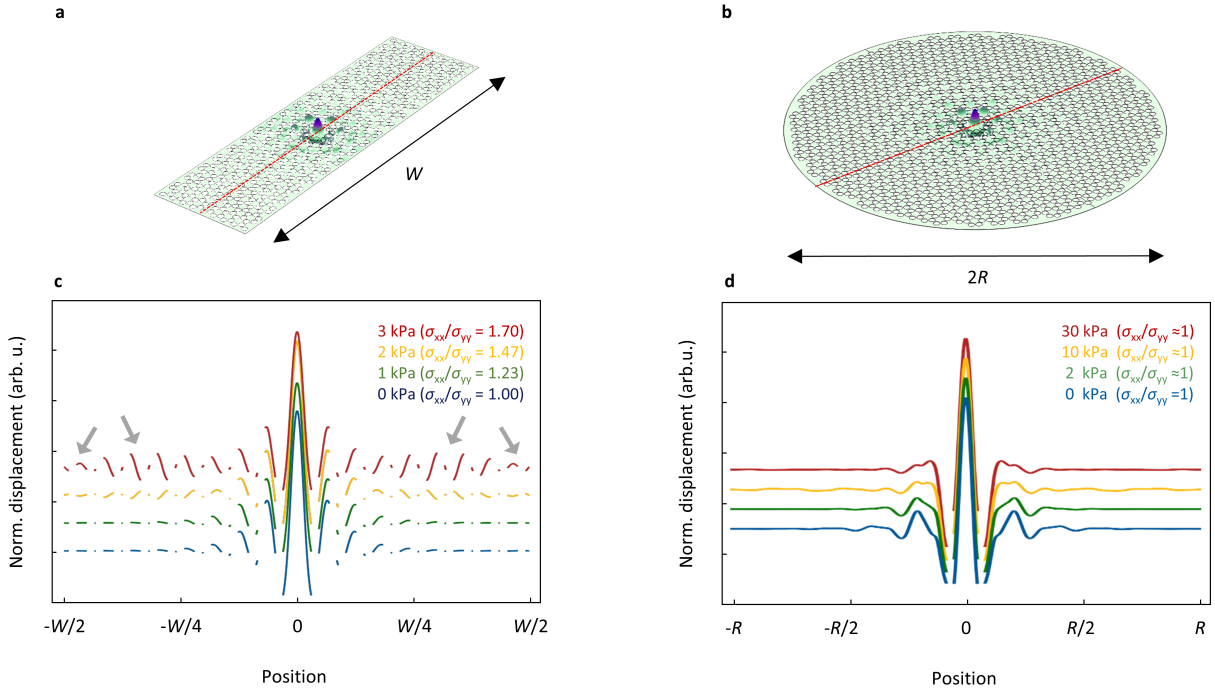

Figure 4.3: Dephasing a localized defect state using uniaxial tension. a,b, Mode shape of a localized mode within the band gap of a rectangular (a) and circular (b) phononic device. **c**, Line-cut of the normalized displacement extracted along the red line in (a) vs. applied pressure (plots are offset for better visibility). With increasing pressure, σ_{xx}/σ_{yy} increases, and the band gap gradually closes. At the same time, the mode that initially was localized near the device center becomes delocalized over the entire device (highlighted by gray arrows). **d**, Same as (c) but for the circular device shown in (b). Here the mode shape remains virtually unchanged under pressure, as the frequency of the defect mode scales together with the phononic band gap and maintains its localization. Figure adapted from Ref. [48].

Next, we simulate the pressure dependence of such a defective phononic lattice using a rectangular and a circular geometry (Fig. 4.3a,b). For the first device, we expect the band gap to close under the application of pressure. The second device is a circular reference (compare Fig. 4.1). At zero pressure, the defect mode falls within the phononic band gap and is localized in both geometries (blue in Fig. 4.3c,d). At the same time, we find starkly different behavior of that mode in the circular and the rectangular devices under applied pressure (red in Fig. 4.3c,d). In the rectangular device, the mode starts to show displacement over the entire device (highlighted by gray arrows) and thus loses its localization as the band gap closes. In the circular device, in contrast, the band gap does not close and the defect mode always stays within it. Correspondingly, the defect mode remains localized over the entire range of applied pressures. We believe that the observed behavior can be compared to a localization-delocalization transition of mid-gap defect states in semiconductors. This further highlights the similarity between phononic and solid-state crystals, despite their very different quasiparticles.

The results introducing uniaxial tension engineering to close the phononic band gap and induce a phase transition from a mechanically insulating to a mechanically conductive system are published in the second of the papers comprising this thesis: Kirchhof *et al.*, npj 2D Materials and Applications **7**, 10 (2023). This publication furthermore investigates the effect of surface contamination and random tension variations on the quality of the phononic band gap and thereby asses the feasibility of realistic phononic devices made from graphene. This paves the way for the experimental observation of tunable phononic systems.

4.2. Nanomechancial spectroscopy of 2D materials

The second main goal of this thesis is to develop a platform for the spectroscopic characterization of 2D materials that overcomes the limitations of classical optical approaches. More precisely, we want to obtain the optical dielectric function of suspended 2D nanostructures, thereby capturing the entire picture of light-matter interaction within the materials.

Why do want a nanomechanical alternative for the spectroscopic characterization of 2D materials? 2D materials offer rich physics (details in the introduction) and a large range of potential applications ranging from energy storage [113, 114] to transistors [24, 86]. Especially their optical properties are of great interest and their potential use for light-emitting diodes [115], solar cells [116, 117], optoelectronic modulators [118, 119], or photodetectors [120, 121] seems promising. Both fundamental science and applications rely on spectroscopic characterization methods, which have certain limitations when it comes to 2D materials. For example, it is not possible to differentiate between scattered and absorbed light in classical methods. Furthermore, the characterization of small samples and measurements at low temperatures or high magnetic fields are very challenging. Additionally, we aim to develop a spectroscopic measurement, that does not require any assumptions on the underlying optical constants. Finally, the dielectric surrounding can have a large effect on the optical response of the 2D material. This motivates us to develop an approach that uses suspended samples and works for small sample sizes.

How can we perform nanomechanical spectroscopy (NMS)? To realize a method free from the issues highlighted above, we design a nanomechanical resonator that allows us to measure the absorption of light in a material of interest. Our sample design consists of a 2D material deposited onto a SiN membrane (Fig. 4.4a). These two components form a hybrid resonator, where they oscillate together in phase. When the resonator absorbs light, its average temperature increases, which results in a reduced resonance frequency as the built-in tension is released due to thermal expansion. By varying the photon energy of the incoming light and recording the frequency shifts (Fig. 4.4b), we can perform spectroscopy. Constructing the resonator primarily from SiN results in

significantly enhanced mechanical quality factors of $Q \approx 8000$, much higher than 2D material-only resonators, that show Qs around ~ 100 [18, 20, 67, 70, 102]. This will allow us to detect small shifts in resonance frequency and forms a sensitive spectroscopic probe. It also makes the resonator predictable and enables optical probing of the mechanical resonance via the SiN substrate without perturbing the 2D materials (e.g. unwanted laser heating or photodoping). The sample is driven electrically, and its motion is detected interferometrically (red laser in Fig. 4.4a). Details on the experimental setup can be found in Sec. 2.3 and A.1. A second, wavelength-tunable laser is focused on the suspended TMD (blue laser in Fig. 4.4a) and allows us to heat the sample controllably.

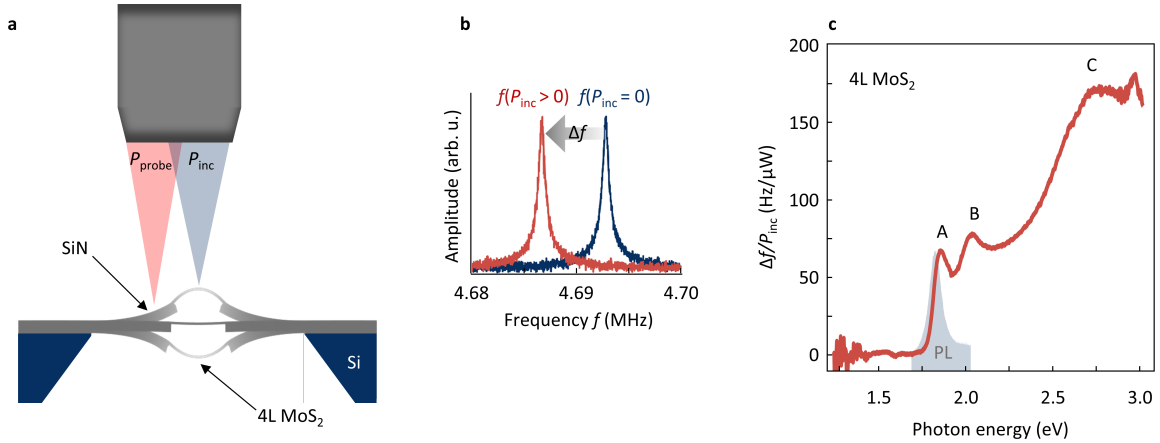

Figure 4.4: Nanomechanical spectroscopy of 2D materials. a, Sketch of the TMD-SiN hybrid resonator. The SiN membrane moves together with the TMD and allows us to measure the resonance frequencies via the substrate interferometrically (red laser). The excitation laser (blue) is focused on the suspended TMD and heats up the resonator when light is absorbed. **b**, Resonance frequency with (red) and without (blue) illumination. When light is absorbed, the entire sample heats up, tension is released, and the resonance frequency downshifts. **c**, Relative responsivity ($\Delta f / P_{\mathrm{inc}}$) vs. photon energy for 4-layer MoS_2. This signal is directly proportional to the absorption and shows clear excitonic features, which match reference PL measurements (gray). Figure adapted from Ref. [23].

To obtain absorption spectra of the 2D material, we sweep the photon energy (E_γ) of the excitation laser and record the corresponding frequency shifts. We normalize the frequency shifts by laser power and plot them in Fig. 4.4c. Clear excitonic features are visible for this 4L MoS_2 sample and they match with reference photoluminescence measurements (gray).

Next, we combine the mechanically measured absorption with optical reflection data (Fig. 4.5a) and restore the full dielectric function of the 2D material, as shown in Fig. 4.5b,c. We model the 2D material as a thin membrane and use the transfer-matrix approach to relate reflected and absorbed light [60]. Except for the thickness, no material parameters are assumed in this derivation and we find good agreement with ab-initio GW-Bethe Salpeter equation (GW-BSE) calculations (shaded in Fig. 4.5b,c).

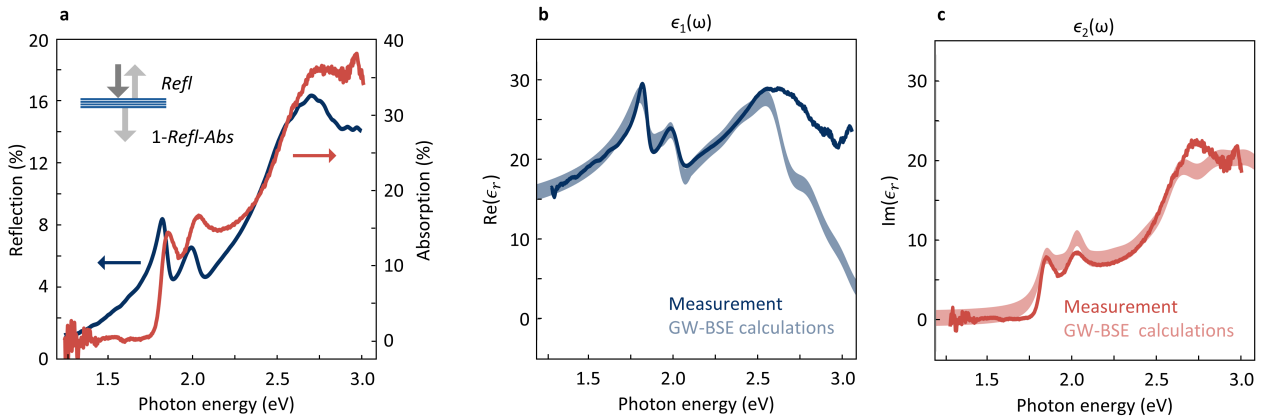

Figure 4.5: Mechanically derived dielectric function of MoS_2. a, Absorption (obtained from nanomechanical spectroscopy, red) and reflection (obtained optically, blue) of 4-layer MoS_2 vs. photon energy. Similar excitonic features are apparent in both measurements. **b,c**, Real (blue) and imaginary (red) parts of the dielectric function derived from absorption and reflection data (a). We find reasonable agreement with ab-initio GW-BSE calculations (red, blue-shaded). Figure adapted from Ref. [23].

Upon benchmarking our method, we find that it is fast (τ_{rise} = 135 ns), sensitive (noise-equivalent power: NEP = 90 pW/$\sqrt{\mathrm{Hz}}$), functions for submicron sample sizes, and allows measurements over a broad spectral range from 1.2 to 3.1 eV (extendable to THz to UV). Our approach does not require complex transmission measurements and therefore should function at low temperatures and/or high magnetic fields. In these measurements, the membrane functions as its own photodetector and is only sensitive to the amount of absorbed light and not, for example, to scattering and other losses. The proof of principle characterization of 2D materials using NMS is published by Kirchhof *et al.* in Nano Letters **22**(20), 8037–8044 (2022).

NMS is a direct measurement of absorption, which has practical advantages compared to traditional optical spectroscopy approaches. It also overcomes long-standing measurement limitations and is unperturbed by scattering of light. So far, however, the implementation of the method described above lacks the sensitivity of classical optical measurements, needs cumbersome sample loading, and relies on simulations for calibration.

In the next step, we aim to improve the sensitivity of NMS while making it easier and more reliable to use. This is accomplished through careful stress engineering of the SiN membranes supporting the 2D material, thermal decoupling, and using mechanical sample actuation. We use our improved approach to spectroscopically characterize a two-dimensional transition metal dichalcogenide (WS_2), a layered magnetic semiconductor ($CrPS_4$) [122–124], and a plasmonic super-crystal consisting of gold nanoparticles [125, 126].

For this second-generation NMS measurements, we optimize our nanomechanical resonators to have an enhanced response upon absorbing light and thus an improved measurement sensitivity.

To this end, we use low-stress SiN, which makes a much softer membrane and undergoes larger frequency shifts when its stress changes (compare Eq. 2.21). We also drive our devices via a piezoelectric element below the sample (base actuation), which makes the thin gold layer that previously contacted the 2D material obsolete and allows us to drive electrically insulating samples (Fig. 4.6a). At the same time, this reduces the thermal conductance of the sample and thus increases its response to laser heating. In Fig. 4.6b, we compare the measured response to laser heating of the first approach to the improved method. From linear fitting, we extract a responsivity ($R_{100\%}$ = 21 810 W^{-1}), which is two orders of magnitude larger than before ($R_{100\%}$ = 175 W^{-1}). This ultimately also results in an improved sensitivity of NEP = 890 $\mathrm{fW}/\sqrt{\mathrm{Hz}}$ – two orders of magnitude lower than in our previous approach. The sensitivity of NMS can now compete with commercially available avalanche photodetectors (APDs) for the same spectral range (e.g. Thorlabs APD130A/M with NEP = 200 $\mathrm{fW}/\sqrt{\mathrm{Hz}}$). At the same time, the method is simplified, allows us to study electrically insulating materials, makes sample loading straightforward, and provides a fast yet robust calibration.

To test our improved measurement protocol, we characterize exotic 2D structures that are particularly suited for our method and for which NMS is expected to produce advantages. One of them is a layered crystal (super-crystal) made from plasmonic gold nanoparticles (shown in the inset of Fig. 4.6c). Plasmonic structures typically scatter a large amount of light that cannot be distinguished from absorbed light by classical optical measurement methods. Contrary, NMS is only sensitive to absorbed light and therefore an ideal tool to study plasmonic systems. In Fig. 4.6c, we show the mechanically determined absorption spectrum of our plasmonic super-crystal, where we can nicely resolve plasmonic modes (j = 1, 2, 3).

The protocol describing the improved method for nanomechanical absorption spectroscopy along with the spectroscopic characterization of exotic 2D materials is published by Kirchhof *et al.* in 2D Materials **10**(3), 035012 (2023) as the last paper forming the body of this thesis.

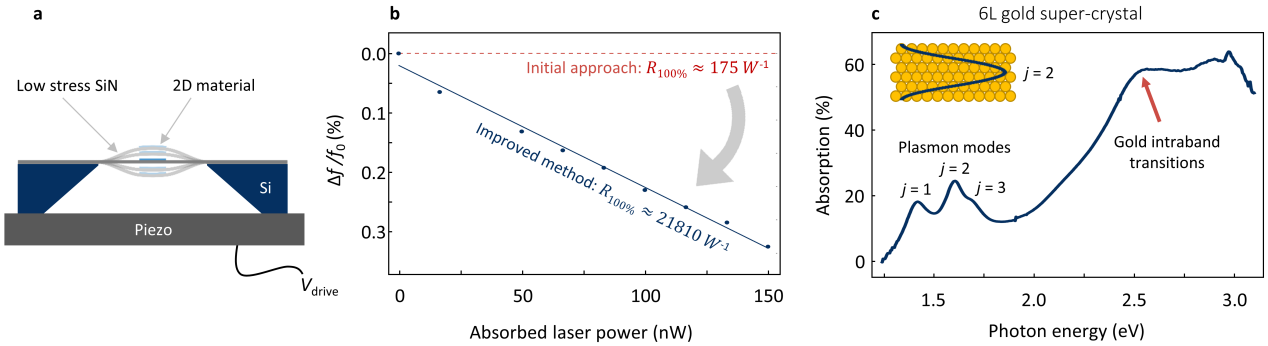

Figure 4.6: Improved nanomechanical spectroscopy. **a**, Sketch of the SiN-TMD hybrid device with an improved responsivity. The 2D material of interest is placed directly on a low-stress silicon nitride membrane and thereby thermally decoupled from its environment. **b**, Responsivity (relative frequency shift normalized to absorbed laser power) for the improved method (blue) and first approach (red). Due to thermal decoupling and careful stress engineering, we achieve a two-orders of magnitude larger response, which results in an improved measurement sensitivity. At the same time, the method is easier to use and allows us to study electrically insulating samples. **c**, Mechanically derived absorption vs. photon energy for a 6-layer gold plasmonic super-crystal. In the low energy range up to 1.8 eV, we find pronounced absorption peaks associated with standing wave plasmon-polaritons within the super-crystal. Above 2.5 eV, the light is absorbed by intraband transitions in the gold particles. The inset shows a sketch of the gold nanoparticles (yellow circles) arranged in a super-crystal, in which plasmonic modes form standing waves (j = 2 mode shown in blue). Figure adapted from Ref. [107].

5. Summary and outlook

In this thesis, I have realized a tunable graphene phononic crystal and developed a nanomechanical approach for the spectroscopic characterization of 2D materials. Both of these storylines rely on controlling the tension in suspended 2D materials and benefit from the extraordinary mechanical properties of this class of materials.

In the case of the presented tunable phononic crystal, an increase in tension induced by electrostatic gating allows us to manipulate the phononic band structure. Towards our goal of adding tunability to phononics, we have reached the following key results:

1. Successful fabrication and spectroscopic characterization (Raman) of graphene PnCs.
   With our fabrication protocol based on He-ion lithography we can reproducibly pattern phononic lattices into suspended monolayer graphene. This transforms the membranes into the thinnest possible PnCs, with a lattice constant a spanning 175 nm to 2 µm.

2. Broadband tuning of the phononic band gap using our electrostatic gating approach.
   For a realistically applied pressure of 30 kPa, we obtain more than 350 % tuning of the entire phononic system.

3. Simulation of a tunable condensed matter physics phenomena in a phononic crystal.
   By using uniaxial tension engineering, we can completely close the phononic band gap and induce a transition from a mechanically insulating to a conductive state. This change in hierarchy/topology in the phononic band structure can be seen as the mechanical analog to a metal-insulator transition (mMIT).

4. Localization of a mechanical defect mode within our phononic lattice.
   This mode is expected to have a significantly enhanced mechanical quality factor, due to the reduction of bending and radiation losses. The unique tunability in our systems furthermore allows controlling the frequency and degree of localization of the defect mode (controlled dephasing). It forms an on-demand tunable mechanical entity, that can be resonantly coupled to external signals and thereby forming an exceptional sensor or a reservoir for storing quantum information.

5. Phononic transistor based on the mMIT.
   The proposed transistor for MHz-phonons can be controlled by simply applying a gate voltage and shows an on-off ratio of 10^5 (100 dB).

6. First experimental confirmation of a tunable phononic band gap.
   In preliminary measurements of a sample made from trilayer graphene, we find strong indications for a phononic band gap, which can be tuned by 30 % (discussed in the next section).

Controlling tension is also key for the presented nanomechanical spectroscopy approach for 2D materials. Here minuscule portions of absorbed light can be detected by measuring changes in the resonance frequency of a SiN-TMD hybrid resonator. The underlying mechanism is thermal expansion leading to the controllable release of tension. This approach overcomes longstanding limitations and is a valuable tool for the characterization of 2D materials. Towards our goal of performing nanomechanical spectroscopy of 2D materials, we have reached the following key results:

1. Development of a new platform for the spectroscopic characterization of 2D materials.
   In our approach, we restore the full dielectric function, without any assumptions of other underlying optical constants. It is fast ($\tau_{\text{rise}} = 135\,\text{ns}$), sensitive ($NEP = 890\,\text{fW}/\sqrt{\text{Hz}}$), and covers a large spectral range of 1.2 – 3.1 eV (extendable to UV - THz).

2. Spectroscopic characterization unaffected by substrate-related screening or doping.
   As we employ suspended samples in our approach and probe the mechanical resonance via the substrate, we can avoid substrate- or laser-related screening and doping effects.

3. Measurements at low temperatures and high magnetic fields.
   Our approach does not require measurements at oblique angles or in a complex transmission setting. This will make measurements at low temperatures and high magnetic fields much more accessible. Also, our approach works well for small sample sizes ($\sim 1\,\mu\text{m}$).

4. Insensitivity to scattering and access to a broad spectral range from THz to UV.
   Using the 2D material itself for the detection of absorbed light will allow us to study a large variety of materials and to discriminate between scattered and absorbed light.

5. Successful spectroscopic characterization of a range of 2D structures.
   This includes various classic binary TMDs, $CrPS_4$ (a layered magnetic semiconducting ternary TMD), and a plasmonic meta-structure consisting of gold nanoparticles.

Looking at these new developments along both storylines of this thesis, I sincerely hope to contribute to the list of exciting physics and useful applications based on 2D materials described in the introduction.

5.1. New perspectives

In the future, I envision more studies on both main storylines of this thesis. The clear first step is the experimental verification of the tunable band gap in graphene phononic crystals, which will prove the experimental feasibility and open the door for a large range of new experiments. There is an ongoing research effort in our group towards this goal and I want to start the outlook by presenting some preliminary experimental results.

Experimental probing of the phononic band gap. To probe signatures of a phononic band gap, we fabricate a phononic crystal made from trilayer graphene, as shown in Fig. 5.1b. By using trilayer graphene, rather than a monolayer, the phononic pattern is less sensitive to disorder and surface contaminations, which comes at the cost of higher stiffness and slightly reduced tunability. We measure the displacement of the sample (electrical drive, cavity-interferometric motion detection) as a function of drive frequency and plot the results in Fig. 5.1a. While we find a densely populated 'forest' of vibrational modes at frequencies above the fundamental mode, we see a region of strong suppression of motion between 26.4 and 31.3 MHz (shaded in Fig. 5.1a). This region is exactly where the phononic band gap is expected from our band structure calculation (Fig. 5.1c). Within the band gap region, we find one faint peak around 30 MHz. This mode shows an increased amplitude when we probe on the edge of the device and hence is probably to be associated with a localized edge mode.

To better understand the measured spectrum, we carry out a 'finite' simulation accounting for the finite size of the PnC and considering the boundary conditions of the device (Fig. 5.1d). We can now directly compare our experimental vibrational spectra to the outcome of the simulation. In both graphs, we find the same region of suppressed displacement, which coincides with the frequency range of the phononic band gap. Also, both graphs show some features within the band gap that we attribute to modes localized at the edges of the device. The expected displacement according to our simulations (blue in Fig. 5.1d) is suppressed to such an extent that it falls below the noise floor of our experiment (gray in Fig. 5.1d). Finally, we see similar broad peaks on both sides of the band gap. These peaks most likely correspond to regions with a large phononic density of states (DOS), which are associated with flat bands at both sides of the band gap (Fig. 5.1c, right). Overall, we interpret the measured response of our sample as a phononic band gap induced by the periodic pattern of holes cut into the graphene membrane.

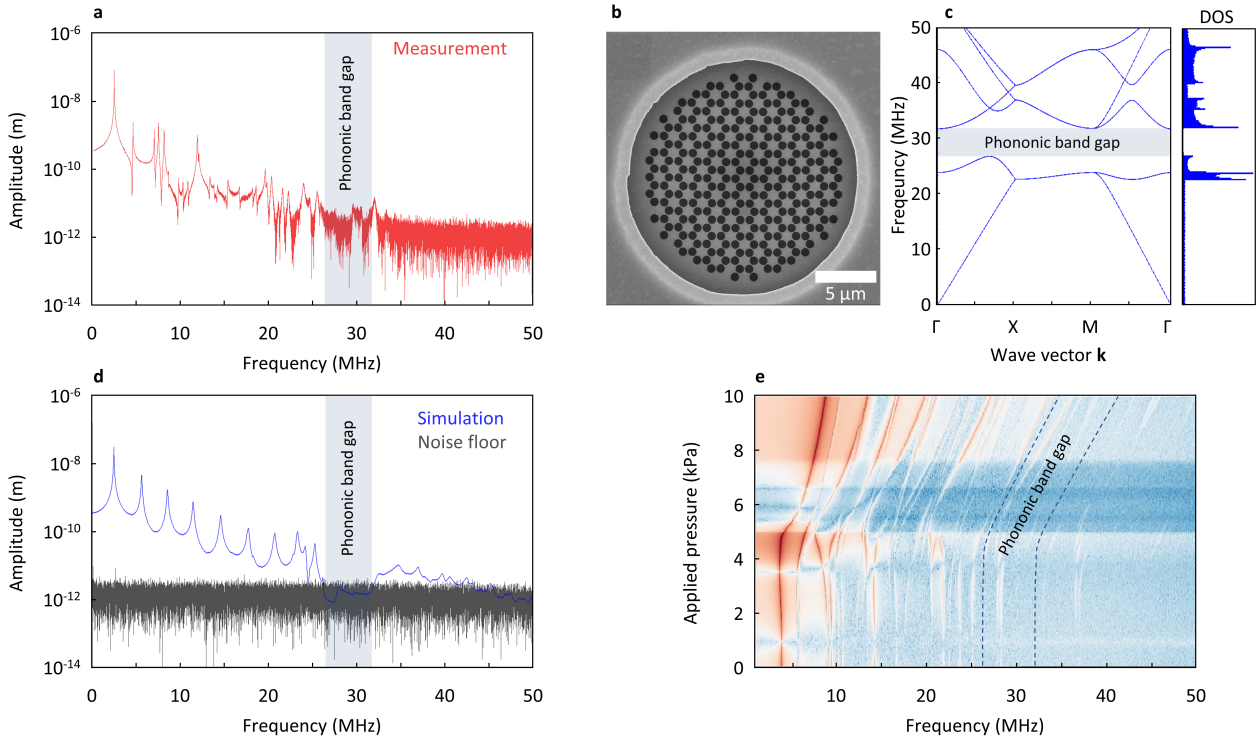

Figure 5.1: Experimental signatures of a tunable graphene phononic crystal. a, Measured displacement as a function of drive frequency of a graphene phononic crystal (sample shown in (b)). **b**, Phononic crystal device made from trilayer graphene with a lattice constant of $a = 1.36\,\mu m$. **c**, Phononic band structure calculations and extracted density of states (DOS) for the phononic lattice of the sample. **d**, Simulated displacement of the device extracted from a finite-size model (blue). The expected displacement in the band gap region (shaded) falls below the noise floor of our experiment (gray). **e**, Pressure dependence of the phononic system. Upon applying an electrostatic pressure of 10 kPa, we can upshift the phononic band gap by 30 %. Panel (a) - (e) are preliminary results from Ref. [127].

To tune our phononic crystal, we apply electrostatic pressure to the device via electrostatic gating. As we vary the gate voltage, we observe a smooth evolution of the vibrational spectrum (Fig. 5.1e). Initially, the frequencies downshift slightly with increasing V_{gate}, due to capacitive softening (explained in Sec. 2.4), while they upshift at higher V_{gate} as the increase in tension starts to dominate the frequency tuning. In total, the fundamental mode upshifts from 3.8 to 7.8 MHz. The higher-order modes show various tuning behavior, which we attribute to a combination of photothermal backaction [13–15] and different coupling to the electrostatic field for different modes. Focusing on the previously identified band gap region, we find an upshift of the band gap center frequency of more than ~9 MHz (~ 30%) for an applied pressure of 10 kPa. This corresponds to a major manipulation of the phononic band structure and makes our device a broadly tunable phononic crystal.

Having shown the first signatures of a tunable phononic crystal made from suspended graphene, which are in line with our theoretical predictions, confirms the overall concept developed in this

thesis and motivates future endeavors. This includes the realization of more tunable condensed matter physics phenomena as well as phononic applications. I will discuss some of these ideas in the following paragraphs.

Topological phononic states. In electronic systems, topological insulators feature surface states, which are protected by time-reversal symmetry and are robust with respect to disorder [128–131]. Electronic transport via these states is virtually loss-free and thus they bring exciting opportunities for information processing. Recently, it has been demonstrated that the concept of a topological insulator also holds in phononic systems [132–135]. In these systems, topological states can be created, for example, at the interface between two different phononic lattices. Analog to their electronic counterparts, these states also show robustness to disorder combined with very low dissipation and thereby form a reservoir for exploring non-classical states in phononic systems. Applying these principles to our tunable phononic crystals opens the door for exciting experiments. We could design a sample such that individual gate electrodes control different spatial regions of the phononic lattice. We can then dynamically manipulate each region and hence the interface between them. This would allow us to create on-demand topological states which we can use to efficiently guide (quantum) information along the interface.

Phonon logic. The proposed phononic transistor (as shown in Fig. 4.2) can be used for phonon logic in the MHz-range, and I expect the realization of various logic gates as the next step. By using large-scale CVD graphene transferred onto pre-patterned substrates, we could realize phononic circuits and process information using phonons. Employing electrical actuation and detection via local gates removes the need for bulky optics and makes an on-chip phonon logic device based on tunable graphene a very attractive option.

Understanding dissipation mechanisms. The dissipation mechanisms in 2D material-based resonators are, as of today, not fully understood [66, 67]. There is a large number of mechanisms that may contribute to the damping of the resonator and the total losses are a mixture of thermoelastic damping (transfer of kinetic energy into heat), bending losses at the clamping points, radiation losses into the substrate, viscous gas damping, losses from defects and contaminants on the membrane, and potentially other loss channels. For SiN resonators, it has been shown, that phononic shielding is a powerful tool to overcome radiation and bending losses, which leads to record-breaking high Qs [36–38]. In our tunable phononic system, we will be able to control the degree of localization (compare Fig 4.3). This in turn will allow us to controllably adjust the relative contribution of bending and radiation losses and therefore makes our system an ideal platform to study dissipation mechanisms in 2D material-based resonators and ultimately overcome the relatively low Qs in these systems.

Tunable Moiré superlattices in phononic crystals. Moiré lattices are another exciting playground for 2D materials, which received a considerable amount of attention due to the richness in

physics of correlated states rising from flat bands in the electronic band structure. This includes a superconducting [77] and a Mott insulator state [136] for twisted bilayer graphene (TBG). Recently, there have been some first studies on Moiré analogs in PnCs [137–140], but they all lack the tunability that makes Moiré lattices based on 2D materials so exciting. So I want to pose the question: Can we realize tunable Moiré analogs in PnCs using our approach? I believe it is feasible because in designing our phononic lattices we have access to a large number of degrees of freedom. PnCs are entirely artificial structures, which means they can be designed into almost any geometry and lattice parameter size instead of relying on naturally given parameters (e.g. the lattice constant graphene for TBG). This also means that we can directly pattern the Moiré superlattice in our devices, rather than creating it by combining two layers of graphene. Combining this with our electrostatic gating approach will make it possible to create tunable Moireé lattices which can be tailored such that they give rise to ultra-flat phononic bands. Of course, phonons are neutral quasi-particles that follow Bose-Einstein statistics and thus do not feature the electron-electron interaction that gives rise to the superconducting and the Mott insulator state in TBG. However, the fundamental principles regarding lattice symmetry, topology, and associated Chern number still hold, which allows mimicking quantum-mechanical features in mechanical systems – with an experimental knob to tune them.

For our nanomechanical spectroscopy approach, I envision the following next steps: **NMS at low temperature and magnetic fields.** The next step for NMS will be measurements at low temperatures and high magnetic fields, where I expect to observe hitherto undetected phenomena and get rid of systematic errors associated with measurements of optical constants of 2D materials. Especially, magnetic fields are interesting to access and manipulate the spin (valley) degree of freedom in 2D materials. Furthermore, the exploration of 2D magnetism, which recently attracted much attention, requires measurements at low temperatures and high magnetic fields [141–143]. These measurements are challenging for conventional optics but will be easier using NMS.

NMS with ultimate sensitivity. Additionally, I anticipate further improvement of the measurement sensitivity of NMS, for example, by controlling the sample temperature and thereby the stress in the SiN membrane. When the entire sample is cooled, the Si frame contracts at a larger rate than the suspended SiN membrane, due to their difference in thermal expansion coefficient. This leads to an effective reduction of stress in the suspended SiN and would allow measuring very close to $\sigma = 0$. At this point, the responsivity ($R_{100\%} \propto \sigma^{-1}$) will increase significantly, which leads to further improvement of the measurement sensitivity.

Cavivity-free cavity optomechanics. The combination of SiN membranes with TMDs on top of them also forms a very attractive playground for cavity optomechanics. On one side, SiN has excellent mechanical properties, but poor light-matter interaction. On the other side, resonators

made from TMDs show low mechanical quality factors, but large light-matter interaction and strong mechanical non-linearity [6–10, 144, 145]. By combining the two materials, we obtain a resonator that features the best from both worlds, namely high Q resonances as it mostly consists of SiN and large light-matter interaction due to the TMD. These devices would also benefit from a recently demonstrated optomechanical back-action effect, in which strain can mediate dynamic heating or cooling effects in TMD-based resonators [15]. The mechanism behind this functions as follows: As the resonator oscillates around its equilibrium position, dynamic strain is introduced, which increases (decreases) the absorption of light, depending on the sample being illuminated by a red (blue)-detuned light relative to an excitonic resonance. The increased (decreased) absorption effectively reduces (increases) the restoring force and results in amplification (damping). This backaction mechanism makes it possible to effectively cool/damp or heat/amplify a specific mechanical mode of the resonator and thereby replaces the need for an optical cavity and all the technical difficulties associated with it. In such a system, it is crucial to also tailor the thermal response time (τ). Assuming $\omega\tau = 1$, for which the dynamic back-action effects will be strongest [146, 147], and plugging in the Qs and resonance frequencies, that I measured in comparable samples, I expect cooling down to $\sim 70\,\mu\text{K}$ starting from liquid helium temperature. This is close to the temperature ($20\,\mu\text{K}$), which is needed to bring the resonator to its quantum ground state (average phonon occupation $n_{\text{ph}} = 1$). Designing the sample such that it has a higher resonance frequency or starting at dilution-fridge temperatures, will result in significantly lower phonon occupation and make the resonator reach its quantum ground state.

In conclusion, this discussion of follow-up research projects based on the concepts presented in this thesis demonstrates that creating tunable graphene phononic crystals and using nanomechanical resonators to perform spectroscopy of 2D materials is only the starting groundwork. Many steps in various directions are to follow. The tunable phononic platform created and described will help to explore more exciting phononic phenomena and applications. The principles of nanomechanical spectroscopy will allow the unlocking of interesting physics in a large range of 2D materials and form an attractive platform for studying optomechanical cooling and self-oscillation phenomena.

With these two new tools made from exceptionally strong and at the same time lightweight materials, an exciting pathway to new experiments on the nanomechanics of 2D materials lies ahead.

Appendix

A. Methods

A.1. Interferometric motion detection in NEMS resonators

This section aims to describe in detail the interferometric readout used to detect motion in our nanomechanical resonators. For this, we are employing a home-built Michelson interferometer, which I designed and built during my time as a Ph.D. candidate. Interferometers allow for highly sensitive measurements of relative displacements and in our setup, we achieve a displacement sensitivity of $\sim 100\,\mathrm{fm}/\sqrt{\mathrm{Hz}}$. In this section, I will first explain the underlying detection mechanism and setup, and then I'll provide a detailed step-by-step protocol for performing sensitivity characterizations and measurements in the optical setup.

Fig. A.1 shows the setup in the top and side view with the beam paths belonging to different light sources drawn in different colors. Let us start with the probe beam (red) and walk along its optical path. We use a HeNe laser with an output power of 5 mW. HeNe lasers provide good stability and coherence length and are therefore suitable for interferometric measurements. The first component in the beam path is an optical isolator (OI), which stops any light from being reflected into the laser, which would destabilize and potentially damage it. Next, the beam diameter is increased using a beam expander (BE) such that it completely fills the used objective and allows us to obtain a tightly focused laser spot. After reducing the laser power through some ND filters down to a couple of µW, a white light source for imaging (yellow path), a heating/excitation leaser (blue path), and modulated laser for possible optothermal drive (green path) are coupled in the main beam path via beam splitters (BS1 and BS2). The combined beams go through the main beam splitter (BS3), which forms the heart of the interferometer and sends half of the light to the reference arm (REF) and half through an objective (40x, 0.6 NA) onto the sample. The reflected light from both paths recombines and now contains the interferometric information on the difference in path length between the two paths. When the sample oscillates at a certain frequency, the path length is modulated at that frequency and thus the laser power after running through the interferometer. Using a piezoelectric element, we can precisely control the position of the mirror in the reference arm and thus the path length. This allows us to stabilize the interferometer using a PID loop (details in measurement protocol below). After running through the interferometer, the combined light is guided through a bandpass filter (BP), that filters out everything except the HeNe laser (with a FWHM of 1 nm). Finally, the red path reached the avalanche photodetector (APD), where the optical signal is converted into a voltage that is detected by the measurement electronics. When the flip mirror (FM) is up, the beam path is directed into a CCD camera (CAM) for imaging. The heating/excitation and driving

laser are coupled into the setup via optical fibers, and their power and beam size are adjusted using ND filters and a reflective beam expander (BE) respectively. We can adjust the optical path of these beams before they combine with the probe beam and thereby change their relative position on the sample. For example, the heating/excitation laser can be positioned in the center of the sample, while the probe detects the mechanical oscillation via the substrate. The sample is placed in an optical cryostat, which is evacuated using a turbo molecular pump to a pressure of 1×10^{-5} mbar. For room temperature measurements, the sample temperature is stabilized at 300 K using the heater of the cryostat. The sample itself or a piezoelectric element below it can be electrically contacted through a feedthrough in the cryostat. The photodetector output is connected to an oscilloscope for alignment and focusing and to the lock-in amplifier (Zurich Instruments MFLI). Next, I will provide a step-by-step protocol on how to use the setup for the characterization of NEMS resonators:

1. After the sample has been loaded and the system is pumped down to sufficiently low pressures of $\sim 1 \times 10^{-5}$ mbar, turn on the lasers, photodetector, and measurement electronics and let them warm up for ~ 30 min.

2. Switch the setup to camera mode by putting up the flip mirror and blocking the reference arm. Then use the manual stage positioned below the cryostat to move the sample to the wished position of probing. Adjust the focus using the manual stage, which holds the objective, such that the red laser spot is tightly focused.

3. Switch the setup to measurement mode (flip mirror down, reference arm unblocked), turn off the white light, and use ND filters to adjust the laser power of the probe HeNe, such that the APD gives out a voltage 30 % below its saturation value (3.7 V).

4. Use the lock-in amplifier to apply a voltage of 2 V at a frequency of 941 Hz to the reference arm piezo (oscillator 2). This results in a variation in the path difference much larger than the wavelength. The resulting interferometric signal no longer depends on the initial position of the reference arm and we can use it to maximize the signal strength. To do so, connect the APD to the oscilloscope and iteratively adjust the focus and reference arm mirror (marked by orange arrows in Fig. A.1b) until the measured oscillation amplitude is maximized. Focus and interferometer alignment are now optimized for signal strength.

5. Next, set the voltage supplied to the reference arm piezo to 10 mV (oscillator 2), and sweep the output DC offset (V_{DC}), whilst plotting the response (Demod 2 Sample R). One should obtain a $\sin^2(V_{\mathrm{DC}})$ behavior, as the beam path difference and thus the interference conditions are continuously varied. The amplitude should be between 10 and 50 mV, depending on the laser power and reflectivity of the sample.

6. To set up the PID loop, we use the integrated functionality of the lock-in amplifier to control Demod 2 Sample R by varying V_{DC}. As the setpoint for the loop, we choose 80 % of the maximum amplitude measured in the last step and start the loop using the following parameters: $P = -20$, $I = -303\,1/s$, $D = 0$ and a band with of 10 Hz

7. We can monitor the stability of the loop using the plotter function of the lock-in amplifier. When the loop is running properly, the relative variation of Demod 2 Sample R should be below 10 %. The setup is now stabilized and maintains constant interference conditions for a long time (multiple days) and we can start to measure mechanical resonances.

8. To find the resonance frequencies, sweep the actuation voltage (V_{AC}) using oscillator 1 of the lock-in amplifier and at the same time plot the corresponding amplitude (Demod 1 Sample R). The setup combines three different possibilities to drive the sample: 1) The actuation voltage drives the piezo below the sample for mechanical actuation, 2) the actuation voltage modulates a fast laser diode (green in Fig. A.1a), that periodically heats the sample and induces motion via thermal expansion and 3) the actuation voltage is mixed with a large DC voltage in a bias-T and drives the sample electrically.

9. To track resonance frequency for fast measurements or for stability measurements (Allan deviation), one should use the phase-locked loop (PLL) functionality of the lock-in amplifier. To initiate the loop, sweep the drive frequency and then manually set the frequency to the measured resonance frequency. Open the PLL tab, and choose the following settings: PLL bandwidth of 1 kHz, a resolution bandwidth of 5 kHz, $P = -9\,\mathrm{Hz/deg}$, $I = -303\,\mathrm{Hz/(deg\,s)}$, $D = 0$, set the currently measured phase as setpoint and start the loop. The lock-in amplifier now adjusts the frequency of oscillator 1 in real-time, such that it maintains a constant phase. This allows us to rapidly measure the changes in resonance frequencies when external perturbations are introduced (e.g. wavelength-dependent laser heating).

A.2. FEM modeling of 2D materials

The goal of this section is to provide some helpful insights for the finite element method (FEM) modeling of 2D material-based mechanical systems using Comsol Multiphysics. While FEM simulations are a very powerful tool, they can have some pitfalls. Comsol is a numerical solver and it will almost always give you a solution. It is up to you to evaluate if the solution is reasonable. Here is some general advice that can improve your simulation routine:

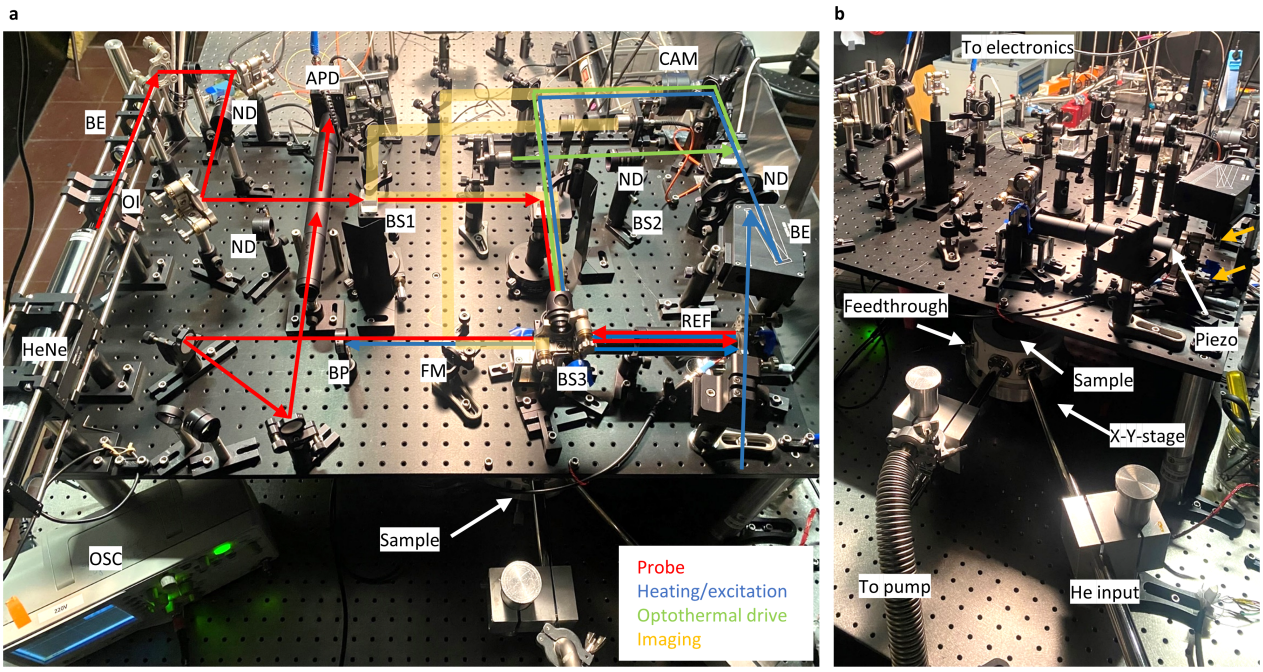

Figure A.1: Setup for interferometric motion detection. a,b, Photographs of the interferometric setup with the optical beam path and components labeled.

1. Include the substrate into your simulations. The substrate can have a large effect on the mechanics of nanomechanical devices (e.g. metal contacts can bend or oscillate). An example is shown in Fig. A.2a.

2. Build your device geometry in the same order as the fabrication of the device takes place (e.g. the gold layer before the 2D material to properly simulate a flake transferred onto a metalized sample).

3. Use a swept mesh for thin domains. It is computationally challenging to model geometries with large aspect ratios. Using a swept mesh helps to overcome this problem and makes the simulations faster at the same time. A meshed device is shown in Fig. A.2b

4. Us the symmetry of your sample geometry to make the simulations faster. This should also be reflected by the mesh (e.g. by using the copy face operator).

5. Make sure your mesh is fine enough to capture the physics you are trying to observe. For example in order to properly capture the phononic order of a sample, the mesh spacing should be roughly 5 to 10 times smaller than the lattice constant. When unsure, increase the density of the mesh until the simulation results converge.

6. Compare your results to back-of-the-envelope calculations. Sometimes the intuition for mechanics on the nanoscale can be off (e.g. vibration amplitudes and deformations of 2D materials are often smaller than anticipated). Simple calculations help to check the simulation results and help to understand the problem better.

7. Use global parameters, variables, and material links. Also importing and exporting geometries can save a lot of time.

Here are the filenames of my most important Comsol files (all stored on the Comsol PC and backed up on the group home server): T18_final.mph, mMit_Transmission_0+10kPa.mph, Infinite_0.01Nm.mph, 306u_defect22_1750modes_sweep_p_024810.mph.

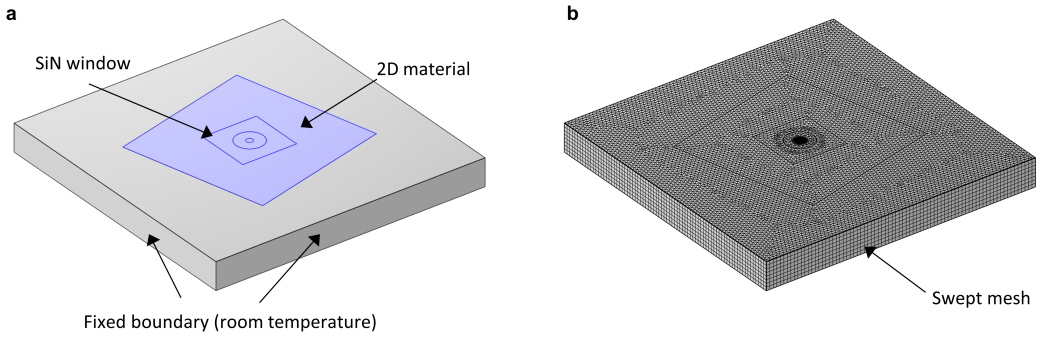

Figure A.2: FEM simulations of 2D materials. a, Sketch of a suspended 2D material transferred onto a SiN membrane. For accurate modeling, it is necessary to include the substrate. **b**, Mesh of the device shown in (a). Using a swept mesh for thin geometrical features reduces the computation time and yields reliable results.

B. Papers as published

B.1. Nano Letters 21(5), 2174–2182 (2020) and Supporting Information

NANO LETTERS

pubs.acs.org/NanoLett

Letter

Tunable Graphene Phononic Crystal

Jan N. Kirchhof,* Kristina Weinel, Sebastian Heeg, Victor Deinhart, Sviatoslav Kovalchuk, Katja Höflich, and Kirill I. Bolotin*

Cite This: *Nano Lett.* 2021, 21, 2174–2182

Read Online

ACCESS | Metrics & More | Article Recommendations | Supporting Information

ABSTRACT: In the field of phononics, periodic patterning controls vibrations and thereby the flow of heat and sound in matter. Bandgaps arising in such phononic crystals (PnCs) realize low-dissipation vibrational modes and enable applications toward mechanical qubits, efficient waveguides, and state-of-the-art sensing. Here, we combine phononics and two-dimensional materials and explore tuning of PnCs via applied mechanical pressure. To this end, we fabricate the thinnest possible PnC from monolayer graphene and simulate its vibrational properties. We find a bandgap in the megahertz regime within which we localize a defect mode with a small effective mass of 0.72 ag = 0.002 $m_{physical}$. We exploit graphene's flexibility and simulate mechanical tuning of a finite size PnC. Under electrostatic pressure up to 30 kPa, we observe an upshift in frequency of the entire phononic system by ∼350%. At the same time, the defect mode stays within the bandgap and remains localized, suggesting a high-quality, dynamically tunable mechanical system.

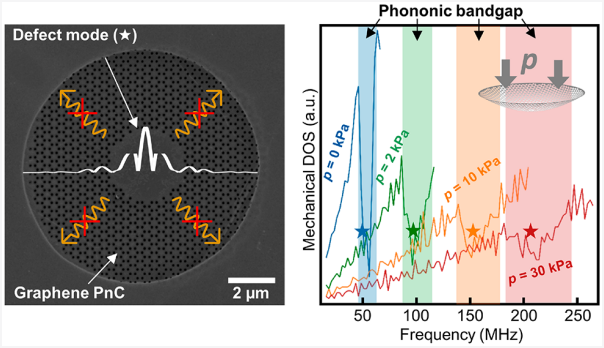

KEYWORDS: *Nanomechanics, phononic crystal, graphene, optomechanics, resonators, NEMS*

INTRODUCTION

A phononic crystal (PnC) is an artificially manufactured structure with a periodic variation of material properties, for example, stiffness, mass, or stress.[1] This periodic perturbation creates a meta-crystallographic order in the system leading to a vibrational band structure hosting acoustic Bloch waves in analogy to the electronic band structure in solids.[1] Designing the lattice parameters of the meta-structure allows one to directly manipulate phonons at various length scales.[2−4] This can be used to guide[5−7] and focus phonons[8,9] or to open a vibrational bandgap.[1,10−12]

Phononic bandgaps in periodic structures suppress radiation losses and allow for highly localized modes (of frequency f) on artificial irregularities.[13,14] The quality factors ($Q = \frac{f}{\Delta f}$) of these so-called defect modes are especially high.[15,16] In particular, resonances with $Q > 8 \times 10^8$ have been observed at room temperature in silicon nitride (SiN) PnCs.[15−17] In these devices, the quality factor exceeds the empirical $Q \sim m^{1/3}$ rule,[17−19] and the vibrational periods overcome the thermal decoherence time limit of $\tau = hQ/k_BT$.[15,17] This, in turn, enables the study of quantum effects in resonators of macroscopic size, all at room temperature.[20,21]

Frequency tunability in PnCs could add an unprecedented knob to control a broad range of phononic application and thereby provides access to new regimes of guiding, filtering, and focusing phonons.[22−33] It would furthermore allow one to resonantly couple to an external optical or mechanical excitation and thus realize sensing applications with mechanical qubits and studies on quantum entanglement.[34] Yet, the mechanical resonances in PnCs are determined by material constants and the crystal geometry.[22,23,26−28] In principle, the mode frequencies can be controlled by changing the temperature[29,30] or by an external magnetic field.[31,32] This, however, only provides limited tunability and necessitates heating the system or inclusion of magnetic materials. While SiN, as well as other conventional low-loss materials, is very stiff and allows only limited mechanical tunability,[24,33] strain has been used to adjust the frequency response of elastic polydimethylsiloxane (PDMS).[25] Unfortunately, low crystalline quality of that material led to limited tunability and very small Qs for mechanical modes.

Recently, PnCs made from two-dimensional (2D) materials have been considered.[35−37] Such materials feature intrinsically low mass, high fundamental frequency, and easily accessible displacement nonlinearity. Most importantly, their high tensile

Received: December 18, 2020
Revised: February 7, 2021
Published: February 23, 2021

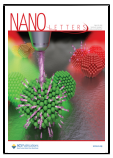

https://dx.doi.org/10.1021/acs.nanolett.0c04986
Nano Lett. 2021, 21, 2174−2182

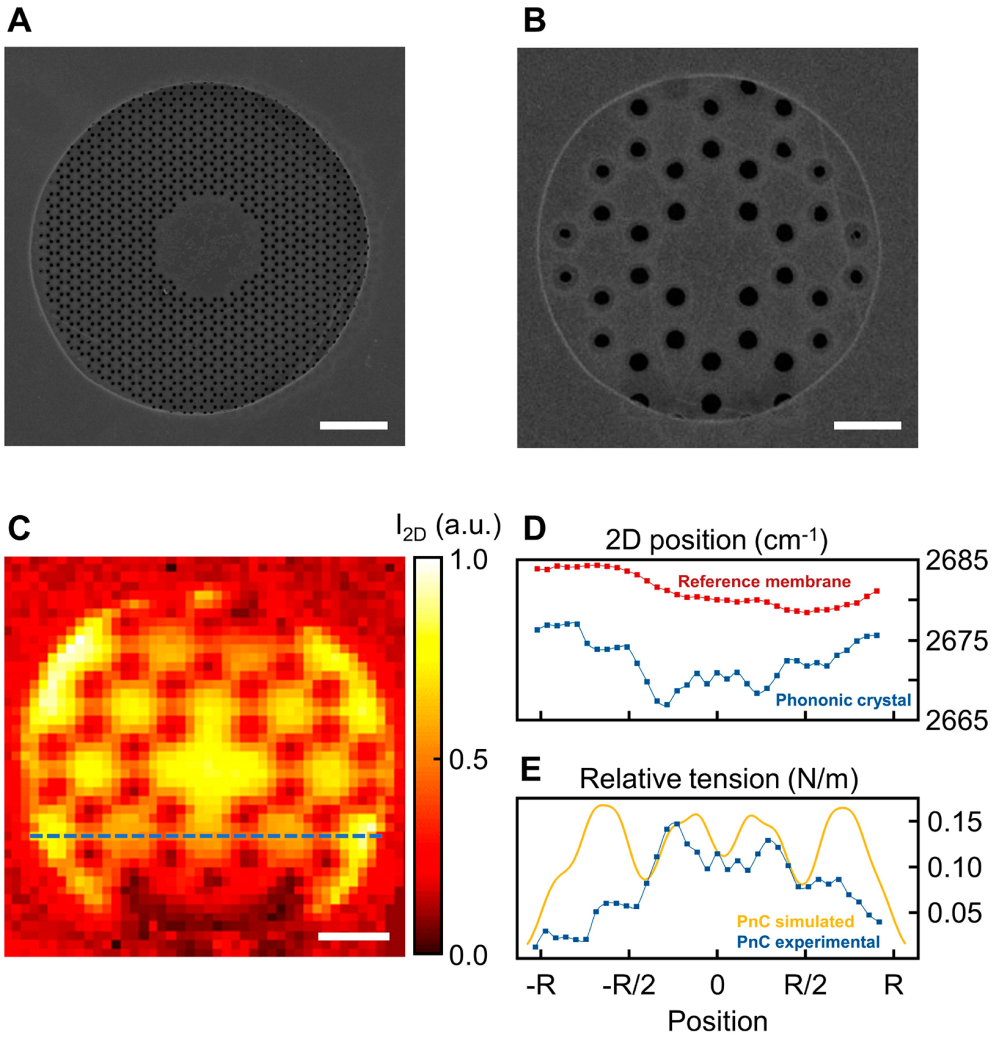

Figure 1. Graphene phononic crystals and tension redistribution. (A,B) Helium ion micrographs of prototype monolayer graphene phononic crystal devices with lattice constants 350 nm and 2 μm, respectively. Scale bar length is 2 μm. The phononic pattern, a honeycomb lattice of holes with a defect in its center, allows us to localize a vibrational defect mode. The ringlike features around the holes in (B) are due to incomplete removal of graphene most likely caused by contamination (details in Supporting Information). (C) Intensity map of the Raman-active 2D mode of graphene for the device shown in (B). The periodic pattern is clearly visible. (D) Raman 2D-mode position along a line cut (dashed line in (C)) for a PnC (blue) and reference membrane (red). The PnC shows a periodic variations of much larger amplitude compared to the fluctuation in the reference sample. (E) Comparison of the relative tension extracted from Raman measurements (blue) to the simulated tension distribution (yellow) confirming the redistribution of tension upon pattering. The simulation includes spatial broadening due to the finite size of the laser spot.

strength and monolayer character allows the ability to mechanically strain them up to 10%.[38] That invites consideration of mechanically controllable 2D-material based PnCs. Specifically, we expect the entire acoustic band structure of such a PnC to be highly tunable by applying mechanical pressure. Nevertheless, tunability of 2D phononic systems as well as localized defect modes in them have not been studied yet.

Here, we investigate mechanical tunability in a realistic graphene PnC. We fabricate a suspended micron-sized monolayer graphene PnC via focused helium ion beam milling (FIB) and characterize it spectroscopically. We then use experimentally established parameters to calculate the phononic band structure of the resulting PnC. We find a phononic bandgap from 48.8 to 56.5 MHz inside of which we localize a defect mode with an effective mass of 0.72 ag. Finally, we computationally investigate the mechanical tunability of the PnC under pressure induced by a local electrostatic gate.[39,40] The applied pressure smears out the phononic bandgap as the out-of-plane displacement breaks the symmetry and causes perturbations of the artificial lattice, yet the mode shape of the defect mode remains highly localized. Overall, we can tune the resonance frequency of the defect mode by more than 350% and access new regimes of strain engineering.

RESULTS

Designing a Tunable Phononic Crystal. Our device design of a tunable, two-dimensional PnC consists of the following key elements. First, the PnC material must be freestanding to allow out-of-plane displacement. Second, it is necessary to use an electrically conductive material. In that case, an electrostatic gate electrode can be used to apply pressure and to induce tension as the membrane is pulled toward the gate. Third, the material needs to be flexible to

https://dx.doi.org/10.1021/acs.nanolett.0c04986
Nano Lett. 2021, 21, 2174−2182

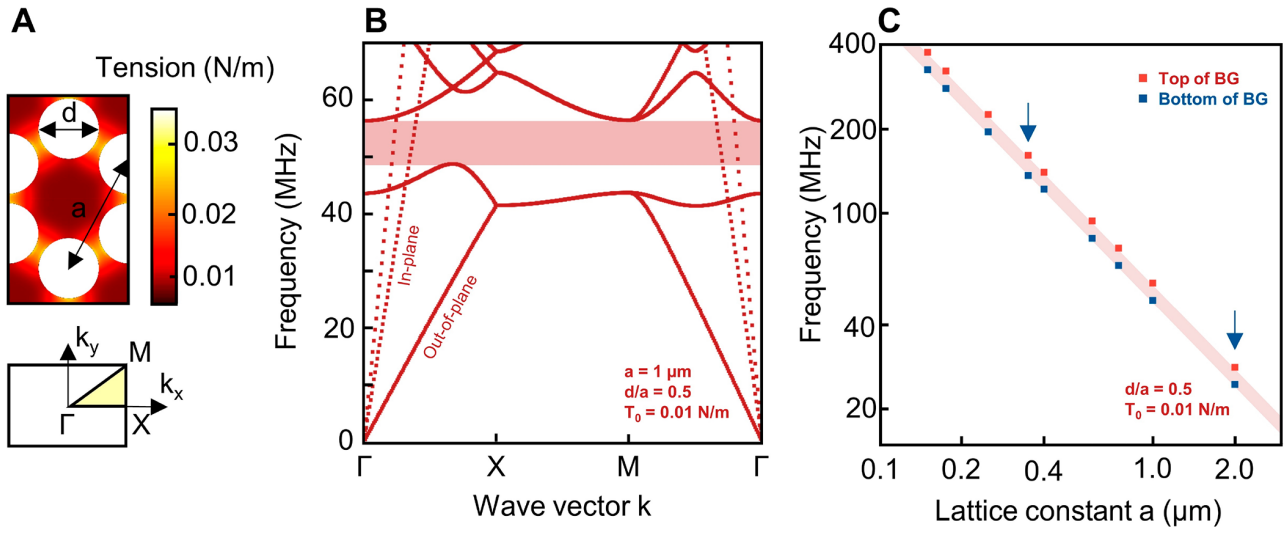

Figure 2. Band structure calculations of an infinite graphene phononic crystal. (A) Unit cell of the honeycomb lattice with redistributed tension (top) and the corresponding first Brillouin zone (bottom). (B) Phononic band structure for the unit cell shown in (A). In-plane modes are shown as dashed lines, out-of-plane modes as solid lines, and the corresponding quasi-bandgap region as the red-shaded area. (C) Top (red) and bottom (blue) of the bandgap versus lattice constant. The blue arrows indicate the lattice constant of the devices from Figure 1.

allow large mechanical tunability with small pressures. Monolayer graphene with its high carrier mobility >200 000 $cm^2/(V\ s)$[41] and large breaking strength >10%[38] perfectly fulfils these requirements. By using large area CVD graphene, we can fabricate many devices on a single chip. Finally, the device needs to host a large enough number of unit cells with sufficient periodicity to form a well-defined PnC. While this task is simple in thick SiN, it is much more challenging for fragile freestanding monolayer graphene. To overcome this, we choose a much smaller unit cell compared to typical SiN-PnCs (~100 μm size) and use helium FIB-milling to pattern the PnC.[42] This direct lithography allows one to pattern graphene down to 10 nm features,[43] while causing little damage.[44,45] A patterned prototype monolayer graphene PnC is shown in Figure 1A. It consists of a honeycomb lattice of holes (lattice constant a = 350 nm, hole diameter d = 105 nm) around a central region. Within its 10 μm diameter, the two-dimensional PnC contains more than 30 unit cells. The honeycomb lattice inspired by Tsaturayn et al.[15] exhibits a robust bandgap[12,15,46] while retaining a relatively large fraction of material to ensure a stable device. Additional PnC with various patterning sizes are shown in Figures S1−S3.

Next, we map the tension within the produced structures using Raman spectroscopy. We expect tension hot spots in the thin ribbons and relaxation in the centers of the hexagons.[47] Such tension redistribution should affect the vibrational properties of our PnC. To this end, we fabricate another prototype device (Figure 1B) with lattice constant a = 2 μm and spatial features comparable to the size of a focused laser spot. The intensity map of the 2D-Raman mode of graphene for this device is shown in Figure 1C. The intensity of the 2D-mode corresponds to the amount of material while its spectral position depends on the tension in the material.[48,49] In the pizza-like image, one can clearly see the removed material from the drop in intensity and identify the honeycomb lattice. In Figure 1D, we compare the spectral position of the Raman 2D-mode for a graphene PnC (blue) along the dashed line shown in Figure 1C to an unpatterend graphene membrane (red). The quasi-periodic variations in the PnC device that are absent in the unpatterned reference correspond to the redistributed tension. In Figure 1E, we compare the extracted relative tension (blue) to a simulation (yellow) and find the expected signatures of tension redistribution, that is, higher tension between the holes and lower tension in the middle of the hexagons (details in Supporting Information).

Phononic Crystal Simulations. Having experimentally established the feasibility of a suspended graphene PnC, we use our findings to simulate its phononic properties in two independent approaches. First, we calculate the phononic band structure for an infinitely repeated unit cell ("infinite model"). This model is well-accepted and fast.[15−17] However, due to the size limits of suspended graphene, our devices are smaller than typical SiN-PnCs (mm size)[15−17] and contain fewer unit cells. Furthermore, we want to apply pressure to the entire system and investigate localized modes in the bandgap. Therefore, we also simulate a more realistic system of finite size ("finite model"). For both models, we use the honeycomb lattice with feasible parameters and account for tension redistribution upon fabrication (Figure 1D,E). We choose a lattice constant a = 1 μm, a filling factor of d/a = 0.5 (slightly larger than in Figure 1), and an initial tension of T_0 = 0.01 N/m, which is a realistic value for clean monolayer graphene.[39,50]

Infinite Model. By applying periodic boundary conditions to the unit cell (Figure 2A), we calculate the band structure for an infinite honeycomb lattice (Figure 2B). We find a mixture of in-plane (dashed lines) and out-of-plane modes (solid lines). From the slope of the out-of-plane modes in Figure 2B, we determine the speed of sound $v_g = \frac{\partial\omega}{\partial k}$ = 83 m/s. In the range from 48.8 to 56.5 MHz (red shaded area), we find a bandgap for out-of-plane modes. This quasi-bandgap (in-plane modes are still present) has a gap-to-midgap ratio of 14.6%. The in-plane modes do not couple to out-of-plane modes[51] and therefore do not hinder radiation shielding. The bandgap originates from Bragg scattering, with each hole acting as a scatterer for out-of-plane oscillations. Upon negative interference conditions, directional Bragg bandgaps open at the high symmetry points. Where these gaps overlap, radiation shielding

https://dx.doi.org/10.1021/acs.nanolett.0c04986
Nano Lett. 2021, 21, 2174−2182

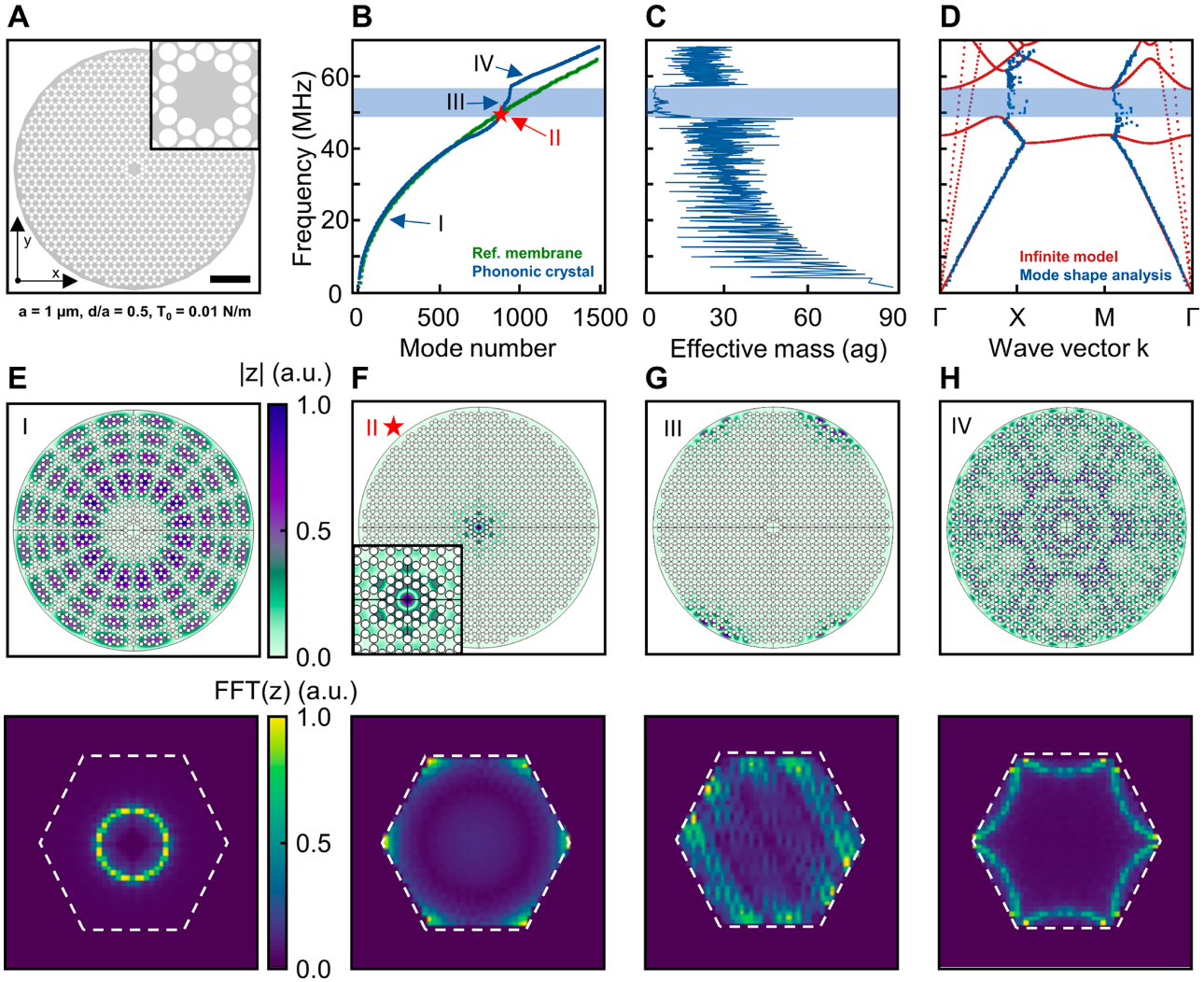

Figure 3. Finite size model of a graphene phononic crystal. (A) Device geometry for the finite system simulations (scale bar is 5 μm). A central "defect" region is designed to localize one vibrational mode and decouple it from its environment. (B) The first 1500 simulated eigenfrequencies versus mode number for a PnC device (blue) and a circular membrane without patterning (green). The bandgap region from the infinite model is shown in blue. (C) Effective mass for each mode. The modes within the bandgap (blue) show a more than a 100-fold decrease in effective mass compared to the fundamental mode. (D) Band structure calculated from the finite model via mode-shape analysis (blue) along with the band structure from the infinite model (red). The low-energy acoustic branches fit well, and the bandgap regions coincide with the simulated results from the infinite model (red). (E–H) Exemplary mode shapes in real (top) and reciprocal space (bottom) for (E) a mode below the bandgap (I), (F) the defect mode (II), (G) another highly localized mode in the bandgap (III), and (H) a mode above the gap (IV).

becomes possible, as wave propagation is isotropically forbidden.[1] The bandgap position depends reciprocally on a. With our fabrication schema, we can tailor the bandgap center from 350 to 26 MHz by varying a from 0.175 to 2 μm (Figure 2C, devices in Figures S2 and S3). Overall, the simulations in the infinite model suggest the possibility of a large quasi-bandgap, which we will next use to control phonons.

Finite Model. To study a realistic device of finite size under electrostatic pressure and to implement a defect into the phononic pattern, we conduct a second independent simulation ("finite model"). In this model, we consider a finite number of unit cells of the honeycomb lattice (same a, d/a, and T_0 as before) and employ fixed boundary conditions along the PnC's perimeter. We choose a circular device as such a geometry allows uniform suspension and minimizes edge effects. In the center of the 30.6 μm device, we create a 1.9 μm hexagonal defect,[15] as sketched in Figure 3A. Freestanding graphene devices of that size have been fabricated[52] and the central defect area is large enough to measure resonances interferometrically.[53,54] Next, we simulate the first 1500 eigenfrequencies and the corresponding spatial mode shape. In Figure 3B, we plot the frequencies f versus mode number N for the PnC (blue) and compare it to an unpatterned graphene membrane as reference (green). The graph for the PnC shows signs of a bandgap, as we observe an initial flattening of the curve followed by a sudden increase. This region of reduced mode density coincides exactly with the bandgap from our infinite model (blue area) and stands in contrast to the unpatterned membrane for which the frequencies gradually increase with mode number. The second indication of the bandgap is evident when we examine the effective mass of the modes

https://dx.doi.org/10.1021/acs.nanolett.0c04986
Nano Lett. 2021, 21, 2174–2182

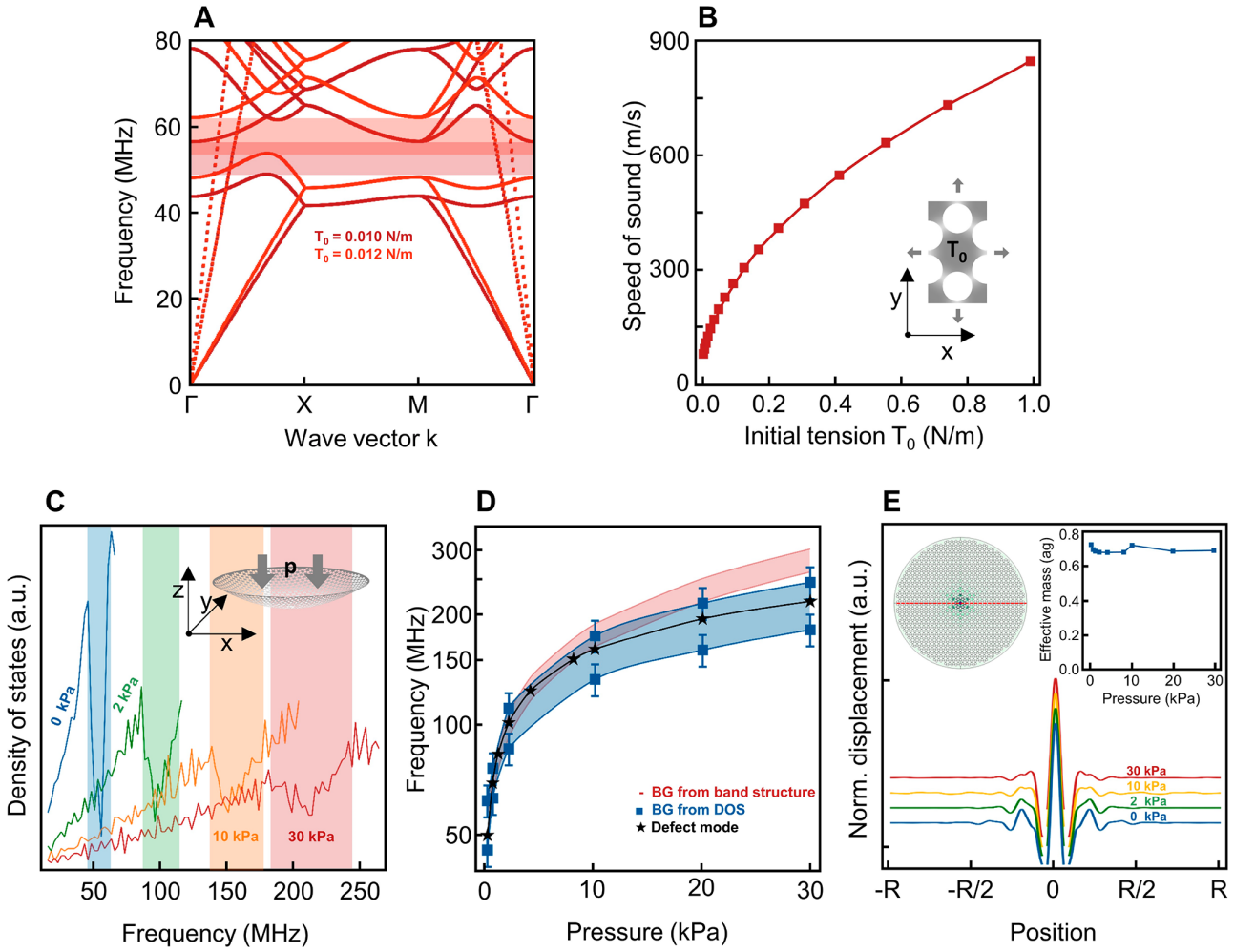

Figure 4. Mechanically tunable graphene phononic crystal. (A) Band structure for initial tension values T_0 = 0.010 N/m (red) and T_0 = 0.012 N/m (orange). The entire out-of-plane branch scales strongly with tension. The position and width of the bandgap are equally tension-dependent. (B) Speed of sound for the out-of-plane modes extracted from (A) versus tension. (C) Density of states calculated from the finite model as a function of pressure applied to the suspended PnC (T_0 = 0.010 N/m). (D) Pressure dependence of resonance frequency of the central defect mode (stars), of the bandgap from infinite model (red shaded), and of the bandgap extracted from the density of states (blue squares). The defect mode remains within the bandgap even at high pressures. (E) Line cut for the spatial profile of the defect mode at different pressures (vertically offset for clarity). Even at large applied loads, the mode shape remains localized, and the effective mass (inset) stays constant.

$$m_{\text{eff}} = \rho_{2D} \iint \frac{z^2}{z_{\text{max}}^2} \, dx \, dy$$

where ρ_{2D} is the areal density of graphene and z (z_{max}) is the (maximum) vibration amplitude in z-direction. For the fundamental mode we obtain m_{eff} = 80.9 ag = 0.252 m_{physical}, which roughly matches the literature value for the mode shape of a uniform, circular membrane of m_{eff} = 0.269 m_{physical}.[55] We observe a pronounced drop of m_{eff} in the bandgap region (Figure 3C). This observation is consistent with localized modes inside the bandgap, which typically show a small average displacement resulting in a reduced effective mass.[17]

Finally, we directly extract the band structure from the results of the finite model and compare it to that of the infinite model. To accomplish this, we analyze the mode shape of each resonance following ref 56. Specifically, we take the spatial FFT of each mode shape to find its representation in reciprocal space and to assign a wave vector k to each mode. In Figure 3E–H, we show real space (top) and reciprocal space (bottom) plots of exemplary modes. Mode I (20.2 MHz, Figure 3E) is below the bandgap and resembles a higher order Bessel mode in real space, which transforms to a near-uniform circle in momentum space. A higher frequency mode IV (60.7 MHz, Figure 3H) is situated above the bandgap. For this mode, we observe zone folding as the mode reaches out beyond the 1.BZ (dashed line). Analyzing all 1500 modes lets us restore the dispersion relation beyond the 1.BZ (Figure 3D, blue), which almost perfectly matches the band structure from the infinite model (red). From our observations of reduced mode density (Figure 3B), drop in effective mass (Figure 3C), and mode shape-analysis (Figure 3D), we confirm the presence of a bandgap for out-of-plane modes in a realistic system of finite size.

Next, we examine the modes located within the bandgap and identify the defect mode. In Figure 3G, we show a typical bandgap mode in real (top) and k-space (bottom). As most modes in the bandgap, this mode is localized at the edges of the PnC in the real space. However, one mode at frequency

https://dx.doi.org/10.1021/acs.nanolett.0c04986
Nano Lett. 2021, 21, 2174−2182

49.9 MHz is localized at the central defect (Figure 3F) and surrounded by the phononic pattern. We therefore identify it as our defect mode of special interest. The m_{eff} of the mode is 0.724 ag, which is more than a factor of 100 smaller than the fundamental mode of the system and orders of magnitude lower than for any reported SiN defect mode.[15−17] Overall, our model confirms the vibrational bandgap for a system of finite size and a localized defect mode within that bandgap.

Phononic Crystal Tuning. We now show the key advantage of our graphene PnC: dynamic and rapid frequency tuning of the bandgap and of the defect mode. To demonstrate this, we model our graphene PnC under pressure, which is applied by an electrostatic gate. The pressure causes displacement of the suspended membrane and increases the in-plane tension. We initially approximate this effect in first order in our infinite model by neglecting out-of-plane displacement and simply increasing the in-plane tension. In Figure 4A, we plot the band structure for T_0 = 0.010 and 0.012 N/m. We observe a frequency increase of the out-of-plane modes and thus an upshift of the quasi-bandgap by 10%. The speed of sound v_g rises from 83 to 830 m/s in the range of tension from 0.01 to 1 N/m (Figure 4B). The system (finite and infinite) behaves like a thin membrane under tension, and the frequencies of the PnC scale directly with tension: $f \propto \sqrt{\frac{T_0}{\rho_{2D}}}$.[55] This scaling makes our system highly sensitive to tension and in combination with graphene's mechanical flexibility allows for broad frequency tuning.

Having demonstrated the overall tunability of our system, we now simulate the effect of electrostatic pressure on the phononic system and the defect mode in a realistic device. To do so, we switch to the finite model and apply pressure in negative z-direction. In our simulations, we stick to experimentally reported pressure values and apply a maximum of 30 kPa.[39] To investigate the influence of pressure on the bandgap, we compute the phononic density of states, DOS = dN/df, and plot it versus pressure (Figure 4C). In this plot, the bandgap is distinguished by a reduced DOS. While at zero pressure the bandgap region is obvious, for higher pressures the drop becomes less pronounced (Figure 4C). We attribute this smearing to a breaking of symmetry, perturbation of the PnC as it deforms under pressure (inset Figure 4C), and rising nonuniformity in the tension distribution (Figure S6E). Nevertheless, we estimate the top and bottom of the bandgap, Figure 4D (blue). A bandgap tuning by more than 300% is evident. We verify the bandgap tuning by an independent approach based on averaging the induced tension (red markers, details in Supporting Information).

Next, we investigate tunability of the defect mode. Upon applying 30 kPa pressure to a device with an initial tension of 0.01 N/m, the resonance frequency of the defect mode upshifts from 49.9 to 217.5 MHz (black stars Figure 4D). Because the bandgap is smeared under pressure (Figure 4C), it is important to check the localization of the defect mode. Hence, we inspect a line cut through the center of the device and plot the normalized mode shape versus pressure in Figure 4E. The shape as well as the effective mass (inset Figure 4E) of the mode remains virtually unchanged and the mode retains its localization. Summarizing, we have shown a tunable speed of sound and realized an upshift of the defect mode resonance under pressure, while maintaining its localization. Such a more than 4-fold frequency increase is unprecedented and remains elusive in any other phononic systems.[22−33]

DISCUSSION

We now discuss experimental signatures of this system. The spatial features of the extended modes in our device (Figure 3E,H) are too fine to be resolved via diffraction-limited optics. At the same time, the extent of the defect mode is in the size of microns (Figure 3F) allowing the detection of that mode via interferometric read-out (Figure S8).[53,54] This mode has a nonzero net displacement and can be directly actuated via electrostatic drive. It will be straightforward to distinguish the defect mode from other modes by its localization in the center of the device and its likely increased quality factor. Indeed, the quality factor is defined by $Q = 2\pi E_{stored}/E_{diss}$, where E_{diss} is the dissipated energy per oscillation including all dissipation mechanisms and E_{stored} is the mode's total energy. As the mode shape shows zero displacement near the clamping points, we expect strongly suppressed bending losses and thus enhanced Q's. Additionally, the phononic shield hinders radiation losses into the substrate, which become especially important at higher frequencies.[16] While bending and radiation losses may play a secondary role among the mechanisms lowering Q in graphene resonators, our experiments nevertheless should determine the contribution of these mechanisms. Finally, by applying pressure we increase the stiffness of the resonator. This increases the energy stored in the system[17] and supposedly further enhances the quality factor. The demonstrated level of strain control in our system invites future studies on dissipation dilution via strain engineering following the work of Ghadimi et al.[17]

We also note that our results can be easily extended to the entire family of two-dimensional materials. Currently, it is challenging for us to experimentally achieve sufficient uniformity in the graphene membrane in order to generate a spatially uniform bandgap and localize the defect mode. Monolayer graphene is rather sensitive to surface corrugations[39] and transferred CVD graphene is often covered by fabrication residues, so using thin exfoliated graphene multilayers could be a solution for which we expect to find experimental signatures. The increased uniformity in multilayer graphene comes along with a decreased tunability, yet we anticipate more than 100% relative tuning for up to ∼35 layers (Figure S9). For our graphene PnC, we do not expect to reach Q's comparable to SiN. Nevertheless, we estimate m_{eff} of our defect mode to be at least 8 orders of magnitude lower than in other 2D-SiN-PnCs.[15] This immensely increases the measurement rate of quantum states $\Gamma_{meas} \propto 1/m_{eff}$ and decreases thermomechanical noise.[15] The frequencies in our system are controlled by simply adjusting a gate voltage, and we expect the tuning to take place on time scales comparable to regular graphene resonators and therefore achieve tuning bandwidths >15 kHz.[57]

CONCLUSION

In summary, we have fabricated and simulated a tunable PnC made from monolayer graphene. For an experimentally informed honeycomb lattice structure, we find a robust vibrational bandgap in the megahertz range. The bandgap persists for a finite-size system, and we use it to localize a defect mode and shield it from its surroundings. This defect mode shows a very small effective mass of 0.724 ag, orders of magnitude smaller compared to traditional PnCs. As our central result, we demonstrate a frequency upshift of the defect mode as well as the entire phononic system by more than

https://dx.doi.org/10.1021/acs.nanolett.0c04986
Nano Lett. 2021, 21, 2174−2182

350% by applying an experimentally feasible pressure of 30 kPa. While the bandgap smears out due to out-of-plane displacement perturbing the lattice, the defect mode stays within the bandgap and remains highly localized. We suggest experimental signatures of the defect mode allowing its differentiation from other modes in the system. Overall, our design of a 2D-material-based PnC adds a new knob to dynamically and rapidly tune frequencies in a broad range of phononic applications. Our results invite future experiments as our approach allows adjustable coupling of a PnC to external systems and may lead to better understanding of the dissipation mechanisms in graphene.

METHODS

Device Fabrication. The pattering of the CVD grown graphene membranes was carried out in a He-ion microscope (Orion Nanofab). Supporting Information Section I provides a detailed process description.

Raman Spectroscopy. Raman mapping was performed on a Horiba Xplora Raman spectrometer using a 100× (NA 0.9) objective and 532 nm excitation. Spectra were acquired with a laser power of 0.5 mW and an integration time of 3 s. Tension (via strain) values were derived from the 2D-mode position following standard procedures, see Supporting Information Section IV.

Simulations. For the finite element modeling we use COMSOL Multiphysics (Version 5.5) and assume the following material parameters for monolayer graphene: Young's modulus E_{2D} = 1.0 TPa,[38] Poisson's ratio of ν = 0.15, thickness of h = 0.335 nm, and a density of $\rho = \frac{\rho_{2D}}{h} =$ 2260 kg/m^3. The initial tension T_0 = 0.01 N/m thus corresponds to an initial strain: $\epsilon_0 = \frac{T_0}{E_{2D}} \approx 0.003\%$. For details see Supporting Information, Sections II and III.

ASSOCIATED CONTENT

Supporting Information

The Supporting Information is available free of charge at https://pubs.acs.org/doi/10.1021/acs.nanolett.0c04986.

Graphene pattering using He-FIB milling, details of the FEM-simulations and the mode shape analysis, detailed Raman spectroscopy analysis, and simulations on experimental signatures (PDF)

AUTHOR INFORMATION

Corresponding Authors

Jan N. Kirchhof − *Department of Physics, Freie Universität Berlin, 14195 Berlin, Germany;* orcid.org/0000-0001-8576-4787; Email: jan.kirchhof@fu-berlin.de

Kirill I. Bolotin − *Department of Physics, Freie Universität Berlin, 14195 Berlin, Germany;* Email: kirill.bolotin@fu-berlin.de

Authors

Kristina Weinel − *Department of Physics, Freie Universität Berlin, 14195 Berlin, Germany; Ferdinand-Braun-Institut gGmbH Leibniz-Institut für Höchstfrequenztechnik, 12489 Berlin, Germany*

Sebastian Heeg − *Department of Physics, Freie Universität Berlin, 14195 Berlin, Germany;* orcid.org/0000-0002-6485-3083

Victor Deinhart − *Ferdinand-Braun-Institut gGmbH Leibniz-Institut für Höchstfrequenztechnik, 12489 Berlin, Germany; Helmholtz-Zentrum Berlin für Materialien und Energie, 14109 Berlin, Germany*

Sviatoslav Kovalchuk − *Department of Physics, Freie Universität Berlin, 14195 Berlin, Germany;* orcid.org/0000-0002-4817-1939

Katja Höflich − *Ferdinand-Braun-Institut gGmbH Leibniz-Institut für Höchstfrequenztechnik, 12489 Berlin, Germany; Helmholtz-Zentrum Berlin für Materialien und Energie, 14109 Berlin, Germany;* orcid.org/0000-0003-4088-2928

Complete contact information is available at: https://pubs.acs.org/10.1021/acs.nanolett.0c04986

Author Contributions

J.N.K. conceived the idea. Suspended graphene devices were fabricated by K.W., S.K., and J.N.K. He-FIB pattering procedures were developed and carried out by K.H. and V.D. at HZB Berlin. S.H. acquired and analyzed Raman spectroscopy data. Sample design and FEM-modeling was performed by J.N.K. with participation by K.W. J.N.K. and K.I.B. cowrote the paper with input from all authors. K.I.B. supervised the project. All authors discussed the results.

Funding

This work was supported by ERC Starting Grant 639739 and DFG TRR 227. V.D. and K.H. acknowledge financial support from DFG under Grant HO 5461/3−1. The He ion beam patterning was performed in the Corelab Correlative Microscopy and Spectroscopy at Helmholtz-Zentrum Berlin and within the framework of the EU COST action CA 19140 'FIT4NANO'.

Notes

The authors declare no competing financial interest.

REFERENCES

(1) Kushwaha, M. S.; Halevi, P.; Dobrzynski, L.; Djafari-Rouhani, B. Acoustic Band Structure of Periodic Elastic Composites. *Phys. Rev. Lett.* **1993**, *71* (13), 2022−2025.

(2) Hopkins, P. E.; Reinke, C. M.; Su, M. F.; Olsson, R. H.; Shaner, E. A.; Leseman, Z. C.; Serrano, J. R.; Phinney, L. M.; El-Kady, I. Reduction in the Thermal Conductivity of Single Crystalline Silicon by Phononic Crystal Patterning. *Nano Lett.* **2011**, *11* (1), 107−112.

(3) Maldovan, M. Sound and Heat Revolutions in Phononics. *Nature* **2013**, *503*, 209−217.

(4) Mousavi, S. H.; Khanikaev, A. B.; Wang, Z. Topologically Protected Elastic Waves in Phononic Metamaterials. *Nat. Commun.* **2015**, *6* (1), 1−7.

(5) Balram, K. C.; Davanço, M. I.; Song, J. D.; Srinivasan, K. Coherent Coupling between Radiofrequency, Optical and Acoustic Waves in Piezo-Optomechanical Circuits. *Nat. Photonics* **2016**, *10* (5), 346−352.

(6) Olsson, R. H.; El-Kady, I. Microfabricated Phononic Crystal Devices and Applications. *Meas. Sci. Technol.* **2009**, *20* (1), 012002.

(7) Khelif, A.; Choujaa, A.; Benchabane, S.; Djafari-Rouhani, B.; Laude, V. Guiding and Bending of Acoustic Waves in Highly Confined Phononic Crystal Waveguides. *Appl. Phys. Lett.* **2004**, *84* (22), 4400−4402.

(8) Lin, S. C. S.; Huang, T. J.; Sun, J. H.; Wu, T. T. Gradient-Index Phononic Crystals. *Phys. Rev. B: Condens. Matter Mater. Phys.* **2009**, *79* (9), 094302.

(9) Zhao, J.; Bonello, B.; Marchal, R.; Boyko, O. Beam Path and Focusing of Flexural Lamb Waves within Phononic Crystal-Based Acoustic Lenses. *New J. Phys.* **2014**, *16*, 063031.

(10) Benchabane, S.; Khelif, A.; Rauch, J. Y.; Robert, L.; Laude, V. Evidence for Complete Surface Wave Band Gap in a Piezoelectric Phononic Crystal. *Phys. Rev. E - Stat. Nonlinear, Soft Matter Phys.* **2006**, *73* (6), 065601.
(11) Khelif, A.; Aoubiza, B.; Mohammadi, S.; Adibi, A.; Laude, V. Complete Band Gaps in Two-Dimensional Phononic Crystal Slabs. *Phys. Rev. E - Stat. Nonlinear, Soft Matter Phys.* **2006**, *74* (4), 043509.
(12) Mohammadi, S.; Eftekhar, A. A.; Khelif, A.; Hunt, W. D.; Adibi, A. Evidence of Large High Frequency Complete Phononic Band Gaps in Silicon Phononic Crystal Plates. *Appl. Phys. Lett.* **2008**, *92* (22), 221905.
(13) Li, F.; Liu, J.; Wu, Y. The Investigation of Point Defect Modes of Phononic Crystal for High Q Resonance. *J. Appl. Phys.* **2011**, *109* (12), 124907.
(14) Yu, P. L.; Cicak, K.; Kampel, N. S.; Tsaturyan, Y.; Purdy, T. P.; Simmonds, R. W.; Regal, C. A. A Phononic Bandgap Shield for High-Q Membrane Microresonators. *Appl. Phys. Lett.* **2014**, *104* (2), 023510.
(15) Tsaturyan, Y.; Barg, A.; Polzik, E. S.; Schliesser, A. Ultracoherent Nanomechanical Resonators via Soft Clamping and Dissipation Dilution. *Nat. Nanotechnol.* **2017**, *12* (8), 776−783.
(16) Ghadimi, A. H.; Wilson, D. J.; Kippenberg, T. J. Radiation and Internal Loss Engineering of High-Stress Silicon Nitride Nanobeams. *Nano Lett.* **2017**, *17* (6), 3501−3505.
(17) Ghadimi, A. H.; Fedorov, S. A.; Engelsen, N. J.; Bereyhi, M. J.; Schilling, R.; Wilson, D. J.; Kippenberg, T. J. Elastic Strain Engineering for Ultralow Mechanical Dissipation. *Science (Washington, DC, U. S.)* **2018**, *360* (6390), 764−768.
(18) Imboden, M.; Mohanty, P. Dissipation in Nanoelectromechanical Systems. *Phys. Rep.* **2014**, *534*, 89−146.
(19) Ekinci, K. L.; Roukes, M. L. Nanoelectromechanical Systems. *Rev. Sci. Instrum.* **2005**, *76* (6), 061101.
(20) Guo, J.; Norte, R.; Gröblacher, S. Feedback Cooling of a Room Temperature Mechanical Oscillator Close to Its Motional Ground State. *Phys. Rev. Lett.* **2019**, *123* (22), 223602.
(21) Delić, U.; Reisenbauer, M.; Dare, K.; Grass, D.; Vuletić, V.; Kiesel, N.; Aspelmeyer, M. Cooling of a Levitated Nanoparticle to the Motional Quantum Ground State. *Science (Washington, DC, U. S.)* **2020**, *367* (6480), 892−895.
(22) Huang, H.; Tan, Z.; Huo, S.; Feng, L.; Chen, J.; Han, X. Topologically Protected Zero Refraction of Elastic Waves in Pseudospin-Hall Phononic Crystals. *Commun. Phys.* **2020**, *3* (1), 46.
(23) Tian, Z.; Shen, C.; Li, J.; Reit, E.; Bachman, H.; Socolar, J. E. S.; Cummer, S. A.; Jun Huang, T. Dispersion Tuning and Route Reconfiguration of Acoustic Waves in Valley Topological Phononic Crystals. *Nat. Commun.* **2020**, *11* (1), 762.
(24) Cha, J.; Daraio, C. Electrical Tuning of Elastic Wave Propagation in Nanomechanical Lattices at MHz Frequencies. *Nat. Nanotechnol.* **2018**, *13*, 1016−1020.
(25) Jang, J. H.; Ullal, C. K.; Gorishnyy, T.; Tsukruk, V. V.; Thomas, E. L. Mechanically Tunable Three-Dimensional Elastomeric Network/Air Structures via Interference Lithography. *Nano Lett.* **2006**, *6* (4), 740−743.
(26) Lin, S. C. S.; Huang, T. J. Tunable Phononic Crystals with Anisotropic Inclusions. *Phys. Rev. B: Condens. Matter Mater. Phys.* **2011**, *83* (17), 174303.
(27) Chen, Z. G.; Wu, Y. Tunable Topological Phononic Crystals. *Phys. Rev. Appl.* **2016**, *5* (5), 054021.
(28) Lin, S. C. S.; Huang, T. J. Tunable Phononic Crystals with Anisotropic Inclusions. *Phys. Rev. B: Condens. Matter Mater. Phys.* **2011**, *83* (17), 174303.
(29) Bian, Z.; Peng, W.; Song, J. Thermal Tuning of Band Structures in a One-Dimensional Phononic Crystal. *J. Appl. Mech.* **2014**, *81* (4), 041008.
(30) Jim, K. L.; Leung, C. W.; Lau, S. T.; Choy, S. H.; Chan, H. L. W. Thermal Tuning of Phononic Bandstructure in Ferroelectric Ceramic/Epoxy Phononic Crystal. *Appl. Phys. Lett.* **2009**, *94* (19), 193501.
(31) Robillard, J. F.; Matar, O. B.; Vasseur, J. O.; Deymier, P. A.; Stippinger, M.; Hladky-Hennion, A. C.; Pennec, Y.; Djafari-Rouhani, B. Tunable Magnetoelastic Phononic Crystals. *Appl. Phys. Lett.* **2009**, *95* (12), 124104.
(32) Bou Matar, O.; Robillard, J. F.; Vasseur, J. O.; Hladky-Hennion, A. C.; Deymier, P. A.; Pernod, P.; Preobrazhensky, V. Band Gap Tunability of Magneto-Elastic Phononic Crystal. *J. Appl. Phys.* **2012**, *111* (5), 054901.
(33) Huang, Y.; Zhang, C. L.; Chen, W. Q. Tuning Band Structures of Two-Dimensional Phononic Crystals with Biasing Fields. *J. Appl. Mech.* **2014**, *81* (9), 1−8.
(34) Thomas, R. A.; Parniak, M.; Østfeldt, C.; Møller, C. B.; Bærentsen, C.; Tsaturyan, Y.; Schliesser, A.; Appel, J.; Zeuthen, E.; Polzik, E. S. Entanglement between Distant Macroscopic Mechanical and Spin Systems. *Nat. Phys.* **2020**, 1−6.
(35) Hatanaka, D.; Bachtold, A.; Yamaguchi, H. Electrostatically Induced Phononic Crystal. *Phys. Rev. Appl.* **2019**, *11* (2), 1.
(36) Midtvedt, D.; Isacsson, A.; Croy, A. Nonlinear Phononics Using Atomically Thin Membranes. *Nat. Commun.* **2014**, *5*, 5.
(37) Wang, Y.; Lee, J.; Zheng, X. Q.; Xie, Y.; Feng, P. X. L. Hexagonal Boron Nitride Phononic Crystal Waveguides. *ACS Photonics* **2019**, *6* (12), 3225−3232.
(38) Lee, C.; Wei, X.; Kysar, J. W.; Hone, J. Measurement of the Elastic Properties and Intrinsic Strength of Monolayer Graphene. *Science (Washington, DC, U. S.)* **2008**, *321* (5887), 385−388.
(39) Nicholl, R. J. T.; Conley, H. J.; Lavrik, N. V.; Vlassiouk, I.; Puzyrev, Y. S.; Sreenivas, V. P.; Pantelides, S. T.; Bolotin, K. I. The Effect of Intrinsic Crumpling on the Mechanics of Free-Standing Graphene. *Nat. Commun.* **2015**, *6*, 8789.
(40) Singh, R.; Nicholl, R. J. T.; Bolotin, K. I.; Ghosh, S. Motion Transduction with Thermo-Mechanically Squeezed Graphene Resonator Modes. *Nano Lett.* **2018**, *18* (11), 6719−6724.
(41) Bolotin, K. I.; Sikes, K. J.; Jiang, Z.; Klima, M.; Fudenberg, G.; Hone, J.; Kim, P.; Stormer, H. L. Ultrahigh Electron Mobility in Suspended Graphene. *Solid State Commun.* **2008**, *146* (9−10), 351−355.
(42) Deinhart, V. fib-o-mat. https://pypi.org/project/fibomat/ (accessed Oct 10, 2020).
(43) Lemme, M. C.; Bell, D. C.; Williams, J. R.; Stern, L. A.; Baugher, B. W. H.; Jarillo-Herrero, P.; Marcus, C. M. Etching of Graphene Devices with a Helium Ion Beam. *ACS Nano* **2009**, *3* (9), 2674−2676.
(44) Archanjo, B. S.; Fragneaud, B.; Gustavo Cançado, L.; Winston, D.; Miao, F.; Alberto Achete, C.; Medeiros-Ribeiro, G. Graphene Nanoribbon Superlattices Fabricated via He Ion Lithography. *Appl. Phys. Lett.* **2014**, *104* (19), 193114.
(45) Fox, D.; Zhou, Y. B.; O'Neill, A.; Kumar, S.; Wang, J. J.; Coleman, J. N.; Duesberg, G. S.; Donegan, J. F.; Zhang, H. Z. Helium Ion Microscopy of Graphene: Beam Damage, Image Quality and Edge Contrast. *Nanotechnology* **2013**, *24* (33), 335702.
(46) Mohammadi, S.; Eftekhar, A. A.; Khelif, A.; Moubchir, H.; Westafer, R.; Hunt, W. D.; Adibi, A. Complete Phononic Bandgaps and Bandgap Maps in Two-Dimensional Silicon Phononic Crystal Plates. *Electron. Lett.* **2007**, *43* (16), 898−899.
(47) Capelle, T.; Tsaturyan, Y.; Barg, A.; Schliesser, A. Polarimetric Analysis of Stress Anisotropy in Nanomechanical Silicon Nitride Resonators. *Appl. Phys. Lett.* **2017**, *110* (18), 181106.
(48) Mohiuddin, T. M. G.; Lombardo, A.; Nair, R. R.; Bonetti, A.; Savini, G.; Jalil, R.; Bonini, N.; Basko, D. M.; Galiotis, C.; Marzari, N.; Novoselov, K. S.; Geim, A. K.; Ferrari, A. C. Uniaxial Strain in Graphene by Raman Spectroscopy: G Peak Splitting, Grüneisen Parameters, and Sample Orientation. *Phys. Rev. B: Condens. Matter Mater. Phys.* **2009**, *79* (20), 1−8.
(49) Mueller, N. S.; Heeg, S.; Alvarez, M. P.; Kusch, P.; Wasserroth, S.; Clark, N.; Schedin, F.; Parthenios, J.; Papagelis, K.; Galiotis, C.; Kalbáč, M.; Vijayaraghavan, A.; Huebner, U.; Gorbachev, R.; Frank, O.; Reich, S. Evaluating Arbitrary Strain Configurations and Doping in Graphene with Raman Spectroscopy. *2D Mater.* **2018**, *5* (1), 015016.

https://dx.doi.org/10.1021/acs.nanolett.0c04986
Nano Lett. 2021, 21, 2174−2182

(50) Chen, C.; Rosenblatt, S.; Bolotin, K. I.; Kalb, W.; Kim, P.; Kymissis, I.; Stormer, H. L.; Heinz, T. F.; Hone, J. Performance of Monolayer Graphene Nanomechanical Resonators with Electrical Readout. *Nat. Nanotechnol.* **2009**, *4* (12), 861−867.
(51) Tsaturyan, Y. *Ultracoherent Soft-Clamped Mechanical Resonators for Quantum Cavity Optomechanics*; University of Copenhagen, 2019. https://www.nbi.ku.dk/english/theses/phd-theses/yeghishe-tsaturyan/Yeghishe2.pdf.
(52) Alemán, B.; Regan, W.; Aloni, S.; Altoe, V.; Alem, N.; Girit, C.; Geng, B.; Maserati, L.; Crommie, M.; Wang, F.; Zettl, A. Transfer-Free Batch Fabrication of Large- Area Suspended Graphene Membranes. *ACS Nano* **2010**, *4* (8), 4762−4768.
(53) Van Der Zande, A. M.; Barton, R. A.; Alden, J. S.; Ruiz-Vargas, C. S.; Whitney, W. S.; Pham, P. H. Q.; Park, J.; Parpia, J. M.; Craighead, H. G.; McEuen, P. L. Large-Scale Arrays of Single-Layer Graphene Resonators. *Nano Lett.* **2010**, *10* (12), 4869−4873.
(54) Bunch, J. S.; Van Der Zande, A. M.; Verbridge, S. S.; Frank, I. W.; Tanenbaum, D. M.; Parpia, J. M.; Craighead, H. G.; McEuen, P. L. Electromechanical Resonators from Graphene Sheets. *Science (Washington, DC, U. S.)* **2007**, *315* (5811), 490−493.
(55) Hauer, B. D.; Doolin, C.; Beach, K. S. D.; Davis, J. P. A General Procedure for Thermomechanical Calibration of Nano/Micro-Mechanical Resonators. *Annals of Physics*. Academic Press, 2013; pp 181−207.
(56) Waitz, R.; Nößner, S.; Hertkorn, M.; Schecker, O.; Scheer, E. Mode Shape and Dispersion Relation of Bending Waves in Thin Silicon Membranes. *Phys. Rev. B: Condens. Matter Mater. Phys.* **2012**, *85* (3), 035324.
(57) Chen, C.; Lee, S.; Deshpande, V. V.; Lee, G. H.; Lekas, M.; Shepard, K.; Hone, J. Graphene Mechanical Oscillators with Tunable Frequency. *Nat. Nanotechnol.* **2013**, *8* (12), 923−927.

https://dx.doi.org/10.1021/acs.nanolett.0c04986
Nano Lett. 2021, 21, 2174−2182

Supporting Information: Tunable graphene phononic crystal

Jan N. Kirchhof[1], Kristina Weinel[1,2], Sebastian Heeg[1], Victor Deinhart[2,3], Sviatoslav Kovalchuk[1], Katja Höflich[2,3] and Kirill I. Bolotin[1*]*

[1]Department of Physics, Freie Universität Berlin, Arnimallee 14, 14195 Berlin, Germany.

[2]Ferdinand-Braun-Institut gGmbH Leibniz-Institut für Höchstfrequenztechnik, Gustav-Kirchhoff-Str. 4, 12489 Berlin, Germany

[3]Helmholtz-Zentrum Berlin für Materialien und Energie, Hahn-Meitner-Platz 1, 14109 Berlin, Germany.

*jan.kirchhof@fu-berlin.de *kirill.bolotin@fu-berlin.de

I. Sample synthesis and device pattering using He-FIB milling

Monolayer graphene was synthesized on copper by low pressure chemical vapor deposition (CVD). Upon reaching the growth temperature of 1035 °C a mixture of methane (5 sccm), hydrogen (10 sccm), and argon (5 sccm) was introduced into the CVD chamber. After 7 min growth time and a rapid cooldown, graphene was wet transferred onto a perforated SiN membrane, covered by Cr/Au (5 nm/35 nm) to electrically contact the graphene.

To pattern the suspended graphene, we used a beam of focused helium ions in the Orion Nanofab microscope. The local material removal upon ion beam impact is a complex interplay between physical sputtering (ions kick out surface atoms), the redeposition of the sputtered surface atoms in the close vicinity, chemical reactions (like polymerization of organic residues by the generated secondary electrons) as well as the introduction of heat and amorphization.[1] In case of two-dimensional material only physical sputtering contributes. The holes were patterned with a dwell time of 1.5 ms and a pixel spacing of 1 nm at a beam current of 4-5 pA (device settings: $2x10^{-6}$ Torr He , U_{acc} = 30 kV, UBIV = 34 kV, aperture 2 µm). The holes on the outside of device were cut first, following a spiralling milling strategy to the centre of the suspended area (Figure S1B). Here each single hole is milled in an opposite spiral order – starting at the centre of the hole (Figure S1C). If the graphene layer is completely intact and free of contamination, the process is highly reproducible (see Figure S2). In Figure S3A we show fabricated phononic crystal devices with varying lattice constant a: 0.175…2 µm. While the patterning allows for highly flexible variation of geometrical parameters, like lattice constant and hole diameter, the process of He-ion induced physical sputtering is highly sensitive to surface contamination. In Figure S3B this effect becomes visible by the bright regions around the

spot. Here, the secondary electrons induced polymerization of the organic residues and therefore material build-up (deposition). The amount of contamination increases the minimum dose to achieve a full cut and may even dominate over physical sputtering as shown here for the smallest spots. As the coverage of organic residues may locally vary also the required minimum dose for complete graphene removal can vary locally. This can be seen in Figure 1B of the main manuscript. Holes with sizes down to 5 nm can be fabricated by He ion beam milling in relatively uniform and uncontaminated monolayer graphene (Figure S3B).

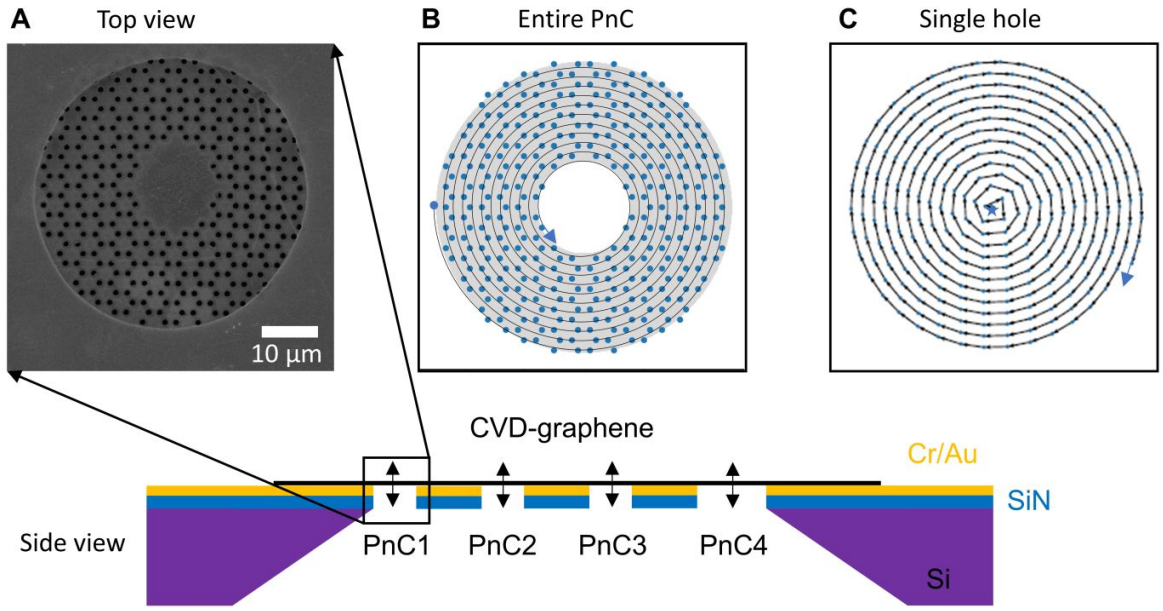

Figure S1. Milling strategy for PnC-device patterning. (**A**) Device with lattice constant a = 700 nm. By transferring CVD graphene onto pre-pattered substrates with many through holes, many PnC can be milled on a single chip. (**B**) Corresponding design file including the pattering order – starting at the outside and spiralling towards centre of the device. (**C**) Patterning of a single hole – starting in the centre moving to the outside.

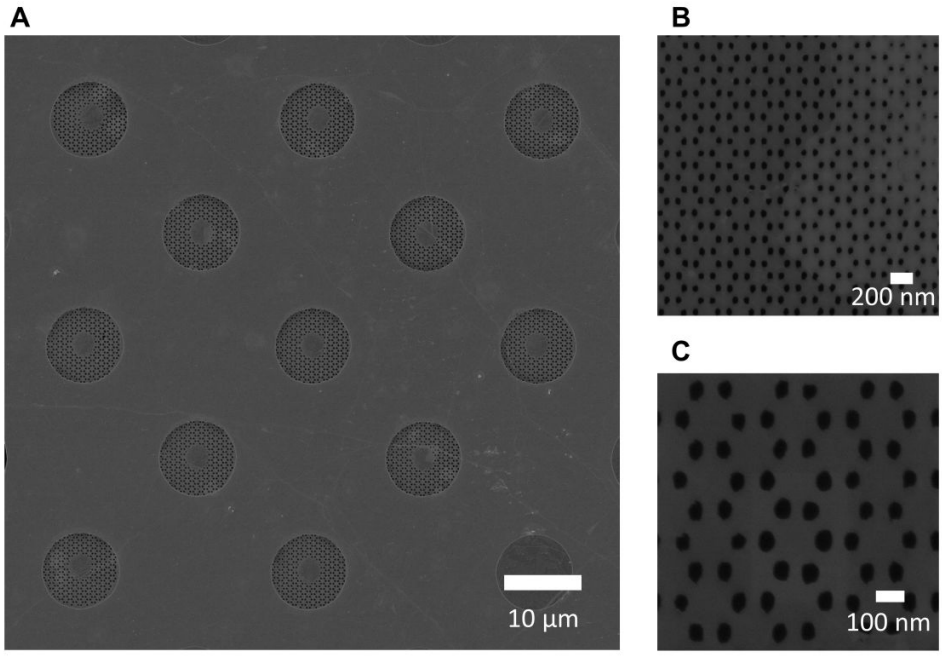

Figure S2. Reproducible PnC patterning. (**A**) Repeated pattering of a device with lattice constant a = 700nm. For uniform graphene the process is highly reproducible. (**B**,**C**) Zoom-in on the honeycomb lattice with a = 175 nm. The milling process is less efficient on add-layer regions – visible on the right half in (**B**).

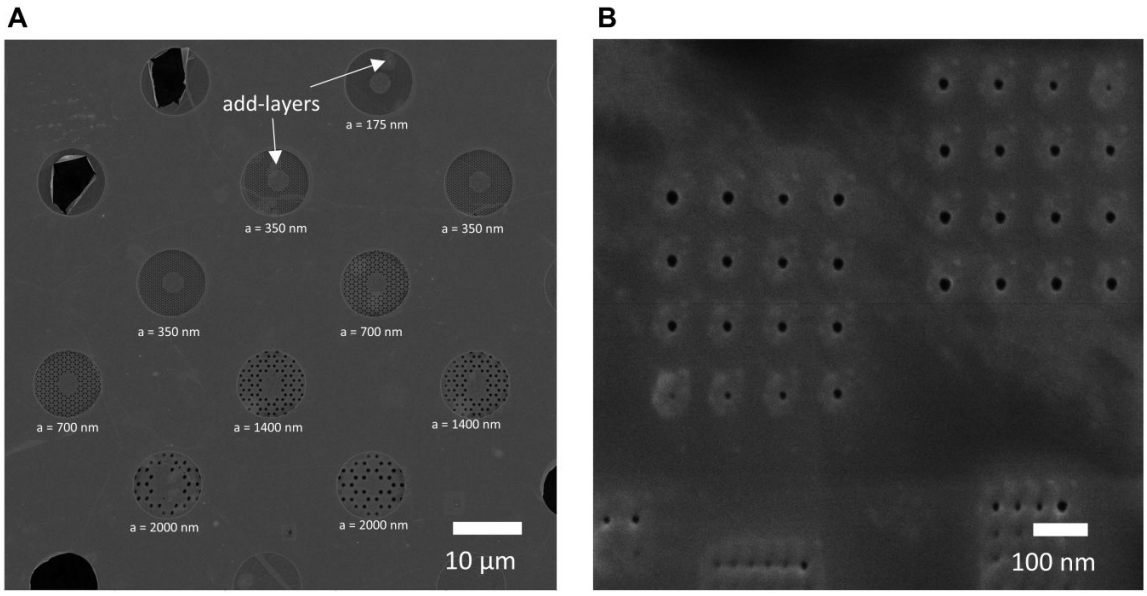

Figure S3. Scalable PnC patterning. (**A**) PnC devices of varying lattice constant a = 175 nm - 2 µm. Occasional add-layer regions from CVD growth are marked. (**B**) Dose tests on uniform and clean graphene, show that pores with sizes well below 5 nm can be fabricated by He ion beam milling.

II. Finite element method simulations

We use the solid mechanics module of Comsol Multiphysics (Version 5.5) to carry out the FEM-simulations presented in the main paper.

The **infinite model** for the band structure calculations consist of two studies within one model. We use a large square containing many unit cells of the phononic pattern and implement uniform tension in the solid (Figure S4). In a stationary study with fixed boundary conditions at the edges, we simulate the tension redistribution, which occurs upon cutting holes into a system under tension.

We then add a second study (eigenfrequency domain) within in the same model to simulate the resonances und thus plot the band structure. To accurately depict the tension distribution, we crop the central unit cell of the large square from the first study and component-wise transfer the tension distribution to the second study (Fig S4). To obtain the band structure, we apply periodic boundary conditions (Floquet) to the edges of the unit cell and parameterize k_x and k_y (in an auxiliary sweep) along the high symmetry lines in the first Brillion zone and calculate the first 6-10 eigenfrequencies for every value of k. By plotting the frequencies f vs. k, we get the dispersion relation for the geometry of interest. We use a swept mesh as we simulate a very thin system. Furthermore, we apply copy operators within in the unit cell when building the mesh to completely capture the symmetry of the system (Fig S5B). In general, the size of the bandgap depends on the filling factor d/a. Choosing d/a~0.5 (slightly larger than for Figure 1 in the main paper) results in a reasonably sized bandgap, whilst leaving behind enough material to reproducibly fabricate devices. In Figure S5, we provide a detailed study of bandgap width vs. d/a. Taking into account for tension redistribution overall reduces the size of the bandgap. For the second estimate of the bandgap tuning with applied pressure (main text,

Figure 4D) we extract the average tension in the finite model at each pressure value and feed the average values as input into our infinite model.

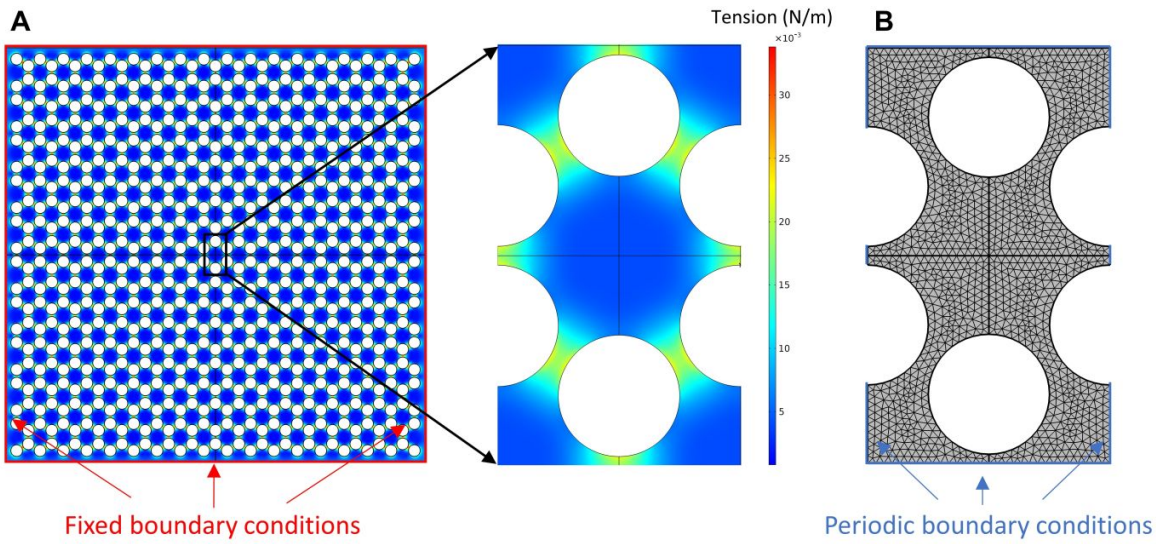

Figure S4. Infinite model PnC simulations. (**A**) A large membrane is needed to correctly calculate the tension redistribution. A central unit cell is cropped and used for the band structure calculations (**B**) Corresponding mesh of the unit cell.

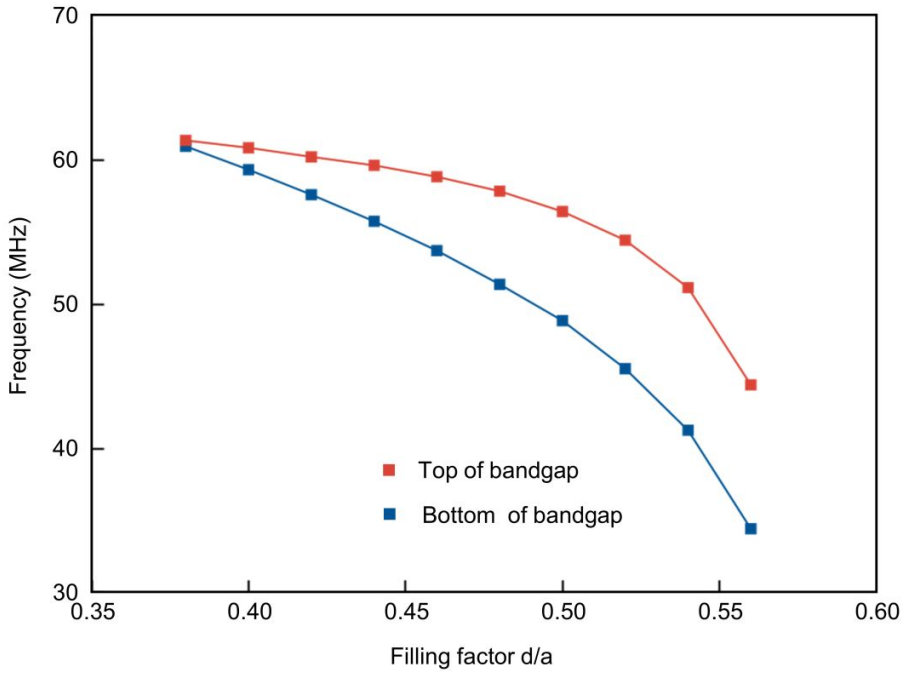

Figure S5. Phononic Bandgap vs. filling factor. Frequencies of the top and of the bottom of the bandgap vs. the filling factor d/a for a = 1 μm and an initial tension of T_0 = 0.01 N/m. Tension redistribution is accounted for.

For the calculations in the **finite model** we use a membrane model from the solid mechanics module with two study steps (Figure S6). In the first step, we again let the system relax after adding uniform built in tension. The resulting tension distribution is shown in Figure S6 C and D. We then calculate the first 1500-2500 resonances of the system in an eigenfrequency study step. The mode shapes and frequencies are exported for further analysis in a python script (see section III). Also here it is important for the mesh to represent the symmetry of the modelled geometry – compare Figure 6B.

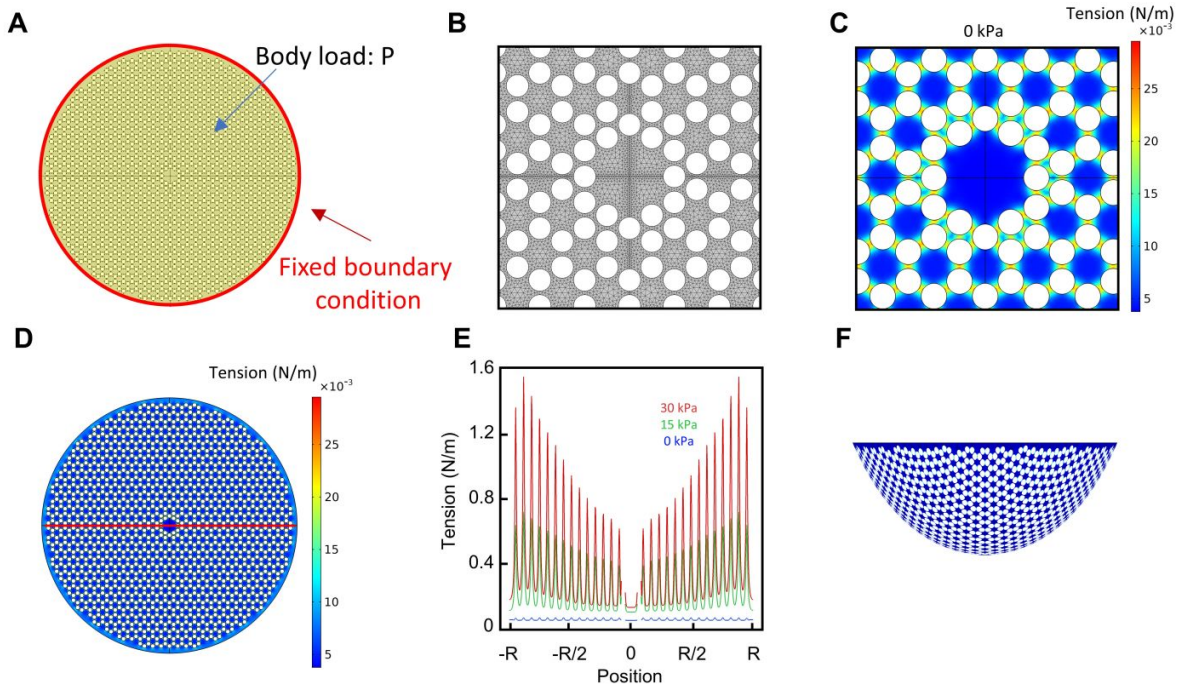

Figure S6. Finite model PnC simulations. (**A**) Circular PnC of 30.6 µm size. The electrostatic pressure is applied as a body load (yellow). (**B**) Symmetric mesh. (**C**) Tension after the redistribution step around the central defect region and in the entire device (**D**). (**E**) Tension along a line cut (marked red in (**D**)) for different pressures. With larger pressures, the distribution becomes increasingly non-uniform. (**F**) Deformation of the finite system under large pressures (100 kPa) to illustrate the perturbation of the phononic pattern.

III. Mode shape analysis

We first export the mode shape for each mode obtained from our Comsol simulations and interpolate it onto a square grid with 1000 nodes. Next, we carry out a fast Fourier transform (FFT) on such an array to obtain the reciprocal space representation of each

mode. Most modes, except for the ones within the bandgap, have a well-defined momentum along each specific direction. To determine the momentum content of each mode, we take a cut of each mode in the momentum space and find a peak along each particular direction. To aid in this procedure and reduce noise, we average over 10 neighboring modes. Knowing the momentum, we finally export the dispersion relation along the direction of interest.

IV. Raman spectroscopy analysis

In the main paper, we use initial tension T_0 as a device parameter to avoid confusion. For Raman data however it is more common characterize graphene in terms strain ϵ_0, which is directly linked to tension value via the 2D-Youngs-modulus $T_0 = \epsilon_0 E_{2D}$. In this section, we discuss in detail the signatures of strain redistribution obtained by Raman spectroscopy of the graphene phononic crystal presented in the main paper. Figure S7A shows a Raman map of the integrated 2D-mode intensity of the suspended membrane, see Figure 1D of the main paper. The holes forming the phononic crystal are clearly marked by a local decrease in 2D-mode intensity. We show a representative Raman spectrum from the centre of the phononic crystal in Figure 7B, marked by (#) in Figure S7A. The experimentally observed intensity ratio between the Raman G and D peaks, I(2D)/I(G)>1, proves that the phononic crystal is made from a single layer of graphene. We used SEM imaging to avoid measuring the devices with bilayer graphene areas (Fig. S3A). The appearance of the D, D' and D+D' mode indicate the presence of defects, which arise mainly from repeated electron beam imaging of the graphene membrane.

To demonstrate the onset of strain relaxation, we focus on a horizontal line cut (along x within out laboratory frame) across the phononic crystal at y = 2.3 μm as indicated by the dashed line in Figure S7A. Figure S7C shows the corresponding integrated 2D-mode

intensity (squares) and position (triangles) as a function of x, where the origin (0,0) was set at the centre of the membrane. We observe four equidistant drops in intensity, indicated by arrows, which corresponds to the narrow graphene stripes between the holes (compare to Figure S7A). The drop in intensity occurs because at the strips, the laser spot overlaps with the holes in the graphene membranes such that less material is probed compared to regions further away from the holes. For the two narrow graphene stripes closest to 0, we find that the 2D-mode position drops by 3-5 cm^{-1} compared to the central region of the graphene membrane. As hydrostatic strain lowers the energy of phonons probed by Raman spectroscopy,[2,3] our observation suggests that the narrow stripes carry a higher strain then neighbouring parts of the graphene phononic crystal, which is in qualitative agreement with the strain redistribution introduced in the main paper. A similar but less pronounced behaviour occurs for the two additional narrow stripes closer to the edge of the suspended graphene membrane at $x\sim \pm 3\mu m$, where the local decrease in 2D-mode position (increase in strain) is overlaid with a general increase of the 2D-mode position (decrease in strain) towards the edge of the suspended part of the graphene membrane at $x\sim \pm 4\mu m$. The overall lower position 2D-mode in the centre of the membrane could be due to laser heating. The pattering reduces the thermal conductance of the system and thus even at small powers (0.5 mW) heating can occur.

Next, we quantify the hydrostatic strain in our phononic crystal, which is presented in Figure 1E of the main paper. Hydrostatic strain ε_h in graphene leads to a shift $\Delta\omega_{2D}$ of the 2D-mode position ω_{2D} following the relation.[2,3]

$$\Delta\omega_{2D} = -\,\varepsilon_h\,\gamma_{2D}\,\omega_{2D}^0 \quad (1)$$

where $\gamma_{2D} = 2.6$ is the Grüneisen parameter of the 2D-mode in graphene, and ω_{2D}^0 is the intrinsic 2D-mode position without strain or doping ($\omega_{2D}^0 = 2678\ cm^{-1}$ for $532\ nm$

excitation) [4]. From the measured 2D-position ω_{2D}^{epx} , $\Delta\omega_{2D} = \omega_{2D}^{0} - \omega_{2D}^{epx}$, and equation (1) we extract the strain values from Figure S7C and show them together with the 2D-mode position in Figure 1 of the main paper.

The general trend of lower strain towards the edge of the suspended graphene phononic crystal suggests that strain relaxation is not complete across the entire structure. We attribute this behaviour to two main reasons. First, strain in suspended graphene membranes is never homogeneous, see reference membrane in Figure 1D of the main paper, and the degree of strain relaxation scales with the absolute strain values. Therefore, we do not expect homogenous strain relaxation across the entire phononic crystal. Second, strain in suspended graphene visibly varies on length scales comparable to the size of the holes in the suspended graphene membrane, see Figure 1D of the main paper, which makes strain relaxation less effective. Here we chose a PnC with rather large lattice constant a such that strain variation and relaxation can be probed by Raman spectroscopy with diffraction limited spatial resolution. For phononic crystals with holes sizes and periodicities that are much smaller than the variations of initial strain in suspended graphene structures, we expect strain relaxation to be more efficient than what is observed for the phononic crystal discussed here.

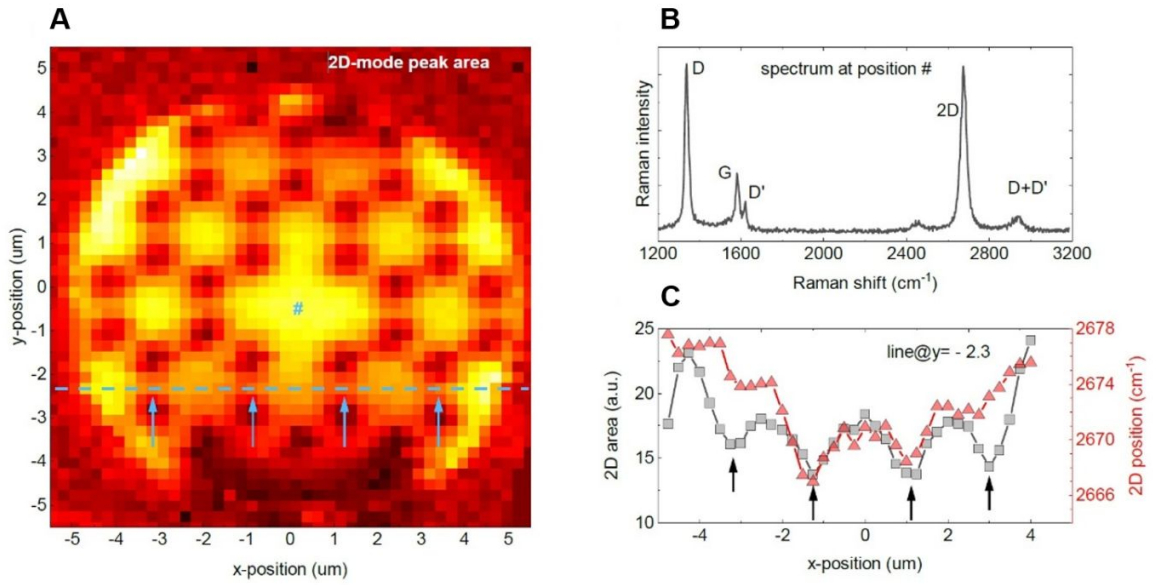

Figure S7. Raman characterization of the graphene PnC. (A) Raman map of the graphene 2D-Raman mode (integrated intensities. Intensity drops mark the locations of the holes in the hexagonal arrangement that forms the phononic crystal. (**B**) Representative Raman spectrum of the graphene membrane extracted at the location marked as (#) in (**A**). The dominant Raman modes of graphene are labelled. (**C**) Integrated 2D mode intensity (area, grey squares) and 2D-mode position (red triangles) along a line cut at y = 2.3um in x-direction as indicated by the dashed line in (**A**). Arrows in (**A**) and (**C**) mark the locations of narrow graphene bridges between the holes where strain relaxation is expected.

V. Experimental signatures of the defect mode

We propose detecting the defect mode by interferometric detection. In this approach a laser beam reflected from the device interferes with a reference beam providing an accurate measurement of membrane's position.[5–8] We need to confirm, however, that diffraction-limited laser spot is small enough to measure signatures of a realistic defect mode. To confirm that the defect mode in the center of the PnC presented in the main text is detectable, we simulate the spatial signal read out by the interferometer by implementing a Gaussian averaged laser spot for a realistic source reflected from our structure. In Figure S8 we show this for multiple laser spot sizes. For the smallest possible spot with a FWHM of 720 nm, even small spatial features of the mode shape are detectable (Figure S8A). For a realistic spot size (FWHM of 2400 nm) including the window of a vacuum chamber and a larger working distance objective we are still able to measure the mode (Figure S8B). And finally, we take a very large spot (FWHM of 7.2 μm) and thereby probe the entire mode shape (Figure S8C). We can confirm that the mode will not be fully averaged out, as it has net displacement (in contrast to e.g. mirror symmetric modes). Overall, we confirm that we should be able to detect the motion of the defect mode for all realistic laser spot sizes.

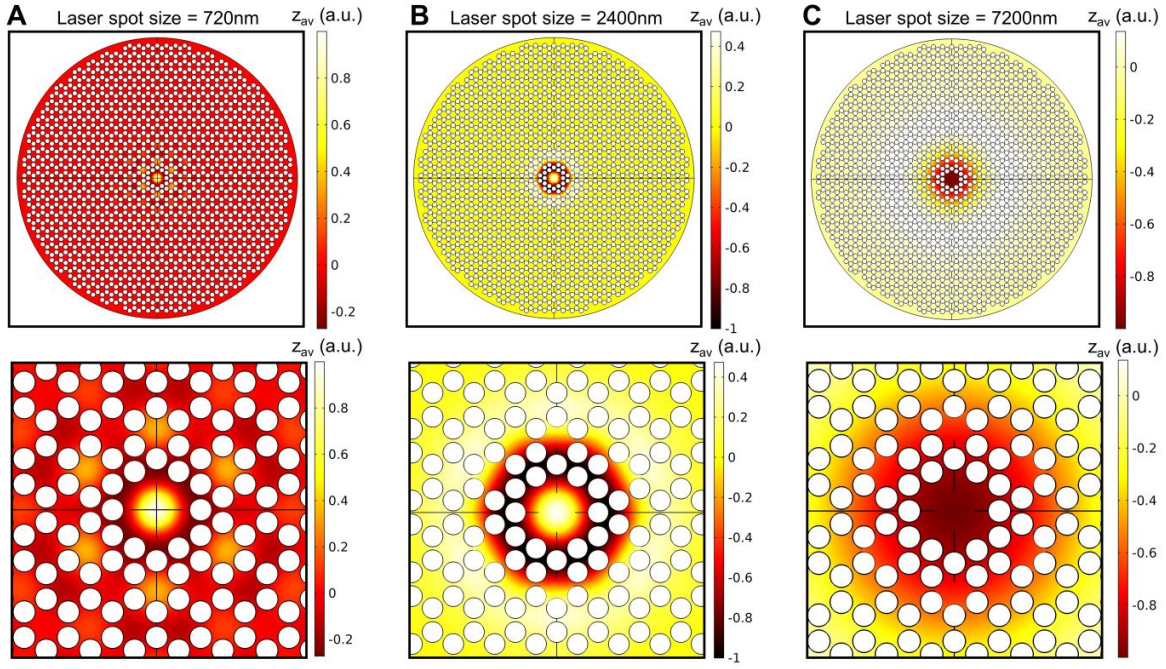

Figure S8. Interferometric detection of the defect mode. (**A-C**) Mode shape of the defect mode with local Gaussian averaging to simulate the displacement detection via a focused laser spot of different width (Zoom-ins are shown below). Different panels correspond to different spot sizes. Even for the largest laser spot size a net displacement is evident.

As mentioned in the main text spatial uniformity is necessary to fabricate a phononic crystal with a well-defined band structure. Monolayer graphene is sensitive so surface effects, wrinkling and fabrication residues. Using multilayer graphene would solve this problem yet will also be less responsive to the experimentally possible pressure maximum of roughly 30 kPa. To check if a PnC made from multilayer graphene would still show frequency tuning, we simulate the resonance frequency of a uniform circular membrane (initial tension 0.01 N/m) with and without applied load of 30 kPa. In Figure S9 we plot the relative frequency change under pressure vs. number of graphene layer. Even though the tunability drops quickly for thicker graphene, we still find more than 100% possible upshift for 35 layers.

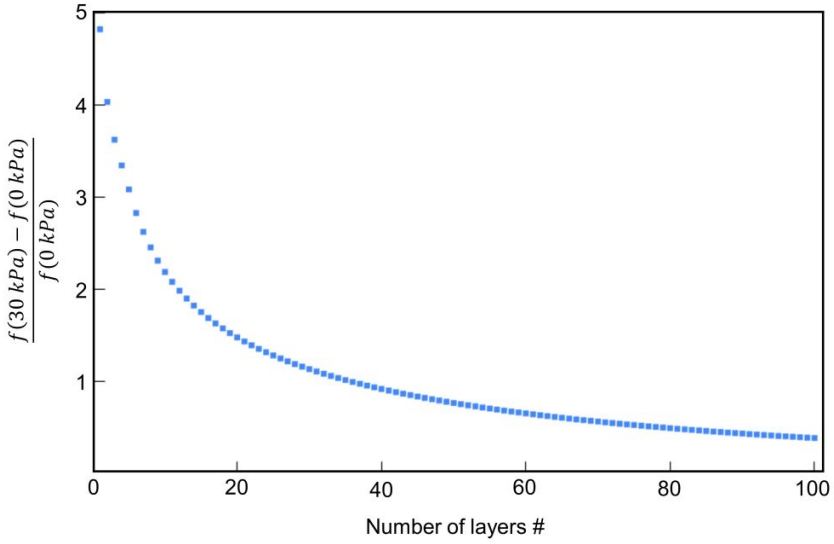

Figure S9. Frequency tunability vs. number of layers. Relative frequency shift of the fundamental mode of a circular multilayer graphene resonator upon applying 30 kPa of pressure vs. number of graphene layers.

References

(1) Utke, I.; Hoffmann, P.; Melngailis, J. Gas-Assisted Focused Electron Beam and Ion Beam Processing and Fabrication. *J. Vac. Sci. Technol. B Microelectron. Nanom. Struct.* **2008**, *26* (4), 1197.

(2) Mohiuddin, T. M. G.; Lombardo, A.; Nair, R. R.; Bonetti, A.; Savini, G.; Jalil, R.; Bonini, N.; Basko, D. M.; Galiotis, C.; Marzari, N.; Novoselov, K. S.; Geim, A. K.; Ferrari, A. C. Uniaxial Strain in Graphene by Raman Spectroscopy: G Peak Splitting, Grüneisen Parameters, and Sample Orientation. *Phys. Rev. B - Condens. Matter Mater. Phys.* **2009**, *79* (20), 1–8.

(3) Mueller, N. S.; Heeg, S.; Alvarez, M. P.; Kusch, P.; Wasserroth, S.; Clark, N.; Schedin, F.; Parthenios, J.; Papagelis, K.; Galiotis, C.; Kalbáč, M.; Vijayaraghavan, A.; Huebner, U.; Gorbachev, R.; Frank, O.; Reich, S. Evaluating Arbitrary Strain Configurations and Doping in Graphene with Raman Spectroscopy. *2D Mater.* **2018**, *5* (1).

(4) Froehlicher, G.; Berciaud, S. Raman Spectroscopy of Electrochemically Gated Graphene Transistors: Geometrical Capacitance, Electron-Phonon, Electron-Electron, and Electron-Defect Scattering. *Phys. Rev. B - Condens. Matter Mater. Phys.* **2015**, *91* (20), 205413.

(5) Singh, R.; Nicholl, R. J. T.; Bolotin, K. I.; Ghosh, S. Motion Transduction with Thermo-Mechanically Squeezed Graphene Resonator Modes. *Nano Lett.* **2018**, *18* (11), 6719–6724.

(6) Singh, R.; Sarkar, A.; Guria, C.; Nicholl, R. J. T.; Chakraborty, S.; Bolotin, K. I.; Ghosh, S. Giant Tunable Mechanical Nonlinearity in Graphene-Silicon Nitride Hybrid Resonator. *Nano Lett.* **2020**, *20* (6), 4659–4666.

(7) Zande, A. M. Van Der; Barton, R. A.; Alden, J. S.; Ruiz-vargas, C. S.; Whitney, W. S. Large Scale Arrays of Single Layer Graphene Resonators. - Supplementary Information. *Nano Lett.* **2010**, *10* (12), 4869–4873.

(8) Bunch, J. S.; Van Der Zande, A. M.; Verbridge, S. S.; Frank, I. W.; Tanenbaum, D. M.; Parpia, J. M.; Craighead, H. G.; McEuen, P. L. Electromechanical Resonators from Graphene Sheets. *Science (80-.).* **2007**, *315* (5811), 490–493.

B.2. npj 2D Materials and Applications 7, 10 (2023) and Supporting Information

npj | 2D materials and applications

www.nature.com/npj2dmaterials

ARTICLE OPEN

Check for updates

Mechanically-tunable bandgap closing in 2D graphene phononic crystals

Jan N. Kirchhof[1]✉ and Kirill I. Bolotin[1]✉

We present a tunable phononic crystal which can be switched from a mechanically insulating to a mechanically conductive (transmissive) state. Specifically, in our simulations for a phononic lattice under biaxial tension ($\sigma_{xx} = \sigma_{yy} = 0.01\ \mathrm{N\,m^{-1}}$), we find a bandgap for out-of-plane phonons in the range of 48.8–56.4 MHz, which we can close by increasing the degree of tension uniaxiality (σ_{xx}/σ_{yy}) to 1.7. To manipulate the tension distribution, we design a realistic device of finite size, where σ_{xx}/σ_{yy} is tuned by applying a gate voltage to a phononic crystal made from suspended graphene. We show that the bandgap closing can be probed via acoustic transmission measurements and that the phononic bandgap persists even after the inclusion of surface contaminants and random tension variations present in realistic devices. The proposed system acts as a transistor for MHz-phonons with an on/off ratio of 10^5 (100 dB suppression) and is thus a valuable extension for phonon logic applications. In addition, the transition from conductive to isolating can be seen as a mechanical analogue to a metal-insulator transition and allows tunable coupling between mechanical entities (e.g. mechanical qubits).

npj 2D Materials and Applications (2023)7:10 ; https://doi.org/10.1038/s41699-023-00374-4

INTRODUCTION

Phononic crystals (PnCs) are artificial structures in which the periodic variation of material properties (e.g. stiffness, mass, or tension) give rise to a phononic band structure—in analogy to Bloch waves in crystalline solids on the atomic scale. In contrast to conventional solids, the parameters of the band structure can be broadly controlled via artificial patterning. Because of that, PnCs allow realising analogues of fundamental solid state physics phenomena over a very large range of sizes (10 nm–100 m) and frequencies (Hz–THz)[1,2]. This ranges from quantum entanglement[3,4] to topological states[5,6] and negative refraction[7]. The ability to engineer phononic spectra gave rise to applications such as phononic shielding in ultracoherent mechanical resonators[8–11], wave guiding[12,13] or thermal management[14]. Due to the much lower propagation speed of phonons compared to photons or electrons, PnCs are also promising candidates for quantum information technology based on guiding and storing mechanical motion, especially on length scales too small for photonic approaches[6,15–18]. Most of these applications and phenomena rely on phononic bandgaps, the range of frequencies where no phonons are allowed and mechanical motion is heavily damped.

The velocities of all phonons in a material depend on its tension σ. In conventional rigid PnCs, e.g. those fabricated using silicon nitride membranes (SiN_x), the built-in tension is determined during the growth step and cannot be tuned. As a result, it becomes challenging to couple a PnC to an external system, for example for processing and storing of quantum information[19–21]. In contrast, it has been recently demonstrated that the tension in much more flexible two-dimensional (2D) materials can be dynamically controlled by applying electrostatic pressure via an external gate electrode[22–25]. The resulting tunable (biaxial) tension allows broad tunability of the bandgap centre frequency[23]. Nevertheless, the hierarchy of the bands in the systems explored so far has not been affected by tension—i.e. a gapped system remained gapped at any tension level. The precise control of the bandgap size and thus the coupling strength between mechanical entities remains elusive.

Here, we show that the application of uniaxial tension to a PnC (in contrast to biaxial tension studied previously) changes the band hierarchy. Specifically, for a 2D phononic lattice patterned into a suspended graphene membrane under biaxial tension ($\sigma_{xx}/\sigma_{yy} = 1$), we observe a bandgap for out-of-plane phonons at any tension (e.g. 48.8–56.4 MHz at $\sigma = 0.01\ \mathrm{N\,m^{-1}}$), which disappears completely when the degree of tension uniaxiality (σ_{xx}/σ_{yy}) reaches 1.7. This can be seen as the observation of a mechanical analogue to a metal-insulator transition. Of course, the analogy is not complete. The chemical potential for the phononic system is zero rather than falling into the gap, as is the case for electrical insulators, which are described by the Fermi-Dirac statistics. Also, the analogy is only applicable to out-of-plane modes. These modes are especially relevant in phononic crystals made from 2D materials as they are easy to excite and detect. Nevertheless, the transition from a gapped to non-gapped phononic crystal shows many similarities to an actual metal-insulator transition in terms of transfer of energy and localisation of modes (see Supplementary Note 8). To control σ_{xx}/σ_{yy}, we propose a simple experimental geometry based on electrostatic gating and show that bandgap closing can be reached in experimentally feasible devices, which we probe via acoustic transmission studies. Our simulations show that applying a small gate voltage of ~8 V to the suspended graphene PnC is sufficient to close the phononic bandgap. For frequencies within the bandgap region, the system functions as a mechanical transistor with an on/off ratio of 10^5 (suppression of 100 dB) and can be used in phonon logic circuits. Furthermore, the ability to dynamically control the bandgap size allows to realise tunable coupling strength between mechanical entities e.g. two mechanical resonators acting as qubits. Finally, we investigate the challenges associated with the fabrication of 2D materials. We find that the mass of contaminants on top of the device must be smaller than ~4 times the weight of the suspended graphene and

[1]Department of Physics, Freie Universität Berlin, Arnimallee 14, 14195 Berlin, Germany. ✉email: jan.kirchhof@fu-berlin.de; kirill.bolotin@fu-berlin.de

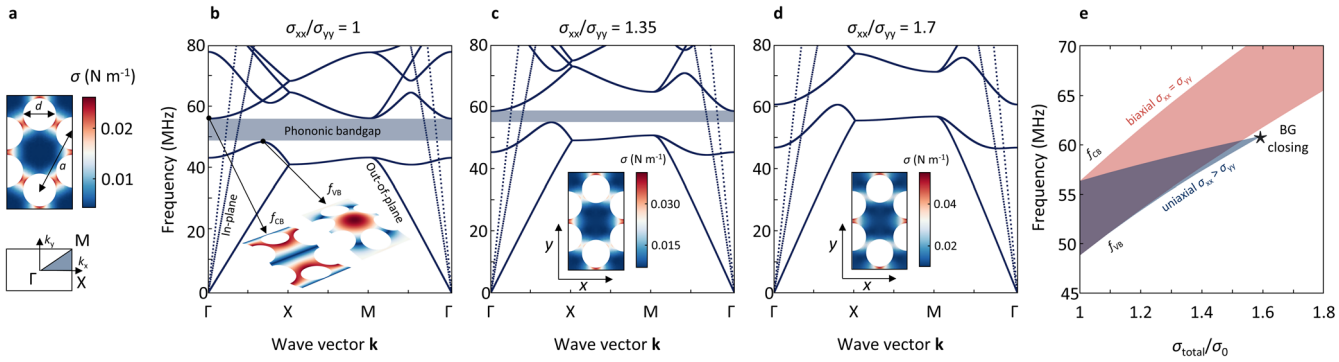

Fig. 1 Phononic bandgap closing induced by uniaxial tension. a Unit cell of the honeycomb lattice with redistributed tension (top) and the corresponding first Brillouin zone (bottom). **b** Phononic band structure for the unit cell shown in **a** under uniform tension ($\sigma_{xx} = \sigma_{yy} = 0.01$ N m^{-1}). For out-of-plane modes (solid lines) a clear phononic bandgap is visible (blue shaded region). The insets show the mode shape (displacement) within the unit cell at the points above and below the bandgap. **c**, **d** Phononic band structure and tension distribution in the unit cell (insets) for σ_{xx}/σ_{yy} of 1.35 and 1.7. With increasing uniaxiality in tension ($\sigma_{xx}/\sigma_{yy} > 1$), the phononic bands show different frequency scaling behaviour along different high symmetry lines. At $\sigma_{xx}/\sigma_{yy} = 1.7$, the phononic bandgap closes. **e** Phononic bandgap for biaxial (red) and uniaxial (blue) tension vs. total normalised tension. When the tension is increased biaxially ($\sigma_{xx} = \sigma_{yy}$), the bandgap centre frequency rises, and the bandgap width increases. On the contrary, uniaxial upscaling ($\sigma_{xx} > \sigma_{yy}$) leads to a bandgap closing.

that the relative tension variation in the graphene must be smaller than 40% to observe a clear bandgap and its closing.

RESULTS

PnC design

For the design of our tunable 2D phononic system we choose a honeycomb lattice (lattice constant a) of holes (diameter d), which provides a relatively broad and robust phononic bandgap for out-of-plane modes, while leaving a large fraction of the material untouched. The latter is crucial for making a PnC from fragile 2D materials. The honeycomb lattice also features an indirect phononic bandgap, which allows selective tuning of phononic bands via uniaxial tension, as we will see later. We select graphene as a suitable material for our PnC as it is the most conductive[26,27] and the strongest member of the family of 2D materials[28]. Our results are also applicable to other conductive 2D materials. The phononic pattern shows the same symmetry as the atomic lattice structure of graphene, with the difference that in our approach the unit cell is much larger and contains ~4·10^7 carbon atoms. We consider a free-standing PnC to allow mechanical tuning via out-of-plane pressure. Fabrication of such devices has recently been demonstrated by He-Ion beam milling[23,29,30]. To obtain the phononic band structure, we start by performing finite element method (FEM) simulations of the tension distribution within the conventional unit cell of the honeycomb lattice (Fig. 1a, top). We find tension hotspots in the thin ribbons and relaxed regions in the centre of the unit cell. This redistribution of tension occurs when holes are cut into the initially uniform membrane. In a next step, we use the first Brillouin zone (Fig. 1a, bottom) to calculate the phononic band structure along the high symmetry lines for an infinite lattice, as shown in Fig. 1b for $a = 1$ µm, $d/a = 0.5$ and a reasonable initial biaxial tension of $\sigma_{xx} = \sigma_{yy} = 0.01$ N m^{-1} [23,31,32]. For out-of-plane modes (solid lines) we find a bandgap between 48.8 and 56.4 MHz (blue shaded), in agreement with previous work[23,30]. These modes are qualitatively comparable to atomic scale flexural (ZA) phonon modes in graphene, but at much lower frequencies and for much smaller wave vectors. The entire phononic lattice behaves like a thin membrane with vibrational mode frequencies f determined by the built-in tension ($f \sim \sqrt{\sigma}$), that also results in a linear dispersion for the flexural modes, instead of the quadratic behaviour expected for an unstrained 2D material[33,34]. Also, in agreement with previous work, we find that an uniform increase in tension ($\sigma_{xx}/\sigma_{yy} = 1$) leads to monotonic upscaling of both the top of valence (f_{VB}) and bottom of conduction band (f_{CB}) frequencies as shown in Fig. 1e (red). Here, the centre frequency of the bandgap follows a square root behaviour vs. tension, and the relative bandgap size ($\frac{f_{CB}-f_{VB}}{(f_{CB}+f_{VB})/2}$) remains constant.

Bandgap closing for highly uniaxial tension

Our next goal is to show that we can use uniaxial tension (unlike biaxial tension) to control the relative bandgap size and even completely close it. The phononic bandgap of our honeycomb lattice is indirect with the conduction band minimum f_{CB}, located at the Γ point in momentum space and the valence band maximum f_{VB}, at a point along the ΓX line (Fig. 1b). Critically, uniaxial tension, in contrast to biaxial tension, produces different frequency scaling of the band structure at different points of the Brillouin zone. With increasingly uniaxial tension, f_{VB} strongly upshifts in frequency while f_{CB} is barely tension-dependent. As a result, the indirect bandgap of the phononic lattice acquires a strong tension-dependence. To quantify these changes, we determine the average tension components (after redistribution upon phononic pattering) $\sigma_{ij} = <\sigma_{ij}>$ and use the ratio σ_{xx}/σ_{yy} as a metric for tension uniaxiality. For the honeycomb lattice with its initial tension distribution (as introduced above), $\sigma_{xx}/\sigma_{yy} = 1$. For an increased $\sigma_{xx}/\sigma_{yy} = 1.35$, we find increased tension in the areas stretched in the x direction (Fig. 1c, inset). This is accompanied by a much more pronounced upshift of f_{VB} compared to f_{CB} and thus a reduced bandgap size (Fig. 1c). To give an intuitive understanding of this scaling behaviour, we look at the spatial shape of modes corresponding to f_{VB} and f_{CB}. The mode f_{CB} at the Γ point (Fig. 1b, left inset) resembles a standing wave along the y direction, and it therefore does not depend strongly on tension in the x direction. The mode corresponding to f_{VB}, between Γ and X (Fig. 1b, right inset), resembles a linear combination of standing waves in the x and y directions. The frequency of this mode however does depend on σ_{xx}. For a higher uniaxiality of 1.7 as shown in Fig. 1d, the tension distribution becomes even more distorted (Fig. 1d inset) and the lower branches (f_{VB}) overtake the upper ones (f_{CB}). At this point, the bandgap closes ($\frac{f_{CB}-f_{VB}}{(f_{CB}+f_{VB})/2} = 0$). In Supplementary Note 1, we provide extended band structure calculations showing the full extent of the Brillouin zone under uniaxial tension.

To summarise the results of bandgap tuning, in Fig. 1e we compare f_{VB} and f_{CB} vs. the total tension σ_{total} for uniaxial (blue) and uniform biaxial (red) tension. For uniaxial tension, we see a closing of the bandgap at $\sigma_{total}/\sigma_0 = 1.6$ (corresponds to $\sigma_{xx}/\sigma_{yy} = 1.7$). In contrast, for biaxial tension scaling, the bandgap

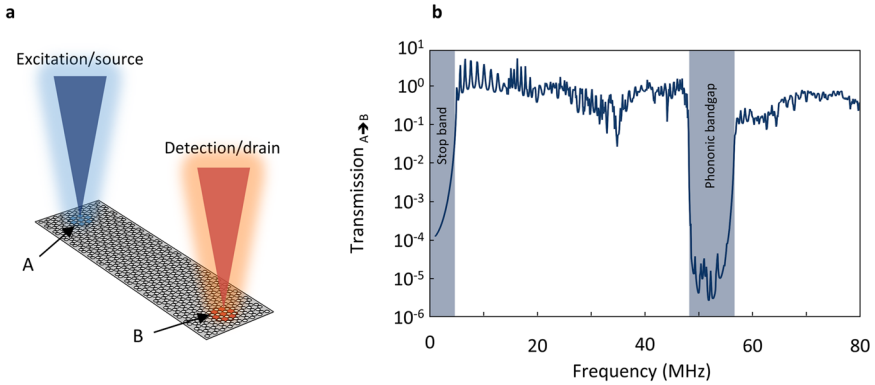

Fig. 2 Probing the band structure via transmission studies in a finite-size phononic crystal. a Transmission geometry for a rectangular phononic device. At point A mechanical motion is excited by a frequency modulated laser (blue). The vibrational wave travels through the device and is detected at point B by a second laser spot (red). **b** Transmission from A to B vs. excitation frequency for the device shown in **a**. A clear bandgap region is visible (blue shaded) where transmission of mechanical motion through the device is suppressed by ~10^5.

increases in absolute size with increased tension, while the relative bandgap size remains constant. Overall, by varying the tension uniaxiality, we find different scaling behaviour for different phononic bands along different directions, which allows us to dynamically tune the size of the bandgap.

Our next goal is to develop a design for an experimentally feasible device realising the phononic bandgap closing. To accomplish this, three challenges need to be overcome. First, how can we probe the phononic bandgap in a realistic finite-size device? This is critical as the band structure calculations considered so far always assume an infinite phononic lattice. Second, how can we generate the highly uniaxial tension distribution needed to close the bandgap? Third, is it feasible to fabricate a sufficiently uniform PnC from experimentally available 2D materials? We now individually address each of these questions in the next sections.

Bandgap probing in a finite-size device

We probe our finite-size phononic system via acoustic transmissions measurements. In general, the transmission across a phononic system is determined by the density of available states at the relevant frequency which serves as a proxy for the phononic band structure. We design a transistor-style PnC with realistic dimensions of 9 µm × 28 µm (7 × 17 unit cells, unlike the infinite system considered in simplified simulations so far), in which instead of electrons we will determine the transmission of mechanical motion (Fig. 2a). At point A (excitation/source) mechanical motion is excited, which then can propagate through the PnC until it reaches point B (detection/drain). Drive and detection in such a device design can be experimentally realised by using either surface acoustic waves (SAW)[15], local gate electrodes[35] or two spatially separated laser beams[12] (blue, red Fig. 2a). Here, we concentrate without loss of generality on the last case. We define the transmission from area A to B as:

$$\text{Transmission}_{A\Rightarrow B}(f) = \frac{1}{T}\int_0^T \frac{\int_A z(x,y,f,t)dA}{\int_B z(x,y,f,t)dA}dt \quad (1)$$

where $z(x, y, f, t)$ is the out of plane displacement of the suspended graphene with a period T $(f = \frac{1}{T})$. The integration is over the illumination areas in points A and B. We concentrate on out-of-plane modes as they are controlled by the in-plane phononic pattern, show strong capacitive coupling to perpendicular electric fields from a gate electrode and are sensitive to interferometric readout. In Fig. 2b, we plot the transmission vs. frequency for the device shown in Fig. 2a. In the region below the fundamental resonance, the stop band (<5 MHz), we find strongly supressed transmission. Towards higher frequencies, we find multiple closely spaced sharp peaks, which correspond to higher order resonances of the device. As the frequency increases further, the transmission is more and more dominated by the phononic band structure, and we observe broad "bands" rather than individual resonance modes. The transmission suddenly drops by an average of 5 orders magnitude in the expected bandgap region between 48.5 and 56.5 MHz (blue shaded). The non-zero transmission inside the bandgap is related to finite-size effects captured by our model. Above the bandgap the transmission recovers and remains close to 1. The frequency range of the bandgap extracted from transmission simulations matches well with the bandgap from band structure calculations (comp. Fig. 1b). To summarise, we can use acoustic transmission studies to probe the phononic bandgap in finite-size devices. Furthermore, transmission of mechanical motion across the device in the bandgap region is strongly suppressed and, in analogy to an electronic system, the system can be considered a mechanically insulating.

Uniaxial tension engineering

After finding the phononic bandgap closing in band structure calculations at a tension uniaxiality of $\sigma_{xx}/\sigma_{yy} = 1.7$ and establishing transmission studies as a suitable approach to probe the bandgap, we now aim to produce the required tension distribution—and hence the bandgap closing—in a realistic device of finite size. Our key idea is to apply electrostatic pressure to a suspended rectangular device (Fig. 3a) with non-unity aspect ratio (W/L). In this case the induced tension is larger along the direction of the smaller spatial dimension (x in Fig. 3a)[36]. We model the membrane as clamped at its perimeter. Electrostatic pressure p_{el} is generated by applying a gate voltage (V_{gate}) between the highly conductive graphene and a gate electrode separated from it by distance d:

$$p_{el} = \frac{\epsilon_0}{2}\left(\frac{V_{gate}}{d}\right)^2 \quad (2)$$

where ϵ_0 is the vacuum permittivity. We assume $d = 300$ nm, a typical oxide thickness for Si/SiO_2 substrates used for 2D materials. At zero gate voltage, corresponding to zero pressure, the membrane is uniformly tensed ($\sigma_{xx} \approx \sigma_{yy}$). The tension distribution inside the centre of the phononic device is plotted in Fig. 3b. With applied pressure the degree of tension uniaxiality σ_{xx}/σ_{yy} increases and the distribution of tension becomes rotationally asymmetric (Fig. 3c). For $p_{el} = 3$ kPa (8 V), σ_{xx}/σ_{yy} reaches 1.7 and we thus expect the bandgap closing to occur. The generated tension distribution also matches the prediction for the bandgap closing from our band structure calculations—compare dashed outline in Fig. 3c with the inset of Fig. 1d. In Fig. 3d we summarise the results

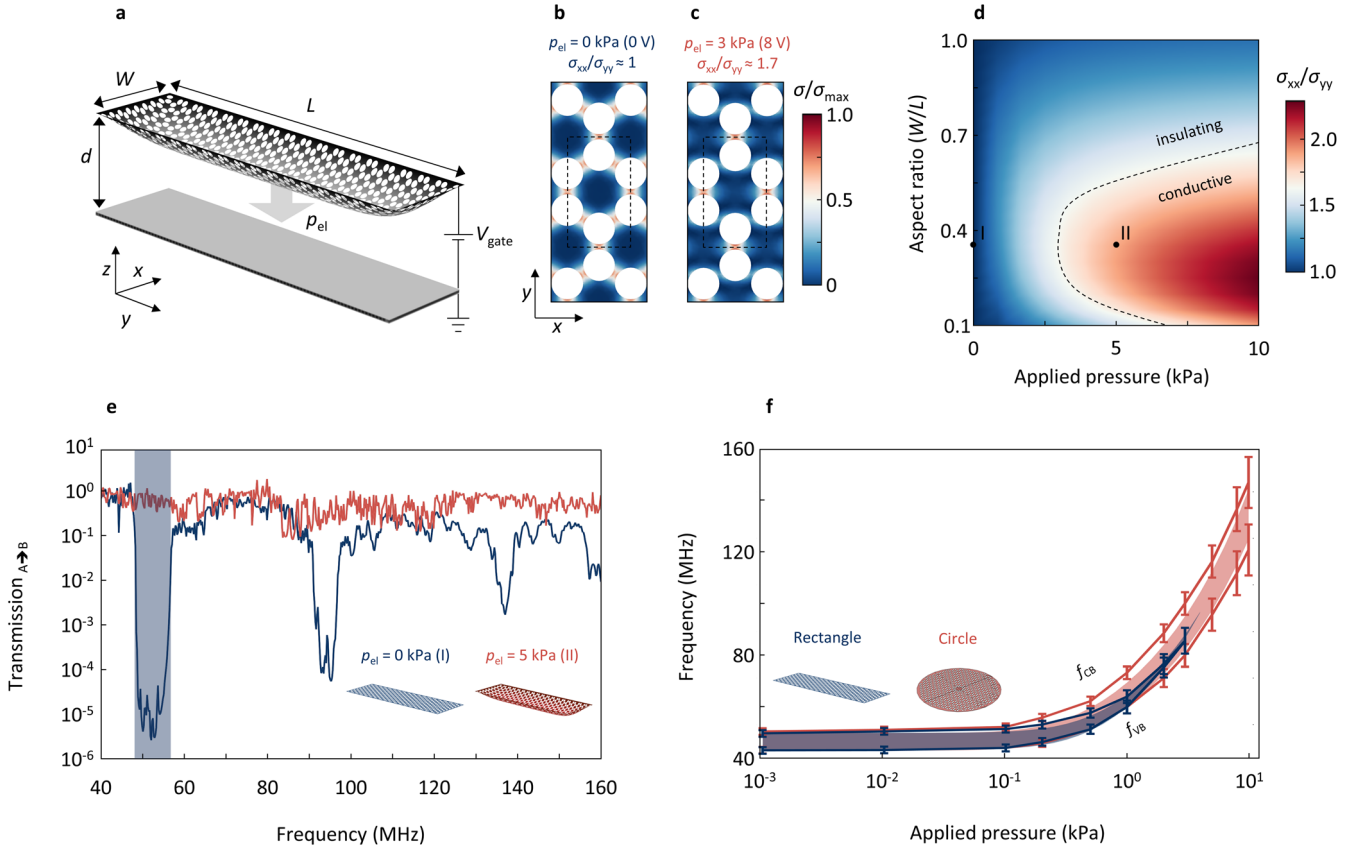

Fig. 3 Uniaxial tension engineering in a finite-size phononic system. a Sketch of a finite-size system phononic device, which is mechanically deformed under electrostatic pressure, p_{el}, generated by a gate electrode below the graphene. **b**, **c** Spatial tension distribution in the centre of the device with and without applied pressure. The dashed lines indicate the unit cell of the lattice. **d** Mechanical phase diagram: Tension uniaxiality (σ_{xx}/σ_{yy}) vs. pressure vs. device aspect ratio (W/L). The dotted line corresponds to $\sigma_{xx}/\sigma_{yy} = 1.7$, the degree in uniaxiality needed to close the bandgap. **e** Transmission for a device with an aspect ratio of 0.32 for $p_{el} = 0$ kPa (blue) and 5 kPa (red). The initially pronounced bandgap vanishes with applied pressure. **f** Extracted valence band maximum (f_{VB}) and conduction band minimum (f_{CB}) vs. applied pressure for a rectangular device (blue, shown in **a**) and a circular device (red) as reference for uniform scaling ($\sigma_{xx}/\sigma_{yy} \approx 1$). For the rectangular device the bandgap closing occurs at 3 kPa, whereas the circular device maintains a bandgap over the entire range of applied pressures. The error bars depict the reading error of the simulation results, and the shaded areas correspond to the phononic bandgap extracted from band structure calculations.

of tension engineering for our finite-size system in a phase diagram, where we plot σ_{xx}/σ_{yy} vs. applied pressure vs. aspect ratio. When σ_{xx}/σ_{yy} reaches the critical value of 1.7 (dashed line), we expect bandgap closing according to our band structure calculations for the infinite lattice. This line can therefore be viewed as a boundary separating a mechanically insulating from a mechanically conductive (transmissive) state. We see that the conductive state is reached at lowest applied pressure for an aspect ratio of $W/L = 0.32$.

Next, we calculate the transmission spectra for applied pressures of 0 and 5 kPa (Fig. 3e). While we find a clear bandgap (and higher order harmonics) for the un-pressured state (blue), the bandgap completely vanishes with applied pressure (red, 5 kPa), confirming the expected bandgap closing for a finite-size phononic crystal. The system is now transmissive and mechanically conductive. Continuing the analogy between phononic and electronic devices, our system can be viewed as a mechanical transistor for MHz phonons with an on/off ratio of ~10^5 (100 dB suppression). This corresponds to 6 dB suppression per unit cell.

In Fig. 3f, we show combined results from multiple pressures by plotting f_{VB} and f_{CB} for the rectangular device ($W/L = 0.32$, blue) and a circular reference device (red). In accordance with previous simplified calculations (Fig. 1e), we see that the bandgap $\frac{f_{CB}-f_{VB}}{(f_{CB}+f_{VB})/2}$ gradually decreases in size with applied pressure for the rectangular device. The applied pressure increases σ_{xx}/σ_{yy} and drives the system towards the bandgap closing. In contrast, the circular reference device for which we expect entirely biaxial tension tuning ($\sigma_{xx} \approx \sigma_{yy}$) exhibits a clear bandgap up to 30 kPa (see Supplementary Note 3). To better relate our results to the phononic band structure calculations, we take the average tension values (σ_{xx}, σ_{yy} and σ_{total}) from the finite-size system under pressure as input for our infinite model and plot the expected bandgap regions in Fig. 3f (red and blue shaded). While we find comparable behaviour, the bandgap closing however occurs at somewhat higher pressures. This is likely due to boundary-related disorder that is excluded in the infinite model. We extract the average strain from our simulations and obtain $\varepsilon = 0.24\%$ for an applied pressure of 10 kPa. This is well below the onset of phonon instabilities[37] or graphene's breaking strain[28]. To summarise, we find bandgap closing for a highly uniaxial tension distribution generated by applying electrostatic pressure in a realistic finite-size device with optimised geometry. This allows us to change the state of a PnC from mechanically insulating to conductive by simply applying a gate voltage.

Fabrication related challenges

Having demonstrated large frequency tunability as well as phononic bandgap closing in graphene PnCs, we now want to assess the fabrication challenges associated with 2D materials. We therefore investigate the effect on the phononic bandgap for the

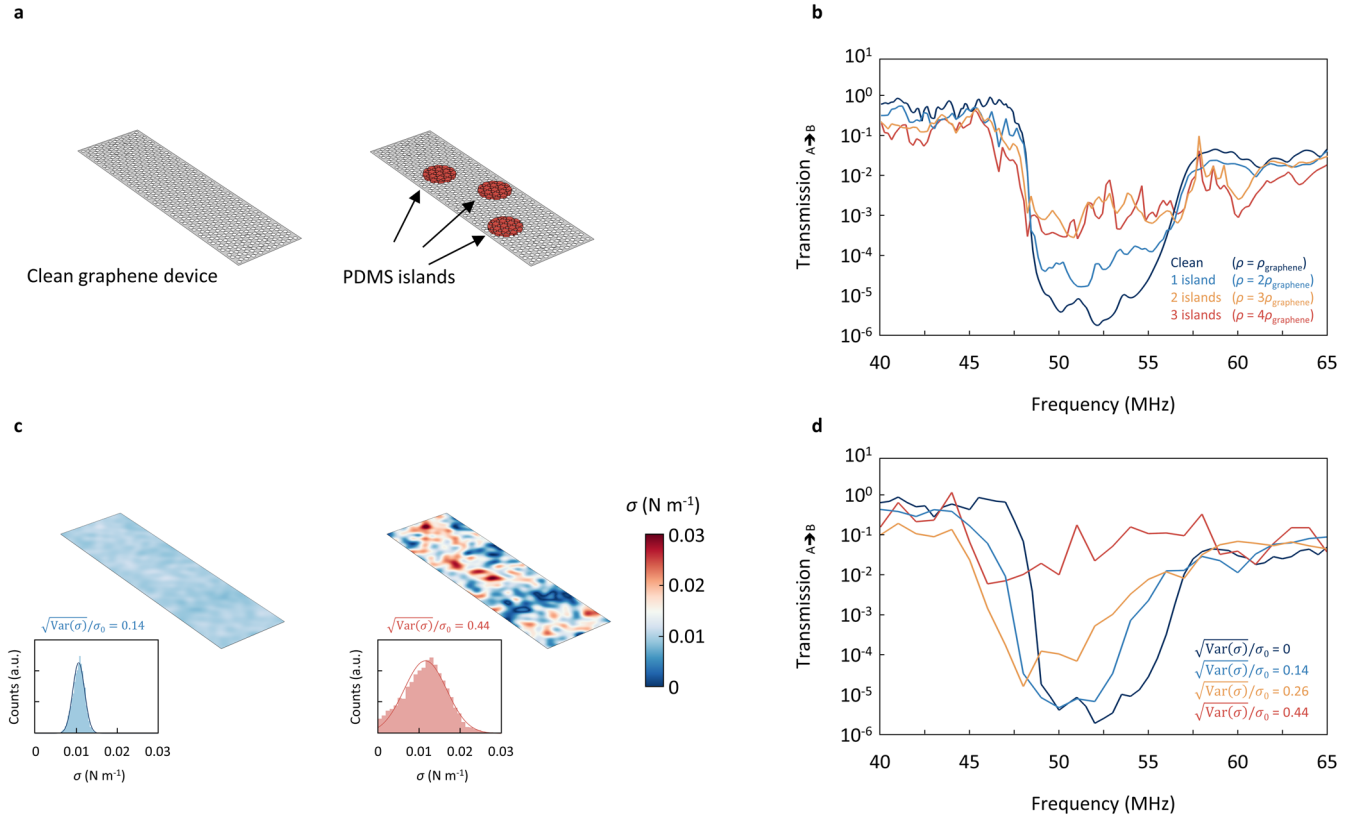

Fig. 4 The effect of disorder on the phononic bandgap. a A phononic device with and without surface contamination. **b** Phononic bandgap vs. added mass. With increasing degree of contamination, the bandgap smears out, yet remains visible up to areal mass density of $\rho_{2D} \approx 4\rho_{graphene}$. **c** Graphene membrane before patterning with small and large tension disorder. The insets show the histograms used to extract the disorder strength: left, $\sqrt{\mathrm{Var}(\sigma)}/\sigma_0 = 0.14$ and right, $\sqrt{\mathrm{Var}(\sigma)}/\sigma_0 = 0.44$. **d** Phononic bandgap vs. tension disorder. At a critical relative variation in tension $\sqrt{\mathrm{Var}(\sigma)}/\sigma_0 \approx 0.40$ the bandgap vanishes.

two most common forms of disorder in 2D materials: surface contamination and random tension variations.

Perhaps the most widespread sources of contamination are "islands" of residues on top of the graphene. To simulate these added pieces of mass, we choose Polydimethylsiloxane (PDMS) as a typical polymer often used for transfer of 2D materials, and randomly place the pieces on the graphene membrane (Fig. 4a). At a thickness of 18 nm and a diameter of 4 µm, each piece has the same weight as the entire clean resonator. Next, we focus on the bandgap region and plot transmission vs. frequency for various amounts of added mass (Fig. 4b). Even for three added pieces (red), we still observe weak signatures of the phononic bandgap and conclude that the combined mass density of graphene and contamination must be on the order of $\rho_{2D} \leq 4\rho_{graphene}$. Values below this threshold have been observed in some graphene resonators in literature[32,38]. We also test the effect of a uniform film of PDMS on the phononic device and still find a clear bandgap (see Supplementary Note 4).

The second potential threat for breaking the phononic order are random tension variations in the suspended membrane commonly observed in both patterned and unpatterned graphene membranes[31]. To model this effect, we generate disorder based on a superposition of randomised plane waves (details in Supplementary Note 5). We take into account variations down to ¼ of the lattice constant of the phononic pattern. Two generated spatial tension distributions for small and large disorder are shown in Fig. 4c. The disorder strength is parametrised by the standard deviation of the distribution, $\sqrt{\mathrm{Var}(\sigma)}/\sigma_0$ (see insets). We now calculate the transmission through the phononic device as a function of disorder strength. As shown in Fig. 4d, we find a gradual smearing out of the bandgap with increasing disorder. Above an estimated critical value of $\sqrt{\mathrm{Var}(\sigma)}/\sigma_0 \approx 0.40$, the bandgap is no longer clearly distinguishable. If we compare this threshold to experimental values derived from Raman spectroscopy[39–41], we find similar spreads in tension. We also investigate the effect of variations in hole size on the phononic bandgap and find it to be robust for the level of disorder seen in realistic devices (see Supplementary Note 6). We conclude that it is challenging but possible to fabricate sufficiently uniform suspended devices. If, however more uniform samples are needed, we propose using thin multilayers of graphene, for which we find a bandgap up to a thickness of ~200 layers (see Supplementary Note 7). For multilayer devices, we need larger pressures to induce the bandgap closing, but commonly used SiO_2/Si (300 nm) substrates allow applying ~100 V gate voltage before dielectric breakdown occurs, which translates to ~50 kPa (sufficient to induce the bandgap closing on multilayer devices). Overall, fabricating a PnC from suspended graphene with a pronounced bandgap is feasible.

DISCUSSION

We have demonstrated the manipulation of the phononic band structure by using uniaxial tension engineering and found closing of a phononic bandgap at $\sigma_{xx}/\sigma_{yy} = 1.7$. This transition from a mechanically insulating to a conductive state may be regarded as the mechanical analogue of a metal-insulator-transition. In a finite-size device, we can generate the required uniaxial tension distribution by applying a voltage of ~8 V to a gate electrode and observe vanishing of the phononic bandgap in transmission studies. This device can be considered a phononic counterpart to

a field effect transistor, with acoustic transmission measurements at the bandgap frequency taking the role of electrical transport. Furthermore, we discuss the feasibility of fabricating such a device with commonly used methods and extract a critical value for surface contamination ($\rho_{2D} \leq 4\rho_{graphene}$) and tension variations ($\sqrt{Var(\sigma)}/\sigma_0 \approx 0.40$).

The proposed system acts as a phononic transistor that can be used for phonon logic in the MHz range and invites realisation of a variety of logic gates as a next step. By varying the lattice constant a, the phononic system can be engineered to function in a broad range of frequencies from ~10 MHz to ~1 GHz. In addition, the proposed device design can serve as a switch controlling the coupling between two remote systems, e.g. mechanical resonators acting as qubits[19–21]. This in principle also allows tunable dispersive readout of qubits via mechanical resonators. The proposed bandgap closing also makes it possible to control the phononic shielding of ultracoherent defect modes from the environment and therefore allows to dynamically study dissipation mechanisms as shown in Supplementary Note 8. Finally, following the analogy between phononic and electronic crystals invites the consideration of analogues to other, more complex condensed matter physics phenomena, e.g. the quantum hall effect, Mott insulator transition, and topological phase transitions.

METHODS

FEM simulations

For the finite element modelling, we use COMSOL Multiphysics (Version 5.5) and assume the following material parameters for monolayer graphene: Young's modulus $E_{2D} = 1.0\,\mathrm{TPa}$[28], Poisson's ratio of $\nu = 0.15$, thickness of $h = 0.335\,\mathrm{nm}$ and a density of $\rho = \frac{\rho_{2D}}{h} = 2260\mathrm{kg\,m^{-3}}$. For details, see Supplementary Notes 1–8.

DATA AVAILABILITY

The data that support the findings of this study are available from the corresponding author upon reasonable request.

CODE AVAILABILITY

Upon request, authors will make available any previously unreported computer code or algorithm used to generate results that are reported in the paper and central to its main claims.

Received: 23 June 2022; Accepted: 10 February 2023;
Published online: 23 February 2023

REFERENCES

1. Kushwaha, M. S., Halevi, P., Dobrzynski, L. & Djafari-Rouhani, B. Acoustic band structure of periodic elastic composites. *Phys. Rev. Lett.* **71**, 2022–2025 (1993).
2. Maldovan, M. Sound and heat revolutions in phononics. *Nature* **503**, 209–217 (2013).
3. Thomas, R. A. et al. Entanglement between distant macroscopic mechanical and spin systems. *Nat. Phys.* 1–6 https://doi.org/10.1038/s41567-020-1031-5 (2020).
4. Riedinger, R. et al. Remote quantum entanglement between two micromechanical oscillators. *Nature* **556**, 473–477 (2018).
5. Mousavi, S. H., Khanikaev, A. B. & Wang, Z. Topologically protected elastic waves in phononic metamaterials. *Nat. Commun.* **6**, 1–7 (2015).
6. Pirie, H., Sadhuka, S., Wang, J., Andrei, R. & Hoffman, J. E. Topological phononic logic. *Phys. Rev. Lett.* **128**, 015501 (2022).
7. He, H. et al. Topological negative refraction of surface acoustic waves in a Weyl phononic crystal. *Nature* **560**, 61–64 (2018).
8. Tsaturyan, Y., Barg, A., Polzik, E. S. & Schliesser, A. Ultracoherent nanomechanical resonators via soft clamping and dissipation dilution. *Nat. Nanotechnol.* **12**, 776–783 (2017).
9. Ghadimi, A. H. et al. Elastic strain engineering for ultralow mechanical dissipation. *Science* **360**, 764–768 (2018).
10. Yu, P. L. et al. A phononic bandgap shield for high-Q membrane microresonators. *Appl. Phys. Lett.* **104**, 23510 (2014).
11. Li, F., Liu, J. & Wu, Y. The investigation of point defect modes of phononic crystal for high Q resonance. *J. Appl. Phys.* **109**, 124907 (2011).
12. Wang, Y., Lee, J., Zheng, X. Q., Xie, Y. & Feng, P. X. L. Hexagonal boron nitride phononic crystal waveguides. *ACS Photonics* **6**, 3225–3232 (2019).
13. Otsuka, P. H. et al. Broadband evolution of phononic-crystal-waveguide eigenstates in real- and k-spaces. *Sci. Rep.* **3**, 1–5 (2013).
14. Yang, L., Chen, J., Yang, N. & Li, B. Significant reduction of graphene thermal conductivity by phononic crystal structure. *Int. J. Heat. Mass Transf.* **91**, 428–432 (2015).
15. Gustafsson, M. V. et al. Propagating phonons coupled to an artificial atom. *Science* **346**, 207–211 (2014).
16. Kumar, S. et al. Temperature-dependent nonlinear damping in palladium nanomechanical resonators. *Nano Lett.* https://doi.org/10.1021/acs.nanolett.1c00109 (2021).
17. Shin, H. et al. Control of coherent information via on-chip photonic-phononic emitter-receivers. *Nat. Commun.* **6**, 1–8 (2015).
18. Zivari, A. et al. On-chip distribution of quantum information using traveling phonons. (2022).
19. Navarathna, A. & Bowen, W. P. Good vibrations for quantum computing. *Nat. Phys.* 1–2 https://doi.org/10.1038/s41567-022-01613-z (2022).
20. Luo, G. et al. Strong indirect coupling between graphene-based mechanical resonators via a phonon cavity. *Nat. Commun.* **9**, 383 (2018).
21. Cirac, J. I., Zoller, P., Kimble, H. J. & Mabuchi, H. Quantum state transfer and entanglement distribution among distant nodes in a quantum network. *Phys. Rev. Lett.* **78**, 3221–3224 (1997).
22. Hatanaka, D., Bachtold, A. & Yamaguchi, H. Electrostatically induced phononic crystal. *Phys. Rev. Appl.* **11**, 1 (2019).
23. Kirchhof, J. N. et al. Tunable graphene phononic crystal. *Nano Lett.* **21**, 2174–2182 (2021).
24. Zhang, Z.-D., Cheng, C., Yu, S.-Y., Lu, M.-H. & Chen, Y.-F. Electrically tunable elastic topological insulators using atomically thin two-dimensional materials pinned on patterned substrates. *Phys. Rev. Appl.* **15**, 034015 (2021).
25. Zhang, Q. H. et al. Graphene-based nanoelectromechanical periodic array with tunable frequency. *Nano Lett.* **21**, 8571–8578 (2021).
26. Novoselov, K. S. et al. Two-dimensional gas of massless Dirac fermions in graphene. *Nature* **438**, 197–200 (2005).
27. Castro Neto, A. H., Guinea, F., Peres, N. M. R., Novoselov, K. S. & Geim, A. K. The electronic properties of graphene. *Rev. Mod. Phys.* **81**, 109–162 (2009).
28. Lee, C., Wei, X., Kysar, J. W. & Hone, J. Measurement of the elastic properties and intrinsic strength of monolayer graphene. *Science* **321**, 385–388 (2008).
29. Deinhart, V. et al. The patterning toolbox FIB-o-mat: exploiting the full potential of focused helium ions for nanofabrication. *Beilstein J. Nanotechnol.* **12**, 304–318 (2021).
30. Kovalchuk, S., Kirchhof, J. N., Bolotin, K. I. & Harats, M. G. Non-uniform strain engineering of 2D materials. *Isr. J. Chem.* https://doi.org/10.1002/ijch.202100115 (2022).
31. Nicholl, R. J. T. et al. The effect of intrinsic crumpling on the mechanics of free-standing graphene. *Nat. Commun.* **6**, 8789 (2015).
32. Chen, C. et al. Performance of monolayer graphene nanomechanical resonators with electrical readout. *Nat. Nanotechnol.* **4**, 861–867 (2009).
33. Bonini, N., Garg, J. & Marzari, N. Acoustic phonon lifetimes and thermal transport in free-standing and strained graphene. *Nano Lett.* **12**, 2673–2678 (2012).
34. Liu, F., Ming, P. & Li, J. Ab initio calculation of ideal strength and phonon instability of graphene under tension. *Phys. Rev. B* **76**, 064120 (2007).
35. Cha, J. & Daraio, C. Electrical tuning of elastic wave propagation in nanomechanical lattices at MHz frequencies. *Nat. Nanotechnol.* **13**, 1016–1020 (2018).
36. Kovalchuk, S. et al. Neutral and charged excitons interplay in non-uniformly strain-engineered WS2. *2D Mater.* **7**, 35024 (2020).
37. Liu, F., Ming, P. & Li, J. Ab initio calculation of ideal strength and phonon instability of graphene under tension. *Phys. Rev. B* **76**, 1–7 (2007).
38. Bunch, J. S. et al. Impermeable atomic membranes from graphene sheets. *Nano Lett.* **8**, 2458–2462 (2008).
39. Couto, N. J. G. et al. Random strain fluctuations as dominant disorder source for high-quality on-substrate graphene devices. *Phys. Rev. X* **4**, 1–13 (2014).
40. Neumann, C. et al. Raman spectroscopy as probe of nanometre-scale strain variations in graphene. *Nat. Commun.* **6**, 8429 (2015).
41. Colangelo, F. et al. Mapping the mechanical properties of a graphene drum at the nanoscale. *2D Mater.* **6**, 025005 (2019).

ACKNOWLEDGEMENTS

This work was supported by Deutsche Forschungsgemeinschaft (DFG, German Research Foundation, project-ID 449506295 and 328545488), CRC/TRR 227 and ERC

Starting grant no. 639739. We thank Yuefeng Yu, Aleksei Tsarapkin, Victor Deinhart and Katja Höflich for the fabrication of a graphene phononic crystal reference sample.

AUTHOR CONTRIBUTIONS

J.N.K. and K.I.B. conceived the idea and wrote the manuscript. J.N.K. performed the FEM simulations.

FUNDING

Open Access funding enabled and organized by Projekt DEAL.

COMPETING INTERESTS

The authors declare no competing interests.

ADDITIONAL INFORMATION

Supplementary information The online version contains supplementary material available at https://doi.org/10.1038/s41699-023-00374-4.

Correspondence and requests for materials should be addressed to Jan N. Kirchhof or Kirill I. Bolotin.

Supplementary Information: Mechanically-tunable bandgap closing in 2D graphene phononic crystals

Jan N. Kirchhof[1*] *and Kirill I. Bolotin*[1*]

[1] Department of Physics, Freie Universität Berlin, Arnimallee 14, 14195 Berlin, Germany

*jan.kirchhof@fu-berlin.de *kirill.bolotin@fu-berlin.de

Supplementary Note 1: Band structure calculations for an infinite lattice

The infinite model for the phononic band structure calculations is based on two studies within the same FEM simulation model (Comsol Multiphysics 5.5). In the first step we simulate the tension redistribution upon pattering (stationary study). We then use the calculated tension distribution as input for a second study step (eigenfrequency study). In this step, we parameterize the x and y component of the k vector to cover the 1.BZ, and implement them into the model as periodic boundary conditions (Floquet) along the outline of the unit cell. We then calculate and plot the eigenfrequencies, what gives us the band structure. For more details see Ref. [1]. To assure that our simulations properly capture the phononic band gaps, we extend our calculations to more high symmetry points. For the unit cell shown in Supplementary Figure 1a, we plot the extended band structure for $\sigma_{xx}/\sigma_{yy} = 1$ and $\sigma_{xx}/\sigma_{yy} = 1.7$ inside the 1.Brillouin zone, see Supplementary Figure 1b,c. We find that the valence band maximum between Γ and X and the conduction band minimum at X, and it is therefore sufficient to focus on the high symmetry points shown in the main paper.

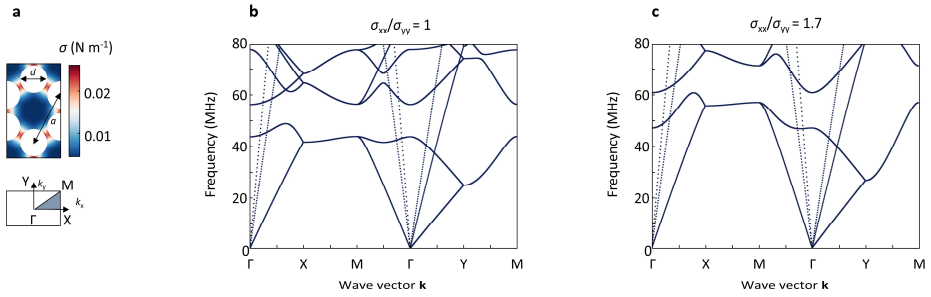

Supplementary Figure 1 | Extended band structure. a, Unit cell of the honeycomb lattice with redistributed tension (top) and the corresponding first Brillouin zone (bottom). **b,c**, Extended phononic band structure for the unit cell shown in (a) with entirely uniform tension (σ_{xx}/σ_{yy} =1.) and implemented uniaxial tension σ_{xx}/σ_{yy} =1.7.

Supplementary Note 2: Transmission studies

To perform our transmission studies, we use a pre-stressed frequency domain study. In this study the phononic device is clamped along its perimeter (Supplementary Figure 2) and in a first study step we again calculate the tension redistribution upon patterning. In a second step, we add a time depended pressure in z direction at area A, which simulates an optothermal drive. For the transmission study, we then sweep the frequency of this time depended perturbation and calculate the response of the entire geometry (compare Eq. 1 main text). For this study step, we add isotropic damping ($\eta = 0.01$) to the graphene, which reproduces the quality factors ($Q \sim 100$) typically observed for graphene resonators at room temperatures. To simulate the effect of electrostatic pressure to the transmission studies, we add a boundary load to the entire device (including A and B) in z-direction and repeat the frequency sweep.

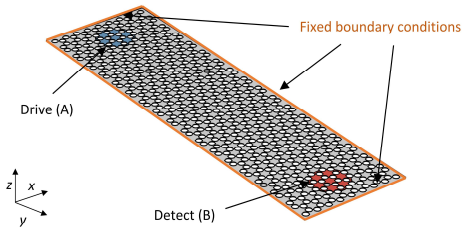

Supplementary Figure 2 | Transmission geometry. The phononic device is clamped at its perimeter via fixed boundary conditions and motion is excited at A (blue) and detected at B (red).

Supplementary Note 3: Transmission circular reference device

As a comparison to the presented bandgap closing in the main text we perform transmission studies on a circular device under applied pressure which is excited at its centre and probed on the outside. The device geometry and resulting transmission spectra are shown in Supplementary Figure 3a,b, where we find clear bandgap features (shaded area) with (red) and without (blue) applied pressure. In circular devices we find band gap features up to at least 30 kPa applied pressure in agreement with previous work.[1]

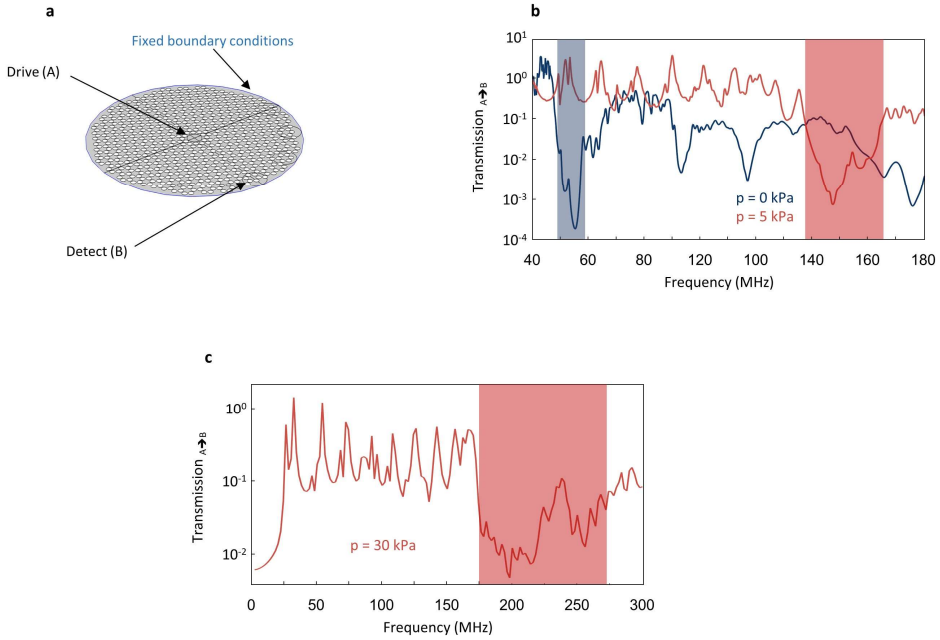

Supplementary Figure 3 | Transmission circular reference device. a, Transmission geometry for a rectangular phononic device. At point A mechanical motion is excited by a frequency modulated laser, which than travels through the device and is detected at point B by a second laser spot. **b**,**c** Transmission from A to B vs. excitation frequency for the device shown in (a) for 0, 5 and 30 kPa applied pressure. A clear bandgap region is visible for all cases.

Supplementary Note 4: Phononic bandgap vs. uniform residues

In addition the added pieces of mass (Figure 4 main text), we also investigate the effect of a uniform layer of resist, which could be present on a device after thermal annealing. In Supplementary Figure 4 we plot transmission for a device made from clean graphene (blue) and one contaminated with a 3 nm layer of PDMS (green). For both cases we find a clear bandgap, the added PDMS however causes a downshift in frequency as the entire device becomes heavier. Also the bandgap is slightly less pronounced, but still clearly noticeable. For PDMS we assume a Young's modulus of 0.75 MPa, a Poisson's ratio of 0.49 and a density of 970 kg m^{-3}.

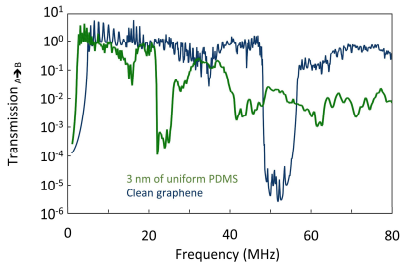

Supplementary Figure 4 | Phononic bandgap vs. uniform residues. Transmission vs. frequency for a phononic device made from clean graphene (blue) and with a 3 nm uniform layer of PDMS residues (green).

Supplementary Note 5: Phononic bandgap vs. tension disorder

To represent a random but smooth enough spatial tension distribution in our devices we use a sum of plane waves with randomized amplitude $a(m,n)$ (between -1 and 1) and phase $\phi(m,n)$ (between 0 and π) of each mode:

$$\sigma(x,y) = p\sum_{m=-M}^{M}\sum_{n=-N}^{N} a(m,n)\cos(2\pi(mx+ny)+\phi(m,n)) \qquad (1)$$

The factor p controls the disorder strength.

Supplementary Note 6: Phononic bandgap vs. hole size variations

We also investigate the effect of disorder within the phononic pattern in terms of a) variations of the radius of individual holes (so that the holes are not perfectly round) or b) size variations between the different perfectly circular holes that make up the phononic crystal.

Before we simulate the effect of a) and b) on the phononic bandgap, we need to get a feeling for the experimentally relevant disorder in patterned phononic crystals. To this end, we look at a real phononic crystal made from ~5 layer thick graphene (Supplementary Figure 5). We patterned this sample using the honeycomb lattice described in the manuscript by focused ion beam milling (FIB). The spatial resolution of this process is in the order of ~20 nm, which is compared to the hole diameter (500 nm) rather small, and we expect high precision and reproducible hole diameters. And indeed, we find a regular patterned phononic crystal as shown in Supplementary Figure 5.

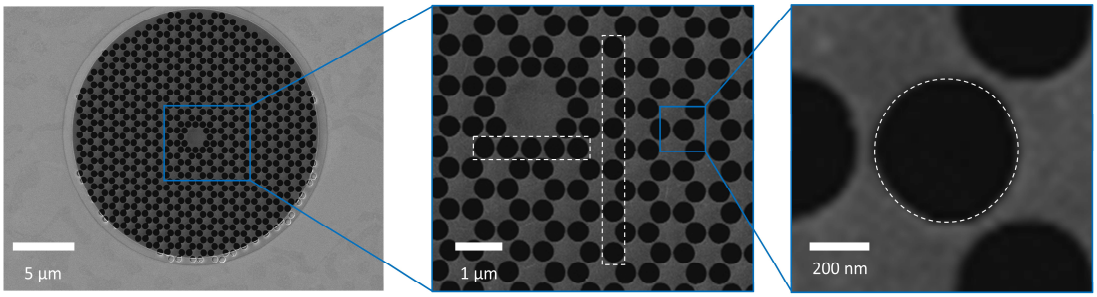

Supplementary Figure 5 | Circular prototype device made from 5 Layer graphene for experimental work. The phononic pattern is regular and the variations in hole size are small.

Next, we study the effect of non-circular holes (a) in our infinite model. We start by replacing two holes in the unit cell by ellipses (90° rotated to each other, eccentricity: $e = \sqrt{1 - \left(\frac{d_1}{d_2}\right)^2} = 0.574$, as shown in Supplementary Figure 6c) and calculate the corresponding band structure (Supplementary Figure 6d). If we compare this to the reference band structure obtained with perfect holes (Supplementary Figure 6a,b), we find that some bands split into closely lying sub-bands. Nevertheless, the bandgap remains. No change in size or position of the bandgap is noticeable. To go a step further, we try to capture variations in hole radius of individual holes comparable to the sample

shown above (Supplementary Figure 5 right). To do so we implement exaggerated “wobbly” holes into the unit cell (Supplementary Figure 6e). Again, we find no major impact on the bandgap region (Supplementary Figure 6e) and thus the robustness of our results.

To check the effect of variations in hole size between different holes (b), we model a structure were the size of randomly picked holes (“defects”) is decreased or increased by 10%. In Supplementary Figure 6g, we show the used structure with a defect density ($\frac{N_{\mathrm{defect}}}{N_{\mathrm{holes}}}$) of 12.5%. If we zoom in on a device with larger defect density of $\frac{N_{\mathrm{defect}}}{N_{\mathrm{holes}}} = 50\%$, the variations in hole size are clearly visible (see Supplementary Figure 6h). Next, we simulate the transmission for devices with defect densities from 0 to 50% (Supplementary Figure 6i). We find that the bandgap clearly persists to a defect density of at least 50%. This level of disorder is clearly much higher than that in experimentally achieved devices (Supplementary Figure 5). We therefore conclude that we can fabricate the devices ordered enough to observe the phenomena we study in the main text.

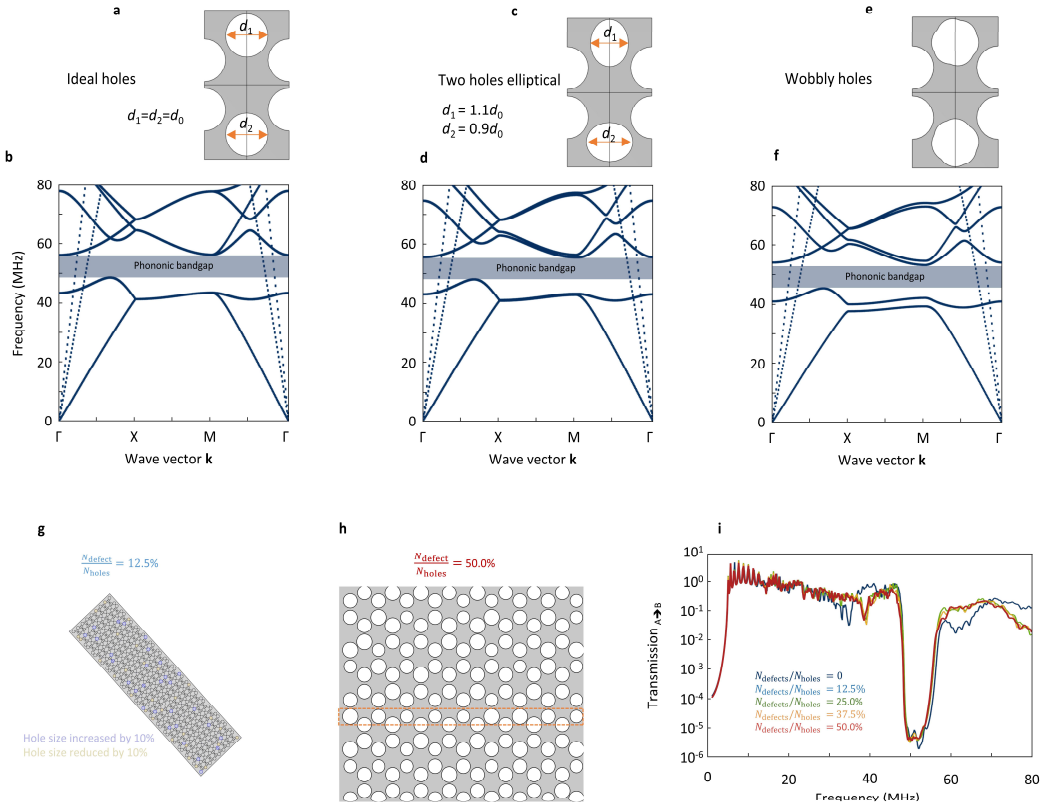

Supplementary Figure 6 | Phononic bandgap vs. hole size variations a,b Unit cell and corresponding band structure calculation for ideal holes (same as in main text Supplementary Figure 1b) **c,d** Unit cell with two elliptical holes and corresponding band structure calculation. The phononic bandgap remains almost unchanged. **e,f** Unit cell with two wobbled holes and corresponding band structure calculation The phononic bandgap remains almost unchanged. **g,h** Finite model with different degree of lattice defects (hole diameter variations) implemented. The blue (yellow) marking indicates holes, which will be increased (decreased) in size by 10%. **i** Transmission simulation for varying defect density. For a defect density of 50% the bandgap is clearly distinguishable in the transmission plots.

Supplementary Note 7: Phononic band gap vs. layer number

As a potential approach to overcome challenges associated with the fabrication of uniform and residue free suspended graphene devices for phononic pattering, we suggest to use thin multilayers. For this we have to check, if the bandgap persist also for thicker devices. We thus perform band structure calculations for various thickness (maintaining a constant stress in the device) and extract the band gap (Supplementary Figure 7). We find a bandgap up to ~350 layers of graphene.

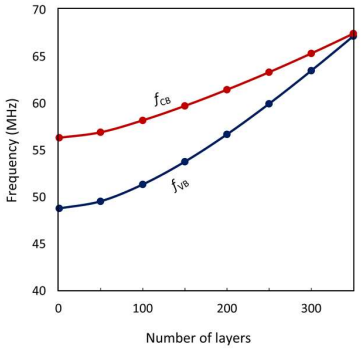

Supplementary Figure 7 | Phononic band gap vs. layer number. Valence band maximum (f_{VB}) and conduction band minimum (f_{CB}) vs. number of graphene layers extracted from band structure calculations.

Supplementary Note 8: Localization-delocalization transition

To further highlight the usefulness of the proposed system and to strengthen the analogy to a MIT, we perform an additional study. In it, we examine the localization of defect vibrational modes that can be compared to the localization of mid-gap defect states in semiconductors. By varying the size of the bandgap using our tension engineering approach, we observed the behaviour similar to the localization-delocalization transition in solids.

In this study, we place an artificial lattice defect within the phononic lattice. When the defect is within a phononic bandgap, it hosts spatially localized vibrational modes. We then simulate the pressure dependence of such a defective phononic lattice using two geometries. The first device is similar to the one shown in the manuscript (Supplementary Figure 8a), where we expect the bandgap closing under the application of pressure. The second one is a circular reference device (Supplementary Figure 8b, as studied in previous work). As explained in the main text, the bandgap does not close for this geometry. At zero pressure, the defect mode is localized in both geometries (Supplementary Figure 8). At the same time, we find starkly different behaviour of that mode in circular and rectangular devices under applied pressure (Supplementary Figure 8c,d). In the rectangular device, the mode starts to show displacement over the entire device (highlighted by grey arrows) and thus loses its localization as the bandgap closes. In the circular device, in contrast, the bandgap does not close, and the defect mode always stays within it. Correspondingly, the defect mode remains localized in the entire range of pressures (Supplementary Figure 8d). This further highlights the similarity between phononic and solid-state crystals, despite their very different quasiparticles. We believe that the behaviour we observe can be compared to the localization-delocalization transition.

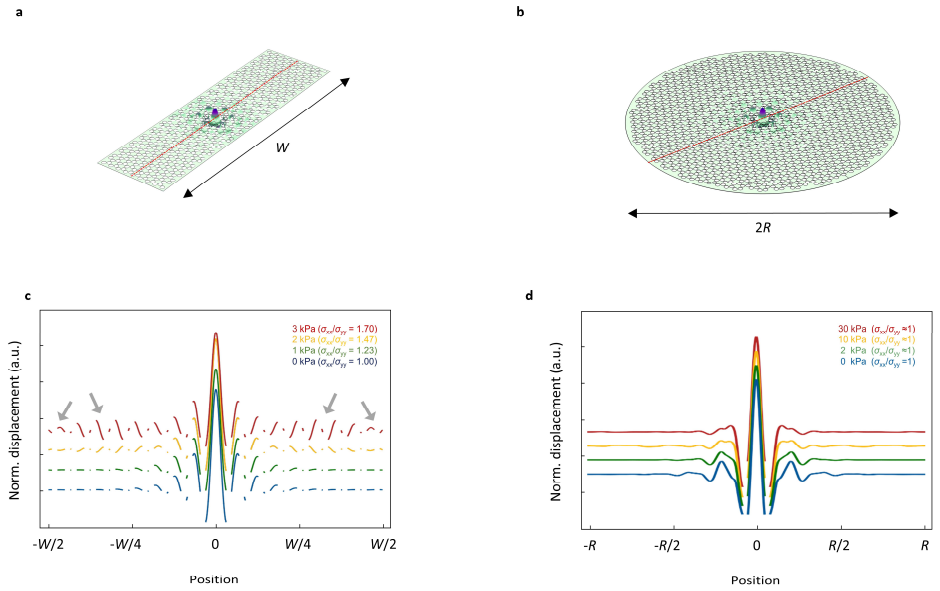

Supplementary Figure 8 | Dephasing a localized defect state using uniaxial tension. a,**b** Mode shape of a localized mode within the bandgap of a rectangular (a) and circular (b) phononic device **c**, Line cut of the normalized displacement extracted along the red line in **a** vs. applied pressure (plots are offset for better visibility). With increased pressure, the degree of uniaxiality is increased and the bandgap gradually closes. At the same time the mode that was localized near device centre at zero pressure becomes delocalized over the entire device. **d,** Same as **c**, but for the circular device shown in (b). Here the mode shape remains virtually unchanged under pressure, as the frequency of the defect mode scales together with the bandgap and maintains its localization.

Supplementary References

1. Kirchhof, J. N. *et al.* Tunable Graphene Phononic Crystal. *Nano Lett.* **21**, 2174–2182 (2021).

B.3. Nano Letters 22(20), 8037–8044 (2022) and Supporting Information

NANO LETTERS

pubs.acs.org/NanoLett Letter

Nanomechanical Spectroscopy of 2D Materials

Jan N. Kirchhof,* Yuefeng Yu, Gabriel Antheaume, Georgy Gordeev, Denis Yagodkin, Peter Elliott, Daniel B. de Araújo, Sangeeta Sharma, Stephanie Reich, and Kirill I. Bolotin*

Cite This: *Nano Lett.* 2022, 22, 8037−8044 Read Online

ACCESS | Metrics & More | Article Recommendations | Supporting Information

ABSTRACT: We introduce a nanomechanical platform for fast and sensitive measurements of the spectrally resolved optical dielectric function of 2D materials. At the heart of our approach is a suspended 2D material integrated into a high Q silicon nitride nanomechanical resonator illuminated by a wavelength-tunable laser source. From the heating-related frequency shift of the resonator as well as its optical reflection measured as a function of photon energy, we obtain the real and imaginary parts of the dielectric function. Our measurements are unaffected by substrate-related screening and do not require any assumptions on the underling optical constants. This fast ($\tau_{rise} \sim 135$ ns), sensitive (noise-equivalent power = 90 $\frac{pW}{\sqrt{Hz}}$), and broadband (1.2−3.1 eV, extendable to UV−THz) method provides an attractive alternative to spectroscopic or ellipsometric characterization techniques.

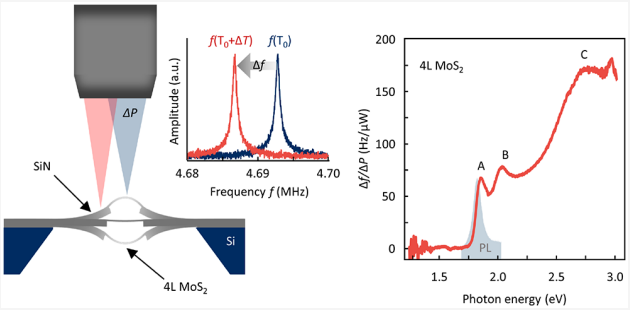

KEYWORDS: *Nanomechanical resonators, NEMS, spectroscopy, 2D materials, transition metal dichalcogenides (TMDs), silicon nitride*

The interaction of light with a solid is encoded in the material's dielectric function $\epsilon_r(\omega) = \epsilon_1(\omega) + i\epsilon_2(\omega)$. Real and imaginary components, ϵ_1, ϵ_2, contain the information regarding light absorption, propagation velocity, excitonic and plasmonic resonances, bandgaps, and many-body effects. The dielectric function is usually experimentally determined via spectroscopic ellipsometry,[1−4] a combination of reflection and transmission measurements,[5] or from spectrally resolved reflection contrast (dR/R) using Kramers−Kronig relations.[6−8] Despite the broad applicability of these techniques, they are hard or impossible to apply in many situations. For example, optical measurements under oblique angles as required by spectroscopic ellipsometry are challenging at low temperature, ultrahigh vacuum environments, and high magnetic fields. Measurements of transmission require large and thin samples on transparent substrates and may be affected by scattering. The Kramers−Kronig analysis requires broadband measurements of reflection and depends on empirical models of optical constants.[9]

For 2D materials, these problems become more severe. On one hand, 2D materials, in particular from the group of transition metal dichalcogenides (TMDs), feature a remarkable zoo of correlated phases including excitonic insulators,[10] Wigner crystals,[11,12] Bose Einstein condensates,[13−15] and superconductors.[15] All these phenomena can be studied by analyzing the dielectric function. On the other hand, their observation requires uniform high-quality samples. Such samples are usually encapsulated in hexagonal boron nitride and have sizes in the micron range. Transmission or ellipsometry measurements of such nanostructures at ultralow temperatures or high magnetic fields are challenging.[16] Especially for studying plasmons or polaritons in patterned 2D materials in the form of photonic[17,18] or phononic crystals,[19] new optical characterization methods are needed. In addition, excitations in 2D materials are strongly screened by the underlying substrate. This screening perturbs the dielectric function also affecting the Kramers−Kronig analysis.

Here, we use nanomechanical spectroscopy[20−23] to accurately and quickly determine the optical dielectric function of 2D materials. For our proof-of principle experiments, we focus on few-layered TMDs, well-understood materials with many pronounced features in their optical response. Our approach employs a suspended membrane made from the 2D material of interest. The mechanical resonance frequency of that membrane depends on its temperature, which, in turn, depends on the amount light absorbed by the material upon illumination. Therefore, by measuring changes of the resonance frequency of the membrane vs the energy of photons ($E_\gamma = \hbar\omega$), we determine the absorption of the material. The membrane functions as its own photodetector,

Received: March 30, 2022
Revised: September 23, 2022
Published: October 17, 2022

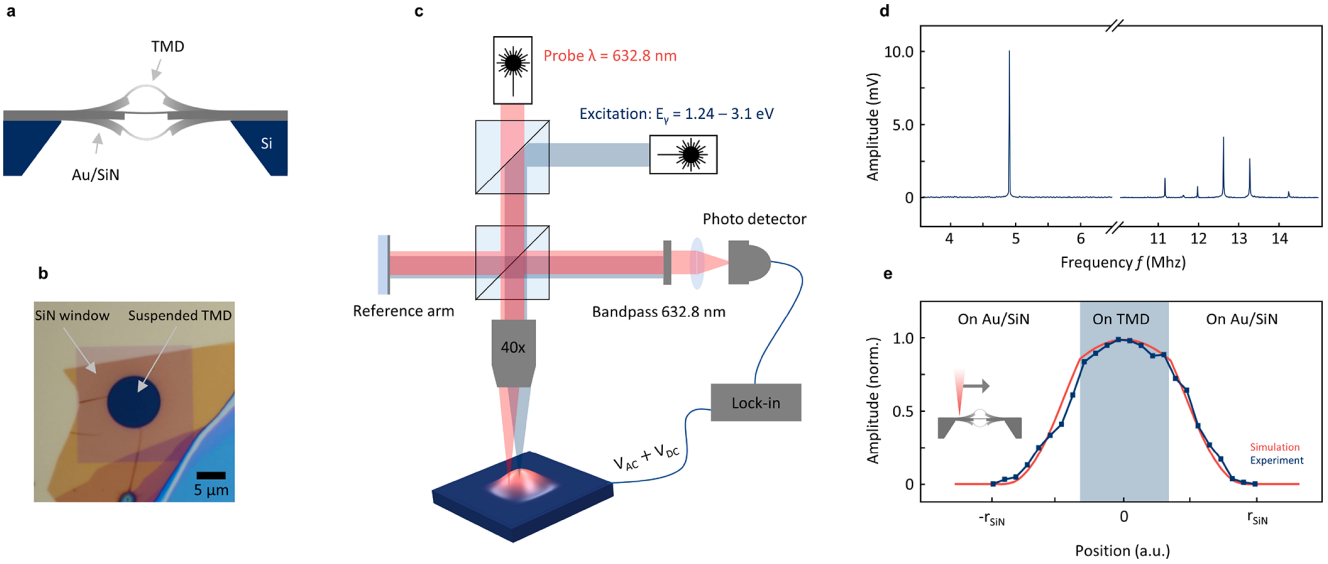

Figure 1. SiN–TMD hybrid devices and interferometric motion detection. (a) Sketch of SiN–TMD hybrid resonance mode. The suspended SiN moves together with the TMD material and allows probing the resonances without focusing the probe laser on the TMD area. (b) Optical micrograph of a WSe_2 trilayer flake suspended on a hole in a SiN window. (c) Interferometric motion detection using a Michelson interferometer (red laser) with an additional broadly tunable laser (blue) to heat the TMD. The sample is placed in vacuum and the motion of the suspended area is actuated electrically. (d) Measured amplitude versus frequency for the trilayer WSe_2–SiN hybrid device. The fundamental mode shows a large amplitude and enhanced quality factor. (e) Relative motion amplitude of the fundamental mode extracted along a spatial line scan over the suspended area (blue) in comparison to simulation results (red). The amplitude of motion increases as the probe laser spot moves toward the center of the device and matches the simulated mode shape.

only sensitive to the amount of absorbed light and not, for example, to scattering and other losses. By combining the mechanically measured absorption with optically recorded reflection, we restore the full dielectric function of the 2D material. We achieve very fast ($\tau_{rise} \sim 135$ ns) and sensitive (noise-equivalent power = 90 $\frac{pW}{\sqrt{Hz}}$) measurements of the dielectric function for TMD materials in the range 1.2–3.1 eV. Our approach uses suspended samples and, therefore, is unaffected by substrate-related screening and unwanted interactions with the probe beam. Furthermore, our approach does not require complex transmission measurements and therefore should function at low temperatures and high magnetic fields. Finally, by using the 2D materials themselves for the detection of absorbed light, we can potentially obtain access to a broad spectral range from THz to UV, allowing the study of a large variety of materials.

Our first goal is to design a TMD-based resonator that controllably changes its frequency as it absorbs light. Such a resonator should have predictable mechanical resonances (the fundamental mode at frequency f) with a small line width (f_{fwhm}) and thus a high quality factor ($Q = \frac{f}{f_{fwhm}}$), linear mechanical response to illumination power, as well as high motion amplitude. To accomplish these goals, we design a hybrid resonator consisting of a TMD suspended over a circular hole in a high quality silicon nitride (SiN) membrane covered with a thin layer of gold. Our finite element method (FEM) simulations show that the fundamental mode of such a resonator involves the TMD and suspended SiN oscillating together (Figure 1a).[24,25] Absorption of light by the suspended TMD causes thermal expansion leading to a reduced tension σ_0 in the material and hence softening the resonance frequency of the entire system. Such a design presents several advantages:

First, the device features resonances with high quality factor at room temperature ($Q > 4000$). This is due to the mechanical quality and low losses in SiN and allows us to resolve frequency shifts with high resolution. This is in contrast to 2D material-only resonators that show mechanical resonance frequencies with low quality factors ($Q \sim 100$).[26−29] Second, our design overcomes the disturbance typically associated with optical probing of mechanical resonances. To probe the mechanical motion of our devices, we focus the probing beam on the suspended SiN area thereby avoiding heating of the material being measured. Third, in our system, the mechanical resonances and their tuning are highly predictable, with device-to-device variations of ∼5% or less. This allows us to simulate our systems with high confidence. The uniformity is also interesting from a technological point of view, as it can potentially allow coupling the oscillator to an external system, for example, an LC-resonator for electrical signal amplification. Again, this is in contrast to 2D material-only resonators that are affected by wrinkling and surface contaminations, resulting in a large spread of mechanical resonance frequencies and unpredictable tuning.[29−31] Finally, by covering the SiN area with a thin layer of gold (also used for electrical actuation), we increase its reflectivity and thus enhance the signal-to-noise ratio. We note that the additional weight of the gold layer and high stiffness of SiN reduce the response of the hybrid mode to laser heating. We thus use micromechanical modeling to design a system, giving a good compromise between signal strength and sufficient responsivity (Supporting Information, Figure 2b,c), resulting in a device with a circular suspended TMD area of 10 μm diameter and a 20 μm square SiN window of 20 nm thickness. By using relatively low-stress SiN (240 MPa) we ensure that the responsivity is large and the sensitivity is improved.[23]

https://doi.org/10.1021/acs.nanolett.2c01289
Nano Lett. 2022, 22, 8037−8044

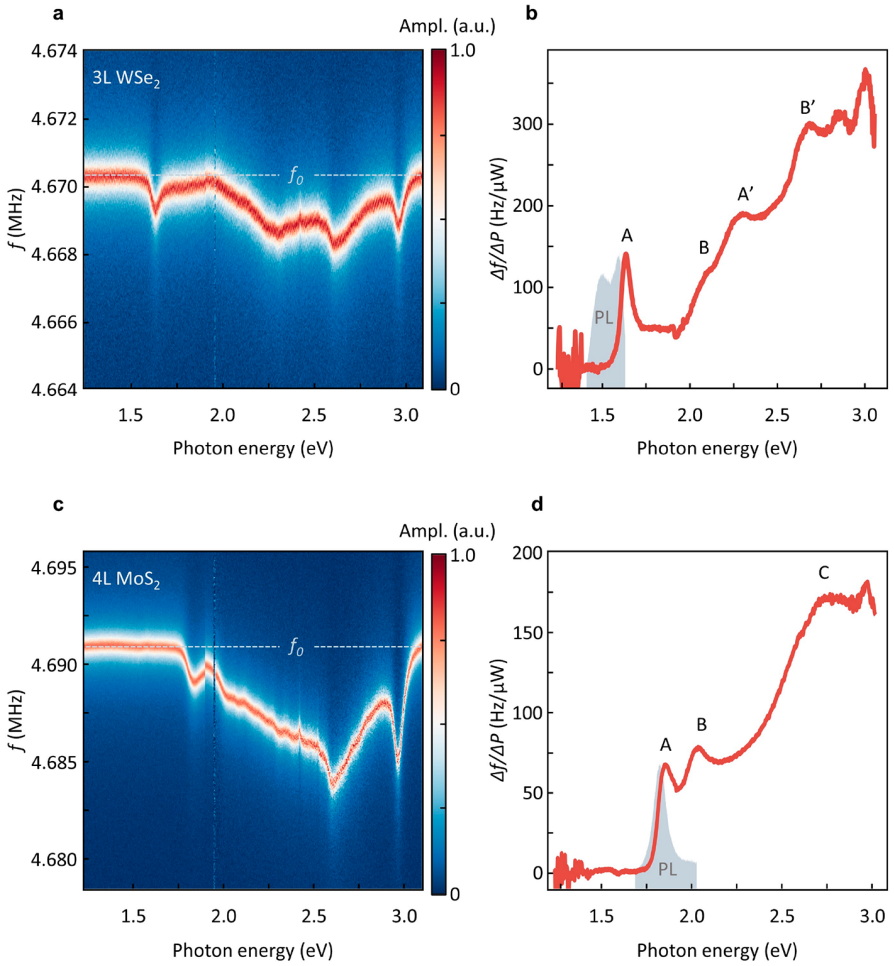

Figure 2. Mechanical absorption spectroscopy in WSe_2 and MoS_2. (a, c) Raw frequency response of the TMD−SiN hybrid device as a function of photon energy for a WSe_2 and a MoS_2 samples. Multiple features are visible and toward higher energies the frequency shift increases as the absorption by the TMD increases. (b, d) Responsivity $\frac{\Delta f}{\Delta P}$ vs photon energy for WSe_2 and MoS_2. This signal is directly proportional to the absorption and shows clear excitonic features in both samples, which match reference PL measurements (gray). The MoS_2 sample was measured using higher laser power, causing larger absolute frequency shifts.

We realize the design described above by transferring a multilayer TMD (3 and 4 layers) onto a circular hole in a square SiN window covered with gold, as shown in Figure 1b (see Supporting Information, section 3). The mechanical motion of the hybrid SiN−TMD mode is excited by applying an AC+DC voltage between the device and a nonreflective gate ∼40 μm below. The motion of the hybrid mode is detected interferometrically (Figure 1c).[24] Critically, the probe beam (red beam in Figure 1c) is focused onto the SiN area and does not significantly heat the device. A second laser source of tunable photon energy between 1.2 and 3.1 eV (blue beam in Figure 1c) is focused on the suspended TMD area. The absorption of light from that beam increases the temperature of the device and downshifts the mechanical resonance, which we detect. All measurements are carried out in vacuum and at room temperature but are easily extendable to low temperatures and fiber-based setups. Figure 1d shows the resonance response of the WSe_2 trilayer sample (device #1) without optical excitation. We find a prominent fundamental mode at f_0 = 4.6702 MHz with a $Q \sim 4500$ and multiple higher order modes. We visualize the shape of the fundamental mode by scanning the probe laser across the device and plot the motion amplitude versus position (Figure 1e, blue). The mode is well described by our simulations (Figure 1a) that give its shape (Figure 1e, red) and frequency ($f_{0,\mathrm{sim}}$ = 4.770 MHz), confirming the well-controlled nature of our devices.

Our goal is to use our nanomechanical system to obtain a broadband absorption spectrum of the TMD. To this end, we continuously vary the photon energy of the excitation laser and record the resonance response of the high Q fundamental mode. In Figure 3a we show the raw data of this measurement for the trilayer WSe_2 sample (device #1). Small laser powers (P < 10 μW) are sufficient to cause clearly resolvable frequency shifts $\Delta f = f_0 - f$. The resonance frequency softens upon illumination, because the absorbed light heats the suspended TMD and reduces the built-in tension σ_0. From lower to higher energy, we observe an increasing down shift, in line with an overall increasing absorption toward the band gap of WSe_2. Within the spectra, there are multiple peaks and dips visible. Some of these features (e.g., the dip at 2.96 eV and the sudden jump at 1.91 eV) stem from the variations in power of our excitation laser. We record the laser power at the sample position (Supporting Information, Figure 5b) and use it to determine the resulting responsivity $\frac{\Delta f}{\Delta P}$ (Figure 2b). As we

https://doi.org/10.1021/acs.nanolett.2c01289
Nano Lett. 2022, 22, 8037−8044

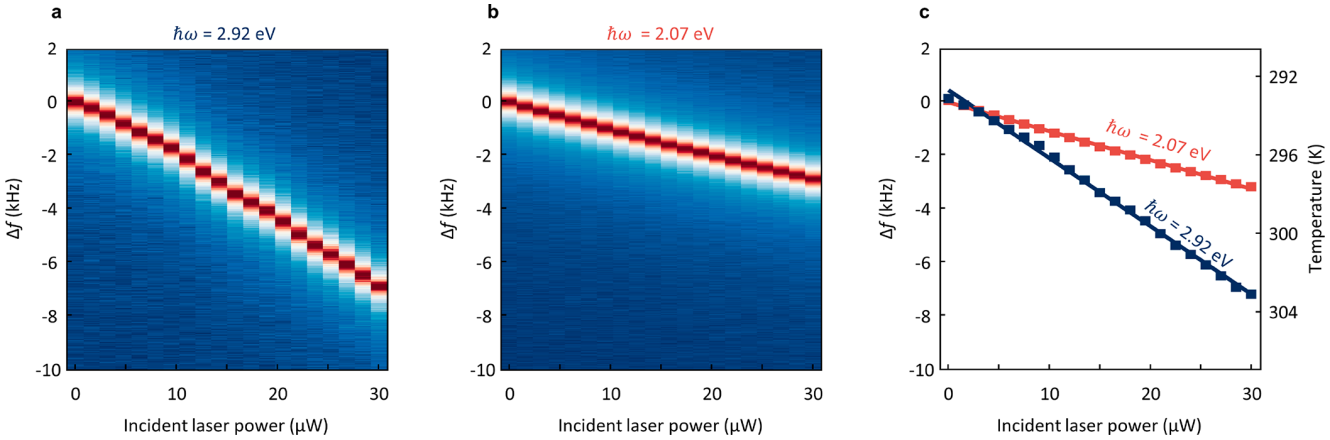

Figure 3. Mechanical response to laser heating. (a, b) Frequency shift of the fundamental mode of a suspended trilayer WSe_2−SiN hybrid device vs incident laser power for 2.92 and 2.07 eV excitation. A fraction of light absorbed by the membrane causes heating, which reduces the built-in tension and softens the mechanical resonance. (c) Fits to the frequency change vs incident laser power, which by comparison to FEM simulations allows to extract the absorption of the material at different energies. Right axis shows the average temperature in the suspended TMD obtained from such simulations.

show later, the measured responsivity is directly proportional to the optical absorption of the material, and the distinct features associated with band-edge excitons of the TMD material are clearly noticeable. We identify the following excitonic transitions: A at 1.63 eV, B at 2.08 eV, A′ at 2.28 eV, and B′ at 2.68 eV. The positions and widths of these peaks agree well with literature values.[6,32−34] As a reference, we perform photoluminescence measurements (PL) of the same device (Figure 2b, gray). As expected, we find the peaks corresponding to the A and I excitons, with the latter corresponding to the indirect bandgap of multilayer TMD. For the A exciton, we find an expected small red shift and matching peak width, whereas the indirect peak is not visible in absorption due to the indirect nature of the transition.

Clear peaks are also apparent in the mechanical responsivity data for a second sample made from a different material from the TMD family (4L MoS_2 in Figure 2c,d). Again, the positions and widths of these peaks match with excitonic transitions dominating optical absorption spectra of MoS_2.[35,36] We note that no assumption regarding material properties has been made in obtaining the spectra in Figure 2b,d. In all measurements we observe a constant mechanical line width around the excitonic peaks (Supporting Information, Figure 4a,b) and therefore exclude any cavity or material governed dynamic optomechanical back action effects.[37,38] We note that we can improve the measurement speed and sensitivity further by using a phase-locked loop (PLL) to directly measure the frequency shift vs photon energy (Supplementary Figure 5c). We obtain the same frequency response, as shown in Figure 2a, but now we record an entire spectrum in ∼3 s, only limited by how fast the filter can change the output energy.

Next, we determine the optical dielectric function of the TMDs. For this, precise knowledge of both reflection Refl(E_γ) and absorption Abs(E_γ) in absolute units is required. To convert the measured frequency shift into absorption, we model our hybrid system as two springs in series (elastic constants: k_{SiN} and k_{TMD}) and link the responsivity (frequency shift Δf normalized to laser power ΔP) to the energy-depended absorption Abs(E_γ) of the TMD via the following:

$$\Delta f \approx f_0 \frac{k_{TMD}}{2(k_{TMD}+k_{SiN})\sigma_{TMD}} \frac{\alpha E_{2D}}{1-\nu} \frac{\beta \mathrm{Abs}(\lambda)}{h\kappa} \Delta P \quad (1)$$

Here m_{eff} is the effective mass of the mode, β is a dimensionless factor determined by the temperature profile in the membrane, α is the thermal expansion coefficient, E_{2D} is the 2D elastic modulus, κ is the thermal conductivity and ν is the Poisson's ratio of the TMD (full derivation in Supporting Information, section 6). This expression shows that the responsivity is indeed proportional to the optical absorption. However, in our system, m_{eff} and β can only be obtained numerically and k_{SiN}, k_{TMD} depend on a range of parameters (tension, thermal conductivity, etc.) in a complex fashion. We thus use FEM modeling to determine the conversion factor linking $\frac{\Delta f}{\Delta P}(E_\gamma)$ to absorption. We first measure the frequency shift vs incident laser power for 2.92 (425 nm) and 2.07 eV (600 nm; Figure 3a,b). For both energies we observe a linear and reversible downshift of the resonance frequency with increasing laser power (Figure 3c). Having experimentally confirmed the linear behavior, we use the computed conversion factor (details on mechanical modeling in Supporting Information, section 1) to convert $\frac{\Delta f}{\Delta P}$ to absorption. For the fitted slopes from Figure 3c (241 ± 14 and 88 ± 11 Hz/μW for 2.92 and 2.07 eV, respectively) we get 30.4% and 11.2% absorption by the TMD membrane at the respective energies. This is close to expectations.[6,33] As a benchmark for our approach, we perform classical optical transmission measurements and find good agreement between the two methods of measuring absorption (see Supporting Information, section 7). The simulation results also allow us to estimate the average temperature increase in the suspended TMD (Figure 3c, right axis). For 30 μW laser power and 30.4% absorption, we find an increase to only a few degrees above room temperature, which is well inside the linear regime and below the TMD damage threshold.

Having extracted absorption, we are ready now to evaluate the dielectric function. In Figure 4a,d, we plot the spectrally resolved absorption (Abs) data for both samples obtained from the frequency shifts using the conversion factor (red traces). Next, we record reflection (Refl) off the TMD in the same

https://doi.org/10.1021/acs.nanolett.2c01289
Nano Lett. 2022, 22, 8037−8044

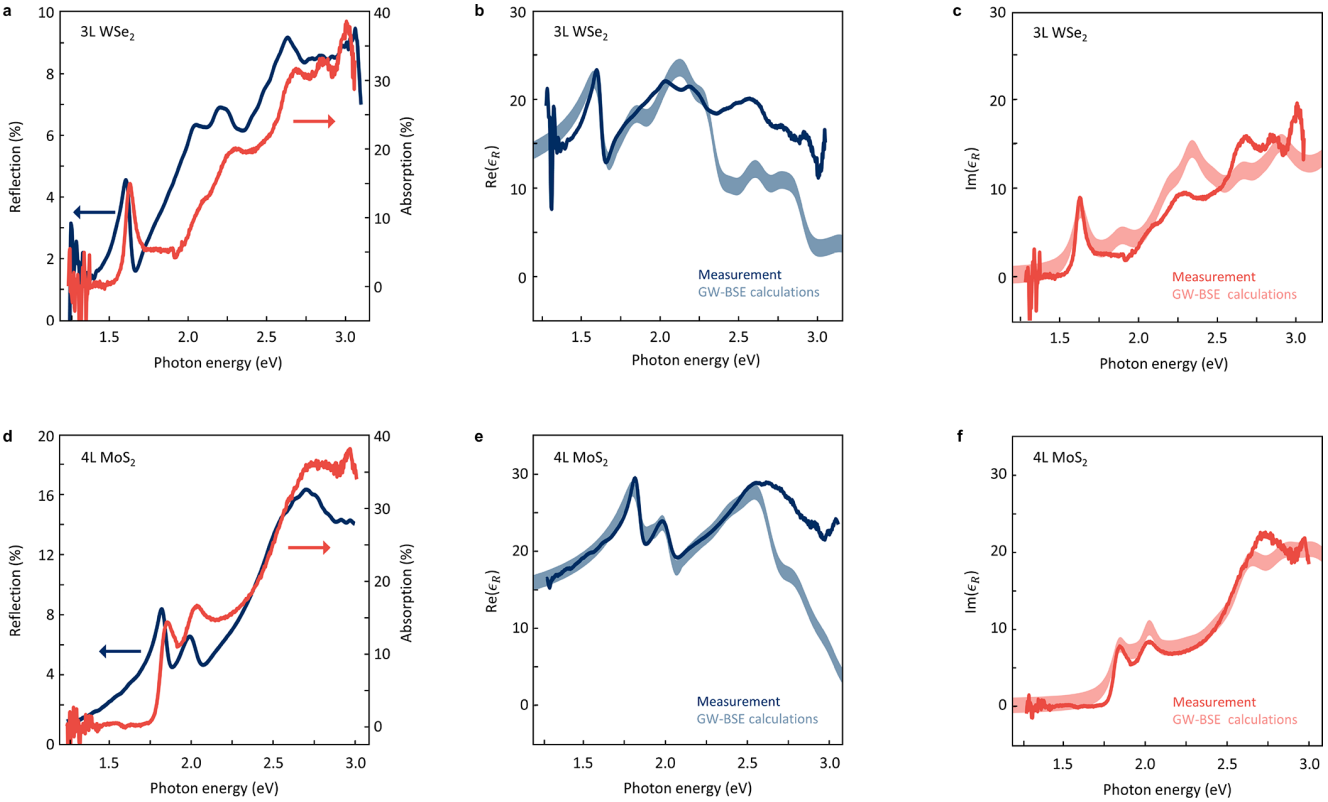

Figure 4. Dielectric function of WSe_2 and MoS_2. (a, d) Absorption (obtained from nanomechanical spectroscopy, red) and reflection (obtained optically, blue) for WSe_2 and MoS_2 vs photon energy. Similar excitonic features are apparent in both measurements. (b, c, e, f) Real (blue) and imaginary (red) part of the dielectric function of both materials derived from absorption and reflection data (a and d). We find reasonable agreement for GW-BSE calculations (red and blue shaded).

sample configuration and same setup (blue traces in Figure 4a,d; for measurement details, see Supporting Information, section 8). We then use the transfer-matrix approach to relate reflected and absorbed light and obtain the complex refractive index n and finally ϵ_1 and ϵ_2 by solving a system of equations at each measured energy (see Supporting Information, section 9):

$$\begin{cases} 1 - \text{Abs} - \text{Refl} = 1/|M_{11}(d, n(\epsilon_1, \epsilon_2))|^2 \\ \text{Refl} = |M_{21}(d, n(\epsilon_1, \epsilon_2))|^2/|M_{11}(d, n(\epsilon_1, \epsilon_2))|^2 \end{cases} \quad (2)$$

Here d is the TMD thickness and M_{ij} is the matrix element corresponding to the reflection and transmission from a thin suspended film (details in SI). No material parameters, except the thickness, are assumed in these formulas. The resulting ϵ_1 and ϵ_2 for 3L WSe_2 and 4L MoS_2 are plotted in Figure 4b,c,e,f. Both real and imaginary parts of the dielectric function agree well with previous measurements.[1−4,6] Furthermore, we find a close agreement with our ab initio GW-Bethe Salpeter equation (GW-BSE) calculations (shaded in Figure 4b,c,e,f). The difference between measurements and theory for the real part of the dielectric function toward higher energies arises due to the known underestimation of the dielectric function by GW-BSE calculations in this regime. Using nanomechanical spectroscopy, we now have obtained full spectroscopic information on the material under test and thereby access to a majority of physical phenomena that make TMDs so exciting.

How fast and how sensitive is our approach? The measurement speed is ultimately limited by the temperature equilibration time in the suspended TMD. To estimate this parameter, in Figure 5a we plot the simulated average temperature of the suspended TMD versus time after turning on the illumination (for a photon energy of 2.92 eV and 30 μW incident laser power). We extract a rise time of $\tau_{\text{rise}} \sim 135$ ns, which corresponds to a bandwidth of 7.4 MHz, in line with experimental data for TMD devices of similar size.[29] To assess the sensitivity of our system, we determine the noise-equivalent power:

$$\eta = \frac{\sigma_A \sqrt{t} f_0}{\Delta f / \Delta P} \quad (3)$$

where $\Delta f/\Delta P$ is the responsivity (determined above), σ_A is the Allan deviation obtained from time stability measurements (Figure 5b,c), and t is the sampling period.[39] For an optimal sampling period of 4 ms, we obtain $\eta = 90 \frac{\text{pW}}{\sqrt{\text{Hz}}}$. This is only slightly higher than, for instance, state-of-the-art bolometers ($2-100 \frac{\text{pW}}{\sqrt{\text{Hz}}}$).[40−43] Nevertheless, the bandwidth is higher by several orders of magnitude for our 2D material-based system, which allows us to measure much faster.

Overall, our nanomechanical measurements are a new approach to obtain the dielectric function of 2D materials. This method is sensitive ($\eta = 90 \frac{\text{pW}}{\sqrt{\text{Hz}}}$), fast ($\tau_{\text{rise}} = 135$ ns), and accurate. The absorption spectrum as well as the dielectric function for WSe_2 and MoS_2 are close to that obtained by others means. The approach does not require complex dielectric modeling or assumption about the material's optical

https://doi.org/10.1021/acs.nanolett.2c01289
Nano Lett. 2022, 22, 8037−8044

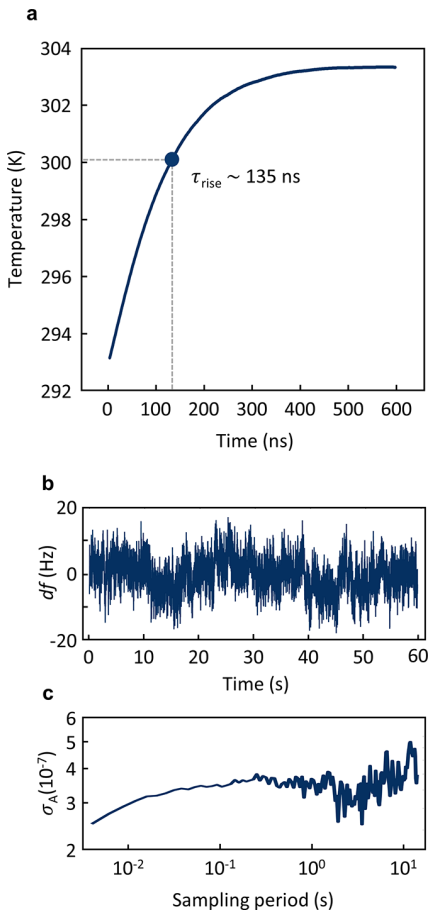

Figure 5. Time resolution and sensitivity. (a) Simulated time response of the average temperature in the suspended TMD as laser heating is introduced at $t = 0$ for 2.92 eV (30.4% absorption) and 30 μW laser power. We extract a rise time of 135 ns. (b) Stability measurement of frequency vs time without laser illumination, measured using a phase-locked loop. (c) Extracted Allan deviation σ_A vs integration time in log−log scale derived from (b).

properties (compared to, e.g., a constrained Kramer−Kronig analysis), optical transmission measurements (that are very difficult, e.g., at low temperatures or high magnetic fields),[16] and works for samples the sizes of a diffraction-limited laser spot (unlike, e.g., ellipsometry approaches). Moreover, our approach directly records optical absorption and is insensitive to scattering that is often hard to discriminate in all-optical techniques. By directly working with suspended samples, our approach is independent of tabulated optical constants of external materials and avoids perturbation of the excitonic features in 2D materials due to screening. Another advantage of using suspended samples is that the incoming light is only absorbed by the materials under test. Finally, as the material serves as its own detector, it is relatively straightforward to extend the approach to different spectral ranges.

The sensitivity of our approach can be increased much further. First, the quality factor of optimized SiN membranes can reach $Q > 10^8$,[44] compared to around 10^3 used here. This should likely result in a correspondingly higher measurement sensitivity. Second, eq 1 shows that the responsivity of our measurement is inversely proportional to the thermal conductivity of the 2D material. This quantity can be reduced by, for example, patterning the membrane into a trampoline shape[43] or, for example, via defect-engineering.[45,46] Third, at low temperatures the mechanical quality factor increases while the ratio of thermal conductivity and thermal expansion entering eq 1 stays roughly constant. Therefore, we expect the low temperature sensitivity of our approach to increase. As most 2D materials show comparable mechanical and thermal properties, we expect our approach to universally work well. Graphene and hBN, however, will show frequency shifts in the opposite direction, as they have a negative thermal expansion coefficient. For them we also expect slightly reduced sensitivity due to their higher thermal conductivity. The combination of 2D materials with low loss SiN results in enhanced Qs and therefore provides an attractive platform for studying optomechanical cooling and self-oscillation phenomena, especially at low temperatures. Finally, we hope to implement our measurement scheme completely on a chip using electrical readout to create a compact, robust, and highly sensitive nanomechanical platform for spectroscopic characterization of 2D materials.

■ ASSOCIATED CONTENT

Supporting Information

The Supporting Information is available free of charge at https://pubs.acs.org/doi/10.1021/acs.nanolett.2c01289.

Details of the FEM-simulations, AFM force indentation measurements, overview of measured samples, details on interferometric motion detection, discussion on dynamical back-action effects, springs in parallel model (derivation of eq 1), optical transmission measurements, details on reflection measurements, obtaining the dielectric function for thin films, RPA and BSE calculations, measuring the Allan deviation, calculating the sensitivity, and details on the photoluminescence measurements (PDF)

■ AUTHOR INFORMATION

Corresponding Authors

Jan N. Kirchhof − *Department of Physics, Freie Universität Berlin, 14195 Berlin, Germany;* orcid.org/0000-0001-8576-4787; Email: jan.kirchhof@fu-berlin.de

Kirill I. Bolotin − *Department of Physics, Freie Universität Berlin, 14195 Berlin, Germany*; Email: kirill.bolotin@fu-berlin.de

Authors

Yuefeng Yu − *Department of Physics, Freie Universität Berlin, 14195 Berlin, Germany*

Gabriel Antheaume − *Department of Physics, Freie Universität Berlin, 14195 Berlin, Germany*

Georgy Gordeev − *Department of Physics, Freie Universität Berlin, 14195 Berlin, Germany; Department of Physics and Materials Science, University of Luxembourg, 4422 Belvaux, Luxembourg;* orcid.org/0000-0002-3273-2105

Denis Yagodkin − *Department of Physics, Freie Universität Berlin, 14195 Berlin, Germany;* orcid.org/0000-0002-9135-8918

Peter Elliott − *Max-Born Institute for Nonlinear Optics and Short Pulse Spectroscopy, 12489 Berlin, Germany;* orcid.org/0000-0002-1572-3872

Daniel B. de Araújo − *Department of Physics, Freie Universität Berlin, 14195 Berlin, Germany;* orcid.org/0000-0001-5216-6035

https://doi.org/10.1021/acs.nanolett.2c01289
Nano Lett. 2022, 22, 8037−8044

Sangeeta Sharma − *Max-Born Institute for Nonlinear Optics and Short Pulse Spectroscopy, 12489 Berlin, Germany*
Stephanie Reich − *Department of Physics, Freie Universität Berlin, 14195 Berlin, Germany;* orcid.org/0000-0002-2391-0256

Complete contact information is available at: https://pubs.acs.org/10.1021/acs.nanolett.2c01289

Notes

The authors declare no competing financial interest.

■ ACKNOWLEDGMENTS

This work was supported by Deutsche Forschungsgemeinschaft (DFG, German Research Foundation, Project ID 449506295 and 328545488), CRC/TRR 227 (Project B08 and A04), ERC Starting Grant No. 639739, and CSC 202006150013.

■ REFERENCES

(1) Liu, H. L.; Shen, C. C.; Su, S. H.; Hsu, C. L.; Li, M. Y.; Li, L. J. Optical Properties of Monolayer Transition Metal Dichalcogenides Probed by Spectroscopic Ellipsometry. *Appl. Phys. Lett.* **2014**, *105* (20), 201905.
(2) Li, W.; Birdwell, A. G.; Amani, M.; Burke, R. A.; Ling, X.; Lee, Y. H.; Liang, X.; Peng, L.; Richter, C. A.; Kong, J.; Gundlach, D. J.; Nguyen, N. V. Broadband Optical Properties of Large-Area Monolayer CVD Molybdenum Disulfide. *Phys. Rev. B - Condens. Matter Mater. Phys.* **2014**, *90* (19), 195434.
(3) Yim, C.; O'Brien, M.; McEvoy, N.; Winters, S.; Mirza, I.; Lunney, J. G.; Duesberg, G. S. Investigation of the Optical Properties of MoS2 Thin Films Using Spectroscopic Ellipsometry. *Appl. Phys. Lett.* **2014**, *104* (10), 103114.
(4) Shen, C. C.; Hsu, Y. Te; Li, L. J.; Liu, H. L. Charge Dynamics and Electronic Structures of Monolayer MoS2 Films Grown by Chemical Vapor Deposition. *Appl. Phys. Express* **2013**, *6* (12), 125801.
(5) Hecht, E.*Optics*, 4th ed.; Addison-Wesley, San Francisco, CA, 2002; pp 426−428.
(6) Li, Y.; Chernikov, A.; Zhang, X.; Rigosi, A.; Hill, H. M.; Van Der Zande, A. M.; Chenet, D. A.; Shih, E. M.; Hone, J.; Heinz, T. F. Measurement of the Optical Dielectric Function of Monolayer Transition-Metal Dichalcogenides: MoS2, Mo S E2, WS2, and WS E2. *Phys. Rev. B - Condens. Matter Mater. Phys.* **2014**, *90* (20), 205422.
(7) de L. Kronig, R. On the Theory of Dispersion of X-Rays. *J. Opt. Soc. Am.* **1926**, *12* (6), 547.
(8) Kramers, H. A.The Quantum Theory of Dispersion. *Nature*; Nature Publishing Group, 1924; pp 310−311.
(9) Kuzmenko, A. B. Kramers−Kronig Constrained Variational Analysis of Optical Spectra. *Rev. Sci. Instrum.* **2005**, *76* (8), 083108.
(10) Ma, L.; Nguyen, P. X.; Wang, Z.; Zeng, Y.; Watanabe, K.; Taniguchi, T.; MacDonald, A. H.; Mak, K. F.; Shan, J. Strongly Correlated Excitonic Insulator in Atomic Double Layers. *Nature* **2021**, *598* (7882), 585−589.
(11) Zhou, Y.; Sung, J.; Brutschea, E.; Esterlis, I.; Wang, Y.; Scuri, G.; Gelly, R. J.; Heo, H.; Taniguchi, T.; Watanabe, K.; Zaránd, G.; Lukin, M. D.; Kim, P.; Demler, E.; Park, H. Bilayer Wigner Crystals in a Transition Metal Dichalcogenide Heterostructure. *Nature* **2021**, *595* (7865), 48−52.
(12) Zarenia, M.; Neilson, D.; Partoens, B.; Peeters, F. M. Wigner Crystallization in Transition Metal Dichalcogenides: A New Approach to Correlation Energy. *Phys. Rev. B* **2017**, *95* (11), 115438.
(13) Wang, Z.; Rhodes, D. A.; Watanabe, K.; Taniguchi, T.; Hone, J. C.; Shan, J.; Mak, K. F. Evidence of High-Temperature Exciton Condensation in Two-Dimensional Atomic Double Layers. *Nature* **2019**, *574* (7776), 76−80.
(14) Tartakovskii, A. Excitons in 2D Heterostructures. *Nature Reviews Physics* **2020**, *2*, 8−9.
(15) Novoselov, K. S.; Mishchenko, A.; Carvalho, A.; Castro Neto, A. H. 2D Materials and van Der Waals Heterostructures. *Science* **2016**, *353* (6298), na.
(16) Stier, A. V.; Wilson, N. P.; Velizhanin, K. A.; Kono, J.; Xu, X.; Crooker, S. A. Magnetooptics of Exciton Rydberg States in a Monolayer Semiconductor. *Phys. Rev. Lett.* **2018**, *120* (5), 057405.
(17) Noori, Y. J.; Cao, Y.; Roberts, J.; Woodhead, C.; Bernardo-Gavito, R.; Tovee, P.; Young, R. J. Photonic Crystals for Enhanced Light Extraction from 2D Materials. *ACS Photonics* **2016**, *3* (12), 2515−2520.
(18) Zhang, L.; Gogna, R.; Burg, W.; Tutuc, E.; Deng, H. Photonic-Crystal Exciton-Polaritons in Monolayer Semiconductors. *Nat. Commun.* **2018**, *9* (1), 713.
(19) Kirchhof, J. N.; Weinel, K.; Heeg, S.; Deinhart, V.; Kovalchuk, S.; Höflich, K.; Bolotin, K. I. Tunable Graphene Phononic Crystal. *Nano Lett.* **2021**, *21* (5), 2174−2182.
(20) Barnes, J. R.; Stephenson, R. J.; Welland, M. E.; Gerber, C.; Gimzewski, J. K. Photothermal Spectroscopy with Femtojoule Sensitivity Using a Micromechanical Device. *Nature* **1994**, *372* (6501), 79−81.
(21) Casci Ceccacci, A.; Cagliani, A.; Marizza, P.; Schmid, S.; Boisen, A. Thin Film Analysis by Nanomechanical Infrared Spectroscopy. *ACS Omega* **2019**, *4* (4), 7628−7635.
(22) Invisible-Light Labs. https://www.invisible-light-labs.com/ (accessed Aug 24, 2022).
(23) Chien, M. H.; Brameshuber, M.; Rossboth, B. K.; Schütz, G. J.; Schmid, S. Single-Molecule Optical Absorption Imaging by Nanomechanical Photothermal Sensing. *Proc. Natl. Acad. Sci. U. S. A.* **2018**, *115* (44), 11150−11155.
(24) Singh, R.; Nicholl, R. J. T.; Bolotin, K. I.; Ghosh, S. Motion Transduction with Thermo-Mechanically Squeezed Graphene Resonator Modes. *Nano Lett.* **2018**, *18* (11), 6719−6724.
(25) Schwarz, C.; Pigeau, B.; Mercier De Lépinay, L.; Kuhn, A. G.; Kalita, D.; Bendiab, N.; Marty, L.; Bouchiat, V.; Arcizet, O. Deviation from the Normal Mode Expansion in a Coupled Graphene-Nanomechanical System. *Phys. Rev. Appl.* **2016**, *6* (6), 064021.
(26) Verbiest, G. J.; Kirchhof, J. N.; Sonntag, J.; Goldsche, M.; Khodkov, T.; Stampfer, C. Detecting Ultrasound Vibrations with Graphene Resonators. *Nano Lett.* **2018**, *18* (8), 5132−5137.
(27) Lee, J.; Wang, Z.; He, K.; Shan, J.; Feng, P. X. L. High Frequency MoS2 Nanomechanical Resonators. *ACS Nano* **2013**, *7* (7), 6086−6091.
(28) Ye, F.; Islam, A.; Zhang, T.; Feng, P. X.-L. Ultrawide Frequency Tuning of Atomic Layer van Der Waals Heterostructure Electromechanical Resonators. *Nano Lett.* **2021**, *21* (13), 5508−5515.
(29) Dolleman, R. J.; Lloyd, D.; Lee, M.; Scott Bunch, J.; Van Der Zant, H. S. J.; Steeneken, P. G. Transient Thermal Characterization of Suspended Monolayer MoS_2. *Phys. Rev. Mater.* **2018**, *2* (11), 114008.
(30) Nicholl, R. J. T.; Conley, H. J.; Lavrik, N. V.; Vlassiouk, I.; Puzyrev, Y. S.; Sreenivas, V. P.; Pantelides, S. T.; Bolotin, K. I. The Effect of Intrinsic Crumpling on the Mechanics of Free-Standing Graphene. *Nat. Commun.* **2015**, *6*, 8789.
(31) Dolleman, R. J.; Houri, S.; Davidovikj, D.; Cartamil-Bueno, S. J.; Blanter, Y. M.; Van Der Zant, H. S. J.; Steeneken, P. G. Optomechanics for Thermal Characterization of Suspended Graphene. *Phys. Rev. B* **2017**, *96* (16), 165421.
(32) Aslan, B.; Yule, C.; Yu, Y.; Lee, Y. J.; Heinz, T. F.; Cao, L.; Brongersma, M. L. Excitons in Strained and Suspended Monolayer WSe 2. *2D Mater.* **2022**, *9* (1), 015002.
(33) Aslan, O. B.; Deng, M.; Heinz, T. F. Strain Tuning of Excitons in Monolayer WSe2. *Phys. Rev. B* **2018**, *98* (11), 115308.
(34) Zhao, W.; Ghorannevis, Z.; Chu, L.; Toh, M.; Kloc, C.; Tan, P. H.; Eda, G. Evolution of Electronic Structure in Atomically Thin Sheets of Ws 2 and Wse2. *ACS Nano* **2013**, *7* (1), 791−797.
(35) Splendiani, A.; Sun, L.; Zhang, Y.; Li, T.; Kim, J.; Chim, C. Y.; Galli, G.; Wang, F. Emerging Photoluminescence in Monolayer MoS2. *Nano Lett.* **2010**, *10* (4), 1271−1275.
(36) Castellanos-Gomez, A.; Quereda, J.; Van Der Meulen, H. P.; Agraït, N.; Rubio-Bollinger, G. Spatially Resolved Optical Absorption

Spectroscopy of Single- and Few-Layer MoS2 by Hyperspectral Imaging. *Nanotechnology* **2016**, *27* (11), 115705.
(37) Barton, R. A.; Storch, I. R.; Adiga, V. P.; Sakakibara, R.; Cipriany, B. R.; Ilic, B.; Wang, S. P.; Ong, P.; McEuen, P. L.; Parpia, J. M.; Craighead, H. G. Photothermal Self-Oscillation and Laser Cooling of Graphene Optomechanical Systems. *Nano Lett.* **2012**, *12* (9), 4681−4686.
(38) Xie, H.; Jiang, S.; Rhodes, D. A.; Hone, J. C.; Shan, J.; Mak, K. F. Tunable Exciton-Optomechanical Coupling in Suspended Monolayer MoSe2. *Nano Lett.* **2021**, *21* (6), 2538−2543.
(39) Allan, D. W. Statistics of Atomic Frequency Standards. *Proc. IEEE* **1966**, *54* (2), 221−230.
(40) Bolduc, M.; Terroux, M.; Tremblay, B.; Marchese, L.; Savard, E.; Doucet, M.; Oulachgar, H.; Alain, C.; Jerominek, H.; Bergeron, A. Noise-Equivalent Power Characterization of an Uncooled Microbolometer-Based THz Imaging Camera. *Terahertz Physics, Devices, Syst. V Adv. Appl. Ind. Def.* **2011**, *8023*, 80230C.
(41) Yang, H. H.; Rebeiz, G. M. Sub-10-PW/Hz0.5 Uncooled Micro-Bolometer with a Vacuum Micro-Package. *IEEE Trans. Microw. Theory Technol.* **2016**, *64* (7), 2129−2136.
(42) Abdel-Rahman, M.; Al-Khalli, N.; Zia, M. F.; Alduraibi, M.; Ilahi, B.; Awad, E.; Debbar, N.Fabrication and Design of Vanadium Oxide Microbolometer. In *AIP Conference Proceedings*; 2017; Vol. *1809*, p 20001.
(43) Blaikie, A.; Miller, D.; Alemán, B. J. A Fast and Sensitive Room-Temperature Graphene Nanomechanical Bolometer. *Nat. Commun.* **2019**, *10* (1), 1−8.
(44) Ghadimi, A. H.; Fedorov, S. A.; Engelsen, N. J.; Bereyhi, M. J.; Schilling, R.; Wilson, D. J.; Kippenberg, T. J. Elastic Strain Engineering for Ultralow Mechanical Dissipation. *Science (80-.)* **2018**, *360* (6390), 764−768.
(45) Malekpour, H.; Ramnani, P.; Srinivasan, S.; Balasubramanian, G.; Nika, D. L.; Mulchandani, A.; Lake, R. K.; Balandin, A. A. Thermal Conductivity of Graphene with Defects Induced by Electron Beam Irradiation. *Nanoscale* **2016**, *8* (30), 14608−14616.
(46) Yan, Z.; Yoon, M.; Kumar, S. Influence of Defects and Doping on Phonon Transport Properties of Monolayer $MoSe_2$. *2D Mater.* **2018**, *5* (3), 031008.

https://doi.org/10.1021/acs.nanolett.2c01289
Nano Lett. 2022, 22, 8037−8044

Supplementary Information: Nanomechanical Spectroscopy of 2D Materials

Jan N. Kirchhof[1], Yuefeng Yu[1], Gabriel Antheaume[1], Georgy Gordeev[1,2], Denis Yagodkin[1], Peter Elliott[3], Daniel B. de Araújo[1], Sangeeta Sharma[3], Stephanie Reich[1] and Kirill I. Bolotin[1*]*

[1] Department of Physics, Freie Universität Berlin, Arnimallee 14, 14195 Berlin, Germany

[2] Department of Physics and Materials Science, University of Luxembourg, 41 Rue du Brill, 4422 Belvaux, Luxembourg

[3] Max-Born Institute for Nonlinear Optics and Short Pulse Spectroscopy,

Max-Born-Strasse 2A, 12489 Berlin Germany

*jan.kirchhof@fu-berlin.de *kirill.bolotin@fu-berlin.de

1. Finite element method (FEM) simulations

For the FEM modelling we use the structural mechanics module of COMSOL Multiphysics Version 5.5. We build a model around the suspended area partially including the silicon support (Fig. S1a) and use a swept mesh for the thin layers with high density around for TMD flake and SiN window (Fig. S1b). To determine the resonance frequency and mode shape (Fig. S1c) we conduct a prestressed eigenfrequency study. To include the effect of laser heating, we add a study step to implement a Gaussian heat source (Fig. S1d, 30.4% absorption and 30 μW laser power – comp. Fig. 3a main paper) and calculate the heat profile upon laser heating of the center of the suspended TMD (Fig. S1e). This allows us to determine the conversion factor, which captures the tuning of the fundamental mode with laser power, following Eq. 1 from the main paper. The conversion factor slightly depends on wavelength of the heating laser because the laser spot size varies with wavelength, what results in a slightly different heat profile in the suspended TMD. To account for this, we measure the spot size of heating laser at different wavelengths and use this as input for our simulations. In Fig. S1f we plot the conversion factor for device #1 (3L WSe_2). For device #2 (4L MoS_2), we obtain a conversion factor in the range of 461 to 476 Hz/μW showing comparable scaling with wavelength as device #1. The difference between devices here is due to different thermal conductivities, hole sizes and layer thickness between devices.

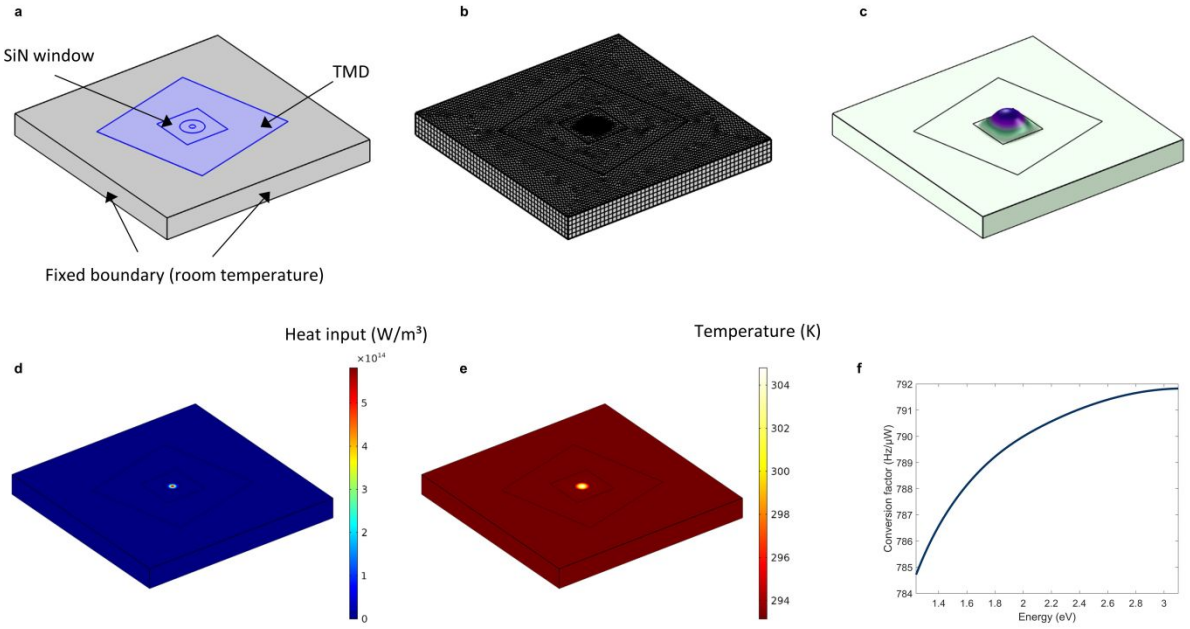

Figure S1 FEM simulations of SiN-TMD hybrid devices a) Model geometry with a thin layer of TMD (blue) placed on the SiN window **b)** Corresponding mesh, all thin layers are meshed as swept layers with high density **c)** Simulated fundamental mode of the hybrid system **d)** Heat input in the shape of a gaussian beam to simulate the effect of laser heating **e)** Resulting heat profile upon 30 μW incident laser power and 30.4 % absorption (corresponds to a photon energy of 2.92 eV for the 3L WSe_2 sample) **f)** Obtained conversion factor for Device #1 (3L WSe_2).

In order to optimize the dimensions of the SiN window, we simulate the driven mechanical resonances in the frequency domain. We start by simulating a circular TMD-only drum resonator (diameter 10 μm) as reference and adjust the isotropic damping to match the experimental Q for such resonators (~100). We then simulate the entire hybrid device (including SiN and gold). In Fig. S2a we plot the simulated displacement vs. frequency for the hybrid device probed on the SiN area, 2 μm away from the suspended TMD area. Again, we adjust the isotropic damping in SiN and gold to match experimental values. We now vary the SiN window size and extract the amplitude of motion at constant drive (signal strength, plotted in Fig. S2b). As expected, larger devices oscillate at large amplitudes providing more signal. Nevertheless, while oscillating at a higher amplitude, larger devices are less responsive to heating. Indeed, in Fig. S2c we plot the relative responsivity (change of resonance frequency for a constant laser heating) vs. window size. Combining the insights from Fig. S2b,c we choose a window size of 20 μm as a reasonable compromise between high vibrational amplitude and high responsivity.

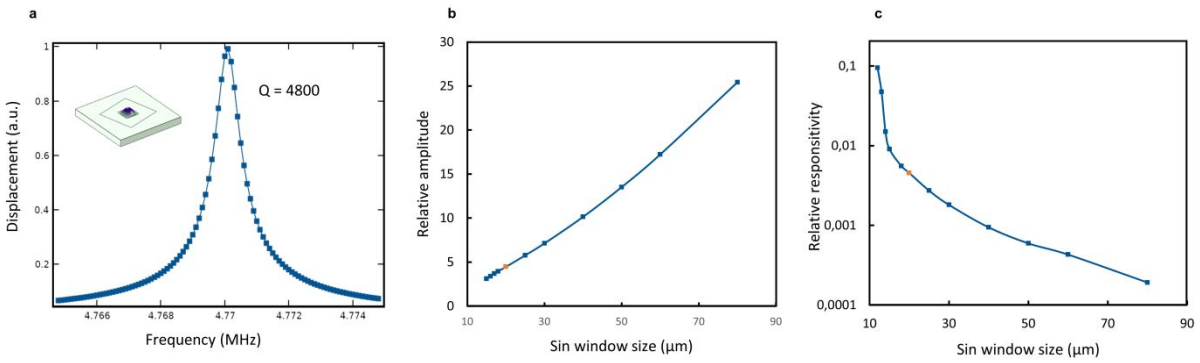

Figure S2 Finding ideal device parameters a) Simulated mechanical motion of the hydride with Q matching experimental results **b)** Simulated amplitude (signal strength) vs. SiN window size **b)** Relative responsivity to laser heating vs. SiN window size. We choose a window size of 20 µm (orange spot) as a compromise between high responsivity and sufficient amplitude amplification

All material properties used in our simulations are summarized in table 1. For quantities that show a large spread in the literature values (values for the TMD materials in particular) we used average values. In general, we preferably choose experimental references for suspended samples of the suitable layer thickness.

Material	Quantity	Value	Reference
MoS_2	Young's modulus E	330 GPa	[1] In agreement with AFM force-indentation measurements (see below)
	Poisson's ratio ν	0.125	[1]
	Densityρ	5060 kg/m³	[2]
	Thermal conductivity κ	60.3 W/(m·K)	[3–6]
	Thermal expansion coefficient α	$7.6 \cdot 10^{-6}$ 1/K	[7] [8]
	Heat capacity at constant pressure c_p	397 J/(kg·K))	[9,10]
	Built-in stress (tension) σ_0	44.7 MPa (σ_{2D} = 0.11 N/m)	Force-indetantion AFM
	Layer thickness d	0.615 nm	[11]

WSe_2	Young's modulus E	167.3 GPa	[12] In agreement with AFM force-indentation measurements (see below)
	Poisson's ratio ν	0.19	[13]
	Densityρ	9320 kg/m³	[14]
	Thermal conductivity κ	26.5 W/(m·K)	[15]
	Thermal expansion coefficient α	$7 \cdot 10^{-6}$ 1/K	[7]
	Heat capacity at constant pressure c_p	188 J/(kg·K)	[9]
	Built-in stress (tension) σ_0	46.2 MPa (σ_{2D} = 0.09 N/m)	AFM force indentation
	Layer thickness d	0.651 nm	[11]
Au	Young's modulus E	78.5 GPa	[16]
	Poisson's ratio ν	0.42	[16]
	Density ρ	19300 kg/m³	[16]
	Thermal conductivity κ	312 W/(m·K)	[16]
	Thermal expansion coefficient α	$14 \cdot 10^{-6}$ 1/K	[16]
	Heat capacity at constant pressure c_p	130 J/(kg·K)	[16]
	Built-in stress	160 MPa	[17]
SiN	Young's modulus E	232 GPa	[18]
	Poisson's ratio ν	0.23	[18]
	Densityρ	2810 kg/m³	[19]
	Thermal conductivity κ	31 W/(m·K)	[18]
	Thermal expansion coefficient α	$2.55 \cdot 10^{-6}$ 1/K	[18]
	Heat capacity at constant pressure c_p	887 J/(kg·K)	[18]
	Built-in stress	240 MPa	Norcada (manufacturer)

Si	Young's modulus E	160 GPa	[20]
	Poisson's ratio ν	0.27	[20]
	Density ρ	2330 kg/m³	[20]
	Thermal conductivity κ	160 W/(m·K)	[20]
	Thermal expansion coefficient α	$3 \cdot 10^{-6}$ 1/K	[20]
	Heat capacity at constant pressure c_p	692 J/(kg·K)	[20]
	Pretension	0	Irrelevant for simulations

2. AFM force indentation

One crucial parameter, which is known to vary from device to device is the built-in tension and 2D elastic modulus. To eliminate this uncertainty in our simulations, we perform force indentation measurements in the centre of the membrane (following Ref. [21]) and extract the built-in tension and 2D elastic modulus for each sample. We use cantilevers of intermediate stiffness (k~3 N/m) and only apply small loads (150 nN) to avoid damaging the sample. In Fig. S3a we show a force-displacement-curve for device #1. We account for cantilever bending and deformation of the SiN membrane. We fit a curve following:

$$F = \pi\sigma_{2D}d + q^3\frac{E_{2D}}{a^2}d^3 \qquad \text{(S1)}$$

Here a is the radius of the drum, and $q = \frac{1}{1.05 - 0.15\nu - 0.16\nu^2}$ is a dimensional factor dependent on the Poisson's ratio ν ($q = 0.98$ for WSe_2 and $q = 0.97$ for MoS_2). For a range of samples, we find a linear dependence on tension with layer thickness (Fig. S3b). We attribute the observed homogeneity to the cleanliness and uniformity in our samples after annealing (comp. Fig. S4).

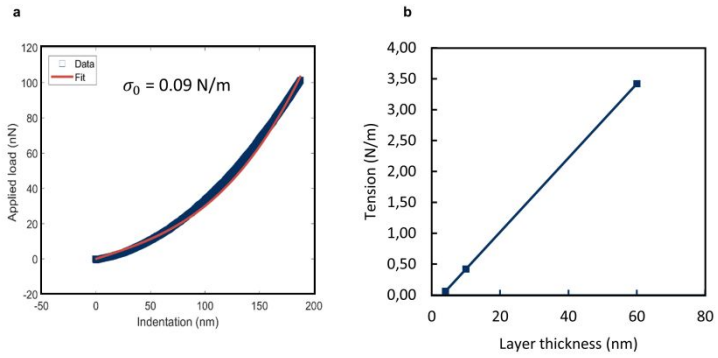

Figure S3 AFM force indentation to determine pre-tension. a) Force vs. displacement as well as a fit to Eq. S1. We extract a pretension of roughly 0.1 N/m for most our devices **b)** Statistics on pre-tension vs. thickness. We find a linear relation between pre-tension and layer thickness in our devices.

3. Sample fabrication and overview

To fabricate our hybrid devices, we transfer TMDs onto a circular hole using the all-dry PDMS method.[22] The SiN chip is beforehand covered with a thin layer of gold (30 nm) to electrically contact the TMD and to increase its reflectivity. After transfer we perform an annealing step (3 h, 200 °C) in vacuum to remove residues and assure good adhesion to the substrate. We fabricate and measure multiple samples. Microscope images and AFM topography scans for device #1-3 are shown in Fig. S4a,b,d,e,g,h. For all samples (Fig. S4c,f,i), we find a high Q fundamental mode of almost constant (except device #3, which has a thicker gold layer). There are some variations in frequency, because the hole size and gold thickness are different for the devices. Our simulations (grey dashed lines) describe the measured frequencies well (Fig. S4c,f,i).

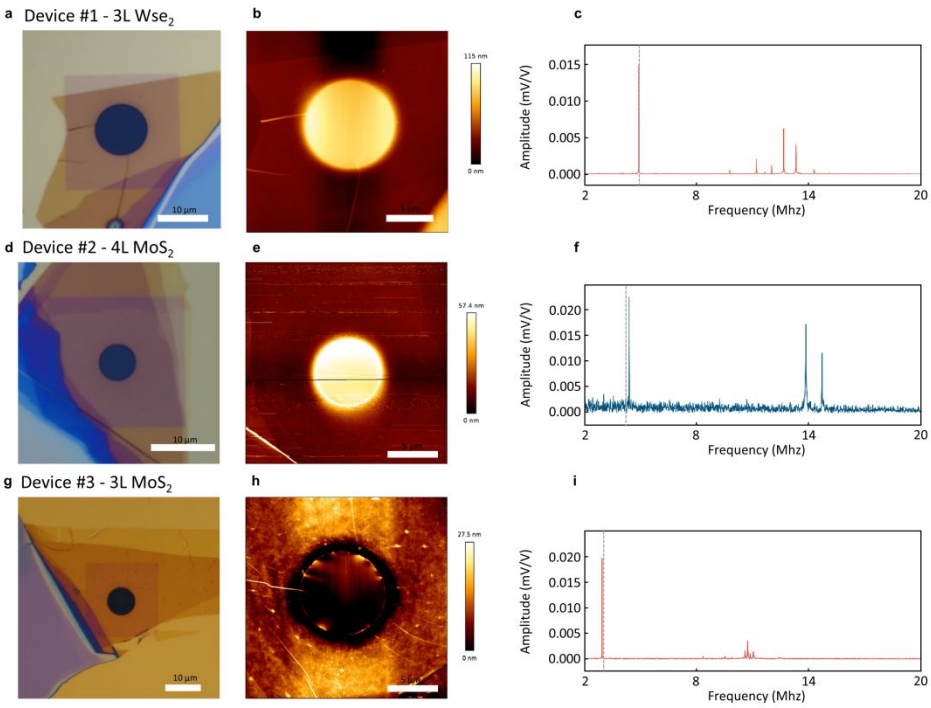

Figure S4 Sample overview. Microscope images **(a,d,g)** and AFM topography **(b,e,h)** of device #1-3. The samples are uniform and well attached to the substrate **c,f,i)** Displacement (amplitude) vs. frequency for device #1-3. We find a dominant high-Q fundamental mode for all samples. The resonance frequencies match with simulated values (grey dashed lines).

4. Details on interferometric motion detection

The sample is placed upside down in a vacuum chamber of $< 10^{-5}$ mbar. By applying a DC+AC voltage relative to the non-reflective gate electrode, we mechanically actuate the suspended area of the chip. The motion of the TMD is detected by a Michelson interferometer. We focus a 632.8 nm HeNe laser (<1 µW, ~1.5 µm spot size) on the SiN area of the sample and the reflected light is superimposed with the light coming from the reference arm and guided into an avalanche photodetector. The resulting interference signal is highly sensitive to relative displacements and allows us to detect the motion of suspended samples. We actively stabilize the relative position of the reference arm via a mirror on a piezo and thereby ensure constant interference conditions and good signal strength over a large period of time. In addition to the probe laser, we implement an excitation laser of tunable colour (1.2 – 3.1 eV, blue in Fig. 1c). We use a band pass filter (BP) to block the excitation laser from reaching the detector and overloading it. The large separation (40 µm) of the non-reflective gate and sample negates all

cavity-related optomechanical backaction effects and allows us to measure purely static heating effects in our sample over a very large range of photon energies.

The interferometric setup is shown in detail in Fig. S5a. Along the beam path of the probe laser, we first implement an optical isolator to avoid back reflected light into the laser, which can cause instabilities and power fluctuations. The beam is then expanded to completely fill the objective (40x 0.6NA). In a first beam splitter we add light from the excitation laser and in a second beam splitter, we guide half the light towards the reference arm and half through the objective onto the sample in a vacuum chamber. The relative position of the reference arm to the sample determines the amplitude of the interferometric signal. We use a piezo electric element to control this distance and stabilize the system using a PID-loop locked to a small reference signal at 941 Hz sourced by Lock-In amplifier (Zurich Instruments MLFI). The sample in the vacuum chamber is clamped upside down onto our sample holder and with a spacing of roughly 40 µm, we place our grounded gate electrode. Electrical driving is realized by mixing a DC voltage (210 V, supplied by a Keithley source meter) with an AC component (typically -5 dBm) from our vector network analyzer (VNA, Agilent E5071C) in a high voltage Bias T (Particulars BT-01) and applying it to the gold layer of the sample, which contacts the TMD flake. For smaller frequency ranges and phase-locked-loop (PLL) measurement, we use a lock-in amplifier (Zurich Instruments MFLI). In Fig. S5b we show the power spectra of our excitation laser source (measured at the sample position) with different neutral density filters (ND) implemented, which are used to calculate the relative frequency shifts $\frac{\Delta f}{\Delta P}$. We perform a small linear correction (order of Hz) to account for temperature changes in the room during measurements of the maps (Fig. 2 a,c). In the PLL-configuration (25 kHz bandwidth) we can measure the heating induced frequency shifts Δf quickly and with high sensitivity even at low laser powers (raw data for ND 1.5 in Fig. S5c).

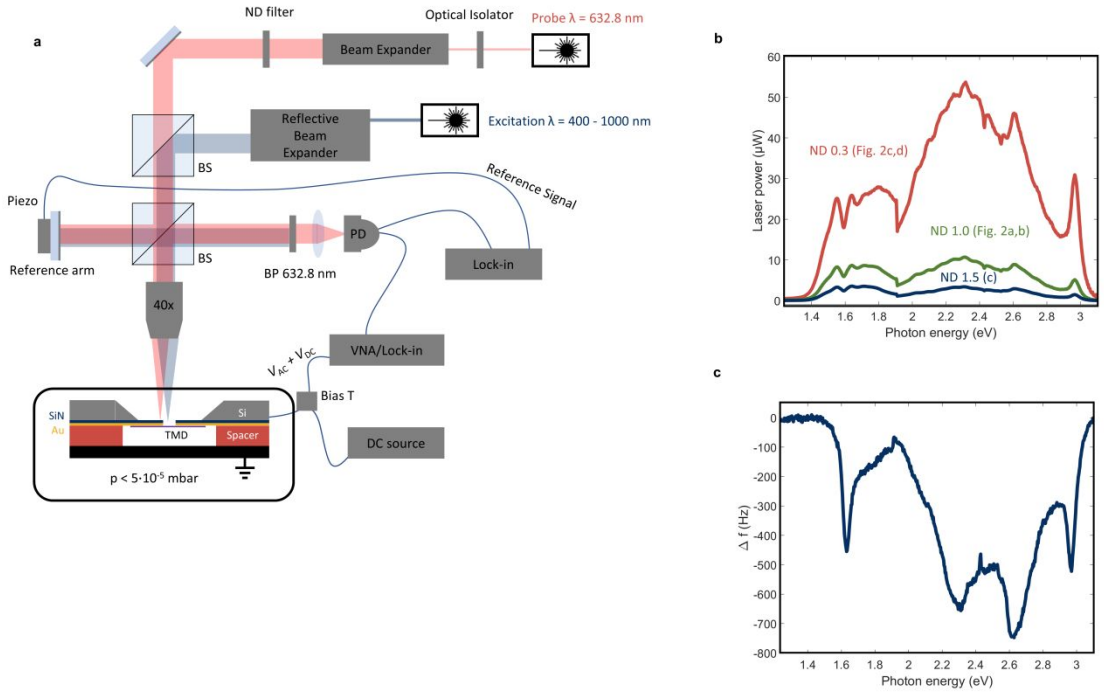

Figure S5 Setup details and PLL-data a) Detailed sketch of setup and **b)** Measured output of the tunable excitation laser at the sample position vs. wavelength. This data is used to normalize the frequency shift. **c)** PLL measurements of device #1, using the laser power plotted in **b)**.

5. Consideration of dynamical back-action effects

In nanomechanical resonators also dynamic optomechanical back-action (in contrast to static heating) effects can alter the resonance frequency (f) and its FWHM (f_{FWHM}) especially at large laser powers.[23–25] This occurs e.g. in cavity interferometers, where the laser power, which the oscillating membrane is exposed to, varies significantly over a short spatial distance.[23,24] For this a reflective surface close to the moving membrane is needed.[23,24] The effects furthermore only occur when the spatial symmetry is broken due to deforming the membrane out of plane.[23,24] In our system the gate is non-reflective and far away from the membrane (~ 40 µm). Additionally, the applied electrostatic pressure by the gate voltage is relatively small and SiN-TMD hybrid system rather stiff, so there is no breaking of symmetry in out of plane direction. Considering all the points above, we can exclude cavity related back-action effects in our system.

Also, strain-induced shifts in absorption in the material itself can cause dynamic back-action effects.[25] Here again a breaking of symmetry, large laser powers and soft systems (small spring constant) are needed. We therefore also exclude material related back-action effects.

To verify this experimentally we extract f_{FWHM}, whilst illuminating the sample at different wavelengths (Fig. S6a,b). If there were any dynamic back-action effects influencing the system, the f_{FWHM} should show significant variations.[23–25] We do not observe such variations and thereby experimentally confirm the absence of dynamic back-action effects.

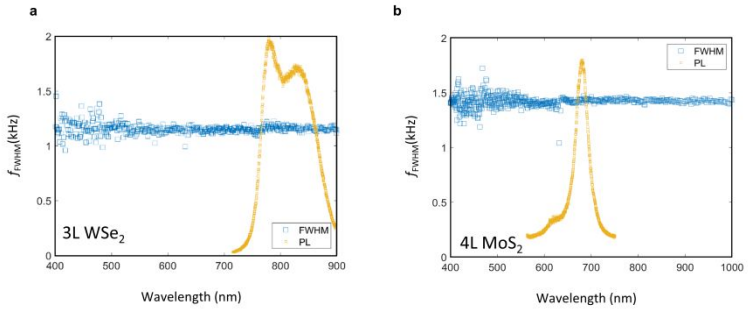

Figure S6 Reference measurements check for dynamic back-action effects. a,b) FWHM vs. wavelength for device #1 (WSe_2) and #2 (MoS_2) and photoluminescence measurements as reference for the excitonic resonances. We observe a constant FWHM over the entire wavelength range and thereby experimentally exclude dynamic optomechanical back action effects.

6. Springs in parallel model (derivation of Eq.1)

The goal of equation 1 from the main text is to intuitively relate the heating-induced change of the overall resonance frequency of our resonator to tension/frequency changes of its components, i.e. the TMD alone and the SiN alone. That expression is important for developing a qualitative understanding of our system, whilst we use FEM simulations to capture the complex device geometry for all quantitative evaluations and results shown in the main text. We express frequencies (f) and frequency changes (Δf) of each resonator upon illumination/heating via effective spring constants defined as $k = 4\pi^2 f^2 m_{eff}$, where m_{eff} is the numerically determined effective mass[4] (see Fig. S7). So, the question we would like to answer: is there a simple expression relating effective spring constants of the SiN (k_{SiN}), the TMD (k_{SiN}), and the compound system (k_{total})?

As a first step towards obtaining a simple model, we numerically obtain the frequency and frequency changes upon illumination (power 30 μW; 30.4 % absorption) of our 3 resonators using detailed FEM-simulations of the experimental geometry (see Fig. S7 a-c). From the resonance frequencies and effective masses, we find: $k_{TMD} \approx$ 0.52 N/m, $k_{SiN} \approx$ 50.43 N/m and $k_{total} =$ 65.48 N/m. For the heating-induced frequency changes upon laser illumination with 30 μW laser power and 30.4% absorption (corresponds to the measurement in Fig. 3a @ 2.92 eV), we find: $\Delta k_{TMD} \approx -0.16\frac{N}{m}$, $\Delta k_{SiN} \approx -0.01\frac{N}{m}$ and $\Delta k_{total} \approx -0.20\frac{N}{m}$. These simulations match experiments: from the experimentally measured heating-induced frequency shift, we extract:

$$\Delta k_{\text{total}}^{\text{Exp}} = -k_{\text{total}}^{\text{Exp}}\left(1 - \frac{(f-\Delta f)^2}{f_0^2}\right) = -64.45\frac{\text{N}}{\text{m}}(1 - 0.9970) \approx -0.19\ \text{N/m}$$

$(\text{with } f_0 =$ 4.67 MHz; $\Delta f =$ 7.2 kHz$)$. Moreover, Δk_{total} linearly depends on Δk_{TMD}. We see that our numerical results can be described with reasonable precision by a simple formula, $k_{total}=k_{TMD}+k_{SiN}$. This formula corresponds to effective springs of the TMD and the SiN connected "in parallel". In fact, this expression can be derived analytically in a 1D toy model of the combined TMD/SiN resonator (see Fig. S7d). We start by assuming that the hole in the SiN does not affect the effective elastic constants of SiN (good approximation when the hole is small) and simplify the membrane profile for ease of estimates (Fig. S7d). In this geometry we can approximate the extension of the central point of the membrane as:

$$\delta x \approx \frac{x^2}{2L} \qquad \text{(S2)}$$

Approximating that both TMD and SiN have the same strain (ϵ), we can now define the potential and kinetic energy as following:

$$E_{pot} = 2\sigma\delta x = 2\epsilon(h_1 E_{2D}^{SiN} + h_2 E_{2D}^{TMD})\delta x = \frac{\epsilon}{L}(h_1 E_{2D}^{SiN} + h_2 E_{2D}^{TMD})x^2 \qquad \text{(S3)}$$

$$E_{kin} = \frac{m(\delta\dot{x})^2}{2} \approx \frac{m(\dot{x})^2}{2} \qquad \text{(S4)}$$

From the conservation of energy, we obtain the angular frequency of the harmonic motion of the combined system:

$$\omega^2 = \frac{2\epsilon(\frac{\epsilon}{L}(h_1 E_{2D}^{SiN} + h_2 E_{2D}^{TMD})}{L m_{eff}} \qquad \text{(S7)}$$

Defining an effective spring constants for the resonator, with $k_{SiN/TMD} = \frac{2\epsilon}{L}(h_{1/2} E_{2D}^{SiN/TMD})$, we see that the resonance frequency of the combined system can be expressed as:

$$f_0 = \frac{1}{2\pi\sqrt{m_{eff}}}\sqrt{k_{SiN} + k_{TMD}} \qquad \text{(S8)}$$

This is exactly the resonance frequency of the resonator with TMD and SiN springs "in parallel".

Next, we will look at changes in frequency ($\Delta f = f(T) - f_0$) caused by laser heating. With the heating laser turned on, light is absorbed, and the TMD resonator heats up and overall softens. The SiN is well heat sunk via the gold layer. Our simulations show that its temperature and stress remain almost constant ($\Delta T \approx 0.03$ K, $\frac{\Delta\sigma}{\sigma_0} \approx 0.02\%$, for 30.4% absorption and 30 μW incident laser power). Therefore, we assume that k_{SiN} is temperature-independent and express the resonances frequency with laser heating as:

$$\Delta f = \frac{1}{2\pi\sqrt{m_{eff}}}\sqrt{k_{SiN} + k_{TMD} - \Delta k_{TMD}} - f_0 \qquad \text{(S9)}$$

We now expand the term to first order for $\frac{\Delta k_{TMD}}{k_{TMD} + k_{SiN}} \ll 1$ and obtain

$$\Delta f = f_0\left(\sqrt{1-\frac{\Delta k_{TMD}}{k_{TMD}+k_{SiN}}}-1\right) \approx f_0\frac{\Delta k_{TMD}}{2(k_{TMD}+k_{SiN})} \quad \text{(S10)}$$

For the "TMD-spring", we can relate the change in spring constant to a change in built-in tension:

$$\frac{\Delta k_{TMD}}{k_{TMD}} = \frac{\Delta\sigma}{\sigma_0} \quad \text{(S11)}$$

The change in tension due to thermal expansion is given by:

$$\Delta\sigma = \frac{\alpha E_{2D}}{1-\nu}\Delta T, \quad \text{(S12)}$$

Where α is the thermal expansion coefficient, E_{2D} is the 2D elastic modulus and ν is the Poisson's ratio of the TMD. The change in temperature ΔT is proportional to the amount of absorbed laser power:

$$\Delta T = \frac{\beta Abs(\lambda)}{h\kappa}\Delta P, \quad \text{(S13)}$$

where κ is the thermal conductivity, h is the thickness of the membrane and β is a pre-factor determined by the temperature profile in the membrane. Combining Eq. S11-13 we obtain Eq. 1 from the main text:

$$\Delta f \approx f_0\frac{k_{TMD}}{2(k_{TMD}+k_{SiN})\sigma_{TMD}}\frac{\alpha E_{2D}\beta Abs(\lambda)}{1-\nu \quad h\kappa}\Delta P \quad \text{(S14)}$$

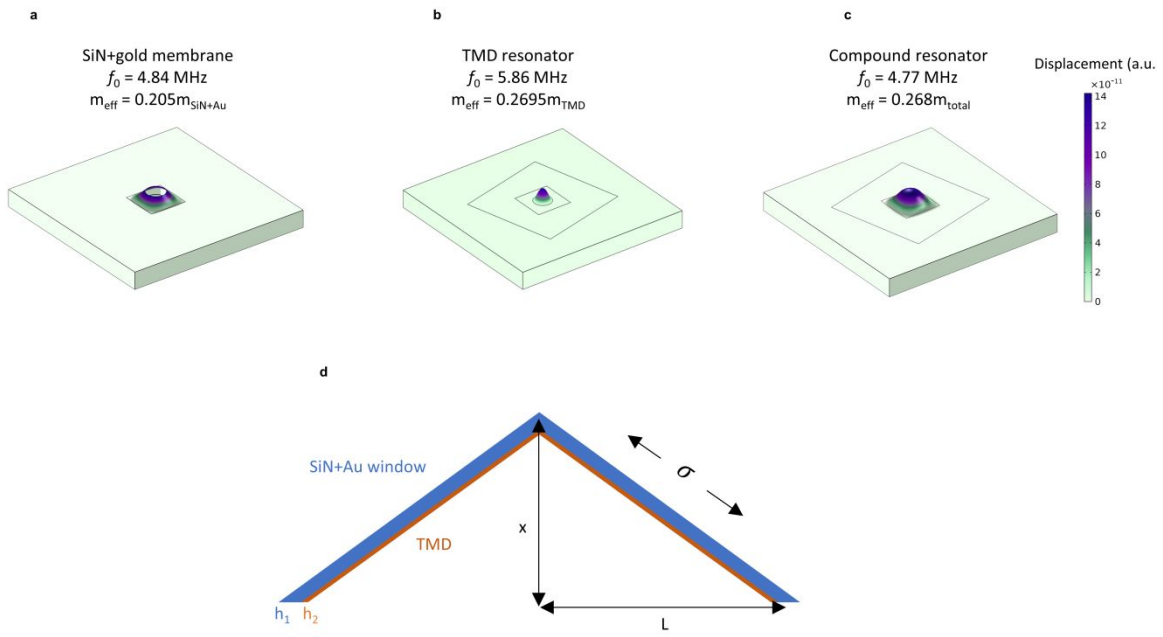

Figure S7 Numerical evaluation of spring constants and springs in parallel model. a-c) Mode shape of the individual resonances of the substrate (SiN+gold), the TMD resonator and the combined system. **d)** Sketch for simplified model describing the springs in parallel.

7. Transmission measurement as benchmark

In order to validate our nanomechanical measurement approach and backup our simulations, we perform optical transmission measurements with an objective below and above the sample (Fig. S8a). We use a broadband white light laser and measure the transmission through the sample (Fig. S8b), deduct the dark counts and normalize to an empty hole without any TMD material to obtain the transmission:

$$T = \frac{T_{sample} - T_{dark}}{T_{hole} - T_{dark}}. \qquad \text{(S11)}$$

To calculate the amount of absorbed light we also measure reflection

$$R = \frac{R_{sample} - R_{hole}}{R_{mirror} - R_{dark}} \qquad \text{(S12)}$$

and use $Abs = 1 - R - T$ to calculate the amount of absorbed light (Fig. S8c). Overall we find very good agreement between this new transmission measurements (blue) and previously obtained data from nanomechanical spectroscopy (red).

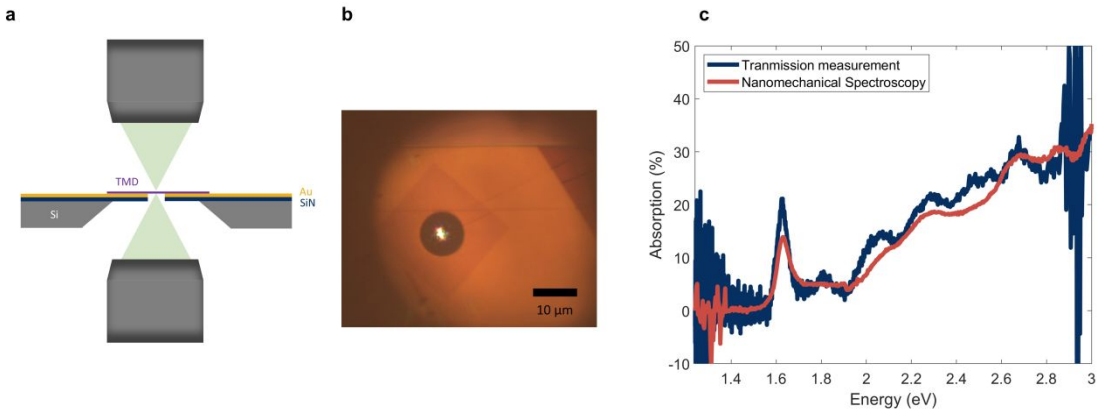

Figure 8. Optical transmission as Benchmark. a, Schematic side view of transmission measurement. **b**, Device #1 from the main paper with a beam from a coherent white light source focused on its center. **c** Comparing nanomechanical spectroscopy to optical transmission measurements. We find very good agreement in the determined absorption of the 2D material.

8. Reflection measurements

The setup presented in the main text also allows us to perform reflection measurements. We block the reference arm, turn off the probe laser and then and use our tunable excitation light source to sweep the wavelength whilst recording the reflected signal off our sample using a chopper (920Hz) and the lock-in amplifier (Fig. S9a, green). We then subtract spectra from that from an empty hole as shown in Fig. S8a (Fig. S9a, blue) and normalize the data by dividing by a "100% reflection reference", which we obtain measuring reflection of a silver mirror (Fig. S9a, red) with known reflection properties (Thorlabs PF10-03-P01). The resulting reflection data is shown in Fig. S9b.

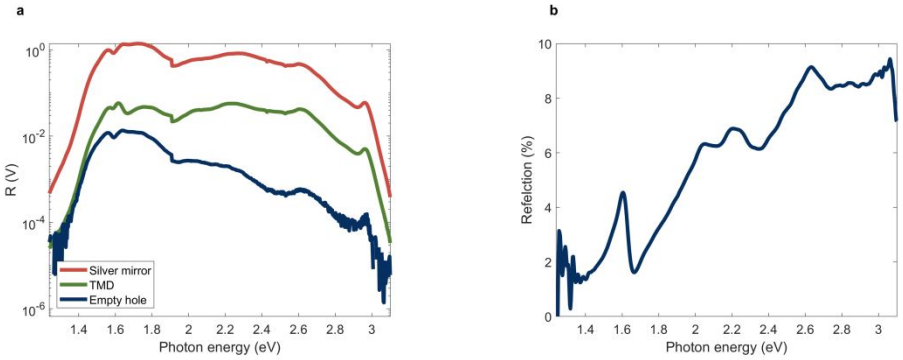

Figure S9 Optical reflection measurements a) Reflection of device #1 (3L WSe_2), a silver mirror, corresponding to our 100% reflection reference and an empty hole **b)** Resulting reflection data for the TMD material.

9. Obtaining the dielectric function

Reflection and transmission of electromagnetic waves was computed with the transfer matrix formalism. Two types of matrices are required: a propagation matrix P and a boundary matrix T. The propagation matrix contains elements responsible for phase change inside a material

$$P(\lambda,n,d) = \begin{pmatrix} e^{2\pi ind/\lambda} & 0 \\ 0 & e^{-2\pi ind/\lambda} \end{pmatrix}, \quad \text{(S13)}$$

where n is complex refractive index of the material, λ wavelength of light, d is the thickness of the material. Whereas the boundary matrix depends on the refractive indices on both sides of the boundary n_1 and n_2:

$$T(n_1,n_2) = \frac{1}{t_{12}} \begin{pmatrix} 1 & r_{12} \\ r_{12} & 1 \end{pmatrix}. \quad \text{(S14)}$$

The $t_{12} = \frac{2n_1}{n_1+n_2}$ is a Frensel transmission coefficient for oblique incidence and the r_{12} is a reflection coefficient $\frac{n_1-n_2}{n_1+n_2}$. The overall transfer matrix M of vacuum suspended TMDC yields

$$M = T(n_{vacuum},n_{TMDC}).P(\lambda,n_{TMDC},d).T(n_{TMDC},n_{vacuum}). \quad \text{(S15)}$$

For each wavelength, we compute the refractive index $n_{TMDC} = n + Ik$ using matrix elements. The system of two equations is solved for two variables n,k.

$$\begin{cases} Trans = 1 - Abs - Refl = 1/|M_{11}|^2 \\ Refl = |M_{21}|^2/|M_{11}|^2 \end{cases}, \qquad \text{(S16)}$$

$Abs, Refl$ are experimentally obtained absorption and reflection, respectively. The dielectric function ε is obtained using relation $\varepsilon = n^2$.

10. RPA and BSE calculations

To determine the theoretical response function the ground-state of the material was first calculated using density functional theory (DFT). Within DFT, the exchange-correlation energy was approximated by the local density approximation (LDA), which is well known for underestimating the bandgap of insulators and semiconductors. In order to estimate the experimental direct bandgap G_0W_0 calculations[25] were performed and the DFT band-structure was then corrected by the scissor operator to obtain the correct direct bandgap.

This corrected band-structure was then used to determine the response function of the material. In order to account for excitonic effects the Bethe Salpeter equation (BSE) was solved[26]. Solving the BSE is computationally very demanding and hence the BSE Hamiltonian was diagonalized in a restricted active space of a few bands around the Fermi level. However, the consequence of this restriction is that the response function is only determined in a limited low energy window around the band-gap. In order to obtain the response function at higher energies, where excitonic effects are negligible, we use the so-called random-phase approximation (RPA) within linear response time-dependent density functional theory (TDDFT).[27,28] This procedure does not account for excitonic effects, but bands up to 100 eV above the Fermi energy are included and is an accurate method for determination of response function away from the band-gap energies.

Computational parameters: Spin-orbit coupling was included for all calculations. For the DFT calculations the in-plane lattice parameter for WSe_2 (MoS_2) was 3.28 Å (3.16 Å) with an interlayer

spacing of 6.48 Å (6.15 Å), a distance of 3.34 Å (3.17 Å) between the chalcogens in each layer, and vacuum spacing between top and bottom layers of at least 12 Å for both the tri- and tetra-layer calculations. A k-point grid of 30x30x1 was used in all cases. The BSE hamiltonian was diagonalized in the restricted active space of 8 valence and 8 conduction states around the Fermi level. In order to account for many-body effects we have performed a single shot, finite temperature (a temperature of 500 K was used), all electron, spin-polarized GW calculations, where the spectral function on the real axis is constructed using a Pade approximation. Spin-orbit coupling was included in the GW calculations and a Matsubara cut-off of 12 Ha was used. All calculations were performed using state-of-the-art, all-electron, full-potential code Elk.[29]

11. Determination of sensitivity via Allan deviation:

The Allan deviation is defined as:[31]

$$\sigma_A^2(t) = \frac{1}{2(N-1){f_0}^2}\sum_{i=2}^{N}(f_i - f_{i-1})^2 \qquad \text{(S15)}$$

where f_i is the average frequency measured over the *i*th time interval of length t. We perform time stability measurements (Fig. 5b, main paper) of the resonance frequency with the heating laser turned off using a PLL with a bandwidth BW = 2.5 kHz. We extract σ_A and find $\sigma_A < 5 \cdot 10^{-7}$ over a broad range (Fig. 5c, main paper). Plugging $\frac{\Delta f}{\Delta P} =$ 792 Hz/μW, $f_0 = 4.6702$ MHz and an optimal $\sigma_A = 2.426 \cdot 10^{-7}$ at a sampling period of $t = 4$ ms into equation S16, we calculate $= 90 \frac{pW}{\sqrt{Hz}}$. The measurement fulfils the condition of $t \gg \frac{1}{BW}$.

$$\eta = \frac{\sigma_f\sqrt{t}}{f_0\left(\frac{\Delta f}{f_0 \Delta P}\right)} = \frac{\sigma_A\sqrt{t}f_0}{\frac{\Delta f}{\Delta P}}, \qquad \text{(S16)}$$

References

(1) Castellanos-Gomez, A.; Poot, M.; Steele, G. A.; Van Der Zant, H. S. J.; Agraït, N.; Rubio-Bollinger, G. Elastic Properties of Freely Suspended MoS2 Nanosheets. *Adv. Mater.* **2012**, *24* (6), 772–775.

(2) GESTIS-Stoffdatenbank https://gestis.dguv.de/data?name=570192 (accessed Jan 24, 2022).

(3) Sahoo, S.; Gaur, A. P. S.; Ahmadi, M.; Guinel, M. J. F.; Katiyar, R. S. Temperature-Dependent Raman Studies and Thermal Conductivity of Few-Layer MoS2. *J. Phys. Chem. C* **2013**, *117* (17), 9042–9047.

(4) Zhang, X.; Sun, D.; Li, Y.; Lee, G. H.; Cui, X.; Chenet, D.; You, Y.; Heinz, T. F.; Hone, J. C. Measurement of Lateral and Interfacial Thermal Conductivity of Single- and Bilayer MoS2 and MoSe2 Using Refined Optothermal Raman Technique. *ACS Appl. Mater. Interfaces* **2015**, *7* (46), 25923–25929.

(5) Aiyiti, A.; Bai, X.; Wu, J.; Xu, X.; Li, B. Measuring the Thermal Conductivity and Interfacial Thermal Resistance of Suspended MoS2 Using Electron Beam Self-Heating Technique. *Sci. Bull.* **2018**, *63* (7), 452–458.

(6) Yuan, P.; Wang, R.; Wang, T.; Wang, X.; Xie, Y. Nonmonotonic Thickness-Dependence of in-Plane Thermal Conductivity of Few-Layered MoS2: 2.4 to 37.8 Nm. *Phys. Chem. Chem. Phys.* **2018**, *20* (40), 25752–25761.

(7) ÇakIr, D.; Peeters, F. M.; Sevik, C. Mechanical and Thermal Properties of h -MX2 (M = Cr, Mo, W; X = O, S, Se, Te) Monolayers: A Comparative Study. *Appl. Phys. Lett.* **2014**, *104* (20), 203110.

(8) Zhang, L.; Lu, Z.; Song, Y.; Zhao, L.; Bhatia, B.; Bagnall, K. R.; Wang, E. N. Thermal Expansion Coefficient of Monolayer Molybdenum Disulfide Using Micro-Raman Spectroscopy. *Nano Lett.* **2019**, *19* (7), 4745–4751.

(9) Min, K.-A.; Cha, J.; Cho, K.; -, al; Jin Yun, S.; Hoon Jung, K.; Hyun Kim -, S.; Lee, J.; Huang, J.; Nakamura, K. First-Principles Simulation on Thermoelectric Propertiesof Transition Metal Dichalcogenide Monolayers. *Japanese J. Appl. Phys. Regul. Pap.* **2018**, *57*, 6–10.

(10) Volovik, L. S.; Fesenko, V. V.; Bolgar, A. S.; Drozdova, S. V.; Klochkov, L. A.; Primachenko, V. F. Enthalpy and Heat Capacity of Molybdenum Disulfide. *Sov. Powder Metall. Met. Ceram.* **1978**, *17* (9), 697–702.

(11) Xu, J.; Zhang, J.; Zhang, W.; Lee, C. S. Interlayer Nanoarchitectonics of Two-Dimensional Transition-Metal Dichalcogenides Nanosheets for Energy Storage and Conversion Applications. *Advanced Energy Materials*. John Wiley & Sons, Ltd December 1, 2017, p 1700571.

(12) Zhang, R.; Koutsos, V.; Cheung, R. Elastic Properties of Suspended Multilayer WSe2. *Appl. Phys. Lett.* **2016**, *108* (4).

(13) Kang, J.; Tongay, S.; Zhou, J.; Li, J.; Wu, J. Band Offsets and Heterostructures of Two-Dimensional Semiconductors. *Appl. Phys. Lett.* **2013**, *102* (1), 012111.

(14) Agarwal, M. K.; Wani, P. A. Growth Conditions and Crystal Structure Parameters of Layer Compounds in the Series Mo1-XWxSe2. *Mater. Res. Bull.* **1979**, *14* (6), 825–830.

(15) Easy, E.; Gao, Y.; Wang, Y.; Yan, D.; Goushehgir, S. M.; Yang, E. H.; Xu, B.; Zhang, X. Experimental and Computational Investigation of Layer-Dependent Thermal Conductivities and Interfacial Thermal Conductance of One- To Three-Layer WSe2. *ACS Appl. Mater. Interfaces* **2021**, *13* (11), 13063–13071.

(16) AZoM. Gold - Properties and Applications of Gold. *AZO Materials*. 2001, pp 1–3.

(17) Wilcock, J. D.; Campbell, D. S.; Anderson, J. C. The Internal Stress in Evaporated Silver and Gold Films. *Thin Solid Films* **1969**, *3* (1), 13–34.

(18) Properties: Silicon Nitride (Si3N4) Properties and Applications https://www.azom.com/properties.aspx?ArticleID=53 (accessed Jan 24, 2022).

(19) Huszank, R.; Csedreki, L.; Kertész, Z.; Török, Z. Determination of the Density of Silicon–Nitride Thin Films by Ion-Beam Analytical Techniques (RBS, PIXE, STIM). *J. Radioanal. Nucl. Chem.* **2016**, *307* (1), 341–346.

(20) Properties: Supplier Data - Silicon (Si) https://www.azom.com/properties.aspx?ArticleID=1851 (accessed Jan 24, 2022).

(21) Lee, C.; Wei, X.; Kysar, J. W.; Hone, J. Measurement of the Elastic Properties and Intrinsic Strength of Monolayer Graphene. *Science (80-.).* **2008**, *321* (5887), 385–388.

(22) Castellanos-Gomez, A.; Buscema, M.; Molenaar, R.; Singh, V.; Janssen, L.; Van Der Zant, H. S. J.; Steele, G. A. Deterministic Transfer of Two-Dimensional Materials by All-Dry Viscoelastic Stamping. *2D Mater.* **2014**, *1* (1), 011002.

(23) Barton, R. A.; Storch, I. R.; Adiga, V. P.; Sakakibara, R.; Cipriany, B. R.; Ilic, B.; Wang, S. P.; Ong, P.; McEuen, P. L.; Parpia, J. M.; Craighead, H. G. Photothermal Self-Oscillation and Laser Cooling of Graphene Optomechanical Systems. *Nano Lett.* **2012**, *12* (9), 4681–4686.

(24) Morell, N.; Tepsic, S.; Reserbat-Plantey, A.; Cepellotti, A.; Manca, M.; Epstein, I.; Isacsson, A.; Marie, X.; Mauri, F.; Bachtold, A. Optomechanical Measurement of Thermal Transport in Two-Dimensional MoSe 2 Lattices. *Nano Lett.* **2019**, *19* (5), 3143–3150.

(25) Xie, H.; Jiang, S.; Rhodes, D. A.; Hone, J. C.; Shan, J.; Mak, K. F. Tunable Exciton-Optomechanical Coupling in Suspended Monolayer MoSe2. *Nano Lett.* **2021**, *21* (6), 2538–2543.

(26) Kim, H. G.; Choi, H. J. Thickness Dependence of Work Function, Ionization Energy, and Electron Affinity of Mo and W Dichalcogenides from DFT and GW Calculations. *Phys. Rev. B* **2021**, *103* (8), 085404.

(27) Salpeter, E. E.; Bethe, H. A. A Relativistic Equation for Bound-State Problems. *Phys. Rev.* **1951**, *84* (6), 1232–1242.

(28) Runge, E.; Gross, E. K. U. Density-Functional Theory for Time-Dependent Systems. *Phys. Rev. Lett.* **1984**, *52* (12), 997–1000.

(29) Sharma, S.; Dewhurst, J. K.; Gross, E. Optical Response of Extended Systems Using Time-Dependent Density Functional Theory. *Top. Curr. Chem.* **2014**, *347*, 235–258.

(30) The Elk Code https://elk.sourceforge.io/ (accessed Jan 24, 2022).

(31) Allan, D. W. Statistics of Atomic Frequency Standards. *Proc. IEEE* **1966**, *54* (2), 221–230.

B.4. 2D Materials 10(3), 035012 (2023) and Supporting Information

2D Materials

PAPER

Nanomechanical absorption spectroscopy of 2D materials with femtowatt sensitivity

Jan N Kirchhof[1,*], Yuefeng Yu[1], Denis Yagodkin[1], Nele Stetzuhn[1,2], Daniel B de Araújo[1], Kostas Kanellopulos[3], Samuel Manas-Valero[4,5], Eugenio Coronado[4], Herre van der Zant[5], Stephanie Reich[1], Silvan Schmid[3] and Kirill I Bolotin[1,*]

[1] Department of Physics, Freie Universität Berlin, Arnimallee 14, 14195 Berlin, Germany
[2] Max-Born-Institut für Nichtlineare Optik und Kurzzeitspektroskopie, Max-Born-Straße 2A, 12489 Berlin, Germany
[3] Institute of Sensor and Actuator Systems, TU Wien, Gusshausstrasse 27-29, 1040 Vienna, Austria
[4] Instituto de Ciencia Molecular, Universidad de Valencia, Calle Catedrático José Beltrán 2, 46980 Paterna, Spain
[5] Kavli Institute of Nanoscience, Delft University of Technology, Lorentzweg 1, Delft 2628 CJ, The Netherlands
[*] Authors to whom any correspondence should be addressed.

E-mail: jan.kirchhof@fu-berlin.de and kirill.bolotin@fu-berlin.de

Keywords: NEMS, resonator, silicon nitride, nanomechanical resonators, 2D materials, spectroscopy, transition metal dichalcogenides (TMDs)

Supplementary material for this article is available online

OPEN ACCESS

RECEIVED
26 January 2023

REVISED
18 April 2023

ACCEPTED FOR PUBLICATION
27 April 2023

PUBLISHED
5 May 2023

Abstract

Nanomechanical spectroscopy (NMS) is a recently developed approach to determine optical absorption spectra of nanoscale materials via mechanical measurements. It is based on measuring changes in the resonance frequency of a membrane resonator vs. the photon energy of incoming light. This method is a direct measurement of absorption, which has practical advantages compared to common optical spectroscopy approaches. In the case of two-dimensional (2D) materials, NMS overcomes limitations inherent to conventional optical methods, such as the complications associated with measurements at high magnetic fields and low temperatures. In this work, we develop a protocol for NMS of 2D materials that yields two orders of magnitude improved sensitivity compared to previous approaches, while being simpler to use. To this end, we use mechanical sample actuation, which simplifies the experiment and provides a reliable calibration for greater accuracy. Additionally, the use of low-stress silicon nitride membranes as our substrate reduces the noise-equivalent power to NEP = 890 fW $\sqrt{\text{Hz}}^{-1}$, comparable to commercial semiconductor photodetectors. We use our approach to spectroscopically characterize a 2D transition metal dichalcogenide (WS_2), a layered magnetic semiconductor ($CrPS_4$), and a plasmonic super-crystal consisting of gold nanoparticles.

1. Introduction

Nanomechanical resonators emerged as sensitive probes for minuscule forces [1–3] and atomic-scale masses [4–8]. By incorporating two-dimensional (2D) materials into nanomechanical resonators, the miniaturization of these devices has been pushed to the ultimate limit of atomic thickness. Along with this comes a massively reduced effective mass, increased resonance frequencies, easily accessible non-linearity, and the ability to tune resonance frequencies [9]. This technological boost allows using such resonators as sensors for light [10], magnetic fields [11, 12], sound [6, 13–15], gases [6, 16] or even to study live bacteria [17].

Recently, the use of 2D materials-based resonators as fast and broadband optical spectrometers has been demonstrated [18]. In this nanomechanical spectroscopy approach (NMS), changes in the mechanical resonance frequency of a freely suspended 2D material are measured as a function of the illumination photon energy E_γ. From this, both real and imaginary components of the dielectric function can be extracted. In this measurement the material effectively acts as its own photodetector, leading to broadband sensitivity (UV-THz) of the approach. Furthermore,

unlike classical optical approaches, NMS can distinguish between scattered and absorbed light. Finally, NMS is suitable for nanostructures with dimensions smaller than a micron and is applicable at low temperatures and high magnetic fields. Whilst NMS has many fundamental advantages, it currently lacks the sensitivity provided by state-of-the-art optical approaches.

Here, we reduce the noise equivalent power of NMS by two orders of magnitude, down to NEP = 890 fW $\sqrt{\text{Hz}}^{-1}$. At the same time, we simplify the method by using mechanical actuation, which allows us to study electrically insulating materials, makes sample loading straightforward and provides a simple, but robust calibration. We use this improved method to spectroscopically characterize a range of 2D structures with high resolution. This includes WS_2, a classic binary transition metal dichalcogenide (TMD), $CrPS_4$, a layered magnetic semiconductor (ternary TMD), and a plasmonic meta-structure consisting of gold nanoparticles forming a super-crystal [19, 20].

2. Results

2.1. Sample design

At the core of our device is a nanostructure or 2D material of interest that we place on top of a silicon nitride (SiN) membrane, thereby forming a hybrid resonator [18, 21, 22]. We use SiN for its excellent mechanical properties and record high quality factors (Q) [23–27]. The device is illuminated by a light source of tunable photon energy (E_γ = 1.2–3.1 eV). The absorption of light by the 2D material heats up the entire hybrid device. Due to thermal expansion, the in-plane tensile stress within the membrane is released and the resonance frequency downshifts. This downshift in frequency is proportional to the amount of absorbed laser power ($P_{\text{abs}}(E_\gamma)$) and allows us to perform absorption spectroscopy. To understand the measurement's underlying mechanics and optimize our sample design, we start by looking at the fundamental resonance of a square prestressed SiN membrane. The resonance frequency is given by $f_0 = \frac{1}{L}\sqrt{\frac{\sigma_0}{2\rho}}$, where L is the length, σ_0 the in-plane tensile stress and ρ the density. When the incoming light heats the material, the stress is reduced by $\Delta\sigma = \alpha\Delta T\frac{E}{1-\nu}$, where α is the thermal expansion coefficient, ΔT is the average temperature increase, E is the Young's modulus and ν is the Poisson's ratio. Here, ΔT is directly proportional to P_{abs}. The resulting frequency shift $\Delta f = f_0 - f$ can be approximated as $\Delta f \approx f_0\frac{\Delta\sigma}{2\sigma_0}$ [10, 23]. Thus, in order to maximize the frequency response to laser heating (responsivity) and ultimately improve the sensitivity of NMS, we aim to minimize the in-plane tensile stress σ_0 within our membranes [23]. To do so, we choose SiN membranes ($L = 120$ μm, thickness $h = 50$ nm) grown by low-pressure chemical vapor deposition. By using a silicon-rich stoichiometry, we obtain membranes with low built-in stress. Thin layers of amorphous SiN also have a reduced thermal conductivity of $\kappa \approx 3$ W m^{-1} K^{-1} [28], which is beneficial for our experiments as it increases the temperature rise within our device in response to laser heating [29]. To complete the hybrid resonators, we transfer a 2D material of interest onto the SiN-membrane using the polydimethylsiloxane (PDMS) dry transfer technique [30]. Here, we ensure that we place the 2D material in the center of the membrane such that there are no thermal links to the rest of the substrate. An optical micrograph of a sample with a trilayer WS_2 is shown in figure 1(a) and schematically in a side view in figure 1(b).

The membrane's motion is actuated mechanically by a piezoelectric element below the sample and detected interferometrically using a HeNe laser (E_γ = 1.96 eV) with a probe power of 300 nW (red in figure 1(c)). A second wavelength-tunable excitation laser (blue in figure 1 (c)), allows us to controllably heat the resonator, whilst we monitor the changes in resonance frequency. Upon sweeping the actuation frequency we find a pronounced fundamental mode at $f_0 = 425.367$ kHz as shown in figure 1(d). From fitting a driven harmonic oscillator response to the experimental data, we estimate (the exact determination requires ring-down measurements) a quality factor of Q = 82 000, comparable to previous results on similar samples [23]. Knowing f_0, L and $\rho = 3000$ m^3 kg^{-1} [23, 25], we calculate the stress in our membrane to be $\sigma_0 \approx 15.6$ MPa—much lower than commercially available SiN membranes (250–1000 MPa). All measurements are carried out at room temperature (stabilized) and at a pressure of $p \approx 1 \times 10^{-5}$ mbar. Next, we determine the responsivity of the resonator to absorbed light $R_{100\%} = \frac{\Delta f}{f_0 P_{\text{abs}}}$. To this end, we focus the probe and excitation beam (set to $E_\gamma = 1.9$ eV) on the SiN area close to the center of the sample and vary the laser power of the excitation laser from 0 to 30 μW. We use the known absorption ($Abs = 0.5\%$) of SiN at that photon energy [23] to convert the incident laser power to absorbed laser power ($P_{\text{abs}} = P_{\text{inc}}Abs$) and plot Δf vs. P_{abs} in figure 1(e). From a linear fit (red), we extract a responsivity of $R_{100\%} = 21\,810$ W^{-1}. We will use this quantity for the calibration of our measurements and to calculate the sensitivity of NMS. The measured $R_{100\%}$ is much higher than in previous approaches ($R_{100\%} = 180$ W^{-1}) [18]. At the same time, the Q of the improved system is more than an order of magnitude higher than in previous measurements (82 000 vs. 5000). Overall, we now have our material of interest implemented into a high quality

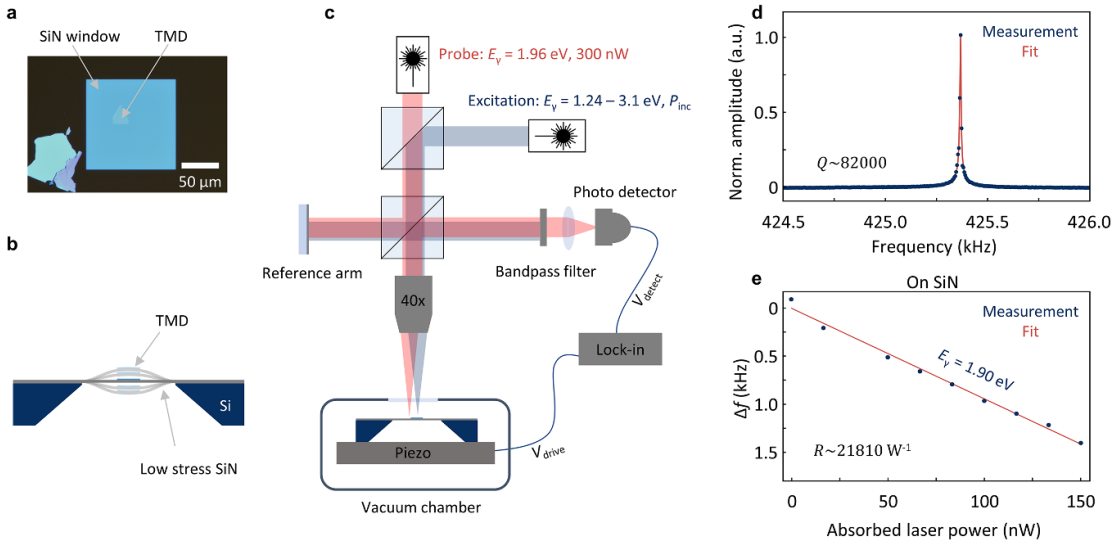

Figure 1. SiN-TMD hybrid devices and interferometric motion detection. (a), Optical micrograph of a trilayer WS_2 transferred on the center of a low-stress SiN membrane (b), Sketch of the SiN-TMD hybrid device. The entire SiN membrane moves out-of-plane and due to the low thermal conductivity of SiN, the TMD flake is thermally decoupled from its environment. (c), Motion detection using a Michelson interferometer (red laser) with an additional broadly tunable laser (blue) to heat the resonator via the TMD. The sample is placed in a vacuum chamber ($p \approx 1 \times 10^{-5}$ mbar) and the motion of the suspended area is actuated mechanically via a piezoelectric element below the sample. (d), Measured amplitude vs. frequency for the device shown in (a). The fundamental mode shows a quality factor of $Q \sim 82\,000$. (e), Response of the fundamental mode to laser heating (excitation focused on SiN area). We extract a responsivity of $R_{100\%} = 21\,810\ \mathrm{W}^{-1}$.

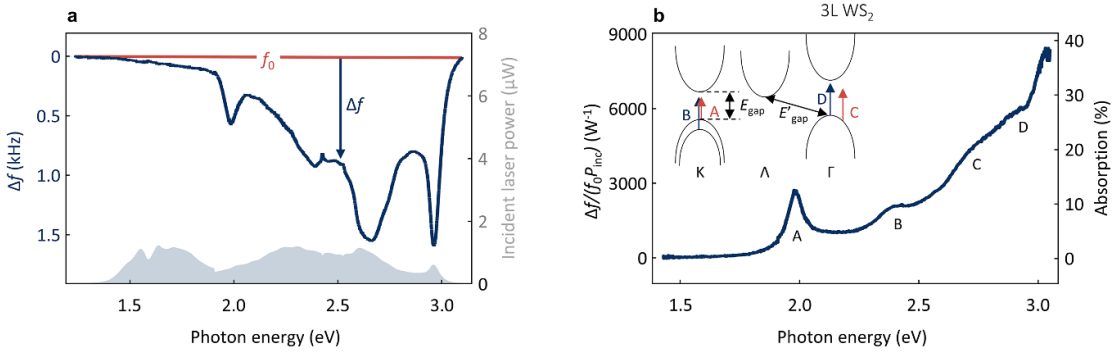

Figure 2. Nanomechanical absorption spectroscopy of WS_2. (a), Raw frequency response (blue, left y-axis) of the trilayer WS_2 device as a function of photon energy. The corresponding incident laser power is plotted in grey (right y-axis). Multiple features are visible and towards higher energies, the frequency shift increases as the absorption by the TMD increases. (b), Relative responsivity $R = \frac{\Delta f}{f_0 P_{inc}}$ vs. photon energy. This signal is directly proportional to the absorption coefficient of the TMD and we convert it to absolute units using $R_{100\%}$ (obtained from figure 1(e)). The curve shows clear excitonic features at the expected photon energies. In the inset, we sketch the corresponding transitions for few-layer WS_2.

mechanical hybrid resonator, that is engineered to strongly react to absorbed light.

2.2. Nanomechanical absorption measurements

After optimizing our mechanical system as a sensor for detecting light, we use it to perform absorption spectroscopy on several candidates, starting with the 2D semiconductor WS_2 (trilayer). To do so, we track the frequency of the fundamental resonance, whilst varying the photon energy of the excitation laser. In this measurement, the excitation laser is focused on the TMD area and the frequency is measured using a phase-locked-loop (PLL) (details in supplementary information). In figure 2(a), we plot the frequency shift Δf (blue, left y-axis) and the corresponding incoming laser power P_{inc} (grey, right y-axis) vs. the photon energy of the excitation laser. Upon dividing the frequency shift by the laser power and normalizing it by f_0, we obtain the relative responsivity $R(E_\gamma) = \frac{\Delta f(E_\gamma)}{f_0 P_{inc}(E_\gamma)}$ (figure 2(b)). This signal is directly proportional to the absorption coefficient of the 2D material. Finally, we use the beforehand determined $R_{100\%}$ to calculate the absorption coefficient of the TDM in absolute units: $Abs(E_\gamma) = R(E_\gamma)/R_{100\%}$ — as plotted in figure 2(b) on the right y-axis. In this spectrum, we find clear peaks (A–D), that correspond

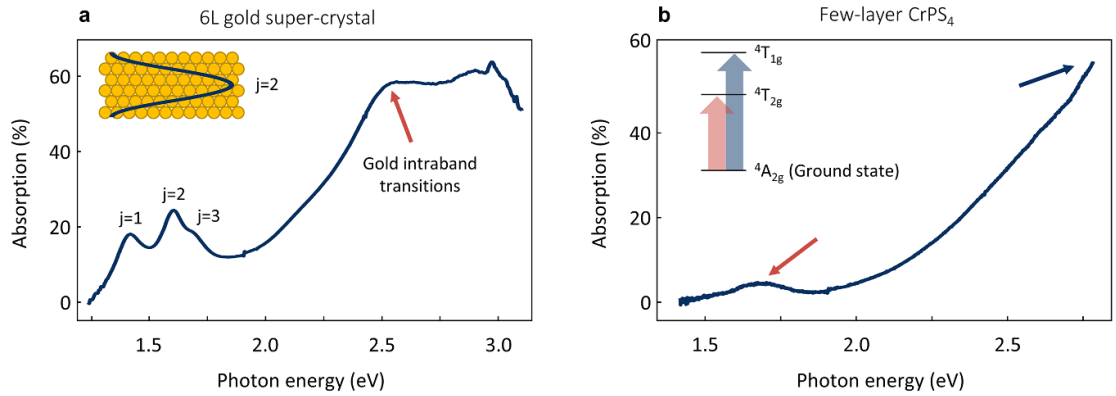

Figure 3. Nanomechanical absorption spectroscopy of exotic 2D materials (a), Absorption vs. photon energy for a 6-layer gold plasmonic super-crystal (thickness of 350 nm). In the low energy range up to 1.8 eV, we find pronounced absorption peaks associated with standing wave plasmon polaritons within the super-crystal. Above 2.5 eV the light is absorbed by intraband transitions in the gold particles. The inset shows a sketch of the gold nanoparticles (yellow circles) arranged in a super-crystal, in which plasmonic modes form standing waves ($j = 2$-mode shown in blue). When excited on resonance these modes absorb light and are visible as peaks in our measurement. (b), Absorption vs. photon energy for a few-layer (∼5) 2D antiferromagnet $CrPS_4$. This material is a semiconductor with a broad absorption edge around 1.68 eV, which we observe in our measurements.

to different excitonic species at the expected energies [31]. In the inset, we sketch the corresponding transitions for few-layer WS_2 (following [31]). Some fraction of light will reach the SiN below the TMD and be absorbed there, which may lead to large relative measurement errors in the spectral range, where the TMD exhibits low absorption. To account for this, we perform the following correction: $\mathrm{Abs}_{2DM} = \frac{\mathrm{Abs}_{total} - \mathrm{Abs}_{SiN}}{1 - \mathrm{Abs}_{SiN}}$. This correction may introduce a small error in the region, where the 2D material exhibits large absorption as we potentially underestimate the absorption in SiN (details in supplementary information), but significantly reduces the relative error in the region of low absorption. SiN is an amorphous insulator with very weak light–matter interaction, resulting in low absorption (∼0.5%) and a rather flat spectrum in the spectral region of interest, which justifies this step.

2.3. Characterizing exotic 2D materials

Next, we extend our method to study more exotic 2D materials. We choose two materials that are particularly suited for our method and for which it is expected to produce advantages. The first one is a layered crystal (super-crystal) made from plasmonic nanoparticles. These gold nanoparticles (diameter 56 nm) are embedded into a polymer matrix forming a closely spaced fcc super-crystal [19, 20]. Such super-crystals have been recently shown to enter the deep strong light–matter coupling regime, in which light within a material can no longer be seen as a perturbation to the properties of the material [19, 20]. Instead, the material properties are almost entirely determined by light–matter interaction [19, 20]. We grow the super-crystals by self-assembly on a liquid-liquid interface (details inf [19, 20, 32]), carefully transfer them onto the SiN membranes by the PDMS dry transfer technique [30] and perform our nanomechanical absorption spectroscopy measurements. We note that for the highest accuracy, all samples are calibrated individually following the protocol described above for the WS_2 sample. In figure 3(a) we show the absorption spectrum obtained for a 6-layer super-crystal. Starting from low photon energies, we find three peaks associated with plasmonic modes within the super-crystal ($j = 1..3$ comp. inset figure 3(a)). As we go to higher energies, the absorption increases towards the intraband transitions of gold and plateaus around 2.5 eV. Interestingly, NMS works excellently despite the super-crystal being much thicker (350 nm vs. 2 nm) and also much heavier than the TMD studied above. Whilst the fundamental resonance frequency and the absolute shifts in frequency for this heavier sample are smaller, the quality factor, responsivity and thus the sensitivity remain comparable to the lighter samples. Plasmonic structures are known to scatter a significant amount of light that cannot be distinguished from absorbed light by common optical measurement methods. In contrast, NMS is only sensitive to absorbed light and therefore ideal to study plasmonic systems.

Our second choice is a 2D antiferromagnet $CrPS_4$ with a Néel temperature for the bulk material of $T_{Neel} = 36$ K [33]. The study of 2D magnetism requires measurements at low temperatures and high magnetic fields, which is challenging for conventional optics but is easier using NMS. We exfoliate and transfer a few-layer (approx. 5) thick flake of $CrPS_4$ onto a SiN membrane and perform NMS (see figure 3(b)). In the spectrum, we find a broad peak around 1.68 eV. This peak belongs to the $d-d$ transition of the Cr^{3+} ions from the $^4A_{2g}$ to the $^4T_{2g}$ state. Towards higher photon energies the absorption

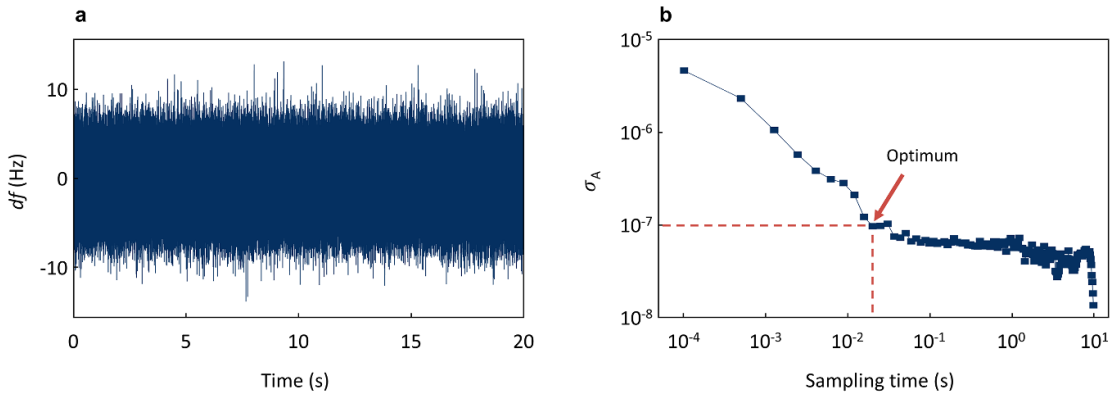

Figure 4. Sensitivity (a), Stability measurement of frequency vs. timewithout laser illumination, measured using a phase-locked loop. (b) Allan deviation σ_A vs. sampling time in log–log scale derived from (a). For an optimal sampling time of 20 ms (red arrow), we extract a noise equivalent power of NEP = 890 fW $\sqrt{\text{Hz}}^{-1}$.

increases, as we approach higher-order transitions (e.g. $^4A_{2g}$ to $^4T_{1g}$). This spectrum measured above the antiferromagnet's Néel temperature is expected and in line with literature reports [33–35]. Thin $CrPS_4$ is rather sensitive to photodamage [33, 35], which can be problematic for classical optical approaches. For NMS however small laser powers ($P_{inc} \approx 1$ μW) are sufficient to induce sizeable frequency shifts (comp. figure 2(a)), which can help preserve the quality of sensitive samples. At the same time, the heating-related temperature changes of our samples (see supplementary information) are small, and we can assume that the thermal constants are unaffected by the laser beam. Overall, we have spectroscopically characterized a range of exotic 2D materials with high resolution and believe that these measurements highlight the broad applicability of NMS.

2.4. Sensitivity

In order to compare NMS to state-of-the-art optical approaches, we determine its sensitivity (noise equivalent power *NEP*) and response time (τ). In our measurements, we use frequency shifts to probe the amount of absorbed light. In order to quantify the noise in our measurements, we, therefore, look at frequency fluctuations, which we then convert into power noise using $R_{100\%}$ [10, 18, 36–38]. Assuming white noise, the *NEP* can be derived from the fractional frequency noise power spectral density ($S_y(0)$) and is given by [39, 40]:

$$\text{NEP} = \frac{\sqrt{S_y(0)}}{R_{100\%}} = \frac{\sigma_A \sqrt{2 t_{\text{sampling}}}}{R_{100\%}} \qquad (1)$$

where σ_A is the Allan deviation of the frequency measurement [41] and t_{sampling} is the sampling time. To obtain σ_A, we perform a frequency stability measurement in the PLL configuration with the excitation laser turned off (figure 4(a)). From this data, we derive σ_A vs. sampling time (figure 4(b)). We choose an optimal value of $\sigma_A = 9.7 \times 10^{-8}$ for $t_{\text{sampling}} =$ 20 ms and using $R_{100\%} = 21810$ W^{-1}, we obtain NEP = 890 fW $\sqrt{\text{Hz}}^{-1}$. This value is two orders of magnitude lower than in our previous approach (NEP = 90 pW $\sqrt{\text{Hz}}^{-1}$) [18].

The sensitivity of NMS is now comparable to commercially available avalanche photodetectors (APDs) for the same spectral range with NEP = 200 fW $\sqrt{\text{Hz}}^{-1}$ (Thorlabs APD130A(/M)). APDs are highly sensitive, but also overload quickly. Compared to these commercial devices, NMS-based devices show a higher dynamic range (84 dB vs. 69 dB—both for 1 s integration time) and can easily detect hundreds of μW (details in supplementary information).

To assess the measurement speed of NMS, we simulate time-dependent laser heating in our sample and extract a response time for our mechanical system of $\tau = 800$ μs (simulations in supplementary information), which is in line with experimental data on similar devices [37, 39]. The fast response time, allows us to sweep the excitation energy rapidly and we obtain the Δf vs. E_γ traces presented above in a matter of seconds.

3. Discussion

We presented a simplified and improved method of nanomechanical absorption spectroscopy. With a sensitivity of NEP = 890 fW $\sqrt{\text{Hz}}^{-1}$ and a response time $\tau = 800$ μs, the method now is a promising alternative to classical optical approaches, whilst it overcomes long-standing limitations. At the same time, we show that using SiN as a reference material provides a robust and straightforward calibration. We demonstrated the broad applicability of NMS by spectroscopically characterizing a 2D semiconductor, a layered plasmonic super-crystal and a novel 2D antiferromagnet. The key points for the improvement of the measurement sensitivity are stress reduction in the SiN membranes and thermal decoupling of

the 2D material, which leads to enhanced responsivity and improved sensitivity. The responsivity almost entirely depends on the thermal properties of the SiN membrane. Therefore, we expect a sensitivity mostly independent of the thermal properties of the 2D materials (details in supplementary information). To further reduce *NEP*, we could use temperature regulation of the sample to controllably minimize the tensile stress σ_0. Upon cooling the sample, the silicon frame shrinks more than the suspended SiN membrane, due to their difference in thermal expansion coefficient. This reduces the stress in the suspended SiN and would allow measuring very close to $\sigma_0 = 0$, which would mean further increased responsivity and thus improved sensitivity. We note that in comparison to our previous experiments, the 2D material is not suspended in this work but in direct contact with the SiN. This changes the dielectric environment of the 2D material and can affect excitons and other quasiparticles in 2D materials. We find that this has a large impact on photoluminescence measurements, where it completely suppresses the emission (see supplementary information), but does not affect absorption spectra [42]. The suppressed emission suggests a very low quantum yield ($<10^{-6}$), which justifies the assumption that all the absorbed light is converted into heat and therefore detected by NMS.

We also aim to characterize 2D materials at low temperatures using NMS. In the limit of $T \to 0$ K, the specific heat of any material goes to zero and along with it the thermal conductivity κ and thermal expansion coefficient α. If α decreases faster than κ, our method will not work anymore, because the responsivity is proportional to $\frac{\alpha}{\kappa}$ [23]. To exclude this scenario, we do preliminary measurements of the responsivity of a bare SiN membrane as a function of temperature. For this, we use a membrane with higher pre-stress ($\sigma_0 = 240$ MPa) to avoid buckling upon cooldown and find that even at 4.2 K, the membrane shows considerable responsivity (see supplementary information). This paves the way for future experiments at low temperatures and will allow the unlocking of exciting physics in a large range of 2D materials.

Data availability statement

All data that support the findings of this study are included within the article (and any supplementary files).

Acknowledgments

This work was supported by Deutsche Forschungsgemeinschaft (DFG, German Research Foundation, Project ID 449506295, 328545488 and 504656879), CRC/TRR 227 (Project B08), ERC Starting Grant Nos. 639739, CSC 202006150013 and the Consolidator Grant DarkSERS (772108). Samuel Mañas-Valero thanks the Generalitat Valenciana for a postdoctoral fellow APOSTD-CIAPOS2021/215.

ORCID iDs

Jan N Kirchhof https://orcid.org/0000-0001-8576-4787
Denis Yagodkin https://orcid.org/0000-0002-9135-8918
Daniel B de Araújo https://orcid.org/0000-0001-5216-6035
Samuel Manas-Valero https://orcid.org/0000-0001-6319-9238
Eugenio Coronado https://orcid.org/0000-0002-1848-8791
Herre van der Zant https://orcid.org/0000-0002-5385-0282
Stephanie Reich https://orcid.org/0000-0002-2391-0256
Silvan Schmid https://orcid.org/0000-0003-3778-7137
Kirill I Bolotin https://orcid.org/0000-0003-1821-3429

References

[1] De Bonis S, Urgell C, Yang W, Samanta C, Noury A, Vergara-Cruz J, Dong Q, Jin Y and Bachtold A 2018 *Nano Lett.* **18** 5324–8
[2] Weber P, Güttinger J, Noury A, Vergara-Cruz J and Bachtold A 2016 *Nat. Commun.* **7** 1–8
[3] Eichler A 2022 *Mater. Quantum Technol.* **2** 043001
[4] Chaste J, Eichler A, Moser J, Ceballos G, Rurali R and Bachtold A 2012 *Nat. Nanotechnol.* **7** 301–4
[5] Chiu H Y, Hung P, Postma H W C and Bockrath M 2008 *Nano Lett.* **8** 4342–6
[6] Lemme M C *et al* 2020 *Research* **2020** 8748602
[7] Desai S H, Pandya A A and Panchal M B 2021 *J. Phys.: Conf. Ser.* **1854** 012029
[8] Lee H L, Yang Y C and Chang W J 2013 *Jpn. J. Appl. Phys.* **52** 025101
[9] Steeneken P G, Dolleman R J, Davidovikj D, Alijani F and Van der Zant H S 2021 *2D Mater.* **8** 042001
[10] Blaikie A, Miller D and Alemán B J 2019 *Nat. Commun.* **10** 1–8
[11] Wittmann S, Glacer C, Wagner S, Pindl S and Lemme M C 2019 *ACS Appl. Nano Mater.* **2** 5079–85
[12] Jiang S, Xie H, Shan J and Mak K F 2020 *Nat. Mater.* **19** 1295–9
[13] Verbiest G J, Kirchhof J N, Sonntag J, Goldsche M, Khodkov T and Stampfer C 2018 *Nano Lett.* **18** 5132–7
[14] Baglioni G, Pezone R, Vollebregt S, Cvetanovic K, Spasenovic M, Todorovic D, Liu H, Verbiest G J, van der Zant H S J and Steeneken P G 2022 Ultra-sensitive graphene membranes for microphone applications (arXiv:2211.03369)
[15] Pezone R, Baglioni G, Sarro P M, Steeneken P G and Vollebregt S 2022 *ACS Appl. Mater. Interfaces* **14** 21705–12
[16] Dolleman R J, Chakraborty D, Ladiges D R, van der Zant H S J, Sader J E and Steeneken P G 2021 *Nano Lett.* **21** 7617–24
[17] Rosłoń I E, Japaridze A, Steeneken P G, Dekker C and Alijani F 2022 *Nat. Nanotechnol.* **17** 637–42

[18] Kirchhof J N, Yu Y, Antheaume G, Gordeev G, Yagodkin D, Elliott P, de Araújo D B, Sharma S, Reich S and Bolotin K I 2022 *Nano Lett.* **22** 8037–44
[19] Mueller N S, Okamura Y, Vieira B G, Juergensen S, Lange H, Barros E B, Schulz F and Reich S 2020 *Nature* **583** 780–4
[20] Mueller N S, Pfitzner E, Okamura Y, Gordeev G, Kusch P, Lange H, Heberle J, Schulz F and Reich S 2021 *ACS Nano* **15** 5523–33
[21] Schmid S *et al* 2014 *J. Appl. Phys.* **115** 054513
[22] Schwarz C, Pigeau B, Mercier de Lépinay L, Kuhn A G, Kalita D, Bendiab N, Marty L, Bouchiat V and Arcizet O 2016 *Phys. Rev. Appl.* **6** 064021
[23] Chien M H, Brameshuber M, Rossboth B K, Schütz G J and Schmid S 2018 *Proc. Natl Acad. Sci.* **115** 11150–5
[24] Verbridge S S, Parpia J M, Reichenbach R B, Bellan L M and Craighead H G 2006 *J. Appl. Phys.* **99** 124304
[25] Schmid S, Jensen K D, Nielsen K H and Boisen A 2011 *Phys. Rev.* B **84** 165307
[26] Luke K, Dutt A, Poitras C B and Lipson M 2013 *Opt. Express* **21** 22829–33
[27] Fong K Y, Pernice W H P and Tang H X 2012 *Phys. Rev.* B **85** 161410
[28] Ftouni H, Blanc C, Tainoff D, Fefferman A D, Defoort M, Lulla K J, Richard J, Collin E and Bourgeois O 2015 *Phys. Rev.* B **92** 125439
[29] Luhmann N, Jachimowicz A, Schalko J, Sadeghi P, Sauer M, Foelske-Schmitz A and Schmid S 2017 *Appl. Phys. Lett.* **111** 063103
[30] Castellanos-Gomez A, Buscema M, Molenaar R, Singh V, Janssen L, van der Zant H S J and Steele G A 2014 *2D Mater.* **1** 011002
[31] Goswami T, Bhatt H, Babu K J, Kaur G, Ghorai N and Ghosh H N 2021 *J. Phys. Chem. Lett.* **12** 6526–34
[32] Bastús N G, Comenge J and Puntes V 2011 *Langmuir* **27** 11098–105
[33] Lee J, Ko T Y, Kim J H, Bark H, Kang B, Jung S G, Park T, Lee Z, Ryu S and Lee C 2017 *ACS Nano* **11** 10935–44
[34] Gu P *et al* 2020 *ACS Nano* **14** 1003–10
[35] Kim S, Yoon S, Ahn H, Jin G, Kim H, Jo M H, Lee C, Kim J and Ryu S 2022 *ACS Nano* **16** 16385–93
[36] Kurek M, Carnoy M, Larsen P E, Nielsen L H, Hansen O, Rades T, Schmid S and Boisen A 2017 *Angew. Chem., Int. Ed.* **56** 3901–5
[37] Piller M, Hiesberger J, Wistrela E, Martini P, Luhmann N and Schmid S 2023 *IEEE Sens. J.* **23** 1066–71
[38] Piller M, Luhmann N, Chien M H and Schmid S 2019 Nanoelectromechanical infrared detector *Proc. SPIE* **11088** 9–15
[39] Snell N, Zhang C, Mu G, Bouchard A and St-Gelais R 2022 *Phys. Rev. Appl.* **17** 044019
[40] Vig J and Kim Y 1999 *IEEE Trans. Ultrason. Ferroelectr. Freq. Control* **46** 1558–65
[41] Allan D W 1966 *Proc. IEEE* **54** 221–30
[42] Li Y, Chernikov A, Zhang X, Rigosi A, Hill H M, van der Zande A M, Chenet D A, Shih E M, Hone J and Heinz T F 2014 *Phys. Rev.* B **90** 205422

Supplementary Information: Nanomechanical absorption spectroscopy of 2D materials with femtowatt sensitivity

Jan N. Kirchhof[1], **Yuefeng Yu**[1], **Denis Yagodkin**[1], **Nele Stetzuhn**[1,2], **Daniel B. de Araújo**[1], **Kostas Kanellopulos**[3], **Samuel Manas-Valero**[4,5], **Eugenio Coronado**[4], **Herre van der Zant**[5], **Stephanie Reich**[1], **Silvan Schmid**[3], **Kirill I. Bolotin**[1]

[1]Department of Physics, Freie Universität Berlin, Arnimallee 14, 14195 Berlin, Germany

[2]Max-Born-Institut für Nichtlineare Optik und Kurzzeitspektroskopie, Max-Born-Straße 2A, 12489 Berlin, Germany

[3]Institute of Sensor and Actuator Systems, TU Wien, Gusshausstrasse 27-29, 1040, Vienna, Austria

[4]Instituto de Ciencia Molecular, Universidad de Valencia, Calle Catedrático José Beltrán 2, 46980 Paterna, Spain

[5]Kavli Institute of Nanoscience, Delft University of Technology, Lorentzweg 1, Delft, 2628 CJ, The Netherlands

1. Supplementary information

1.1. Phase locked-loop measurements

All resonance frequency measurements were performed using a lock-in amplifier MFLI from Zurich Instruments. To set up the phase-locked-loop (PLL), we first sweep the drive frequency and then use this frequency and phase information to lock onto the resonance using the built-in PLL functionality of the lock-in amplifier. We choose a PLL bandwidth of 1 kHz and a resolution bandwidth of 5 kHz. To improve the stability and speed of the PLL, we use the lock-in amplifier's PLL advisor to optimize the feedback parameters. For the frequency stability measurements (Fig. 4a), we adjust the drive voltage just below the onset of the non-linearities and try to avoid external noise sources. We use a temperature controller to stabilize the sample temperature at $T = 300\,\mathrm{K}$. To account for the remaining thermal drift in our measurements, we perform a linear correction on the measured frequency traces.

1.2. Finite element method (FEM) simulations

To simulate laser heating in our samples, we use the structural mechanics and heat transfer module of Comsol Multiphysics (version 6.0). The device geometry including the under-laying silicon frame is shown in Supplementary Fig. 1a. Next, we implement a Gaussian heat source centrally on the TMD (P_{abs}=10 µW, $r_{\mathrm{laser}} = 500\,\mathrm{nm}$) and calculate the resulting temperature profile (Supplementary Fig. 1b). To estimate the saturation power of our detector, we increase the amount of absorbed laser power until we reach the damage threshold of the TMD, which we expect at an average temperature of $T_{\mathrm{max}} \approx 550\,\mathrm{K}$ in the TMD. According to our simulations, this value is reached at $P_{\mathrm{abs}} = 145\,\mu\mathrm{W}$. To calculate the dynamic range, we divide the maximum power by the minimum detectable power ($P_{\mathrm{min}} = NEP\sqrt{BW}$) for an integration time of 1 s ($BW = \sqrt{1\,\mathrm{Hz}}$). We calculate a ratio of 2.3×10^8, which expressed in decibel yields 84 dB.

We also use our simulation model to assess the effects of the thermal conductivity of the 2D material on the responsivity of our approach. To this end, we simulate the responsivity of our hybrid-resonator (sketch of sample geometry Supplementary Fig. 1a) whilst varying the thermal conductivity of the 2D material over orders of magnitude from 0.5 to $500\,\mathrm{Wm^{-1}K^{-1}}$, around the literature value of $\sim 50\,\mathrm{Wm^{-1}K^{-1}}$. The simulations nicely reproduce the measured frequency shift (compare Fig. 1e main text). Varying the thermal conductivity over orders of magnitude results in a variation in the responsivity of 3.3%. We believe that this illustrates that the thermal properties of the 2D material only play a secondary role and should have a small effect on the overall responsivity of the system.

Finally, we want to assess if the laser-induced heating in our samples has an effect on the thermal properties of the materials employed in our samples. We can estimate the average temperature raise due to laser illumination from simulations and from back-of-the-envelope estimates. At the photon energy corresponding to the maximal absorption (around 2.7 eV, Fig. 2a), the resonator absorbs 170 nW ($P_{\mathrm{inc}} = 0.97\,\mu\mathrm{W}$, $Abs = 17.5\%$) of laser power. According to our simulations, this raises the average temperature of the suspended region (SiN + TMD) by ∼140 mK. Alternatively, we can analytically estimate the change in temperature from the experimentally measured downshift in frequency (Δf) at this amount of absorbed

light. Using the equations from the main text yields a value agreeing with the outcome of the simulations:

$$\Delta T = \frac{2(1-\nu)\Delta f \sigma_0}{E\alpha f_0} = \frac{2(1-0.23)\cdot 1575\,\mathrm{Hz}\cdot 15.6\,\mathrm{MPa}}{250\,\mathrm{GPa}\cdot 2.2\,\mathrm{ppmK}^{-1}\cdot 425.4\,\mathrm{kHz}} = 162\,\mathrm{mK} \quad (1)$$

This change in temperature is negligible compared to 300 K, our measurement temperature, and we believe that it is reasonable to assume the thermal conductivity to be constant. The agreement between simulations and analytical estimates furthermore confirms the validity of the simulations.

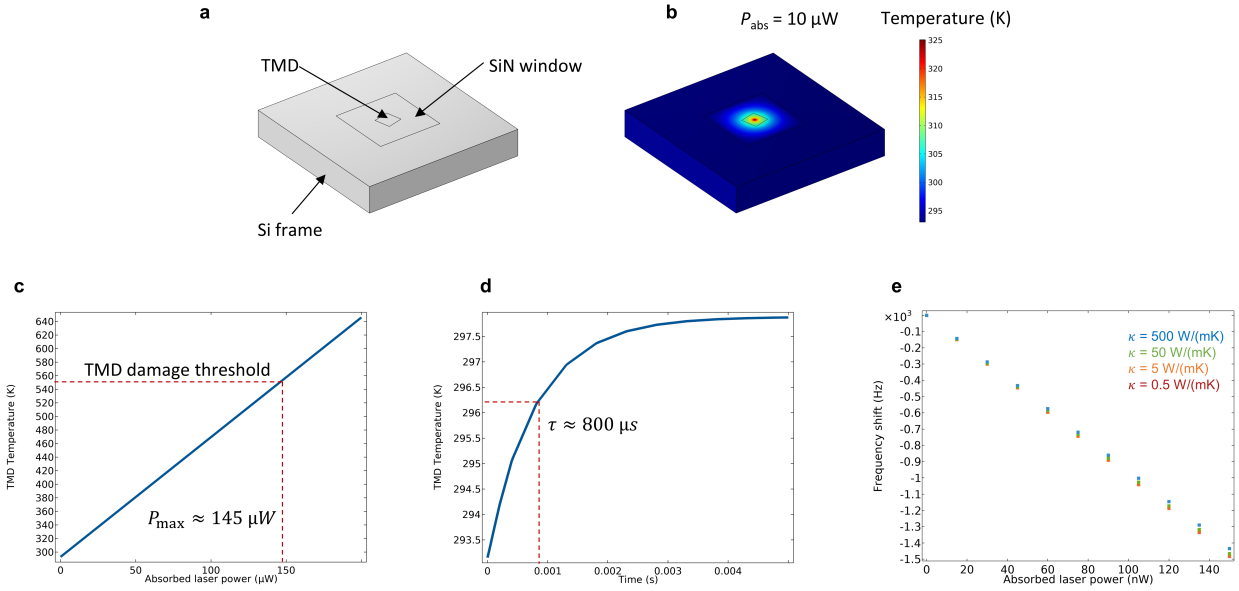

Supplementary Figure 1. FEM Simulations. **a**, Sketch of the device geometry **b**, Temperature profile upon laser illumination **c**, Resulting average temperature in the 3-layer WS_2 sample. **d** Simulated time response of the average temperature in the TMD as laser heating is introduced at t = 0. We extract a response time of $\tau = 800\,\mu s$. To determine the thermal response time, we simulate the average temperature of the TMD vs. time after turning on the illumination (Supplementary Fig. 1d). We extract a response time of $\tau \approx 800\,\mu s$. **e**, Simulated frequency shift vs. absorbed laser power analogue to Fig. 1e from the main text. We vary the thermal conductivity of the 2D materials over orders of magnitude and find 3.3% variation in responsivity.

1.3. Temperature depended responsivity

We aim to extend our NMS measurements to low temperatures. Upon cooling, the thermal constants of the SiN membrane change, which will affect the responsivity ($R_{100\%} \sim \frac{\alpha}{\kappa}$). To ensure that our measurements will work at low temperatures we perform preliminary tests with a bare SiN membrane (Norcada NX5150A). The membrane has higher built-in stress (σ_0 =240 MPa) to avoid buckling when the sample is cooled. In Supplementary Fig. 2a,b, we show the measured responsivity and the fundamental resonance frequency as a function of cryostat temperature. At liquid helium temperature, we find a responsivity comparable to the room temperature value. We conclude that NMS will work over a large range of temperatures.

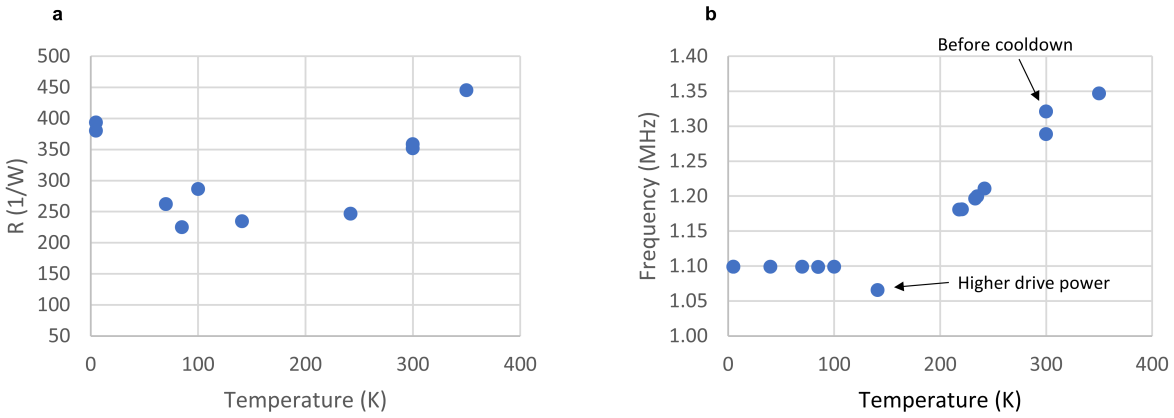

Supplementary Figure 2. Responsivity vs. device temperature. **a**, Responsivity of a SiN membrane (with $\sigma_0 = 240\,\mathrm{MPa}$) as a function of cryostat temperature. **b**, Simultaneously obtained resonance frequency of the sample.

1.4. Photoluminescence measurements

To estimate the portion of light that the TMD emits, which is therefore not converted into heat, we look at the quantum yield of comparable samples. In Ref. [1] they use photoluminescence (PL) measurements to determine the quantum yield of MoS_2 to be on the order of 10^{-5} - 10^{-6} for 2-6-layer samples and 4×10^{-3} in the limit of monolayer thickness. These numbers suggest that the emitted light is much smaller than the amount of absorbed light and thus can be neglected. Of course, the quantum yield depends on many factors and can be significantly higher under certain conditions. However, in our samples, we do not observe any PL from the TMD, only background signal from the SiN as shown below (Supplementary Fig. 3). The exact mechanism behind this suppression of emission is not entirely clear to us, but we regularly observe this effect, when TMDs are placed directly on SiN. The suppressed emission indicates a very small quantum yield for our samples and thus we think it is safe to assume that all the absorbed light is transferred into heat and detected by NMS.

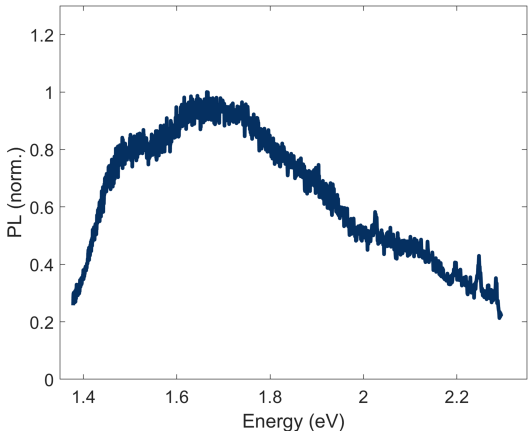

Supplementary Figure 3. Supressed photoluminescence on silicon nitride. Photoluminescence spectra for the trilayer WS_2 sample from the main text. We observe a broad background signal instead of pronounced emission peaks.

1.5. Background substraction

In order to account for the absorption in the underlying SiN membrane, we implement a background subtraction. Since the laser beam first illuminates the 2D material and then the transmitted light falls on the SiN membrane, the total absorption coefficient is given by: $Abs_{\mathrm{total}} = Abs_{\mathrm{2DM}} + (1 - Abs_{\mathrm{2DM}})Abs_{\mathrm{SiN}}$, which is the quantity we measure in our experiments (multiple reflections do not change this result significantly). Rearranging the equation yields:

$$Abs_{\mathrm{2DM}} = \frac{Abs_{\mathrm{total}} - Abs_{\mathrm{SiN}}}{1 - Abs_{\mathrm{SiN}}}, \tag{2}$$

which allows us to correct for the absorption in the SiN membrane. We perform the correction assuming a constant absorption of $Abs_{\mathrm{SiN}} = 0.5\,\%$, which is justified for most of the optical spectrum but might underestimate the absorption of SiN towards the UV range. In this region, the 2D material absorbs a larger fraction of light, such that the correction overall has a smaller effect. To illustrate the effect of the correction on the spectra, we show the plots with and without correction in linear and log-scale (Supplementary Fig. 4). We find a noticeable change towards the low energy end of the spectra, where the absorption in the 2D material is low.

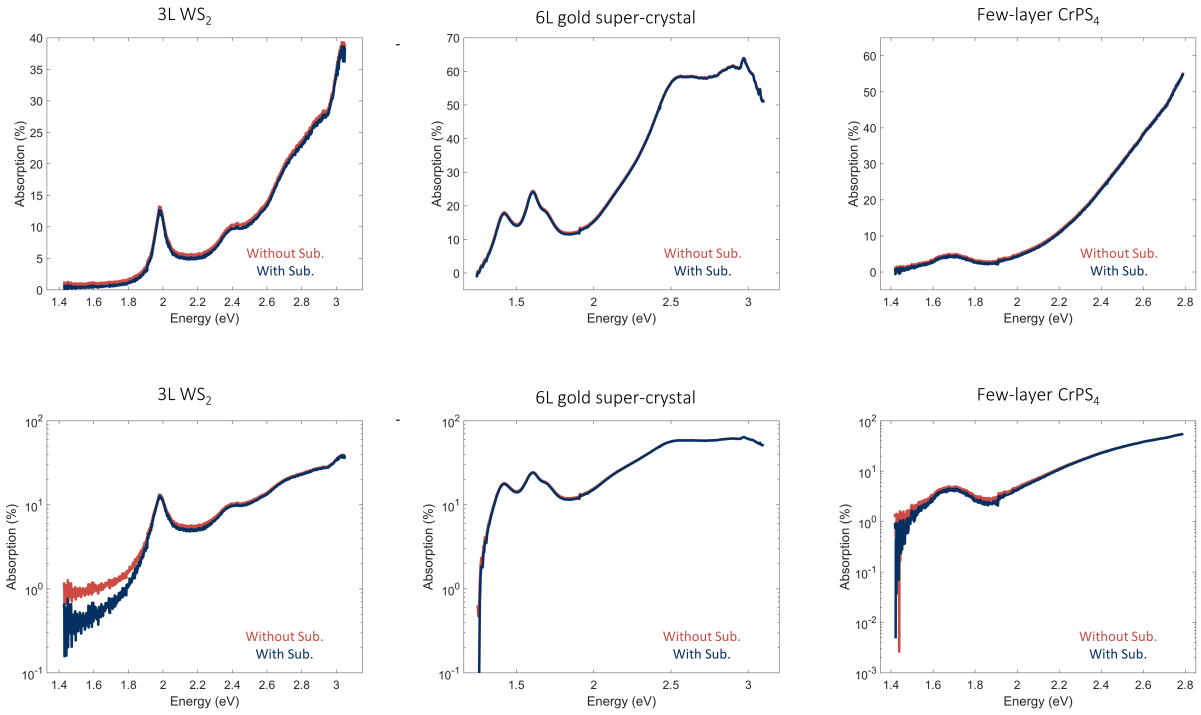

Supplementary Figure 4. Background subtraction. We plot the extracted absorption for the three samples shown in the main text with (blue) and without (red) accounting for the absorption in underlaying SiN membrane.

References

[1] Mak K F, Lee C, Hone J, Shan J and Heinz T F 2010 *Phys. Rev. Lett.* **105**(13) 136805 URL https://link.aps.org/doi/10.1103/PhysRevLett.105.136805

Acknowledgements

This thesis comes to an end, and I really hope you enjoyed reading it, and maybe you discovered some new aspects of the mechanics of 2D materials. It took the support and input from a lot of people to make this work possible, and I want to use this opportunity to express my gratitude.

First of all, I want to thank my supervisor, Prof. Kirill I. Bolotin, for his guidance and support over the past years. You had trust in me and gave me the freedom to chase some rather abstract ideas. At the same time, your view on science is inspiring and I learned a lot from you.

Next, I want to say thanks to Prof. Stephanie Reich, for supporting my research with her knowledge and resources, and for being the second referee of this thesis.

A big thank you goes to Yuefeng Yu, Kristina Weinel, Gabriel Antheaume, Sebastian Heeg, Ben Weintrub, Moshe Harats, Denis Yagodkin, Sviatoslav Kovalchuk, Nele Stetzuhn, Abhijeet Kumar, Oguzhan Yucel, Bianca Höfer, Hans Badow, and all other the members of the Bolotin group. This thesis would not have happened without you. I am grateful for every sample you made, the help you provided in the lab, the feedback you gave on my manuscripts, and all the good fun we had together.

I also want to thank Katja Höflich, Victor Deinhart, and Aleksei Tsarapkin for patterning the beautiful phononic crystal samples, that paved the way for my exploration of tunable phononics.

Furthermore, I want to thank Peter Elliott and Sangeeta Sharma for performing DFT calculations and thereby providing the theoretical background for some of my results.

Moreover, I want to express my gratitude to Georgy Gordeev and Daniel Brito de Araújo for their help and valuable input on the nanomechanical spectroscopy measurements.

In addition, I am grateful for the SiN samples, the CrP_4 crystals, and the input I received from Kostas Kanellopulos, Silvan Schmid, Samuel Manas-Valero, Eugenio Coronado, and Herre van der Zant.

I also want to thank all the other people from FU Berlin and other institutes that helped me during the course of this thesis.

Last but not least, I want to mention the endless support from my family and my friends. You were there for me all the way and made this whole thing here possible. **Thank you!**

Selbstständigkeitserklärung

Name: Kirchhof
Vorname: Jan Niklas

Ich erkläre gegenüber der Freien Universität Berlin, dass ich die vorliegende Dissertation selbstständig und ohne Benutzung anderer als der angegebenen Quellen und Hilfsmittel angefertigt habe. Die vorliegende Arbeit ist frei von Plagiaten. Alle Ausführungen, die wörtlich oder inhaltlich aus anderen Schriften entnommen sind, habe ich als solche kenntlich gemacht. Diese Dissertation wurde in gleicher oder ähnlicher Form noch in keinem früheren Promotionsverfahren eingereicht.

Mit einer Prüfung meiner Arbeit durch ein Plagiatsprüfungsprogramm erkläre ich mich einverstanden.

Datum: 16. Mai 2024

Unterschrift: _____

Bibliography

1. LEE, C. *et al.*, Measurement of the elastic properties and intrinsic strength of monolayer graphene. *Science*. 2008, vol. 321, no. 5887, pp. 385–388.
2. CAO, K. *et al.*, Elastic straining of free-standing monolayer graphene. *Nature communications*. 2020, vol. 11, no. 1, p. 284.
3. NOVOSELOV, K. S. *et al.*, Electric field effect in atomically thin carbon films. *Science*. 2004, vol. 306, no. 5696, pp. 666–669.
4. GEIM, A. K. *et al.*, The rise of graphene. *Nature Materials*. 2007, vol. 6, no. 3, pp. 183–191.
5. NETO, A. C. *et al.*, The electronic properties of graphene. *Reviews of Modern Physics*. 2009, vol. 81, no. 1, p. 109.
6. DE ALBA, R. *et al.*, Tunable phonon-cavity coupling in graphene membranes. *Nature Nanotechnology*. 2016, vol. 11, no. 9, pp. 741–746.
7. KEŞKEKLER, A. *et al.*, Tuning nonlinear damping in graphene nanoresonators by parametric–direct internal resonance. *Nature Communications*. 2021, vol. 12, no. 1, p. 1099.
8. EICHLER, A. *et al.*, Nonlinear damping in mechanical resonators made from carbon nanotubes and graphene. *Nature Nanotechnology*. 2011, vol. 6, no. 6, pp. 339–342.
9. SINGH, V. *et al.*, Negative nonlinear damping of a multilayer graphene mechanical resonator. *Physical Review B*. 2016, vol. 93, no. 24, p. 245407.
10. CROY, A. *et al.*, Nonlinear damping in graphene resonators. *Physical Review B*. 2012, vol. 86, no. 23, p. 235435.
11. ŠIŠKINS, M. *et al.*, Magnetic and electronic phase transitions probed by nanomechanical resonators. *Nature Communications*. 2020, vol. 11, no. 1, p. 2698.
12. ŠIŠKINS, M. *et al.*, Nanomechanical probing and strain tuning of the Curie temperature in suspended $Cr_2Ge_2Te_6$-based heterostructures. *npj 2D Materials and Applications*. 2022, vol. 6, no. 1, p. 41.
13. BARTON, R. A. *et al.*, Photothermal self-oscillation and laser cooling of graphene optomechanical systems. *Nano Letters*. 2012, vol. 12, no. 9, pp. 4681–4686.
14. MORELL, N. *et al.*, Optomechanical measurement of thermal transport in two-dimensional $MoSe_2$ lattices. *Nano Letters*. 2019, vol. 19, no. 5, pp. 3143–3150.

15. XIE, H. *et al.*, Tunable Exciton-Optomechanical Coupling in Suspended Monolayer $MoSe_2$. *Nano Letters*. 2021, vol. 21, no. 6, pp. 2538–2543.

16. DESAI, S. *et al.*, Vibration Characteristics of Graphene nano resonator as mass sensor. In: *Journal of Physics: Conference Series*. IOP Publishing, 2021, vol. 1854, p. 012029. No. 1.

17. LEE, H.-L. *et al.*, Mass detection using a graphene-based nanomechanical resonator. *Japanese Journal of Applied Physics*. 2013, vol. 52, no. 2R, p. 025101.

18. CHEN, C. *et al.*, Performance of monolayer graphene nanomechanical resonators with electrical readout. *Nature Nanotechnology*. 2009, vol. 4, no. 12, pp. 861–867.

19. LEMME, M. C. *et al.*, Nanoelectromechanical sensors based on suspended 2D materials. *Research*. 2020, vol. 2020.

20. BUNCH, J. S. *et al.*, Electromechanical resonators from graphene sheets. *Science*. 2007, vol. 315, no. 5811, pp. 490–493.

21. WEBER, P. *et al.*, Force sensitivity of multilayer graphene optomechanical devices. *Nature Communications*. 2016, vol. 7, no. 1, pp. 1–8.

22. KIRCHHOF, J. N. *et al.*, Tunable Graphene Phononic Crystal. *Nano Letters*. 2021, vol. 21, no. 5, pp. 2174–2182.

23. KIRCHHOF, J. N. *et al.*, Nanomechanical Spectroscopy of 2D Materials. *Nano Letters*. 2022, vol. 22, no. 20, pp. 8037–8044.

24. RADISAVLJEVIC, B. *et al.*, Single-layer MoS_2 transistors. *Nature Nanotechnology*. 2011, vol. 6, no. 3, pp. 147–150.

25. KUSHWAHA, M. S. *et al.*, Acoustic band structure of periodic elastic composites. *Phys. Rev. Lett.* 1993, vol. 71, pp. 2022–2025.

26. SIGALAS, M. *et al.*, Band structure of elastic waves in two dimensional systems. *Solid State Communications*. 1993, vol. 86, no. 3, pp. 141–143.

27. PAGE, J. H. *et al.*, Phononic crystals. *Physica Status Solidi (b)*. 2004, vol. 241, no. 15, pp. 3454–3462.

28. KHELIF, A. *et al.*, Phononic crystals. *Berlin, Germany, Springer*. 2015, vol. 10, pp. 978–1.

29. MALDOVAN, M., Sound and heat revolutions in phononics. *Nature*. 2013, vol. 503, no. 7475, pp. 209–217.

30. KHELIF, A. *et al.*, Guiding and bending of acoustic waves in highly confined phononic crystal waveguides. *Applied Physics Letters*. 2004, vol. 84, no. 22, pp. 4400–4402.

31. PENNEC, Y. *et al.*, Two-dimensional phononic crystals: Examples and applications. *Surface Science Reports*. 2010, vol. 65, no. 8, pp. 229–291.

32. OLSSON, R. H. *et al.*, Microfabricated phononic crystal devices and applications. *Measurement Science and Technology*. 2008, vol. 20, no. 1, p. 012002.

33. ANUFRIEV, R. *et al.*, Heat guiding and focusing using ballistic phonon transport in phononic nanostructures. *Nature Communications*. 2017, vol. 8, no. 1, p. 15505.

34. LIN, S.-C. S. *et al.*, Gradient-index phononic crystals. *Physical Review B*. 2009, vol. 79, no. 9, p. 094302.

35. ZHAO, J. *et al.*, Beam path and focusing of flexural Lamb waves within phononic crystal-based acoustic lenses. *New Journal of Physics*. 2014, vol. 16, no. 6, p. 063031.

36. TSATURYAN, Y. *et al.*, Ultracoherent nanomechanical resonators via soft clamping and dissipation dilution. *Nature Nanotechnology*. 2017, vol. 12, no. 8, pp. 776–783.

37. GHADIMI, A. H. *et al.*, Radiation and internal loss engineering of high-stress silicon nitride nanobeams. *Nano Letters*. 2017, vol. 17, no. 6, pp. 3501–3505.

38. GHADIMI, A. H. *et al.*, Elastic strain engineering for ultralow mechanical dissipation. *Science*. 2018, vol. 360, no. 6390, pp. 764–768.

39. LI, F. *et al.*, The investigation of point defect modes of phononic crystal for high Q resonance. *Journal of Applied Physics*. 2011, vol. 109, no. 12, p. 124907.

40. YU, P. L. *et al.*, A phononic bandgap shield for high-Q membrane microresonators. *Applied Physics Letters*. 2014, vol. 104, no. 2, p. 23510.

41. THOMAS, R. A. *et al.*, Entanglement between distant macroscopic mechanical and spin systems. *Nature Physics*. 2021, vol. 17, no. 2, pp. 228–233.

42. CHIEN, M.-H. *et al.*, Single-molecule optical absorption imaging by nanomechanical photothermal sensing. *Proceedings of the National Academy of Sciences*. 2018, vol. 115, no. 44, pp. 11150–11155.

43. VERBRIDGE, S. S. *et al.*, High quality factor resonance at room temperature with nanostrings under high tensile stress. *Journal of Applied Physics*. 2006, vol. 99, no. 12, p. 124304.

44. SCHMID, S. *et al.*, Damping mechanisms in high-Q micro and nanomechanical string resonators. *Phys. Rev. B*. 2011, vol. 84, p. 165307.

45. LUKE, K. *et al.*, Overcoming Si_3N_4 film stress limitations for high quality factor ring resonators. *Opt. Express*. 2013, vol. 21, no. 19, pp. 22829–22833.

46. FONG, K. Y. *et al.*, Frequency and phase noise of ultrahigh Q silicon nitride nanomechanical resonators. *Phys. Rev. B.* 2012, vol. 85, p. 161410.

47. DEINHART, V. *et al.*, The patterning toolbox FIB-o-mat: Exploiting the full potential of focused helium ions for nanofabrication. *Beilstein Journal of Nanotechnology.* 2021, vol. 12, no. 1, pp. 304–318.

48. KIRCHHOF, J. N. *et al.*, Mechanically-tunable bandgap closing in 2D graphene phononic crystals. *npj 2D Materials and Applications.* 2023, vol. 7, no. 1, p. 10.

49. MA, L. *et al.*, Strongly correlated excitonic insulator in atomic double layers. *Nature.* 2021, vol. 598, no. 7882, pp. 585–589.

50. GU, J. *et al.*, Dipolar excitonic insulator in a moiré lattice. *Nature Physics.* 2022, vol. 18, no. 4, pp. 395–400.

51. ZHOU, Y. *et al.*, Bilayer Wigner crystals in a transition metal dichalcogenide heterostructure. *Nature.* 2021, vol. 595, no. 7865, pp. 48–52.

52. REGAN, E. C. *et al.*, Mott and generalized Wigner crystal states in WSe_2/WS_2 moiré superlattices. *Nature.* 2020, vol. 579, no. 7799, pp. 359–363.

53. WANG, Z. *et al.*, Evidence of high-temperature exciton condensation in two-dimensional atomic double layers. *Nature.* 2019, vol. 574, no. 7776, pp. 76–80.

54. TARTAKOVSKII, A., Excitons in 2D heterostructures. *Nature Reviews Physics.* 2020, vol. 2, no. 1, pp. 8–9.

55. NOVOSELOV, K. S. *et al.*, 2D materials and van der Waals heterostructures. *Science.* 2016, vol. 353, no. 6298, aac9439.

56. LIU, H.-L. *et al.*, Optical properties of monolayer transition metal dichalcogenides probed by spectroscopic ellipsometry. *Applied Physics Letters.* 2014, vol. 105, no. 20, p. 201905.

57. LI, W. *et al.*, Broadband optical properties of large-area monolayer CVD molybdenum disulfide. *Physical Review B.* 2014, vol. 90, no. 19, p. 195434.

58. YIM, C. *et al.*, Investigation of the optical properties of MoS_2 thin films using spectroscopic ellipsometry. *Applied Physics Letters.* 2014, vol. 104, no. 10, p. 103114.

59. SHEN, C.-C. *et al.*, Charge dynamics and electronic structures of monolayer MoS_2 films grown by chemical vapor deposition. *Applied Physics Express.* 2013, vol. 6, no. 12, p. 125801.

60. HECHT, E., Optics (Addision Wesley, San Francisco). *Chap.* 2002, vol. 10, p. 500.

61. KRAMERS, H. A., The quantum theory of dispersion. *Nature.* 1924, vol. 114, no. 2861, pp. 310–311.

62. L, K. R. de, On the theory of the dispersion of x-rays. *J. Opt. Soc. Am.* 1926, vol. 12, no. 6, pp. 547–557.

63. LI, Y. *et al.*, Measurement of the optical dielectric function of monolayer transition-metal dichalcogenides: MoS_2, $MoSe_2$, WS_2, and WSe_2. *Physical Review B*. 2014, vol. 90, no. 20, p. 205422.

64. NOORI, Y. J. *et al.*, Photonic crystals for enhanced light extraction from 2D materials. *Acs Photonics*. 2016, vol. 3, no. 12, pp. 2515–2520.

65. ZHANG, L. *et al.*, Photonic-crystal exciton-polaritons in monolayer semiconductors. *Nature Communications*. 2018, vol. 9, no. 1, p. 713.

66. STEENEKEN, P. G. *et al.*, Dynamics of 2D material membranes. *2D Materials*. 2021, vol. 8, no. 4, p. 042001.

67. XU, B. *et al.*, Nanomechanical Resonators: Toward Atomic Scale. *ACS Nano*. 2022, vol. 16, no. 10, pp. 15545–15585.

68. WITTMANN, S. *et al.*, Graphene Membranes for Hall Sensors and Microphones Integrated with CMOS-Compatible Processes. *ACS Applied Nano Materials*. 2019, vol. 2, no. 8, pp. 5079–5085.

69. JIANG, S. *et al.*, Exchange magnetostriction in two-dimensional antiferromagnets. *Nature Materials*. 2020, vol. 19, no. 12, pp. 1295–1299.

70. VERBIEST, G. J. *et al.*, Detecting ultrasound vibrations with graphene resonators. *Nano Letters*. 2018, vol. 18, no. 8, pp. 5132–5137.

71. BAGLIONI, G. *et al.*, Ultra-sensitive graphene membranes for microphone applications. *Nanoscale*. 2023.

72. PEZONE, R. *et al.*, Sensitive Transfer-Free Wafer-Scale Graphene Microphones. *ACS Applied Materials & Interfaces*. 2022, vol. 14, no. 18, pp. 21705–21712.

73. DOLLEMAN, R. J. *et al.*, Squeeze-Film Effect on Atomically Thin Resonators in the High-Pressure Limit. *Nano Letters*. 2021, vol. 21, no. 18, pp. 7617–7624.

74. ROSŁOŃ, I. E. *et al.*, Probing nanomotion of single bacteria with graphene drums. *Nature Nanotechnology*. 2022, pp. 1–6.

75. BALANDIN, A. A. *et al.*, Superior thermal conductivity of single-layer graphene. *Nano Letters*. 2008, vol. 8, no. 3, pp. 902–907.

76. NOVOSELOV, K. S. *et al.*, A roadmap for graphene. *Nature*. 2012, vol. 490, no. 7419, pp. 192–200.

77. CAO, Y. *et al.*, Unconventional superconductivity in magic-angle graphene superlattices. *Nature*. 2018, vol. 556, no. 7699, pp. 43–50.

78. BOLOTIN, K. I. *et al.*, Observation of the fractional quantum Hall effect in graphene. *Nature*. 2009, vol. 462, no. 7270, pp. 196–199.

79. MIRSKY, S. *et al.*, Elephant Illustrates Important Point. *Scientific American* [scientificamerican.com/article/balancing-act/]. 2011. [Accessed 16-February-2023].

80. BOLOTIN, K. *et al.*, Ultrahigh electron mobility in suspended graphene. *Solid State Communications*. 2008, vol. 146, no. 9, pp. 351–355.

81. NAIR, R. R. *et al.*, Fine structure constant defines visual transparency of graphene. *Science*. 2008, vol. 320, no. 5881, pp. 1308–1308.

82. WIKIPEDIA, *Graphene* [en.wikipedia.org/wiki/Graphene]. 2023. [Accessed 16-February-2023].

83. MAK, K. F. *et al.*, Atomically Thin MoS_2: A New Direct-Gap Semiconductor. *Phys. Rev. Lett.* 2010, vol. 105, p. 136805.

84. SPLENDIANI, A. *et al.*, Emerging Photoluminescence in Monolayer MoS_2. *Nano Letters*. 2010, vol. 10, no. 4, pp. 1271–1275.

85. HERNÁNDEZ LÓPEZ, P. *et al.*, Strain control of hybridization between dark and localized excitons in a 2D semiconductor. *Nature Communications*. 2022, vol. 13, no. 1, p. 7691.

86. SCHWIERZ, F. *et al.*, Two-dimensional materials and their prospects in transistor electronics. *Nanoscale*. 2015, vol. 7, no. 18, pp. 8261–8283.

87. WEINTRUB, B. I. *et al.*, Generating intense electric fields in 2D materials by dual ionic gating. *Nature Communications*. 2022, vol. 13, no. 1, p. 6601.

88. WIKIPEDIA, *Transition metal dichalcogenide monolayers* [en.wikipedia.org/wiki/Transition_metal_dichalcogenide_monolayers]. 2023. [Accessed 11-February-2023].

89. OSSILA LTD., *Molybdenum disulfide, MoS_2: Theory, Structure and Applications* [ossila.com/en-eu/pages/molybdenum-disulfide-mos2]. 2023. [Accessed 21-February-2023].

90. HAUER, B. *et al.*, A general procedure for thermomechanical calibration of nano/micro-mechanical resonators. *Annals of Physics*. 2013, vol. 339, pp. 181–207.

91. ALBRECHT, T. R. *et al.*, Frequency modulation detection using high-Q cantilevers for enhanced force microscope sensitivity. *Journal of Applied Physics*. 1991, vol. 69, no. 2, pp. 668–673.

92. BOKAIAN, A., Natural frequencies of beams under tensile axial loads. *Journal of Sound and Vibration*. 1990, vol. 142, no. 3, pp. 481–498.

93. MICHELSON, A. A. *et al.*, LVIII. On the relative motion of the earth and the luminiferous Æther. *The London, Edinburgh, and Dublin Philosophical Magazine and Journal of Science*. 1887, vol. 24, no. 151, pp. 449–463.

94. LAWALL, J. *et al.*, Michelson interferometry with 10 pm accuracy. *Review of Scientific Instruments*. 2000, vol. 71, no. 7, pp. 2669–2676.

95. LIBBRECHT, K. G. *et al.*, A basic Michelson laser interferometer for the undergraduate teaching laboratory demonstrating picometer sensitivity. *American Journal of Physics*. 2015, vol. 83, no. 5, pp. 409–417.

96. ABBOTT, B. P. *et al.*, GW150914: The Advanced LIGO detectors in the era of first discoveries. *Physical review letters*. 2016, vol. 116, no. 13, p. 131103.

97. FABRY, C., Theorie et applications d'une nouvelle methods de spectroscopie intereferentielle. *Ann. Chim. Ser. 7*. 1899, vol. 16, pp. 115–144.

98. PEROT, A. *et al.*, On the application of interference phenomena to the solution of various problems of spectroscopy and metrology. *Astrophysical Journal, vol. 9, p. 87*. 1899, vol. 9, p. 87.

99. DAVIDOVIKJ, D. *et al.*, Visualizing the motion of graphene nanodrums. *Nano Letters*. 2016, vol. 16, no. 4, pp. 2768–2773.

100. CHEN, C. *et al.*, Modulation of mechanical resonance by chemical potential oscillation in graphene. *Nature Physics*. 2016, vol. 12, no. 3, pp. 240–244.

101. MEI, T. *et al.*, Frequency tuning of graphene nanoelectromechanical resonators via electrostatic gating. *Micromachines*. 2018, vol. 9, no. 6, p. 312.

102. YE, F. *et al.*, Ultrawide Frequency Tuning of Atomic Layer van der Waals Heterostructure Electromechanical Resonators. *Nano Letters*. 2021, vol. 21, no. 13, pp. 5508–5515.

103. KOVALCHUK, S. *et al.*, Neutral and charged excitons interplay in non-uniformly strain-engineered WS_2. *2D Materials*. 2020, vol. 7, no. 3, p. 035024.

104. KOVALCHUK, S. *et al.*, Non-Uniform Strain Engineering of 2D Materials. *Israel Journal of Chemistry*. 2022, vol. 62, no. 3-4, e202100115.

105. HARATS, M. G. *et al.*, Dynamics and efficient conversion of excitons to trions in non-uniformly strained monolayer WS_2. *Nature Photonics*. 2020, vol. 14, no. 5, pp. 324–329.

106. CHAUNSALI, R. *et al.*, Stress wave isolation by purely mechanical topological phononic crystals. *Scientific reports*. 2016, vol. 6, no. 1, pp. 1–10.

107. KIRCHHOF, J. N. *et al.*, Nanomechanical absorption spectroscopy of 2D materials with femtowatt sensitivity. *2D Materials*. 2023.

108. CHOU, M.-H. *et al.*, Measurements of a quantum bulk acoustic resonator using a superconducting qubit. *Applied Physics Letters*. 2020, vol. 117, no. 25, p. 254001.

109. RIEDINGER, R. *et al.*, Remote quantum entanglement between two micromechanical oscillators. *Nature*. 2018, vol. 556, no. 7702, pp. 473–477.

110. WOLLACK, E. A. *et al.*, Quantum state preparation and tomography of entangled mechanical resonators. *Nature*. 2022, vol. 604, no. 7906, pp. 463–467.

111. ZIVARI, A. *et al.*, Non-classical mechanical states guided in a phononic waveguide. *Nature Physics*. 2022, vol. 18, no. 7, pp. 789–793.

112. MIRHOSSEINI, M. *et al.*, Superconducting qubit to optical photon transduction. *Nature*. 2020, vol. 588, no. 7839, pp. 599–603.

113. ZHANG, X. *et al.*, 2D Materials Beyond Graphene for High-Performance Energy Storage Applications. *Advanced Energy Materials*. 2016, vol. 6, no. 23, p. 1600671.

114. MENDOZA-SÁNCHEZ, B. *et al.*, Synthesis of two-dimensional materials for capacitive energy storage. *Advanced Materials*. 2016, vol. 28, no. 29, pp. 6104–6135.

115. PU, J. *et al.*, Monolayer transition metal dichalcogenides as light sources. *Advanced Materials*. 2018, vol. 30, no. 33, p. 1707627.

116. CHOI, W. *et al.*, Recent development of two-dimensional transition metal dichalcogenides and their applications. *Materials Today*. 2017, vol. 20, no. 3, pp. 116–130.

117. DAS, S. *et al.*, The role of graphene and other 2D materials in solar photovoltaics. *Advanced Materials*. 2019, vol. 31, no. 1, p. 1802722.

118. LIU, M. *et al.*, A graphene-based broadband optical modulator. *Nature*. 2011, vol. 474, no. 7349, pp. 64–67.

119. SUN, Z. *et al.*, Optical modulators with 2D layered materials. *Nature Photonics*. 2016, vol. 10, no. 4, pp. 227–238.

120. LOPEZ-SANCHEZ, O. *et al.*, Ultrasensitive photodetectors based on monolayer MoS_2. *Nature Nanotechnology*. 2013, vol. 8, no. 7, pp. 497–501.

121. WAN, X. *et al.*, Controlled Electrochemical Deposition of Large-Area $MoS_2$2 on Graphene for High-Responsivity Photodetectors. *Advanced Functional Materials*. 2017, vol. 27, no. 19, p. 1603998.

122. LEE, J. *et al.*, Structural and Optical Properties of Single- and Few-Layer Magnetic Semiconductor $CrPS_4$. *ACS Nano*. 2017, vol. 11, no. 11, pp. 10935–10944.

123. GU, P. *et al.*, Photoluminescent Quantum Interference in a van der Waals Magnet Preserved by Symmetry Breaking. *ACS Nano*. 2020, vol. 14, no. 1, pp. 1003–1010.

124. KIM, S. *et al.*, Photoluminescence Path Bifurcations by Spin Flip in Two-Dimensional CrPS4. *ACS Nano*. 2022, vol. 16, no. 10, pp. 16385–16393.

125. MUELLER, N. S. *et al.*, Deep strong light–matter coupling in plasmonic nanoparticle crystals. *Nature*. 2020, vol. 583, no. 7818, pp. 780–784.

126. MUELLER, N. S. *et al.*, Surface-Enhanced Raman Scattering and Surface-Enhanced Infrared Absorption by Plasmon Polaritons in Three-Dimensional Nanoparticle Supercrystals. *ACS Nano*. 2021, vol. 15, no. 3, pp. 5523–5533.

127. YU, Y. *et al.*, Towards tunable graphene phononic crystals. *arXiv preprint: 2301.00116*. 2023.

128. KONIG, M. *et al.*, Quantum spin Hall insulator state in HgTe quantum wells. *Science*. 2007, vol. 318, no. 5851, pp. 766–770.

129. BERNEVIG, B. A. *et al.*, Quantum spin Hall effect and topological phase transition in HgTe quantum wells. *Science*. 2006, vol. 314, no. 5806, pp. 1757–1761.

130. HASAN, M. Z. *et al.*, Colloquium: topological insulators. *Reviews of Modern Physics*. 2010, vol. 82, no. 4, p. 3045.

131. HSIEH, D. *et al.*, A topological Dirac insulator in a quantum spin Hall phase. *Nature*. 2008, vol. 452, no. 7190, pp. 970–974.

132. NASSAR, H. *et al.*, Nonreciprocity in acoustic and elastic materials. *Nature Reviews Materials*. 2020, vol. 5, no. 9, pp. 667–685.

133. TIAN, Z. *et al.*, Dispersion tuning and route reconfiguration of acoustic waves in valley topological phononic crystals. *Nature Communications*. 2020, vol. 11, no. 1, p. 762.

134. REN, H. *et al.*, Topological phonon transport in an optomechanical system. *Nature Communications*. 2022, vol. 13, no. 1, p. 3476.

135. XIA, B.-Z. *et al.*, Topological phononic insulator with robust pseudospin-dependent transport. *Physical Review B*. 2017, vol. 96, no. 9, p. 094106.

136. CAO, Y. *et al.*, Correlated insulator behaviour at half-filling in magic-angle graphene superlattices. *Nature*. 2018, vol. 556, no. 7699, pp. 80–84.

137. DENG, Y. *et al.*, Magic-angle bilayer phononic graphene. *Physical Review B*. 2020, vol. 102, no. 18, p. 180304.

138. ZHENG, S. *et al.*, Topological network and valley beam splitter in acoustic biaxially strained moiré superlattices. *Physical Review B*. 2022, vol. 105, no. 18, p. 184104.

139. JIN, Y. *et al.*, Topological states in twisted pillared phononic plates. *Extreme Mechanics Letters*. 2020, vol. 39, p. 100777.

140. OUDICH, M. *et al.*, Twisted pillared phononic crystal plates. *Applied Physics Letters*. 2022, vol. 120, no. 23, p. 232202.

141. LI, Y. *et al.*, Emergent phenomena in magnetic two-dimensional materials and van der waals heterostructures. *ACS Applied Electronic Materials*. 2022, vol. 4, no. 7, pp. 3278–3302.

142. GIBERTINI, M. *et al.*, Magnetic 2D materials and heterostructures. *Nature Nanotechnology*. 2019, vol. 14, no. 5, pp. 408–419.

143. JIANG, X. *et al.*, Recent progress on 2D magnets: Fundamental mechanism, structural design and modification. *Applied Physics Reviews*. 2021, vol. 8, no. 3, p. 031305.

144. SINGH, R. *et al.*, Motion transduction with thermo-mechanically squeezed graphene resonator modes. *Nano Letters*. 2018, vol. 18, no. 11, pp. 6719–6724.

145. SINGH, R. *et al.*, Giant tunable mechanical nonlinearity in graphene–silicon nitride hybrid resonator. *Nano Letters*. 2020, vol. 20, no. 6, pp. 4659–4666.

146. METZGER, C. H. *et al.*, Cavity cooling of a microlever. *Nature*. 2004, vol. 432, no. 7020, pp. 1002–1005.

147. METZGER, C. *et al.*, Optical self cooling of a deformable Fabry-Perot cavity in the classical limit. *Physical Review B*. 2008, vol. 78, no. 3, p. 035309.